ELNAGMI

STRUCTURE-PROPERTY-PROCESS STUDIES DURING AXIAL FEED HOT FORMING AND FRACTURE OF EXTRUDED POLYPROPYLENE TUBES

Ph.D.

STRUCTURE-PROPERTY-PROCESS STUDIES DURING AXIAL FEED HOT FORMING AND FRACTURE OF EXTRUDED POLYPROPYLENE TUBES

By

MOHAMED ELNAGMI, B.Sc., M.Sc. (MECHANICAL ENGINEERING)

A Thesis

Submitted to the School of Graduate Studies

in Partial Fulfillment of the Requirements

for the Degree

Doctor of Philosophy

McMaster University

DOCTOR OF PHILOSOPHY (2009) McMASTER UNIVERSITY

(Mechanical Engineering) Hamilton, Ontario, Canada

TITLE: Structure-Property-Process Studies during Axial Feed Hot forming and Fracture of Extruded Polypropylene Tubes

AUTHOR: Mohamed A. Elnagmi, B.Sc., M.Sc. (Mechanical Engineering, Al-Fatah University)

SUPERVISOR: Professor M. K. Jain

NUMBER OF PAGES: xxxi, 217

Abstract

Oriented thermoplastics offer interesting opportunities for making structural automotive components due to their higher strengths. A new process, referred to as the axial feed hot oil tube forming (AF-HOTF) process, has been developed and studied for the forming of oriented thermoplastic tubes. The starting material for AF-HOTF process is an oriented polypropylene (OPP) tube produced by the solid state extrusion process. AF-HOTF was used to study forming and fracture behaviour of OPP tubes at large strains.

Mechanical properties and molecular orientation of starting and post-formed materials were investigated to gain a better understanding of structure-property-process relationships during solid state extrusion and subsequent forming of OPP tubes. The development of molecular orientation and other microstructural changes and damage development in extruded and bulged OPP tubes during solid state extrusion and AF-HOTF processes were studied with optical microscopy, wide-angle X-ray diffraction (WAXD) and field emission scanning electron microscope (FE-SEM) techniques. Also, the development of large strains during AF-HOTF of OPP samples were experimentally studied in the form of spatial strain maps, strain/stress state and forming limit strains using an on-line strain mapping method based on digital image correlation (DIC). In addition, tensile tests have been carried out at room temperature on samples machined from the extruded and bulged tubes along the axial and hoop directions.

Experimental quantitative relationships amongst molecular orientation parameters and extrusion and AF-HOTF process parameters such as draw ratio, strain and strain state have been obtained. These relationships in the form of White and Spruiell biaxial orientation factors provide a useful insight into molecular reorientation that occurs during extrusion and subsequent forming of OPP tubes. Also, an analytical model for forming limit prediction that takes into account OPP tube properties, tube dimensions and AF-HOTF process parameters was developed based on existing model of tube hydroforming in the literature.

In addition, a new biaxial ball stretching test (BBST) system was developed and utilized to subject the thermoplastic tube to biaxial stretching. The design of the test-rig and results were presented for polypropylene (PP) tubes subjected to BBST at various temperatures. The BBST system was combined with an available on-line imaging and strain analysis system (ARAMIS® system from GOM) to observe the development of strains in the biaxial tensile region during the test. BBST samples were studied with wide angle X-ray diffraction (WAXD) pole figures.

Three different hot forming processes (Solid-state extrusion, AF-HOTF and BBST) were used in this research. The structure of the extruded samples at draw ratio 5 and higher was completely changed to fibrils structure, and the yield strength and elastic modulus increased by 50%. Also the crystallinity increased from 47% to 68% with an increase in draw ratio. An increase in axial feed during the hot forming process resulted

in higher formability (strains values of 0.55 major strain and -0.25 minor strain) and delayed failure. The analytical model prediction of bursting shows good agreement with the experimental results.

The results provide an understanding of the orientation development in solid state extrusion of PP tubes as well as an understanding of tube formability, flow localization and fracture characteristics of PP tube from AF-HOTF process and other related processes.

Acknowledgements

First and foremost, praise be to God, Who created the heavens and the earths, made the darkness and light, and taught man that which he knew not.

I would express my deepest gratitude to Professor Mukesh Jain, my supervisor, for his guidance and patience throughout this research thesis work. Professor Jain has always encouraged me to think creatively and deeply into many aspects of this research work.

I would also like to thank Dr. M. Bruhis, Research Engineer, in the Materials Forming Laboratory of the McMaster Manufacturing Research Institute. His efforts and valuable assistance in helping with design and commissioning of the test equipment as well as for carrying out the experiments successfully is much appreciated.

I would also like to sincerely thank my thesis supervisory committee members, Dr. M. Thompson, Dr. J. R. McDermid and Dr. D. Metzger for their comments, helpful suggestions and for the time they spent reviewing my earlier progress reports and this thesis.

I would like to thank the Libyan Scholarship Program, Decoma International Inc., PSAC and the Natural Sciences and Engineering Research Council for financial support of this research. I would also thank Mr. Ealrlby Wakefield and Mr. Keith Ward of

Decoma and Dr. Frank Maine and Mr. Bill Newson of PSAC for their help with tube production and material characterization trials.

I will always be grateful for the help, cooperation, and cheer that I received from my dear friends and colleagues in the Department of Mechanical Engineering. In particular, I would like to thank Elizabeth Azhikannickal, Quan Situ, Diaa Elkott, Mohamed ElTobgy and Omar Omar.

Many thanks to the Mechanical Engineering technicians, Ron Lodewyks, Joe Verhaeghe, Mark Mackenzie, Dave Schick and Jim McLaren for their help and continuous support during the machining of PP tubes and commissioning of the tube hot forming test rig.

I would like to extend my thanks to Ms. Janet Murphy, Ms. Betty Anne Bedell-Ryc and Ms. Florence Rosato and for their warm reception, instantaneous help and general administrative support during my stay at McMaster.

Special thanks are to Dr. J. Britten from the Department of Chemical Engineering for his extended technical help with X-ray diffraction experiments and interpretation of some of the results.

Finally, I would like to thank my parents for their understanding, endless patience and encouragement. I am also grateful to my wife for her great support throughout my studies. To her, and to our amazing children, I present this work.

Contents

List of Tables

List of Figures

Nomenclature

b^c	half width at half height for the diffraction peak (Figure C.1)
d_i, d_o	initial inner and outer tube diameter
DR	Extrusion Draw ratio
F	compressive axial force applied to the tube during forming
F, G, H, L, M and N	anisotropy parameters in Hill's quadratic yield criterion
$f_{j,n}$	Herman's orientation factor where j-crystallographic axis (j= a, b or c) and processing direction (n= ED, TD and ND)
f	fiber axis of OPP test samples for WAXD
f_c	fractional crystallinity
$f^B_{ED,j}$	biaxial orientation factor in extrusion direction (j= a, b or c axes)
$f^B_{TD,j}$	biaxial orientation factor in transverse direction (j= a, b or c axes)
$f^c(g)$	Gaussian model function
g^c	preferred orientation
h	bulge height
h	preferred crystal direction
I_c	intensity of the detector signal
I_c	integrated areas of crystalline diffraction peaks

I_a	integrated areas of amorphous diffraction peaks
K	strength coefficient in power law ($\sigma = K\varepsilon^n$)
K_C	crystal axis (monoclinic crystal system)
K_S	sample axis (coordinate system)
l_f	length of the 'free' tube
l_o	initial tube length
n	work hardening exponent
Ph(y)	volume fraction of crystallites (from Multex Area 2 software)
p_i	internal pressure
R	normal anisotropy parameter in Hill's anisotropic theory
R_0	strain ratio in axial direction ($=\varepsilon_2/\varepsilon_3$)
R_{90}	strain ratio in hoop direction ($=\varepsilon_1/\varepsilon_3$)
r	Current radius of bulge in tube bulging
r_d	clamp profile radius in tube bulging (Figure B.2)
s	axial feeding displacement
T_c	crystallization temperature
T_m	melting temperature
t	thickness of lamellar crystals (also current tube thickness)
λ	X-ray wavelength
θ	half of the diffraction angle
β	strain ratio ($=\varepsilon_2/\varepsilon_1$)

α	stress ratio ($=\sigma_2/\sigma_1$)
ω	orientation distance (Figure C.2)
ε_1	strain along hoop direction
ε_2	strain along axial direction
ε_3	strain along thickness direction
$\bar{\varepsilon}$	effective strain
ε_1^c, ε_2^c	critical principal strains
$\phi_{j,n}$	angle between the j-crystallographic axis (j= a, b or c) and processing direction (n= ED, TD and ND)
σ_1	principal hoop stress
σ_2	principal axial stress
$\bar{\sigma}$	effective stress
ρ_1	radius of the tube along the hoop direction
ρ_2	radius of the tube along the axial direction
χ^2	least squares (from Multex Area 2 software)

Chapter 1

Introduction and Objectives

1.1 Oriented Thermoplastic Tubes Produced by Solid-state Deformation Processes

Achievement of a high modulus in polymers depends on the draw ratio (i.e., the ratio of initial cross sectional area to the final product). A high modulus and strength polymer can be produced by using solid-state deformation processes, such as extrusion and drawing that work toward orienting the molecules of a polymer in the axial direction. This process is carried out at a temperature close to the melting point of polymer. In general, however, the strength of the extruded product is adversely affected in the transverse (or hoop) direction. The ductility is reduced along the extrusion axis but remains largely unaffected in the transverse direction. The material as a whole becomes highly anisotropic after solid-state extrusion. This anisotropy persists during forming of the tube at high temperature. It is not known how this will affect the forming behaviour.

The advantages (and disadvantages) of the solid-state extruded tube versus conventional melt extruded tube are [Maier and Calafut, 1998]:

1. The solid state extruded tube is produced at a temperature close to the melting point. Under this condition the thermoplastic material is relatively strong. So solid-state extruded tube requires more force than melt state extruded tube and results in higher residual stresses.
2. Wall thickness distribution is more even in convention melt extruded tube compared to solid-state extruded tube.
3. A better transparency exists in solid-state extruded tube and less heat resistance.
4. The mechanical property parameters such as yield strength of solid-state extruded tube are higher than the melt-state extruded tube.
5. Solid-state extruded tube is more anisotropic due to the orientation that occurs during the process.

When the polymer crystallizes with no external forces, the polymer chains are arranged randomly. Preferred orientation can occur if the polymer is subjected to external forces (stress) after crystallization while the polymer is still hot. The stretching is usually carried out at a temperature slightly below the melting temperature. Orientation is used to tailor mechanical properties of films, fibers and various blow-molded parts (sheets, rods and tubes) [Maier and Calafut, 1998].

Skin-core formation of polymer objects arise from melt-processing as a result of shearing forces generated between the die wall and the polymer melt during extrusions of polymers. These variations of orientation through the thickness may lead to early fracture

and, as a consequence, reduce the final mechanical properties of the object. This phenomena has been studied in detail for melt extrusion of polymers [Gamez-perez et. al., 2005 and Hua-shan et.al., 2006]. However, the orientation of chains through the thickness of polymer tube and its influence on microstructure changes during solid state extrusion have not been studied.

1.2 Conventional Metal Tube Hydroforming and Conventional Thermoplastic Tube Hot Forming Methods

The main objective of the manufacturing process is to produce parts that satisfy design specifications, at the most economical cost possible. Today, in the automotive industry, one can see mass production of automotive components by using advanced hydroforming machinery. Unsupported (dieless) bulge forming of tubes by hydroforming serves little purpose in the manufacture of practical components. Room temperature hydroforming of metallic tubes in a die is a relatively new technology that has become a routine forming process in the area of automotive component forming. In this process, an added axial feed of the tube leads to delayed thinning or necking of the material during forming application resulting in enhanced formability compared with conventional tube hydroforming process (i.e without the axial feed). Currently, axial feed tube hydroforming technology has been applied only to metallic materials.

The use of thermoplastics (e.g. polypropylene) to manufacture automotive structural components is rapidly growing. It is believed that polymer tubes are strong candidates for manufacturing automotive structural components. This is due to their light weight, high bending stiffness, high strength-to-weight ratio, moisture resistance, and energy absorption characteristics. Polymers (and particularly thermoplastics) exhibit significant shape recovery (or relaxation) when deformed at room temperature, and therefore traditional room temperature hydroforming is not a viable option. High temperature forming of thermoplastics also remains a challenge. This is due to their more complex microstructure and deformation behaviour compared to metals, which requires careful control of the process parameters such as pressure (strain rate), temperature and cooling after forming.

In conventional sheet thermoforming process, the polymeric sheet is heated close to melting temperature and, therefore, can be easily formed. Polypropylene exhibits low melt strength resulting in pronounced sag and inconsistent sheet thinning during thermoforming. Axial feeding has not been utilized in conventional thermoforming operations in the past.

1.3 New Axial Feed Hot Forming Process

To improve forming characterizes and post-forming mechanical property of thermoplastic tubular components parts and to reduce the cost of the process, a new axial

feed hot forming process has been developed at McMaster. It merges the conventional room temperature metal tube hydroforming process and high temperature conventional polymer sheet thermoforming process to form polymeric tube components. This new process is referred to as axial feed hot forming (AFHF) process for thermoplastic tubes. This process is significantly cheaper than the metal tube hydroforming due to reduced force and pressure requirements. Also, the part thickness uniformity is superior to conventional thermoforming of polymers. AFHF appears to be a promising new process for making polymeric tubular components. It is therefore important to assess and understand the deformation behaviour of oriented polypropylene tube produced by solid state extrusion and subsequently formed by AFHT process.

Solid-state extrusion as well as tube thermoforming of thermoplastics, and particularly of oriented polypropylene (OPP), are not well understood especially at the microstructural level. In order to optimize the extrusion process, it is important to understand how the microstructure and mechanical properties of tubes relate to the extrusion process parameters. Similarly, it is important to understand how the microstructure and mechanical properties of solid state extruded tube relate to the formability and fracture of the tube during the AFHF process.

1.4 Research Objectives

The specific objectives of the present research are:

1. Assessment of the relationship between the most significant solid-state extrusion process parameters and the resulting microstructure of the tube. This objective also includes an investigation of the effect of these parameters on microstructure changes through the tube thickness and mechanical properties in the longitudinal and transverse directions.

2. Development of the axial feed hot forming process of oriented polypropylene tube up to fracture under different forming conditions in order to establish the relationship between the hot forming process parameters, microstructure (molecular orientation), and biaxial limit strains.

3. Quantitive characterization of the microstructure, mechanical properties and formability under optimized conditions:

Based on the results from objectives (1) and (2), an optimum tube from the extrusion process and tube hot forming process was subjected to various biaxial strain states up to large strains and possibly fracture. The changes in the microstructure and onset of instability and fracture as a function of strain path (or strain state) and strain-value was experimentally assessed to establish formability characteristics of oriented polypropylene (OPP) tubes in AFHF and other related processes.

Chapter 2

Literature Review

2.1 Thermoplastics

Thermoplastics are the most commonly recycled plastics. They can be repeatedly heated to a liquid state and then rehardened by cooling with no significant change in the properties of the material. At the microstructural level the individual chains slip when a thermoplastic is heated, causing the plastic to flow. The chains of atoms and molecules are held firmly again when cooled, the slippage taking place with subsequent heating. Thermosets and elastomers, on the other hand, can be cured once and can not be remelted and thus can not change their shape by heating once they have been hardened. The most common thermoplastic resins utilized for consumer goods are HDPE (high density polyethylene), LDPE (low density polyethylene), LLDPE (linear-low density polyethylene), PET (polyethylene terephthalate), PS (polystyrene), PP (polypropylene), and PVC (polyvinyl chloride). The advantages of plastic parts in comparison with metal parts are reduced mass, design flexibility and parts consolidation. A large percent of polymers used in the automobile industry and one of the most attractive is polypropylene. It provides a good price to performance ratio, recyclability, weight reduction, and improved acoustic damping [Maier and Calafut, 1998].

A semi-crystalline polymer such as polypropylene resists fatigue better than amorphous thermoplastics and also has much better chemical resistance than the amorphous thermoplastics. The maximum use temperature of semi-crystalline thermoplastic is up to the melting temperature rather than the glass transition temperature in amorphous thermoplastics. Amongst semi-crystalline thermoplastics, oriented polypropylene (OPP) has a special place. For example, OPP has a lower density than Polyethylene terephthalate (PET) and offers weight savings accordingly. Also, OPP is more rigid than polyethylene and has a higher melting point [Drozda, et al., 1996].

2. 1. 1 Microstructure of Polypropylene

Polypropylene is a semicrystalline polymer and the crystalline phase contains crystallites which are formed from molecular chains folded back and forth several times to form plates called lamellae stacked side by side and connected by amorphous regions (disordered molecular chains, spaghetti like) called tie molecules. Figure 2.1 shows in a schematic form the basic crystalline microstructure of semicrystalline polymers where the chain axis within the crystalline lamellae lies along the molecular direction [Aboulfaraj et al., 1995]. Between the lamellae, the amorphous layers contain chain ends, tie chains and fully included chains. At the crystallization temperature, the lamellae grow radially from nucleation points in the form of spherulites. The glass transition temperature (T_g) of polypropylene is -20°C and below this temperature there is no chain mobility [Maier and

Calafut, 1998, Aboulfaraj et al., 1995]. At room temperature, the interlamellar chains are in a rubber like state.

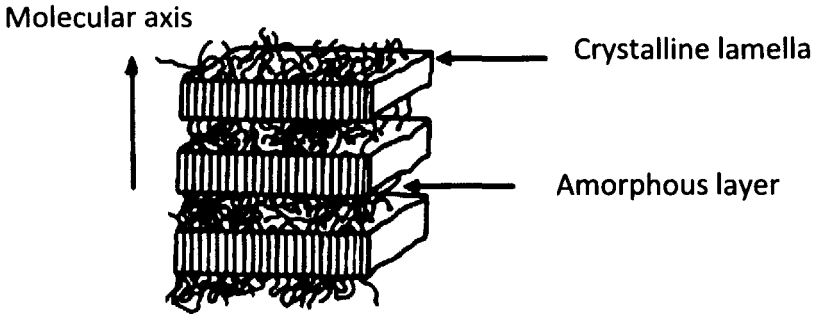

Figure 2.1 Sketch of the basic crystalline microstructure of semicrystalline polymers [Aboulfaraj et al., 1995].

2. 1. 2 General Mechanical Properties of Polypropylene

Mechanical properties of polypropylene are strongly dependent on its molecular orientation and crystallinity, the two most important microstructural parameters. Increasing crystallinity increases stiffness, yield stress, and flexural strength but decreases toughness and impact strength. In uniaxial orientation of molecular chains with respect to the extrusion direction, the material develops significant anisotropy of mechanical properties. The polymer can be oriented uniaxially (machine direction) or biaxially (machine direction and transverse direction).

The mechanical properties of polypropylene compared with other thermoplastics are shown in Table 2.1. Polypropylene homopolymer has a higher tensile strength and is less flexible than the copolymer. Elongation at break indicates that the material responds in a ductile manner at a high elongation while a brittle rupture is exhibited at low elongations. Polypropylene copolymer also has a higher elongation than the homopolymer. However, a small difference between polypropylene homopolymer and copolymer is observed in the strain at yield, an indication of the rigidity of the material. Polypropylene copolymer performs reasonably well in impact and better than the homopolymer.

Polymer	Tensile strength (MPa)	Flexural modulus (GPa)	Elongation at break (%)	Strain at yield (%)	Notched Izod impact strength (KJ/m)
polyethylene terephthalate	75	3	70	4	0.02
Polystyrene, general purpose	34	3.4	1.6	1.4	0.02
PVC-U	51	3	60	3.5	0.08
Polycarbonate	65	2.8	110	7.5	0.7
Polyamide 6/6	59	1.6	60	4.5	0.11
Polypropylene homopolymer	33	1.5	150	10	0.07
HD polyethylene	32	1.3	150	15	0.15
Polypropylene copolymer	25	1.2	300	12	0.1
Polyamide 11	52	0.9	320	20	0.05
LD polyethylene	10	0.3	400	19	no break

Table 2.1 A comparison of mechanical properties of polypropylene with other thermoplastics [Maier and Calafut, 1998].

2. 1. 3 General Fracture Characteristics

Crazing and shear yielding modes of deformation are responsible for brittle and ductile fracture of many polymers. Crazing or stress whitening in thermoplastics is a clear sign of significant damage that typically arises from microvoid initiation, and coalescence leading to the formation of cracks [Ward, 1983]. Crazing occurs at right angles to the applied stress in uniaxial tension and the material usually fails after 1% - 2% extension in a brittle manner [Sperling, 2001]. Shear yielding, on the other hand, involves molecular slip at 45° to the applied stress in uniaxial tension and the material can usually be stretched to 10% - 20% and fails in a ductile mode [Sperling, 2001]. Steger el. al. proposed that when the strain hardening of fibrils-microfibrils is not adequate to compensate for the void content, craze is mechanically unstable and continues to accumulate strain until a macroscopic crack propagates leading to fracture [Steger el. al., 1978].

Shear yielding is referred as distortional deformation occurring at a constant volume and accompanied by necking and is characterized by excessive plastic flow leading to a fibrillated mode of fracture [Steger el. al., 1978]. The mode of failure in polymers can change from brittle to ductile on raising the temperature. Similarly, if the polymer is tested under compression, or under hydrostatic pressure, it tends to fail by shear yielding. Both crazing and shear yielding failure modes should be avoided during forming of polymers and during in-service use of formed polymeric components.

Mechanical properties of PP such as tensile modulus, yield stress and percent strain to fracture are influenced by differences in crystallinity arising from the differences in cooling rates [Dasari et al., 2003]. The delamination or splitting in the longitudinal-transverse plane as a failure mode has been observed in longitudinal tensile tests for PP strips of draw ratio 7.5 and in polyethylene strips of draw ratio 13.5. At lower draw ratios, little delamination has been observed for both polypropylene and polyethylene [Bekhet et al., 1993].

2.2 Solid State Extrusion Process for Oriented Polymer

Several processing techniques have been used to produce high modulus polymer in solid state such as rolling, extrusion, drawing and high pressure crystallization [Ward, 1993, Ward, 1995]. In semicrystalline polymers these techniques result in molecular structure alignment into a highly oriented fibrillar structure. Solid state extrusion is usually carried out by two different methods [Rauwendaal, 2001]. The first is direct solid state extrusion (ram extrusion) where the billet is in direct contact with the plunger and the extrusion die, as shown in Figure 2.2(a). The second method is referred to as hydrostatic extrusion where the ram is replaced by fluid under high pressure that reduces friction and consequently the extrusion pressure, Figure 2.2(b). Both hydrostatic and ram extrusion have been used as methods of producing high modulus polymers since the early 1970s. The investigation in this area has been initiated by Nakamura et al. in Japan [Nakamura et al., 1972], Weeks et al. (1974) in the U.S., and Gibson et al. (1974) in the

U.K. A newer die-drawing process has been extensively developed by Ward and co-workers [Gibson et al., 1980, Coates et al., 1980] since 1980.

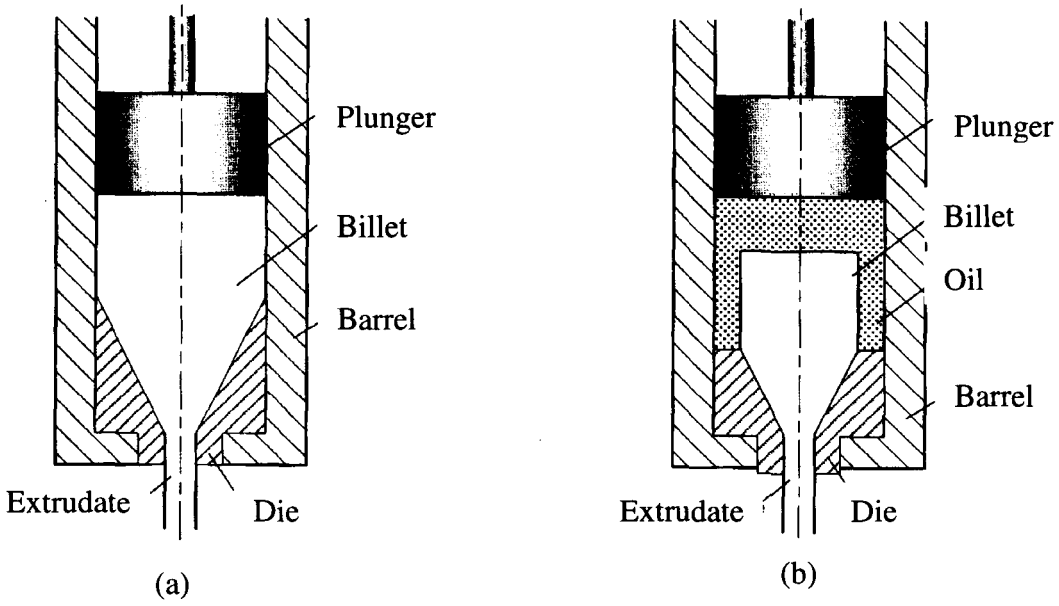

Figure 2.2 A schematic of two common extrusion processes; (a) Direct solid state extrusion and (b) Hydrostatic solid state extrusion [Rauwendaal, 2001].

Solid state extrusion is a discontinuous and relatively slow process. Because of this limitation most work on solid state extrusion has been limited to lab work in universities and institutes such as the University of Massachusetts in Amherst, USA [Snelling and Lontz, 1960, Zachariades and Porter, 1979], Rutgers University, New Brunswick, New Jersey [Pae and Mears, 1968, Pae et al., 1968, Mears et al., 1969], University of Leeds, England [Capaccio and Ward, 1974, Gibson and Ward, 1978, Parsons and Ward, 1982], Fyushu University, Fukuoka, Japan [Imada et al., 1971, Imada and Takayanagi, 1973, Nakamura et al., 1974], Research Institute for Polymers and

Textiles, Yokohama, Japan [Nakamura and Kanetsuna, 1975, Nakamura and Kanetsuna, 1979], and Battelle Memorial Institute, Columbus, Ohio, USA [Bigg, 1976, Bigg et al., 1978, Bigg et al., 1981]. It is likely that some companies are keeping the information on solid state extrusion work proprietary.

A recent application of solid state extrusion by Synthetic Hardwood (SHW) Technologies, Inc., USA has been in the development of an expanded, oriented, wood-filled polypropylene (EOW-PP). The process is based on initial studies at the Aluminum Company of Canada Ltd. (Alcan) in the early 1990s on solid state extrusion. EOW-PP has been reported to be 300% stronger than regular unoriented PP [Schut, 2001]. A combination of extrusion with drawing is the key to the SHW process. The mechanical properties, flexural strength and modulus, achieved with EOW-PP compared to ordinary PP, wood, and oriented PP are shown in Table 2.2.

	Flexural Strength [MPa]	Flexural Modulus [MPa]
Regular PP	50	1850
Wood	100	9000
Oriented PP	275	7600
EOW-PP	140	7600

Table 2.2 Mechanical Properties of PP, Wood, OPP, and EOW-PP [Rauwendaal, 2001].

Polymer processing via solid-state extrusion has an impact on the crystallinity of the structure in addition to molecular orientation. Figure 2.3 shows percentage crystallinity as a function of draw ratio for polypropylene homopolymer (PP1) and polypropylene copolymer (PP2) undergoing solid-state ram extrusion and roll-drawing respectively [Karger-Kocsis, 1999]. As the draw ratio increases the crystallinity also increases.

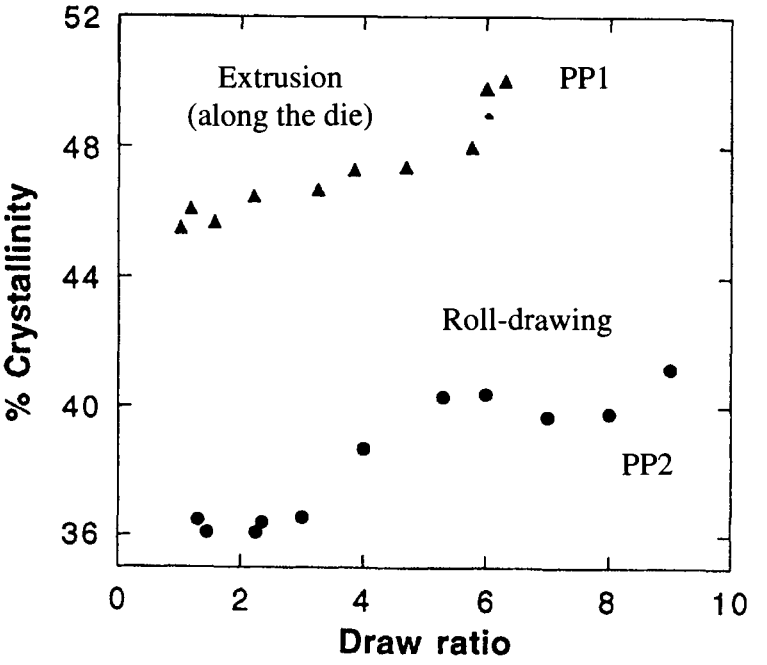

Figure 2.3 Crystallinity as a function of draw ratio for ram extruded and roll-draw polypropylene [Karger-Kocsis, 1999].

Recently, Mourad et al., (2005) studied the effect of die drawing through conical dies on the mechanical properties of polypropylene (PP) rods. Also, the influence of process parameters on the elastic moduli and strengths under tensile and compression

tests was studied on uniaxially oriented and isotropic PP. In this work, extruded rods of polypropylene copolymer (a melt flow index (MFI) of 0.8) were used with an initial diameter of 20 mm and an initial length of 450 mm. The drawing was conducted at three different constant drawing speeds (1.8, 3.6 and 5.4 cm/min) and temperatures (120, 135 and 150 °C) to draw ratios of 3.3 and 1.8. The drawing load increased with draw ratio and draw speed. In addition, the tensile strength and modulus of drawn PP increased significantly with increase of draw velocity and draw ratio while a decrease in the above properties was observed with increasing drawing temperature.

Kim et al. (2004) investigated the processing, structure and property relationships for artificial wood made from stretched wood fiber polypropylene (WFPP) (a 30 wt% composite) by die drawing. The rods were preheated at various oven temperatures (110, 120, 130, 140, and 150°C) for different preheating times of 1, 2, 3, 4, and 5 hours and then immediately stretched by a puller. A pulling speed of 35 cm/min was applied for all stretching experiments. The stretched samples released from the stretching die were immediately air-cooled to prevent post-necking. The results show that the tensile strength and elongation at break of the stretched WFPP were increased by 5 times, but the tensile modulus (stiffness) was lowered by 25%. The tensile properties of the stretched WFPP were found to be insensitive to preheating time and temperature.

Legro et al. (1997) and Ajji et al. (1998) examined the effects of draw ratio and tensile modulus as well as crystallinity on the final properties of the deformed materials.

A laboratory-scale ram extruder was used to extrude, in solid state, isotropic billets of high-density polyethylene (HDPE) and polypropylene (PP) at a temperature below the melting point. The billet was forced by a piston through a die of reducing cross-section to obtain extrusion ratios of 6 and 11. The main effect of increasing the temperature was to decrease the extrusion force of the polymer and increase the polymer deformability. The highest Young's modulus was obtained for the lowest extrusion rate and temperature. The crystallinity at different locations in the extrudate, as measured by differential scanning calorimetry (DSC) measurements, increased with draw ratio.

Bartczak et al. (2002) studied the development of orientation in isotactic polypropylene (iPP) through rolling with side constraints as well as the properties of resultant bars of highly oriented iPP. The slabs, 100 mm x 12 mm in cross-section, and 1 m long, designed for rolling experiments, were machined from sheets of commercial polypropylene homopolymers. The rolling of the slabs was performed at a speed of 200 mm/min and the temperature of the rolls was kept at 90°C, 110°C, and 120°C. The iPP slabs were preheated to the desired temperature in an oven before being rolled to deformation ratios from 2 to 10.4. The resulting stress-strain curves for specimens tested along the direction of the molecular orientation, after rolling at 120°C to various draw ratios, are shown in Figure 2.4 and other material data in Table 2.3. The data show an increase in the elastic modulus and ultimate strength measured along the rolling direction with increasing draw ratio. For samples deformed to a draw ratio of 10.4, the ultimate strength reaches a value of 341 MPa, rather close to that of conventional steels.

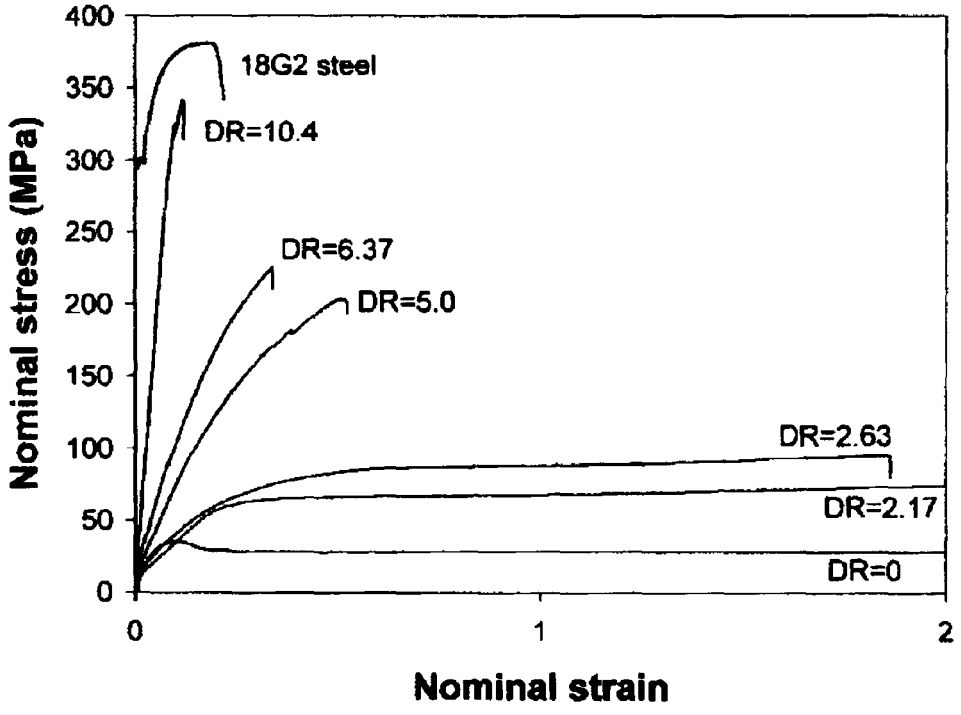

Figure 2.4 Nominal stress/nominal strain curves determined for the tensile deformation of rolled iPP-1 samples with various draw ratios. Tensile tests were performed at room temperature, and the initial deformation rate was 50%/min. The curve for 18G2 concrete reinforcing steel is plotted for comparison [Bartczak et al., 2002].

Draw ratio	Elastic modulus (MPa)	Tensile strength (MPa)	Ultimate elongation (%)
1	0.96	34	450
2.17	2.04	76	225
2.63	2.70	97	180
5.00	4.08	202	49
6.37	4.66	215	33
10.40	6.30	341	18

Table 2.3 Tensile material parameters of rolled iPP material [Bartczak et al., 2002].

2.3 Tube Hydroforming Process for Metallic Automotive Components

In tube hydroforming a metallic tube is formed into the complex shape of a die cavity using internal pressure. The tube is placed in the forming die cavity and sealed at both ends. Axial force (or end feed) is applied at both ends of the tube simultaneously with the injection of the pressurized hydroforming fluid (e.g. oil, gas, water, etc.) inside the tube. As a result of the internal fluid pressure and axial feed, the tube expands and deforms to the desired shape controlled by the geometry of the die-cavity, as shown in Figure 2.5 [Asnafi and Skogsgardh, 2000].

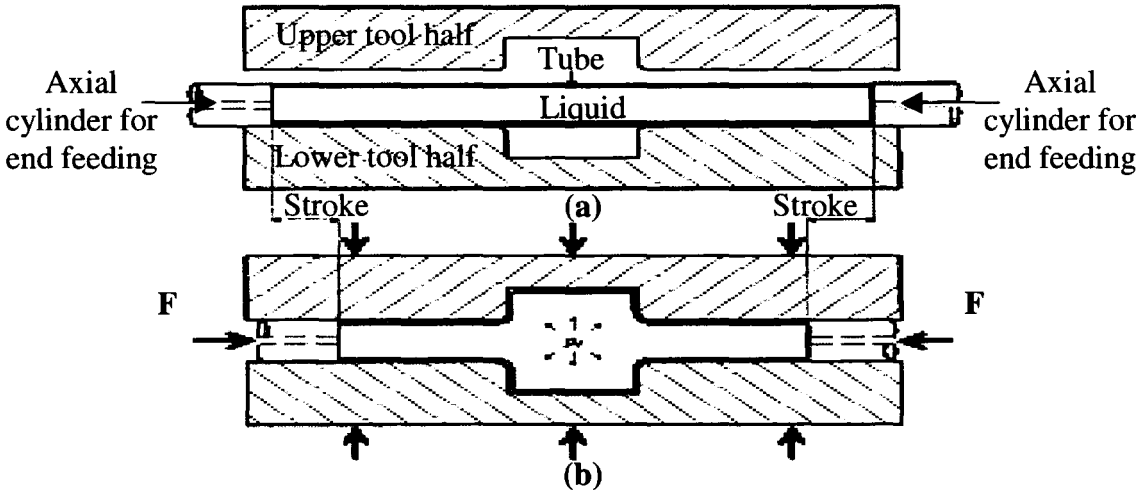

Figure 2.5 A schematic of tube hydroforming process; (a) original tube placed between two die halves and (b) final tube shape after forming (and before unloading) [Asnafi and Skogsgardh, 2000].

Tube hydroforming became a feasible forming process for the automotive industry in the 1990s and its use has been steadily growing. An enhanced formability can be achieved in this process compared with conventional sheet stamping or deep drawing. Various automotive components made by tube hydroforming such as camshafts, radiator frames, front and rear axle parts, engine cradles, crankshafts, seat frames, space frames, roof rails, etc. are shown schematically in Figure 2.6. Tube hydroforming is generally applied to seam-welded steel tubes and extruded aluminium tubes. Currently most components in hydroforming application are made from steel. Aluminium has also become accepted in structural automotive components due to its light weight compared to steel.

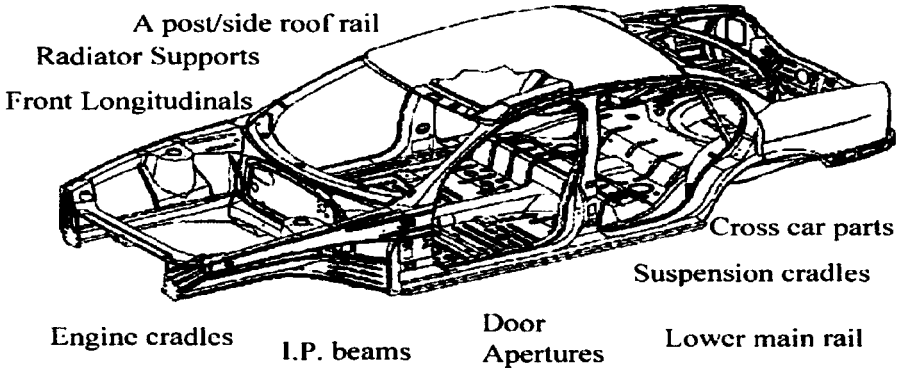

Figure 2.6 A schematic diagram showing various parts manufactured by tube hydroforming [Chu and Xu, 2004].

The three important failure modes encountered in this operation are bursting, wrinkling and buckling. Bursting occurs as a result of excessive tensile deformation in

the circumferential direction due to high internal pressure [Kulkarni et al., 2004]. On the other hand, wrinkling and folding occur if the tube is subjected to excessive axial compression (due to excessive end feeding) and when there is insufficient internal pressure. Carleer et al. (2000) and Asnafi and Skogsgardh (2000) conducted combined experimental and finite-element investigations of free hydroforming of tubes. Davies et al. (2000) obtained forming limits for aluminium alloy tubes in the form of a forming limit diagram (FLD) by free hydroforming experiments. A FLD is a measure of formability of a sheet material [Keeler and Backofen, 1963, Goodwin, 1968]. In determining forming limits sheet specimens are subjected to a variety of strain paths by a punch stretching process. A plotted curve of major-minor strain pairs that are closest to the neck on multiple specimens is defined as the forming limit curve (FLC, Figure 2.7).

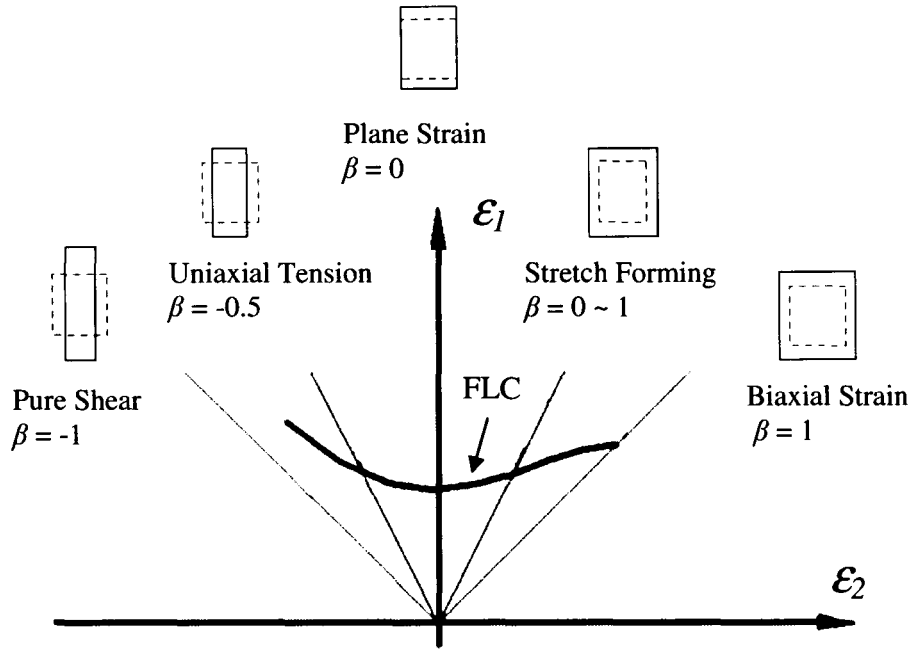

Figure 2.7 A typical FLD showing various forming processes [Keeler et. al., 1963].

Imaninejad et al. (2004) investigated the influence of end-conditions on the resulting forming limit diagram (FLD) and tube failure modes for aluminum alloys. These end conditions were ''free-end'' hydroforming where no external axial load was applied, ''fixed-end'' or ''pinched-end'' hydroforming where the ends of the tube were constrained in the longitudinal (axial) direction, and ''forced-end'' hydroforming where axial feed was employed on the tube-ends. Axial and hoop strains were measured from hydroforming experiments with different end-conditions using the imprinted deformed circles on the surface of the starting tube in the vicinity of the rupture site. Figure 2.8 shows that ''free-end'' hydroforming gives the lowest forming limits compared to ''pinched-end'' and ''forced-end'' hydroforming.

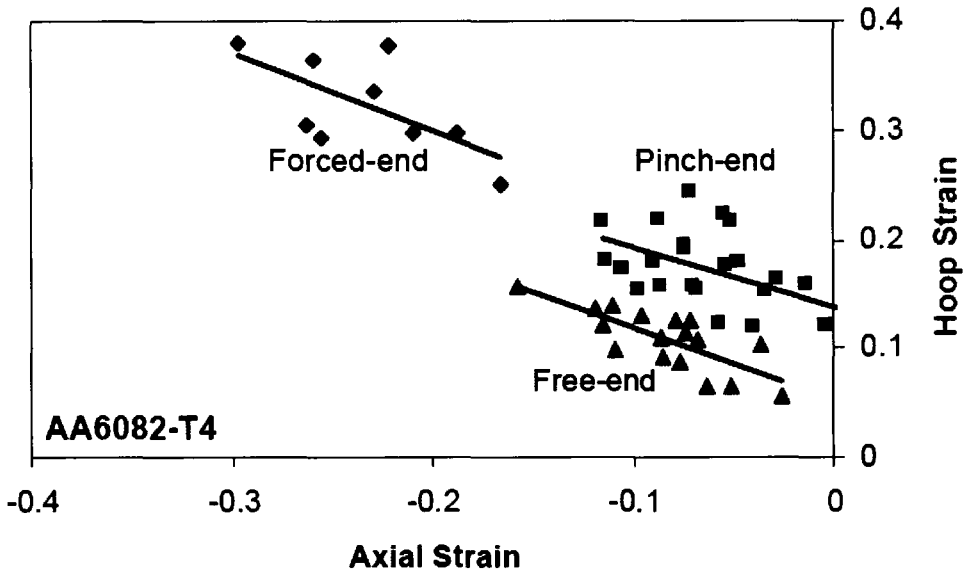

Figure 2.8 Comparison of forming limits obtained from free bulge, pinch test and axial feed experiments [Imaninejad et al., 2004].

Free expansion of tubes or ''open-die'' hydroforming is one of the methods used to obtain the FLD for circular tubes of various materials [Asnafi and Skogsgardh, 2000, Nefussi and Combescure, 2002, Xing and Makinouchi, 2001] but has limited use in the manufacture of practical components. On the other hand, supported bulge forming in a "closed-die" is more practical and provides increased limits of expansion of the tube in the die cavity. Experimental, analytical and numerical simulation based failure diagrams for aluminum and steels have also been established for end feed and internal pressure conditions existing in tube hydroforming [Xia, 2001, Chow and Yang, 2002, Brunet et al., 2004]. Bursting failure in the tube hydroforming process has been predicted using a combination of finite element simulation and the ductile fracture criterion and compared

with a series of experimental results [Kim et al., 2003, Lei et al., 2002]. Theoretical and experimental studies show that the FLD, determined by hydroforming, can be helpful in component and process design [Asnafi and Skogsgardh, 2000].

2.4 Thermoforming Process for Thermoplastic Sheet Components

Thermoforming process for cut plastic sheet is widely used in the plastic industry for various commercial applications due to its advantage of low processing cost and short cycle times. In thermoforming process the sheet is heated until it becomes pliable and is subsequently deformed into the shape of a mould by an applied pressure, vacuum, a moving plug or a combination of these media. There are many types of thermoforming processes, the most common among them are vacuum, pressure, drape and plug assist forming. For example, in pressure forming process, a positive air pressure is used to form clamped and heated plastic sheet as shown in Figure 2.9. After forming, the sheet is cooled to below the glass transition temperature before removal from the forming system [Maier and Calafut, 1998].

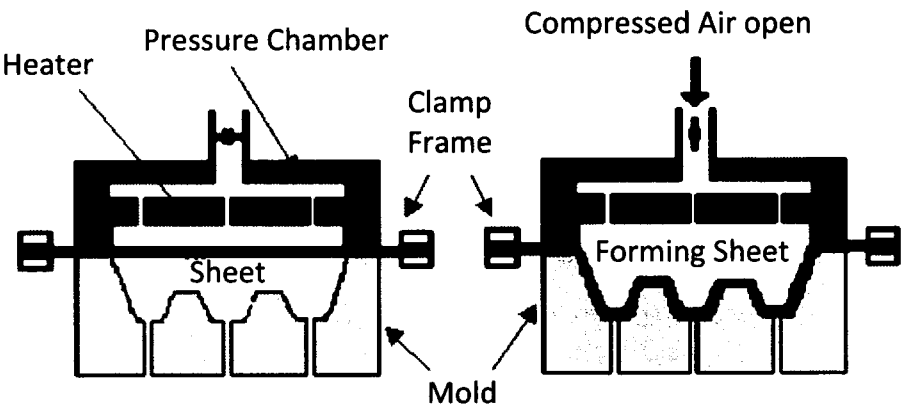

Figure 2.9 Basic pressure forming process [Maier and Calafut, 1998].

Polypropylenes for thermoforming usually have a melt flow index (MFI) in the range 1.8-8.0. For thick walled parts homo-polymer polypropylene with a low MFI and a high molecular weight is utilized. The main problems of thermoforming polypropylene sheet are: (i) sagging of the sheet during heating because polypropylene has low melt strength, and (ii) the process temperature window may be very narrow, requiring precise temperature control across the thickness and surface of the sheet. Temperature variations across the sheet thickness should not be greater than 3°C for thin-walled polypropylene packaging products [Maier and Calafut, 1998].

Sheet thermoforming temperature has a large influence on the wall thickness, orientation, and mechanical properties of the part due to the semicrystalline nature of polypropylene. Typically the temperature range for solid phase forming is from 155°C to 165°C, see Figure 2.10. In solid phase forming, a higher degree of orientation and improved transparency can be achieved when forming is performed at temperatures

towards the lower end of the solid phase temperature range. On the other hand, forming at the higher end of the range results in more uniform distribution of wall thickness. In melt phase thermoforming, a lower force is required resulting in lower residual stresses in the finished part.

Four different thermoforming processes (V-bending, matched-die forming (dome), pressure forming (dome) and deep drawing (cup)) were used to study the formability of woodfiber-polypropylene composite sheets [Bhattacharyya et al., 2003]. The results show that the addition of woodfibre improves both tensile strength and modulus, as well as reduces the tendency of polypropylene to exhibit localized thinning.

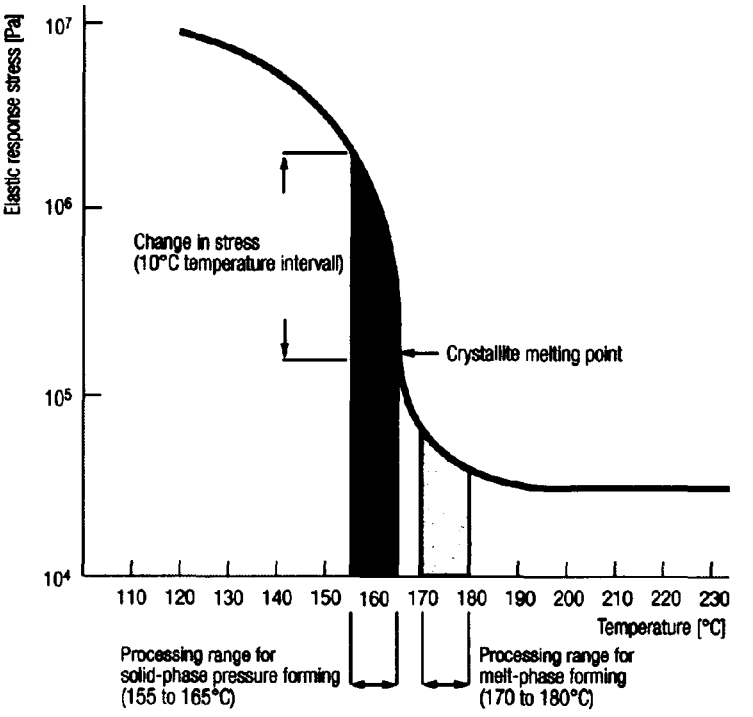

Figure 2.10 Process phases for thermoforming polypropylene [Maier and Calafut, 1998].

2.5 Thermoforming Process for Thermoplastic Tubes

Burst experiments in polyamide tubes at room and elevated temperatures using free-bulge hydroforming process shows that the most significant parameter that causes bursting in the tube is hoop stress. The latter is dependent on the hydroforming temperature and varies with respect to the polymer grade [Germain, 1998].

Taraiya and Ward (1996) of the University of Leeds, U. K., described methods for the production of biaxially oriented polyethylene tubes and studied their resulting mechanical and structural properties. Biaxial orientation was achieved by drawing the tubular material through a die and over an expanding mandrel. Taraiya and Ward (1996) subsequently studied the tensile behaviour of the drawn tubes at room temperature. One of the drawn tube samples tested had the same axial and hoop draw ratios and several combinations of drawn tubes were tested which had varying axial draw ratios but nearly constant hoop draw ratios. The results are given in Table 2.4 where the hoop draw ratio refers to the average value of the inner and outer hoop draw ratios.

As shown, when the axial draw ratio and the average hoop draw ratio are the same, the tensile strength and percent elongation at break in both directions are also the same (row 1 of Table 2.4). However, the axial tensile strength increases with axial draw ratio, with the hoop draw ratio remaining nearly constant (rows 2-4 and 6 of Table 2.4). As the axial draw ratio increases, the difference in the tensile strength in the axial and

hoop directions also increases, which indicates increasing anisotropy in the tensile strength. The percentage elongation at break in both directions decreases with an increase in axial draw ratio. It is to be noted that large elongation values (a measure of formability) greater than 75% were achieved for all draw ratios. No spatial strain data was measured in this study.

Draw Ratio		Tensile Strength (MPa)		% Elongation at Break	
Axial	Hoop	Axial	Hoop	Axial	Hoop
1.0	1.0	22	22	700	700
2.9	1.6	86	34	260	550
4.1	1.6	98	40	100	550
4.9	1.6	114	44	80	500
3.4	1.7	95	37	150	500
4.4	1.6	110	42	95	480
5.2	1.5	120	40	80	500
6.2	1.4	140	39	75	520

Table 2.4 Tensile properties of biaxially drawn polyethylene [Taraiya and Ward, 1996].

The microstructural evolution of long chain high and low crystallinity polypropylene and ethylene-propylene di-block copolymer iPP-L, PP-L, and EP-L and short chains referred to as iPP-S, PP-S, and EPS was examined after tensile deformation by field emission scanning electron microscopy (FE-SEM) [Dasari et al., 2003]. The injection molding process was used to cast tensile samples of the polymeric materials.

Tensile properties of these materials are shown in Table 2.5. A range of mechanical properties and percent crystallinity values are noted.

	PP-L	PP-S	EP-L	EP-S	iPP-L	iPP-S
Modulus, MPa	1500	1500	1150	950	2075	2125
Yield strength, MPa	34	34	21	19	43	43
Melt flow rate at 230/2.16 (g 10 min^{-1})	6	23	7.5	48	5	45
% Crystallinity	46	49	19	23	59	63

Table 2.5 Tensile properties of long and short chain of PP, iPP, and EP at a displacement rate of 50 mm min^{-1} [Dasari et al., 2003].

Axial feed hot gas tube forming (AF-HGTF) and axial feed hot oil tube forming (AF-HOTF) are two new processes that have been developed by Jain and co-workers at McMaster University. These processes are similar to metal tube hydroforming except that a thermoplastic tube is heated to a softened state (as in sheet thermoforming process) and subsequently deformed by a combination of applied internal gas or oil pressure and axial feeding from the two ends (similar to water-based tube hydroforming).

The investigation of axial-feed thermoforming for extruded polypropylene tubes by Jain and co-workers has evolved into three primary areas. First, studies have been carried out to characterize the axial-feed hot gas tube forming (AF-HGTF) process parameters by experiments as well as by modeling AF-HGTF for extruded polypropylene

tubes via the Finite Element (FE) method [Gavrilidou, 2005]. Augmented Hybrid model (a viscoelastic-viscoplastic model), and Ogden material models have been used in FE model to capture material failure such as wrinkling and buckling, as well as tube wall thickness distribution in a cylindrical part. Second, an analytical model of tube forming with axial feed has been developed for predicting the forming limits of oriented polypropylene tubes at various temperatures based on a pressure-modified Hill yield criterion, a criterion for localized necking of the tube and mechanics of hot gas axial-feed tube forming process [Azhikannickal et al., 2007, Azhikannickal et al., 2008]. Both of these topics have not considered the microstructural aspects of solid-state extrusion for the AF-HGTF or AF-HOTF processes for oriented thermoplastics tubes. The research presented in this thesis is the third area and deals with structure-property-process studies during extrusion and subsequent axial feed tube forming of polypropylene tubes [Elnagmi and Jain, 2007, Elnagmi et al., March, 2009, Elnagmi et al., May, 2009].

Microstructural changes that occur in polypropylene as a result of solid state tube extrusion or subsequent thermoforming of the polypropylene tube have not been studied in the past. These changes are expected to affect the forming performance of polypropylene tubes and hold the key to optimizing the extrusion and forming processes. It is therefore useful to investigate the newly developed AF-HGTF and AF-HOTF processes at the scale of the microstructure development, since it has the potential to reduce the cost of a process or product and to improve the properties of products made from PP.

Solid-state extrusion as well as tube thermoforming of thermoplastics, and particularly of oriented polypropylene (OPP), are not well understood especially at the microstructural level. In order to optimize the extrusion process, it is important to understand how the microstructure and mechanical properties of tubes relate to the extrusion process parameters. Similarly, it is important to understand how the microstructure and mechanical properties of solid state extruded tube relate to the formability and fracture of the tube during AFTF process. This is reviewed in sub-section 2.8 after a brief review of the microstructural characterization techniques for polymers in sub-sections 2.6 and 2.7.

2.6 Review of X-ray Diffraction Technique for Analysis of Polymers

Four main capabilities of X-ray diffraction typically utilized in polymer analysis are as follows [Campbell and White, 1989, Alexander, 1969, Cullity and Stock, 2001]:

2.6.1 Indexing of Crystal Structures

By using standard methods of X-ray analysis, the crystal structure of crystalline polymer phases can be determined. Polymer crystals, however, are not formed as perfect crystals, eliminating the use of diffractometric techniques, Also, polymer crystals tend to be of low symmetry, due to the asymmetry in bonding of the crystalline lattice, i.e. the c-axis is bonded by covalent bonds and the a and b axis are bonded by van der Waals

interactions or hydrogen bonds. In polymer crystals the lattice parameters are strongly temperature dependent, due to weak bonding in various directions causing a large temperature-vibration coefficient that leads to a rapid fall in the intensity. This means the analysis is generally based on fewer reflections and with less precision.

2.6.2 Microstructure

With a monochromatic incident beam the diffraction pattern from a single crystal is a sequence of spots where the Bragg condition is met for certain orientations of crystals. Polymer crystals are on the order of 100 Å in thickness. The breadth of the diffraction lines can be used to measure the thickness of lamellar crystals using the Scherrer equation:

$$t = \frac{0.9\lambda}{B\cos(\theta)} \tag{2.1}$$

where t is the thickness of lamellar crystals, λ is the X-ray wavelength, B is the half width at half height for the diffraction peak in radians, and θ is half of the diffraction angle.

2.6.3 Degree of Crystallinity

The degree of crystallinity of a semi-crystalline polymer can be obtained from an analysis of peaks from crystalline and amorphous regions. The crystalline parts give sharp narrow diffraction peaks while the amorphous component gives a very broad peak (halo). The ratio of these two intensities, $\left(\frac{I_c}{I_a}\right)$, can be used to calculate the amount of crystallinity in the material. Fractional crystallinity (f_c) is defined as,

$$f_c = \frac{I_c}{I_c + I_a} \tag{2.2}$$

where I_c and I_a are the integrated areas of crystalline and amorphous diffraction peaks.

2.6.4 Orientation

X-ray scattering can also provide a complete distribution of orientations of crystallites based on the intensity of a particular Bragg reflection over the total volume of the crystallites that are oriented at the Bragg angle [Bower, 2002]. Crystal orientation with respect to the three perpendicular axes is widely used to construct a pole figure [Ward et al., 2000]. The pole figure is a graphical representation of the orientation of objects in space. Pole figures in the form of stereographic projections show the density of

crystallographic poles of certain planes as a function of orientation [Kasai, and Kakudo, 2005].

2.7 Representation of Orientations in Deformed Polymers

The most common morphological measure of orientation is Herman's orientation function [Alexander, 1969]. The Herman's orientation factor, $f_{j,n}$ for a given plane can be calculated by

$$f_{j,n} = \left(3 < cos^2 \phi_{j,n} > -1\right)/2 \qquad (2.3)$$

where $\phi_{j,n}$ is the angle between the j-crystallographic axis (j= a, b or c) and the fiber axis as represented by processing directions; extrusion, transverse and normal directions (n = ED, TD and ND respectively). The symbol <...> implies an average over the entire pole figure. Table 2.6 shows the relationship between $f_{j,n}$ and $\phi_{j,n}$ for the different chain axis orientations.

Orientation	$\phi_{c,ED}$	$< \cos^2 \phi_{c,ED} >$	$f_{c,ED}$
Chain axis is parallel to the fiber axis	0	1	+1.0
Chain axis is perpendicular to the fiber axis	90	0	-0.5
Chain axis is oriented randomly	Random	1/3	0.0

Table 2.6 The relationship between $f_{c,ED}$ and $\phi_{c,ED}$ for the different chain axis orientations.

The Herman's orientation factors are directly calculated from (*h00*) and (*00l*) poles in equation (2.3) for orthogonal crystal systems. It is to be noted that there are no strong (*00l*) type diffractions in isotactic polypropylene that are perpendicular to the c-axis of the unit cell (monoclinic crystal). Wilchinsky (1962) has developed an equation to determine $<\cos^2\phi_{c,ED}>$ values indirectly by means of intensity measurements from strongly diffracting planes. Only two pole figures, (110)α and (040)α, are required for the evaluation of $<\cos^2\phi_{c,ED}>$ in monoclinic crystal system using the following expression:

$$< cos^2\phi_{C,ED} > = 1 - 1.099 < cos^2\phi_{110,ED} > -0.901 < cos^2\phi_{040,ED} > \qquad (2.4)$$

Another useful representation of orientation in deformed polymers is in the form of Stein triangles. Stein triangles are plotted using $f_{a,ED}$ and $f_{c,ED}$ Herman's indices as shown in Figure 2.11. The origin marked (0, 0) corresponds to a randomly oriented state, the three apexes of the triangle correspond to complete alignment of the crystallographic axis (a, b and c) parallel to the z-axis of the sample. Each side of the triangle represents the orientation of a crystallographic axis (a, b and c) perpendicular to the z-axis.

The Herman's orientation factor satisfactorily describes the degree of axial orientation in crystalline fibers. However, as described in the book by Alexander (1969), it is insufficient to describe the orientation characteristics of biaxially oriented products such as blown films, injection-molded, and blow molded container parts. The biaxial

orientation factors are defined after White and Spruiell (1981) to quantify the orientation with respect to extrusion (ED) and transverse (TD) directions as follows:

$$f^{B}_{ED,j} = 2 < cos^2\phi_{j,ED} > + < cos^2\phi_{j,TD} > -1 \quad (5)$$

$$f^{B}_{TD,j} = 2 < cos^2\phi_{j,TD} > + < cos^2\phi_{j,ED} > -1 \quad (6)$$

where $<\cos^2\phi_{j,n}>$ is the average value of the square of the cosine of the angle between the j-crystallographic axis (j = a, b or c) and the fibre axis as represented by the processing directions (n = ED, TD).

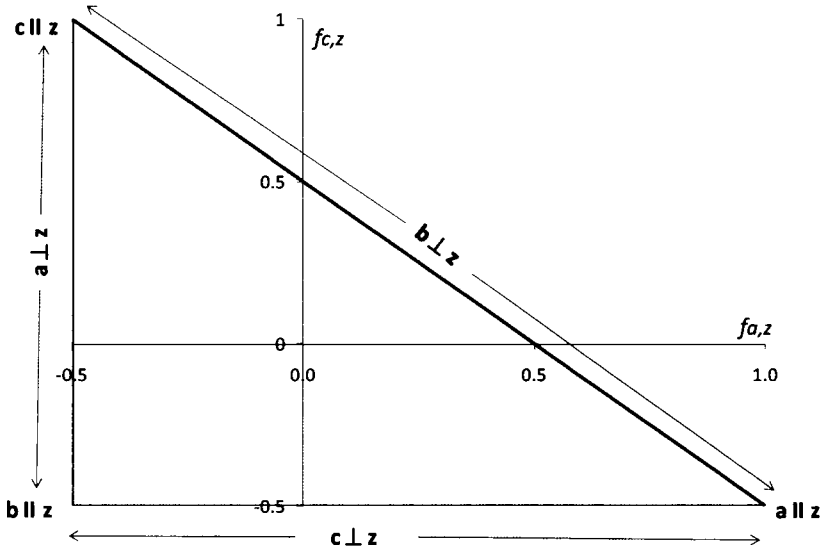

Figure 2.11 A plot of Stein triangle with Herman's indices $f_{a,ED}$ and $f_{c,ED}$ [Alexander, 1969]

A schematic of White and Spruiell triangle is plotted in Figure 2.12 using the biaxial orientation factors f_{ED}^{B} and f_{TD}^{B} values for deformed samples. States of uniaxial orientation with respect to the extrusion and transverse directions lie along the respective coordinate axes. The biaxial orientation factors take values between +1 and -1, with 0 representing random orientation, +1 representing perfect orientation, and -1 representing the orthogonal orientation. The path marked by a dashed line through the center of the triangle represents the case of equal biaxial orientation where the orientation with respect to the extrusion and transverse directions is the same. The base of the triangle which is between the apex (1, 0) and (0, 1) represents the case of planar deformation (film surface) and the middle of the base represents equal planar orientation. The side of the triangle between the apex (1, 0) and (-1,-1) represent the case of planar deformation where the machine direction is perpendicular to the surface.

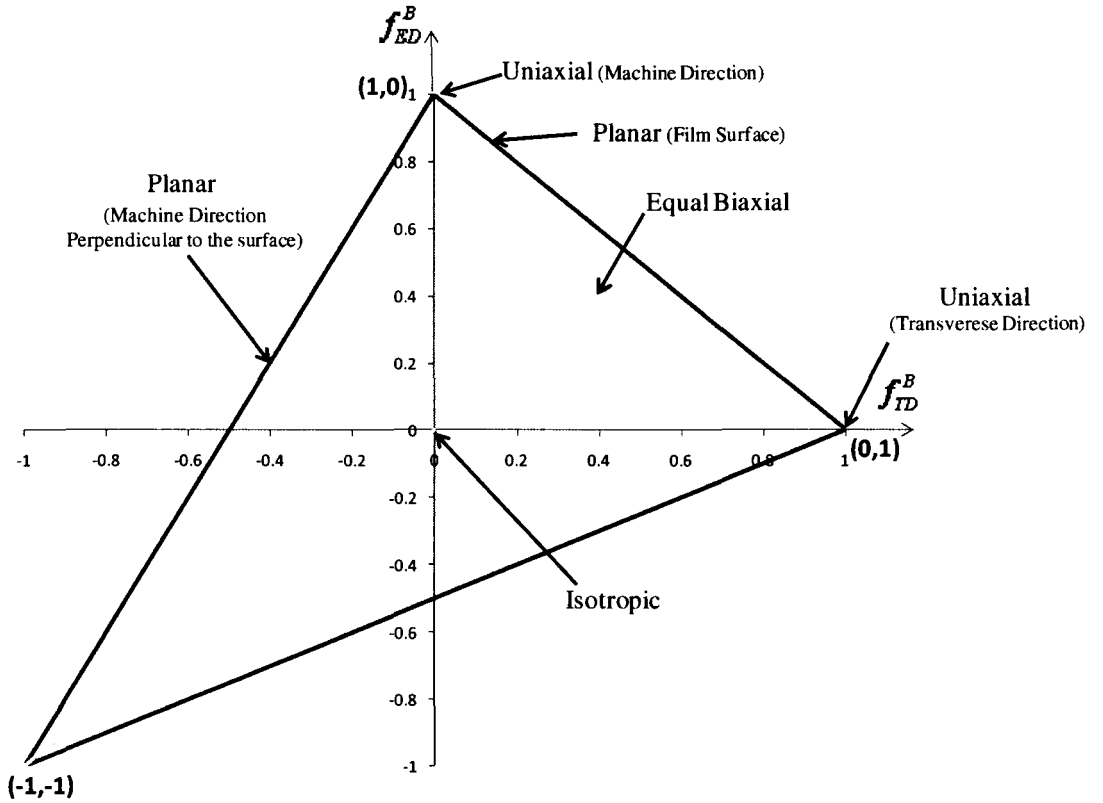

Figure 2.12 Graphical representation of orientation, the orientation triangle diagram [White and Spruiell, 1981].

2.8 Structure-Mechanical Property Relationships in Semicrystalline Polymers

White-Spruiell orientation representation has been used to characterize the biaxial orientation features of linear low-density polyethylene (LLDPE) blown films [Krishnaswamy, 2000, Krishnaswamy and Sukhadia, 2000, Chen et al., 2006] and tubular low-density polyethylene (LDPE) blown films [Pazur and Prud'homme, 1996]. In a study

dealing with polypropylene blown film [Shimomura, 1982], it is shown that orientation factors are close to the biaxial line, indicating that the kinematic condition of the orientation is close to equal biaxial strain state. Rhee and White (2004) investigated the development of crystalline structure orientation of polyamide 11 and polyamide 12 films in the biaxial stretching process. In this study, White-Spruiell biaxial orientation factors of the crystalline phase were calculated with WAXD pole figure data. Significant levels of orientation were achieved from blowing of polyamides 11 and 12. Choi and White (2001) investigated the differences in crystal structures and orientation of isotactic-polypropylene (iPP) and syndiotactic-polypropylene (sPP) materials subjected to biaxial stresses in the melt through the tubular film extrusion process. The film samples were produced at different draw-down ratio (DDR) and blow-up ratio (BUR) at the same extrusion temperature of 230°C. WAXD was used to characterize the crystalline orientation in terms of the White-Spruiell biaxial orientation factors as shown in Figure 2.13. The chain axis (c-axis) for all iPP films are oriented towards the machine direction, MD. With increasing DDR the c-axis increases gradually at the beginning for both orientation factors f_{ED}^{B} and f_{TD}^{B}, but at the high DDR/BUR ratios, f_{TD}^{B} of the c-axis orientation decreases rapidly while f_{ED}^{B} remains unchanged.

X-Ray diffraction has been also used to study the crystalline structure of polypropylene blends [Tang and Martin, 2003]. The effect of loading rate on orientation and morphological aspects of thermoplastic olefins in the neck has been investigated [Dasari and Misra, 2003]. Several plaques of 1, 2, and 3 mm thickness made of

polypropylene and three ethylene-propylene block copolymers obtained by different processing methods (injection molding, injection and annealing, and compression molding) have been studied for their microstructure and mechanical behaviour. The presence of β-phase in the skin of the plaques, and its absence in the core, has been analyzed by the WAXD. Also, the thickness of lamellar crystals increased in the core of the 2 mm plaques due to the annealing process [Maspoch, 2004]. Wide angle X-ray scattering (WAXS) was used to verify a molecular mechanism in Poly (ethylene-2.6-naphthalate) at different structural levels. The sample planes before the neck were randomly oriented but rapidly aligned parallel to the film surface after the neck [Cakmak and Lee, 1995]. Wide-angle X-ray diffraction (WAXD) patterns of extruded polypropylene sheet samples, machined and stretched at high temperatures, revealed that β-crystal modification did not occur during the entire machine direction (MD) hot-stretching process [Yang et al., 2003].

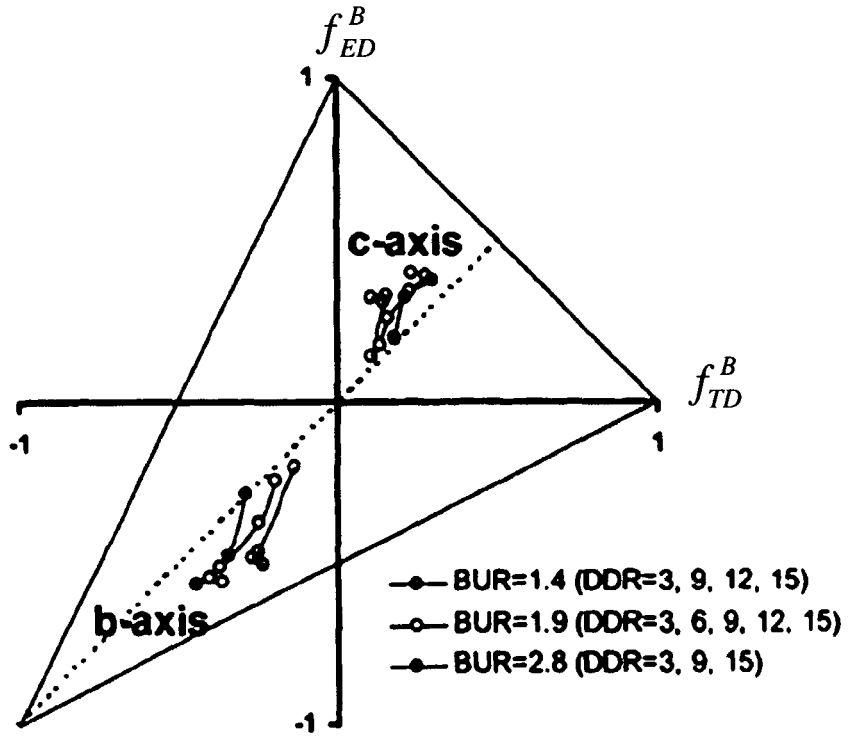

Figure 2.13 White-Spruiell biaxial orientation factors of iPP films [Choi and White, 2001].

Lupke et al. (2004) studied biaxial drawing of polypropylene films. Small angle X-ray scattering (SAXS) and WAXS were used to characterize the structure of drawn polypropylene films along the deformation paths at different draw ratios. For X-ray analysis, samples were prepared by stacking several layers of the drawn film to a total thickness of 0.6 mm. Tensile samples were cut in the machine direction (MD) and transverse direction (TD) from drawn polypropylene films, 3 mm in width and 15 mm in length, and tested at room temperature at a cross-head speed of 5 mm/min. The influence of transverse draw ratio (λ_{TD}) on the stress–strain behaviour is shown in Figure 2.14. In

machine direction, the tensile strength is significantly reduced with increasing λ_{TD} (Figure 2.14 (a)). In the transverse direction at draw ratios λ_{TD} = 1-2, however, the samples deform in a more ductile manner (Figure 2.14 (b)). For draw ratios $\lambda_{TD} \geq 5$ the tensile strength was significantly increased and was accompanied by a reduction in ductility.

No studies dealing with microstructural aspects of thermoforming of structural thermoplastic tubes, and particularly of structural oriented polypropylene (OPP) tubes, for forming into automotive structural components, have been reported in the literature. It is expected that deformation behaviour will depend on molecular orientation and most strongly on processing conditions, i.e., the thermal-mechanical history experienced by the billet and tube in the extrusion and subsequent thermoforming processes. Such relationships between microstructure and process characteristics will be important in order to understand the final properties of a product. Due to the rather complex microstructure present in thermoplastics, and PP in particular, compared to metals, the process parameters such as pressure (strain rate), temperature and cooling after forming will need to be carefully optimized and controlled to obtain satisfactory product properties.

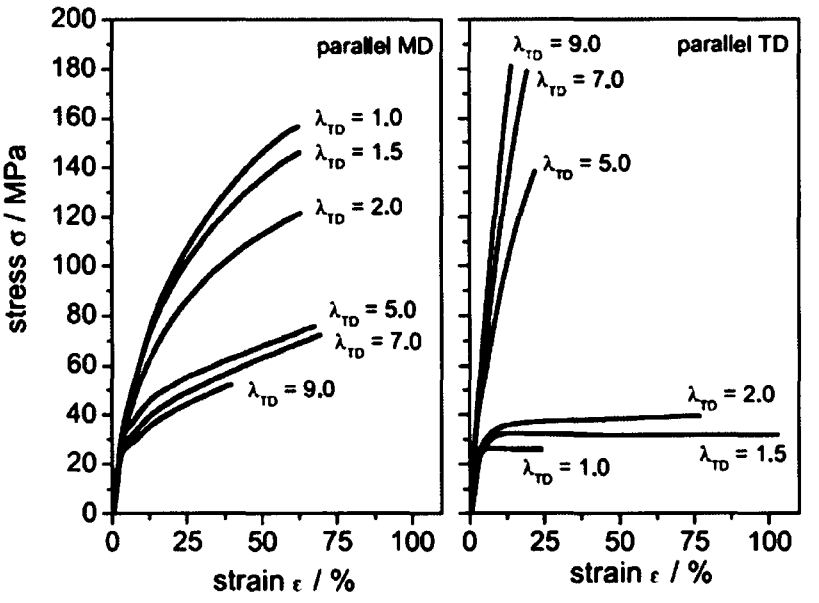

(a) (b)

Figure 2.14 Stress–strain behaviour of sequentially drawn polypropylene films with different transverse draw ratios λ_{TD} ((a) stress–strain in machine direction MD, (b) stress–strain in transverse direction TD) [Lupke et al., 2004].

The objective of this study is to understand the structure-property-process relationships by investigating the deformation and failure behaviour of OPP tubes and to relate the deformation processes of extrusion and bulging to the change in preferred orientation. It is clear from a survey of the literature that the Herman's orientation factor and the White–Spruiell biaxial orientation factor are useful descriptions of deformation process but have not been applied to solid state extrusion and bulging of structural thermoplastic tubes.

Chapter 3

Experimental Methodology for Solid State Extrusion Experiments and Microstructural Studies

3.1 Starting Solid Polypropylene Billets

The material employed in this study is a polypropylene homopolymer with a melt flow index, MFI, of 0.75 and a density of 0.9071 g/cm^3. The as-received solid cylindrical bars of polypropylene (2.75 inch in diameter) were produced at PSAC Inc. in Guelph, Ontario. The extrudate, in the melted state (230°C), was cooled and solidified directly in a water-cooled bath.

The tubes used in the experimental portion of this research were ram extruded in the solid state. For this purpose, a large number of starting tubular billets were machined from the as-received solid cylindrical billets to produce tubes with two different inner diameters of 1.0 and 1.74 inches. The billets were machined to various outer diameters depending on the desired draw ratios. The inner diameters of the tubular billets were machined at McMaster University to match the outer diameters of the mandrel of the extrusion press at PSAC. Tubular billet dimensions to achieve different draw ratios of 4.5, 5.0, 5.7 and 6.3 for small diameter tubes and 4.0, 4.5 and 5.0 for large diameter tubes

are shown in Table 3.1. Figure 3.1 shows the tools used in the machining of the tubular polypropylene billets. The following set of figures show the detailed steps involved in machining the solid cylinder polypropylene bars to tubular billets for use as starting material in solid state extrusion experiments, Figure 3.2 (a-h). Machining was carried out at slow speed (90-140 rpm) with cooling water to prevent a rise in temperature.

The draw ratio, DR, was limited to available extrusion dies and mandrel with the extrusion machine at PSAC. Since the inner diameters of the extrusion dies were 1.4 and 2.0 inch and the outer diameters of the mandrels were 1.0 and 1.76 inches, the outer and inner dimensions of the final oriented small tubes were 1.4 and 1 inches and the large tubes were 2.0 and 1.74 inches respectively.

Tubular billet dimensions		Nominal draw ratio (based on extrusion die and mandrel)
Outer diameter (inch)	Inner diameter (inch)	Draw ratio (DR)
2.68	1.0	6.3
2.58	1.0	5.7
2.43	1.0	5.0
2.33	1.0	4.5
2.53	1.74	4.0
2.61	1.74	4.5
2.69	1.74	5.0

Table 3.1 Tubular billet dimensions to achieve different draw ratios.

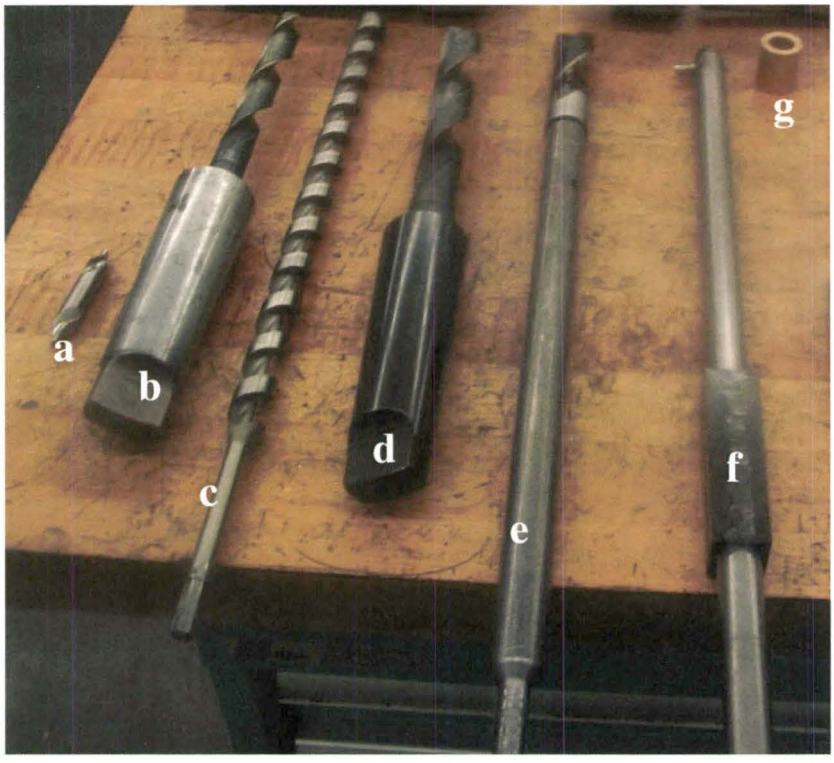

Figure 3.1 Tools used in machining of tubular polypropylene billets (a) centre drill (b) ¾ inch short drill (c) ¾ inch spiral drilling (d) 1 inch short drill (e) 1 inch long drill (f) special tool for boring (g) push.

(a)

(b)

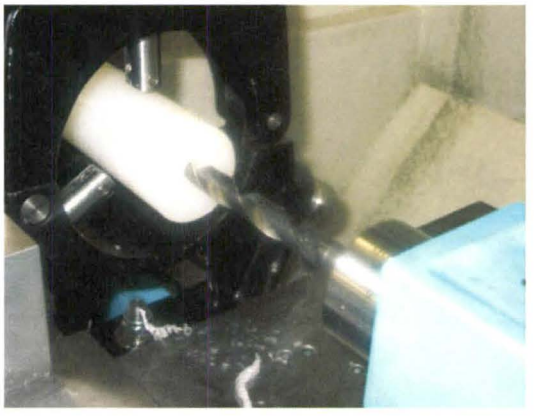

(c)

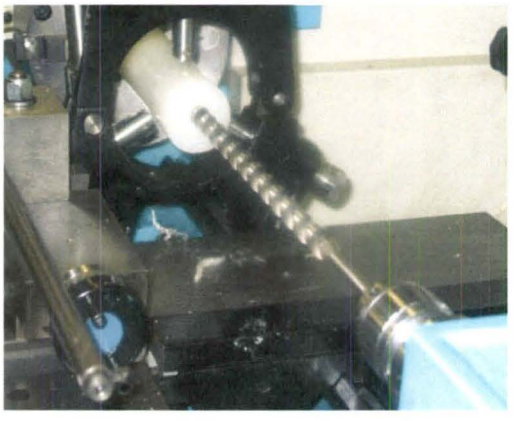

(d)

Figure 3.2 Various steps in machining of the solid cylinder polypropylene bars to tubular polypropylene billets (a) starting solid cylinder polypropylene bars (b) centre drilling (c) ¾ inch short drilling (d) ¾ inch long spiral drilling.

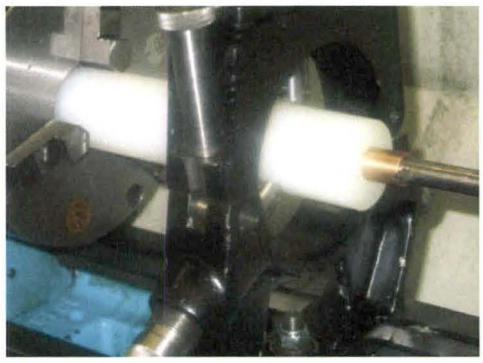

(e)

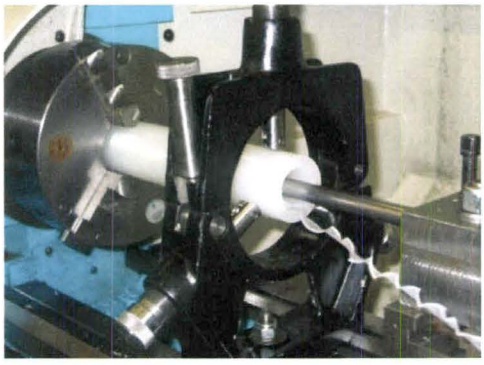

(f)

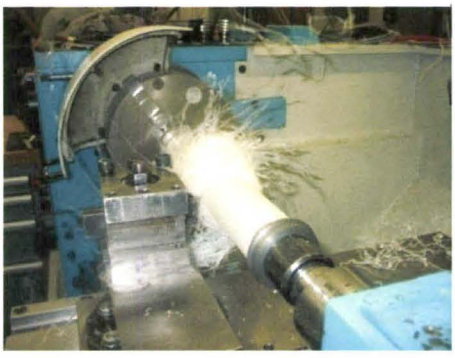

(g)

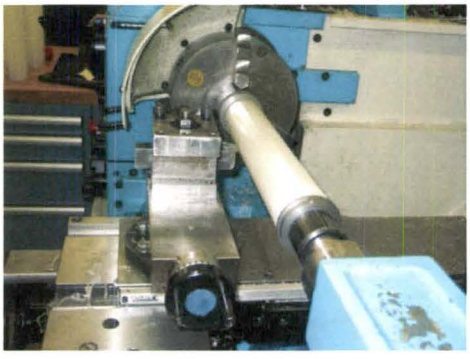

(h)

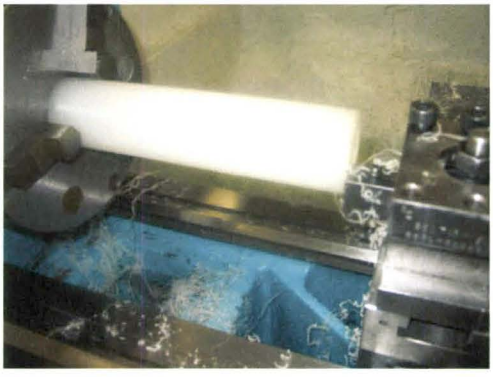

(i)

(j)

Figure 3.2 (continued) (e) centre of a special long tool with bush (f) boring of 1 inch (small tube) and 1.74 inch (large tube) hole using a special long tool with bush (g) machining of outer diameter of billet (h) end of machining (i) facing the two ends of tubular billet (j) final tubular billets for extrusion experiments.

3.2 Solid State Extrusion Process Conditions

The orientation machine utilized the "ram extrusion" and "die drawing" steps to produce oriented polypropylene tubes at different draw ratios. The ram extrusion machine consisted of two heaters at the front and rear chambers and two heaters at the front and rear dies that were controlled by switches and digital temperature displays as shown in Figure 3.3. Ram motion was controlled by two valves as shown in Figure 3.4. The first valve was used to control the forward movement of the ram (during extrusion) and its backward movement to remove the ram from chamber. The second valve was used for moving the ram up and down (to insert a new tubular billet). Figure 3.5 shows a haul-off tension controller system used to pull (or draw) the extruded tube from the exit side of the die. The haul-off tension could be applied at different speeds while recording the tension load. Typical solid state extrusion parameter values are shown in Table 3.2.

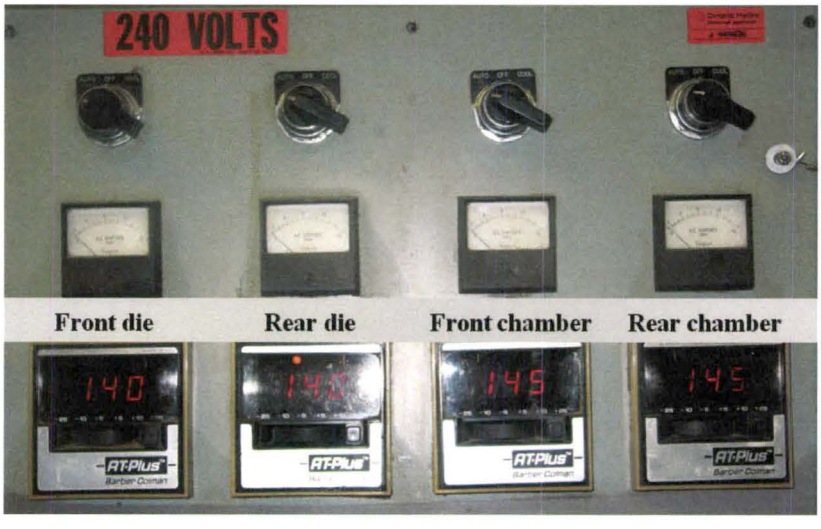

Figure 3.3 The controller for heating of chambers and dies in ram extrusion machine.

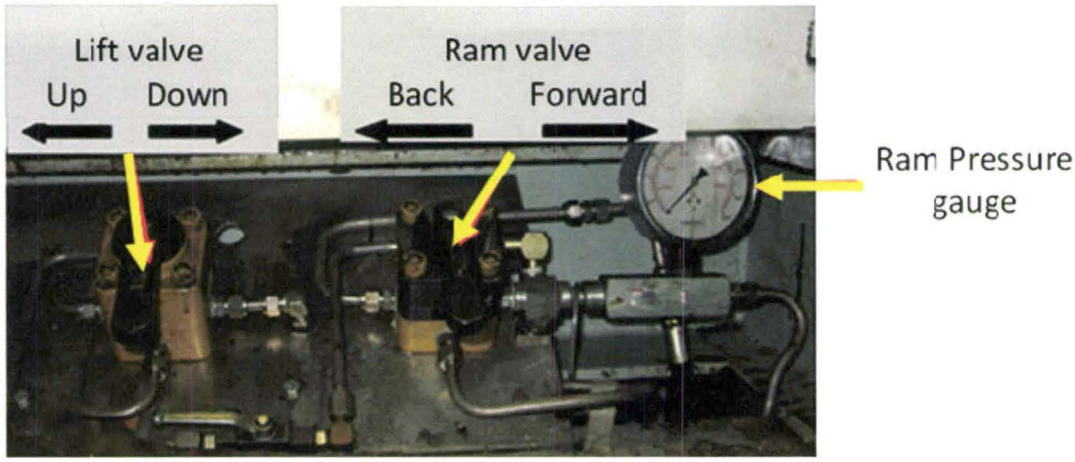

Figure 3.4 valve based control of movement of ram extrusion and pressure gauge.

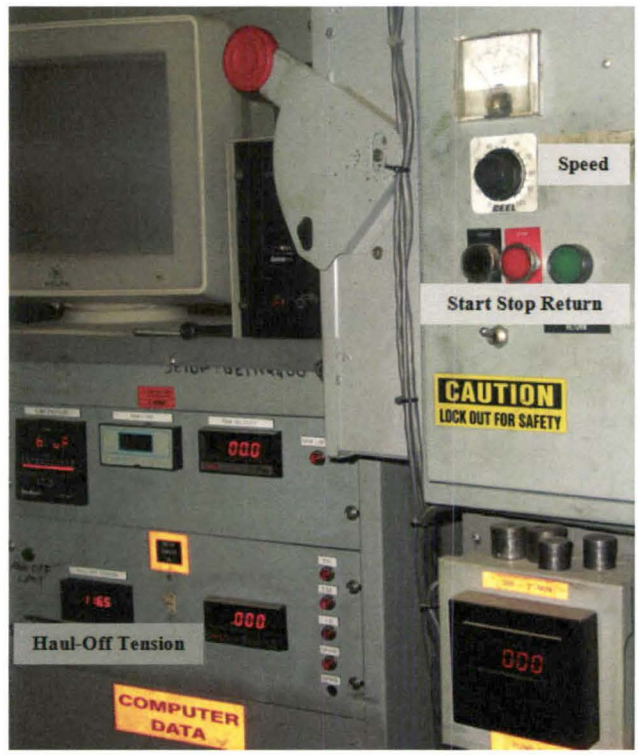

Figure 3.5 Haul-off tension controller system.

Die and ram dimensions (inch)	Inner diameter of the extrusion die	1.4
	Outer diameter of the mandrel	1.0
Pre-heating	Tubular billet heating temperature (°C)	150
	Average tubular billet heating time (hr)	3.0
Ram extruder temperatures (°C)	Rear chamber	145
	Front chamber	145
	Rear die	140
	Front die	140
Extrusion process data	Haul-off tension (lbs)	510
	Running hydraulic pressure (psi)	1800
	Average extrusion speed (inch/min)	4.0
	Max. tension withdrawal tube (lbs)	1700

Table 3.2 Solid state extrusion parameters.

To achieve good sealing of the ends of the tube during AF-HGTF and AF-HOTF processes, extrusion dies were modified to produce the exact size (inner and outer diameter) with a good clearance to match the plugs in the open tube hot oil bulge testing and the closed die hot gas tube forming systems (to be described in the next chapter). In addition, the die drawing load (or haul-off tension) was adjusted to achieve better shape control of the tube. The extruded tubes were then used as test samples in the tube forming

experiments as described later in Chapter 4. A procedure was developed to standardize the OPP tube production at PSAC, as given below:

1. Preheat the machined tubular billets in the external air oven for 3 hours at 150°C (refer to Figure 3.6).
2. Heat up front and rear chambers to 145°C, as well as front and rear die to 140°C and pressurize clamping cylinder to 5000 psi (with the use of a hand pump).
3. Lubricate inner and outer surfaces of the billet and mandrel with Castor oil.
4. Insert tubular billet and mandrel into the chamber and then extrude (refer to Figure 3.7).
5. After approximately 1 foot long section of the extruded tube emerges from the die, clamp tube with haul-off clamp and draw out of the die using a constant load of 510 lbs and 460 lbs for small and large tubes, respectively (refer to Figure 3.8).
6. Cool tube using 40 psi air compressor with 4 pressure nozzles positioned around the extruded tube at the exit side.
7. Apply a large load (1700 lbs) on extruded tube to release the last section (approximately 1 foot long from end of tube, i.e., tail section) from the extrusion die.

Since the first section of the tube was extruded without tension and the last section of the tube experienced a large load (tension) only to pull tube out of die, this variation of load affected its level of orientation and final tube dimensions. Therefore, only the middle sections of the extruded tubes (extruded with a constant tension) were

used for all subsequent tube forming and mechanical tests. In other words, the first and the last sections (head) and (tail) of the tubes were discarded.

Figure 3.6 Pre-heating of tubular billets in an external air oven.

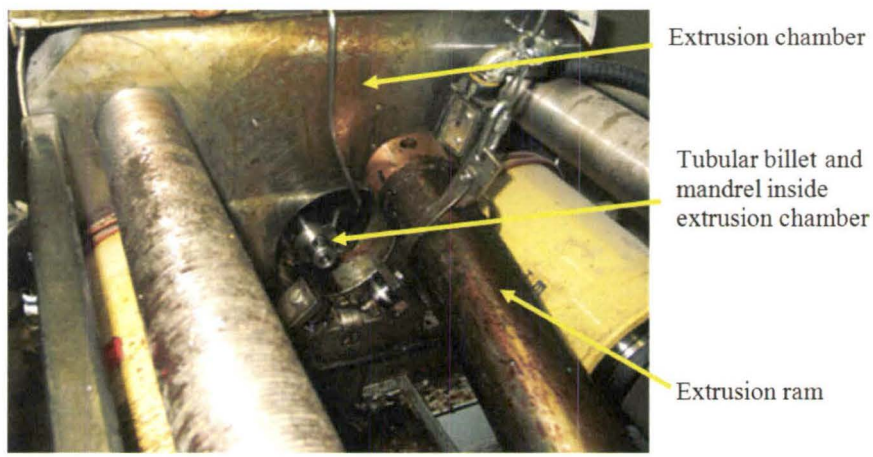

Figure 3.7 Insertion of tubular billet and mandrel into the chamber.

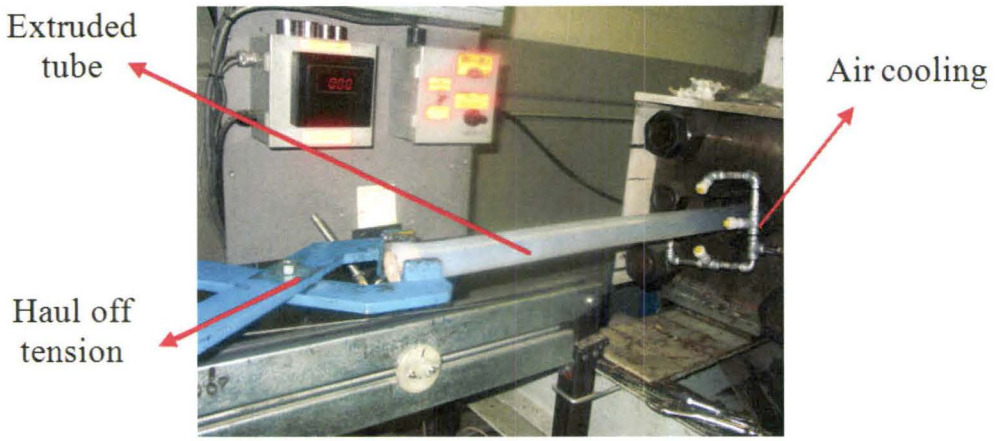

Figure 3.8 Application of a haul-off tension on extruded tube to draw it during extrusion with cooling air.

3.3 Sample Preparation Procedure for Microstructural Examination

For microstructural examination, samples of approximately 0.5 mm thickness, from both the billet and extruded tubes, were cut parallel and perpendicular to the extrusion direction using a rotary steel cutter with cooling water (refer to Figures 3.9 - 3.11). These samples were cut for use with the following physical techniques:

a. For examination in a polarizing microscope, cryomicrotomy was performed at -100°C to produce 2-3 μm thick sections.

b. For Field Emission Scanning Electron Microscopy (or FE-SEM), each sample was dipped in liquid nitrogen and then fractured along the extrusion direction.

c. For X-ray studies, the specimens were cut out of the extruded tubes at different positions in the extrusion direction from the inner to the outer surface, the size of these fibers was about 0.5mm x 0.5mm.

The distribution of crystalline orientation within a sample was obtained through a pole figure analysis. The results of pole figure measurements were plotted by using GADDS Software (Bruker-AXS). The preferred orientation was recorded using the Debye patterns. The data collected from XRD was utilized to obtain an estimate of % crystallinity and phase form from a single frame. Also, pole figures were generated from a sequence of frames and used to calculate the ODF.

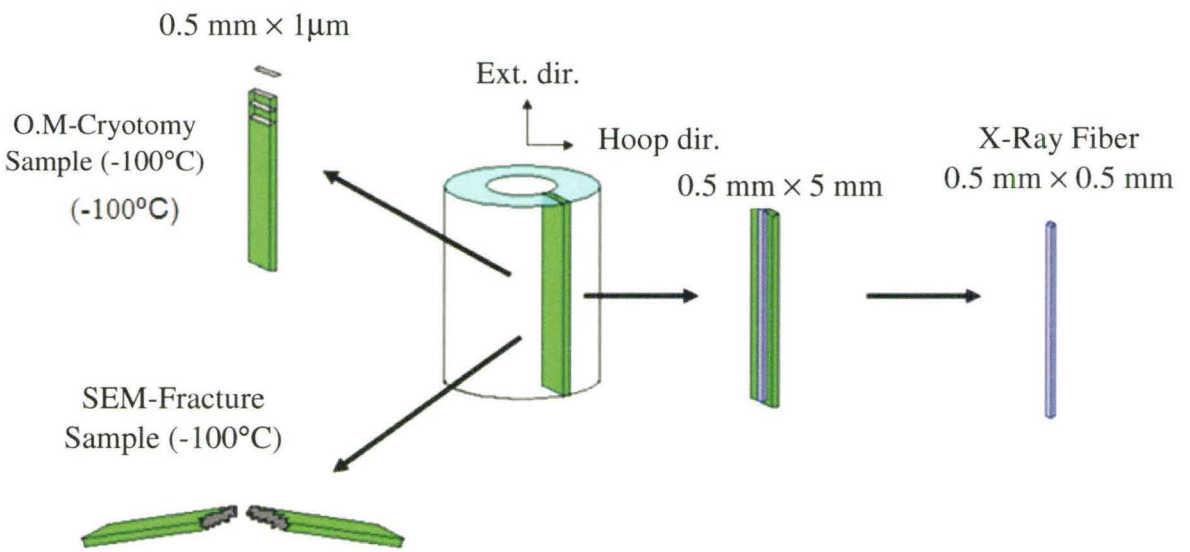

Figure 3.9 A schematic showing specimens cut parallel to the extrusion direction from billet and extruded tube.

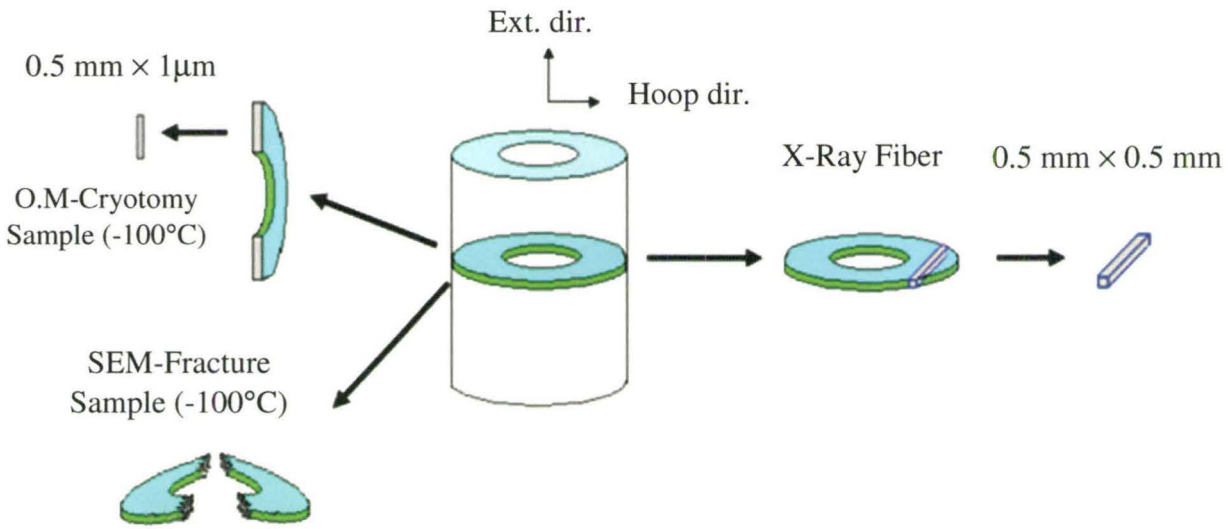

Figure 3.10 A schematic showing specimens cut out from billet and extruded tube perpendicular to the extrusion direction.

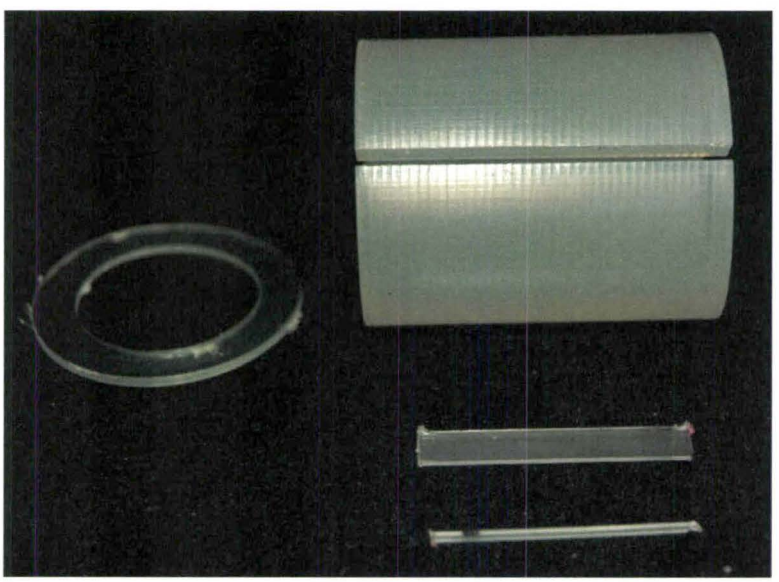

Figure 3.11 A photograph showing specimens cut out from extruded tube parallel and perpendicular to the extrusion direction.

3.4 Investigation of the Effect of Preheating and Extrusion Process on Degradation of OPP Tube

As the billets were annealed (preheated) three hours in air oven at 150°C prior to extrusion, they were examined for thermo-oxidative degradation during heating and extrusion, a high-shear conversion process. Therefore, the dynamic rheological properties were measured by an Advanced Rheometric Expansion System (ARES) in the parallel plate mode (see Figure 3.12). Polypropylene samples were machined from billet and extruded tube and cut to 1 mm thick and 25.4 mm outer diameter curved disks (refer to Figure 3.13). The disk samples were analyzed with a Stress Tech rheometer. A sample was placed between the plates and dynamic torsional shear was applied to the sample under 2.5 % strain while keeping a gap of 1 mm between the plates. Frequency sweep (0.1-100 rad/sec) measurements of storage modulus (G') and dynamic viscosity (η') were carried out on the samples while the temperature was maintained constant at 190°C. The test was repeated three times for each sample. Average results in terms of Log G' versus frequency are shown in Figure 3.14.

Identical characteristics are obtained for the billet and the extruded tube suggesting that thermo-oxidative degradation was negligible during the heating and extrusion of oriented polypropylene tube.

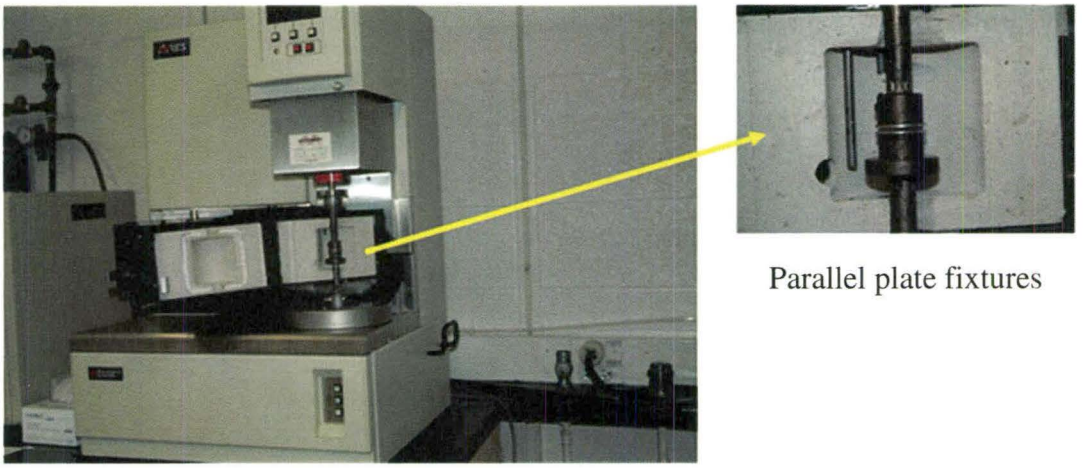

Figure 3.12 Advanced Rheometric Expansion System (ARES).

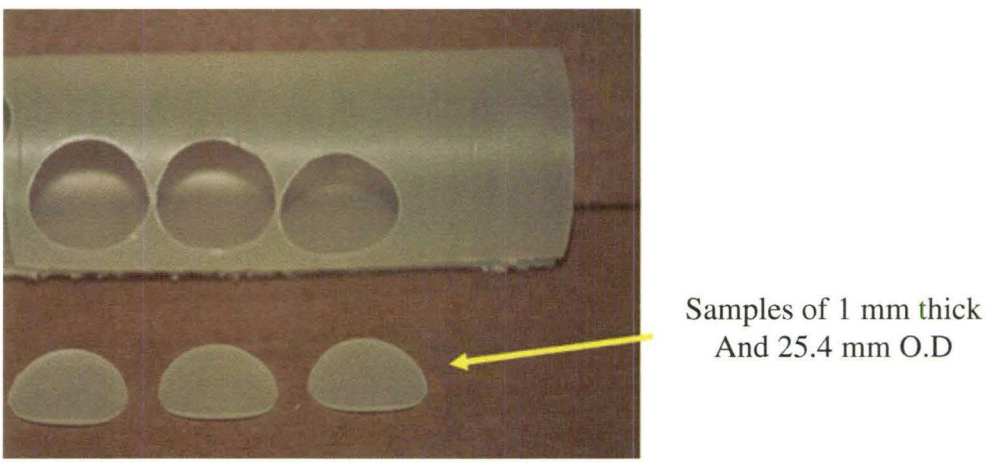

Figure 3.13 Samples machined from billet and extruded tube.

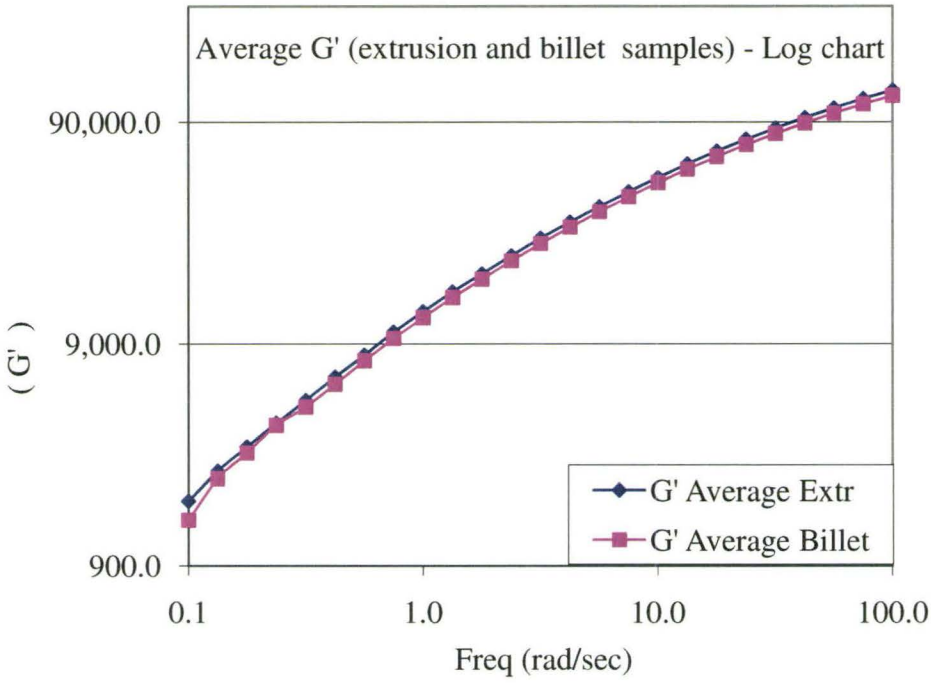

Figure 3.14 Frequency sweep measurement of storage modulus (G') at constant temperature 190°C.

3.5 Investigation of Material Heating due to Cutting and its Influence on Microstructure

The issue of heating up of OPP tube samples during specimen cutting and its influence on the microstructure was also investigated. Cut samples were examined in a polarizing microscope and FE-SEM. A piece of extruded tube, 30 ×20 × 3 mm in size, was used for this purpose. Two locations, 5 mm apart, were marked on the surface of the piece (locations 1 and 2 in Figure 3.15-a). X-ray diffraction was used to collect data from both locations. A cut, perpendicular to the extrusion direction, was made by using a

rotary steel cutter with cooling water, Figure 3.15-b. It should be noted that the cut was made close to location 2 and not far from location 1. Again, the X-ray diffraction was used, with the same settings, to collect data from the same two locations.

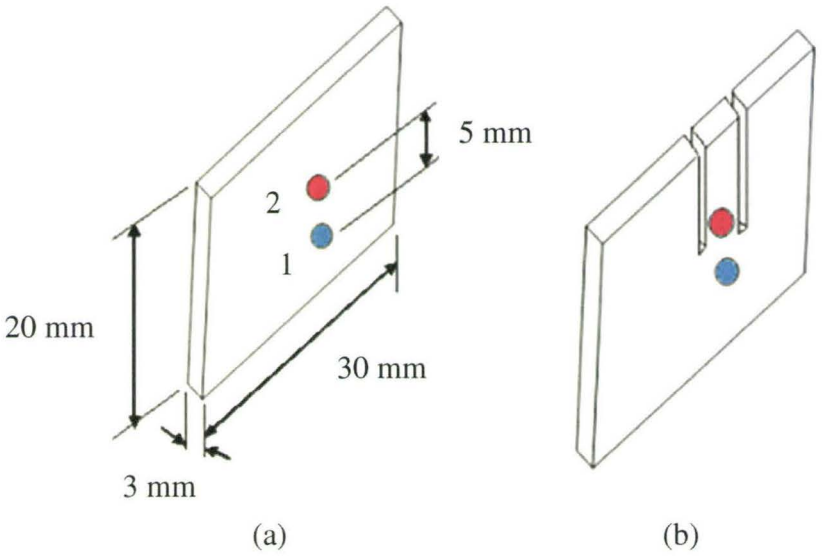

Figure 3.15 (a), (b) Fiber cut out of extruded tube in the extrusion direction.

The X-ray diffraction patterns for the two locations before and after the cut using the Debye patterns are shown in Figure 3.16. The preferred orientations before and after the cut indicate that all reflections in the frames are quite similar. The X-ray diffraction profiles of the two locations before and after the cut are shown in Figure 3.17. The 2 theta-intensity plots for the 2 locations, before and after the cut, have the same profile and the same peaks with almost the same intensity. No change in phase form was observed. Both samples contained only the α-phase form.

The percent of crystallinity were calculated from the collected data. The results in Table 3.3 show that the percent of crystallinity for both locations, before and after the cut, remained largely unchanged.

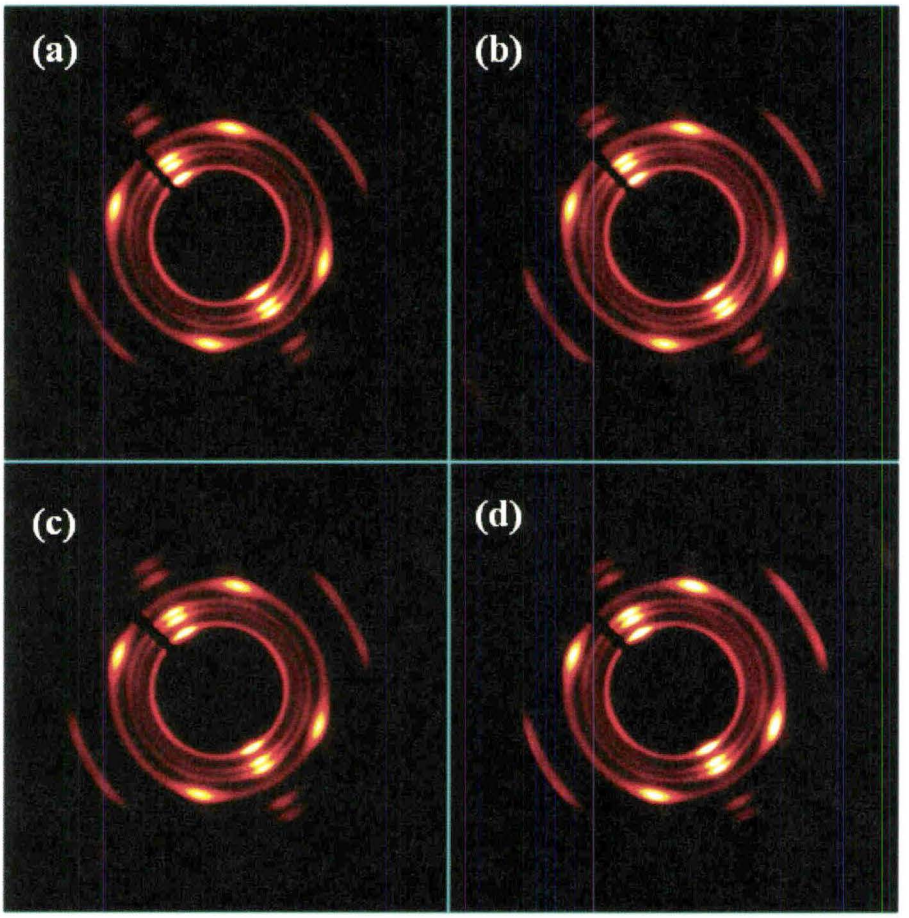

Figure 3.16 X-ray diffraction pattern for the two locations 1 and 2 before and after cut on the piece of extruded polypropylene tube: (a) point 1 before cut, (b) point 2 before cut, (c) point 1 after cut and (d) point 2 after cut.

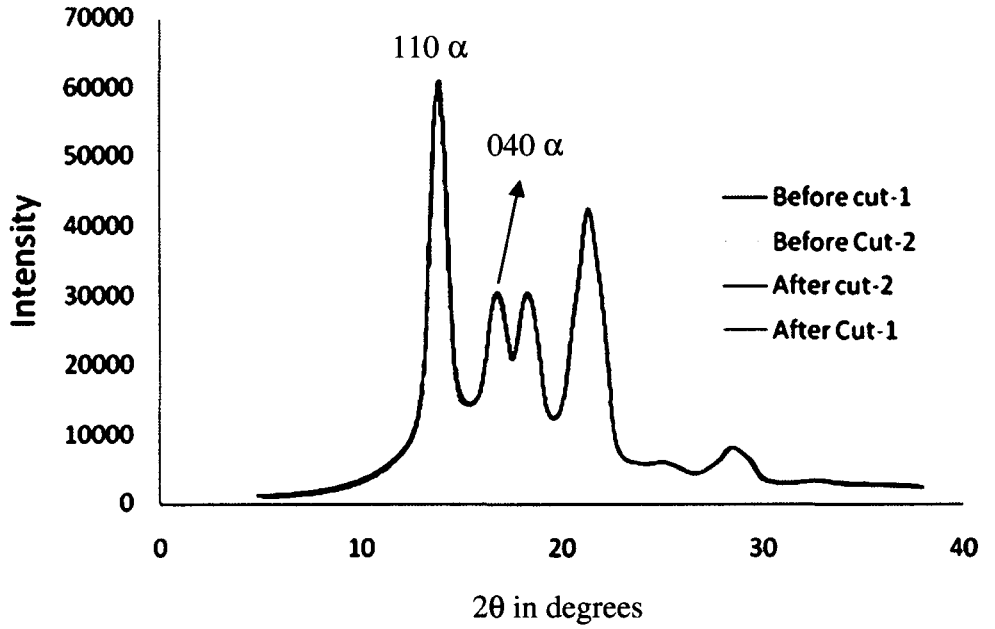

Figure 3.17 The X-ray diffraction profiles of the two locations before and after cut.

Sample name	% Crystallinity
Before cut-1	48.2
Before cut-2	48.2
After cut-1	48.34
After cut-2	49.1

Table 3.3 Percentage crystallinity at locations 1 and 2 before and after cut.

For a further investigation, a sample of thickness approximately 0.5 mm was cut perpendicular to the extrusion direction using a rotary steel cutter with cooling water. The sample was dipped in liquid nitrogen and then fractured along the extrusion direction. The fractured surface was coated by a very thin layer of gold using a sputter coater

(S150B) and then observed under a low voltage (3.0 kV) field emission scanning electron microscope (FE-SEM JEOL JSM-7000F). Figure 3.18 shows the fractured surface along the extrusion direction and cut surface perpendicular to it at two different magnifications. Clearly, the damage to the fibres arising from the steel cutter is only of the order of 5-10 μm in depth.

The other sample of thickness approximately 0.5 mm of extruded PP tube was cut using a rotary steel cutter with cooling water. Cryomicrotomy was done at –100°C. A thin section of about 1-3 μm was examined in a polarizing microscope (refer to Figure. 3.19). It is shown that the edge of cut surface did not have significant change in texture and there are fibres continuously up to the edge of the cut surface. The results showed that the cut material did not exhibit a significant change in its microstructure.

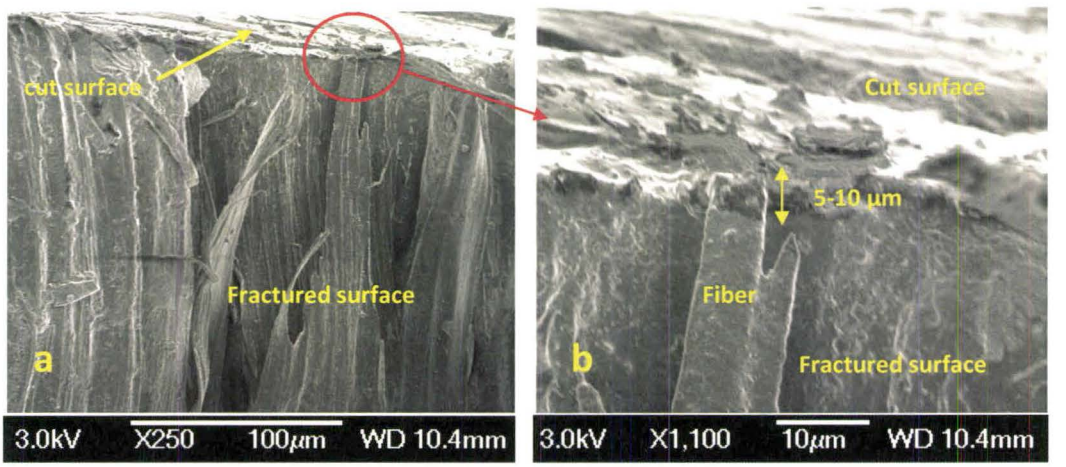

Figure 3.18 FE-SEM micographes of extruded PP fracture surface in liquid nitrogen after cut by a rotary steel cutter with cooling, (a) magnification at ×250 and (b) magnification at ×1100.

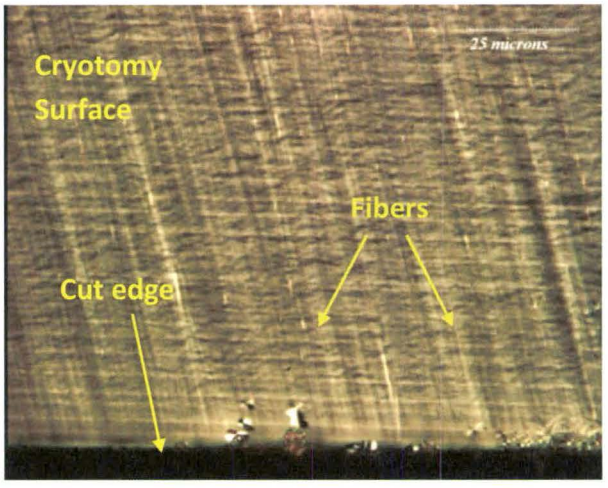

Figure 3.19 Polarizing microscopy image of extruded PP tube after cut using a rotary steel cutter with cooling water and cryotomy at low temperature.

3.6 Room Temperature Axial Tension Test

Longitudinal tensile specimens were machined along the extrusion direction from unoriented polypropylene billets and large extruded diameter polypropylene tubes produced with draw ratios of 4.0 and 5.0. Tensile specimens were machined according to type 5 of ASTM D638 (refer to Figure 3.20). All tests were carried out on a 100 kN servo-hydraulic mechanical testing system with a load cell of capacity 22.24 kN (5 kipf) at initial strain rates of 0.002/sec and 0.044/sec at room temperature. Each test was continued until failure of the specimen. Experimental load data and cross-head displacement were then recorded and later processed to obtain true stress-strain curves.

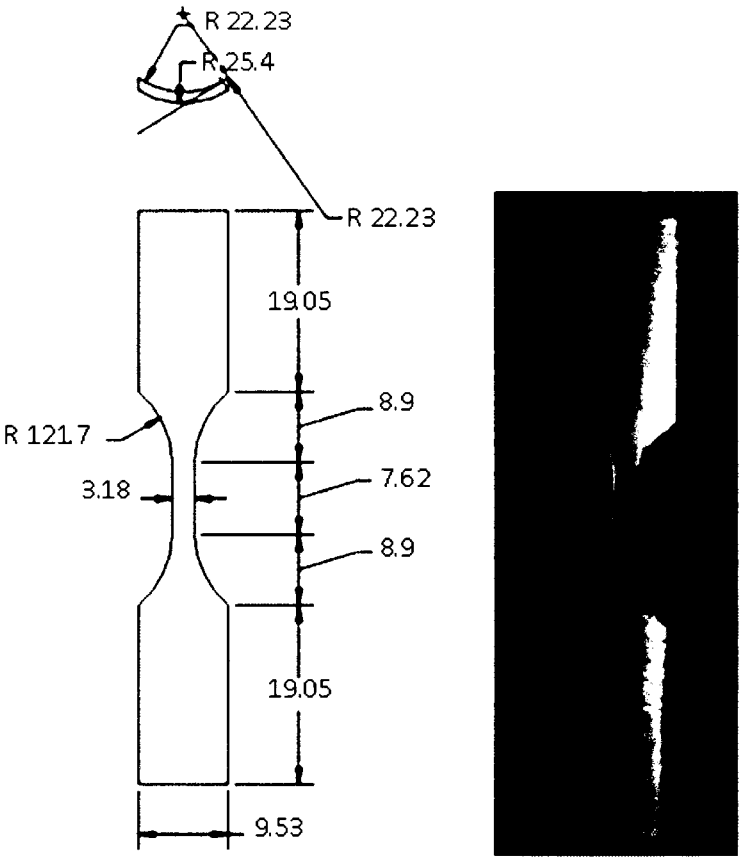

Figure 3.20 Tensile specimen cut along extrusion direction of OPP tube specimen dimensions are in mm.

3.7 Cryotomy and Optical Microscopy

To reduce the damage during microtomy the specimen were hardened by cooling below the glass transition temperature. For this purpose, cryomicrotomy of PP tube samples was performed at low temperatures to produce thin sections suitable for examination in a polarizing microscope. Thin-sections of approximately (1-2 μm) were

prepared at about –100°C, using liquid nitrogen, and a microtomy equipment (Reichert Ultracut E) with a Reichert FC4E 'cryo' attachment and equipped with a glass knife as shown in Figure 3.21. Sections were cut from billet and extruded tubes parallel and perpendicular to the extrusion direction (refer to earlier Figures 3.9 and 3.10). The thin sections were supported on glass slides using a Tungsten wire loop and hair to obtain good sections before they curled. The samples were then examined with optical microscopy under polarized light.

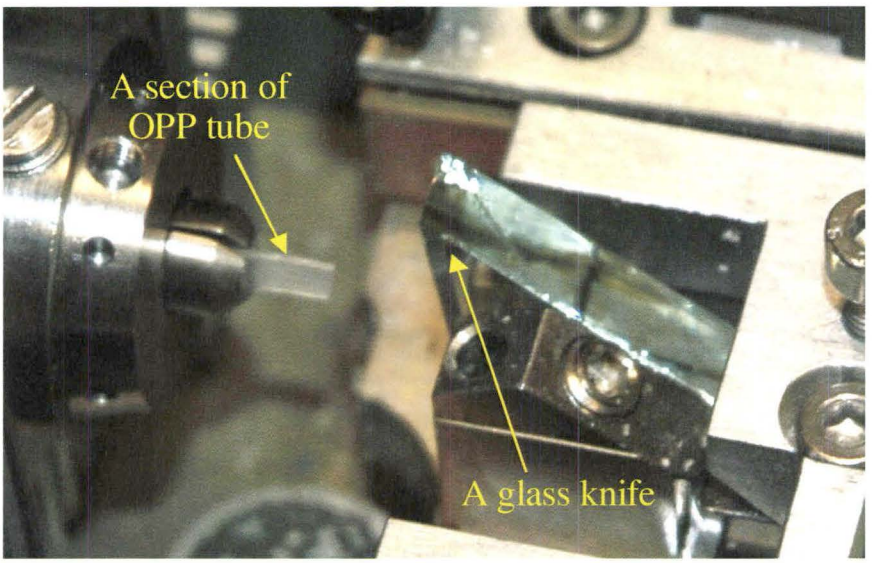

Figure 3.21 A section of OPP tube fixed in microtomy equipment with a glass knife.

3.8 FE-SEM Experiments

The purpose of using a FE-SEM was to evaluate the morphological changes in the extruded tubes at various draw ratios. The advantage of FE-SEM is that it operates at lower voltage which lessens damage to specimen surfaces. In addition, crystalline morphology can be directly observed without any chemical treatment to the samples and with minimal coating.

Samples of thickness approximately 0.5 mm parallel and perpendicular to the extrusion direction were cut using a rotary steel cutter with cooling water (refer to section 3.3). Each sample was dipped in liquid nitrogen and then fractured along the extrusion direction as shown in Figure 3.22. The fractured surface was coated by a very thin layer of gold using a sputter coater (S150B) and then observed under a low voltage (3.0 kV) FE-SEM, JEOL JSM-7000F.

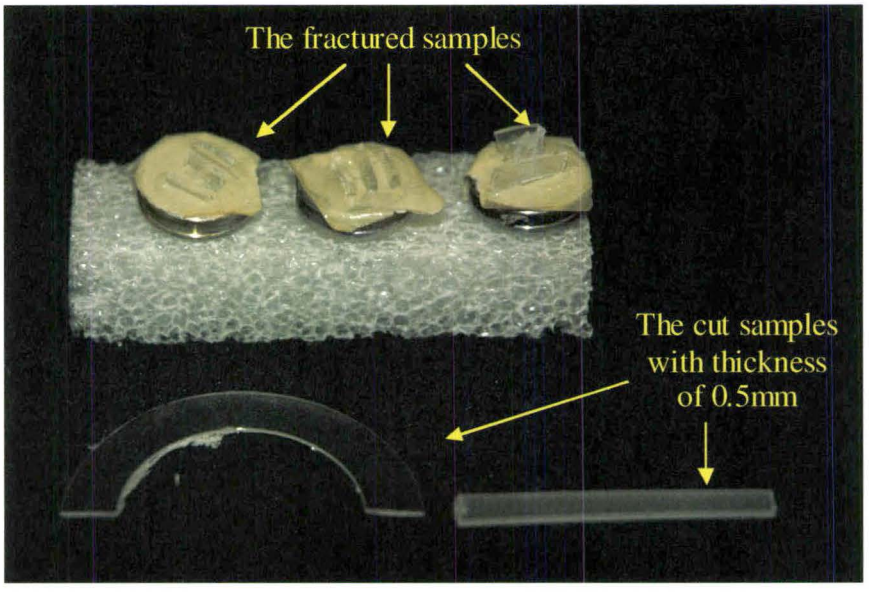

Figure 3.22 Cut and fractured samples prepared for Field-Emission Scanning Electron Microscope (FE-SEM).

3.9 WAXD Experiments

A complete picture of the distribution of crystalline orientation within a sample was obtained through pole figure analysis of X-ray diffraction (XRD) data. A XRD system operating at 50 kV and 90 mA, with a Cu K_α (λ = 1.54 Å) line, was utilized. The specimens were cut out of extruded tubes at different positions in the extrusion direction from inner to outer surface (refer to earlier section 3.3), the size of these fibers was 15 mm x 0.5mm x 0.5mm.

The diffraction experiments were conducted in the transmission mode and the output signal was recorded on a flat CCD area detector at a distance of 50 mm. The

specimen was mounted on an automated single crystal orienter as shown in Figure 3.23. A rotation of ϕ (0°-360°) was made with 5° intervals.

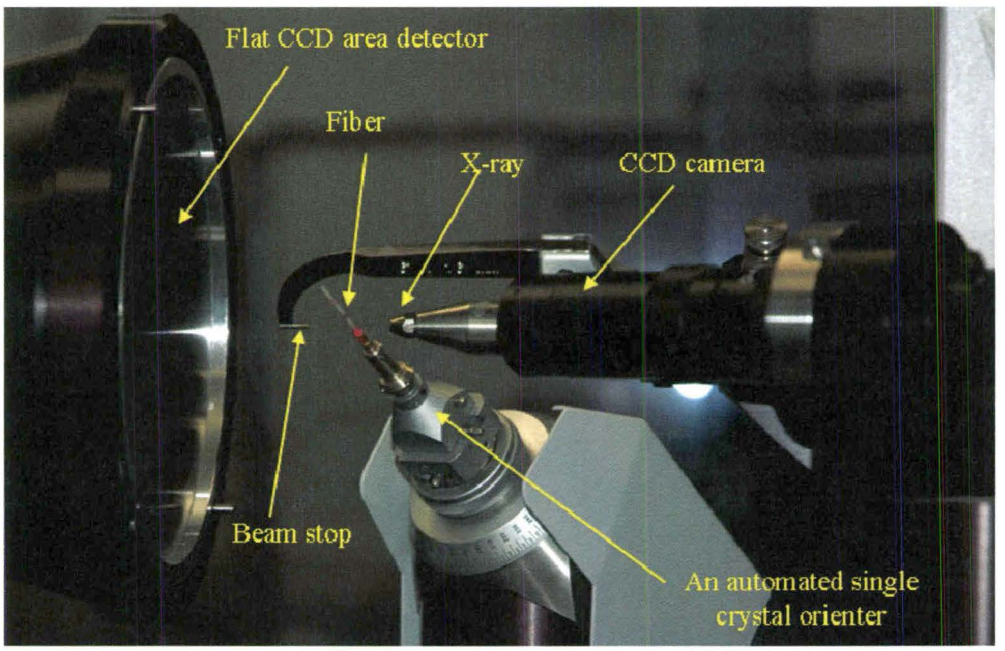

Figure 3.23 A photograph of fiber positioned in a typical X-Ray system.

Chapter 4

Experimental Methodology for Tube Forming Experiments

4.1 Initial Tube Geometry for AF-HOTF

Tube hot forming experiments were conducted on oriented tubes that had been produced by solid state extrusion (refer to chapter 3). The initial tube length was estimated by adding the necessary axial feed distances and by accounting for the shrinkage of the tube after preheating. Tube samples for axial feed hot oil tube forming (AF-HOTF) experiments were cut from the middle part of the extruded tube to the desired length of 6 inches. The inner edge of the tube was slightly chamfered to obtain a good seal between inner surface of the tube and outer surface of the plug. As mentioned earlier in chapter 3, the outer and inner dimensions of the small tube were 1.4 and 1 inch respectively and for the large tube were 2.0 and 1.74 inch respectively. Tube end preparation steps for AF-HOTF experiments tests are shown in Figures (4.1- 4.3).

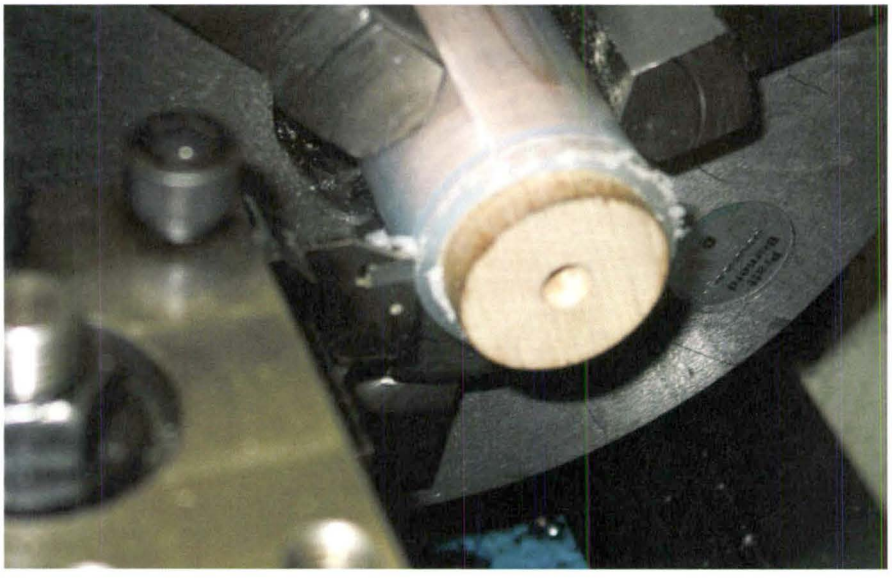

Figure 4.1 Cutting of tube to required length using wood support.

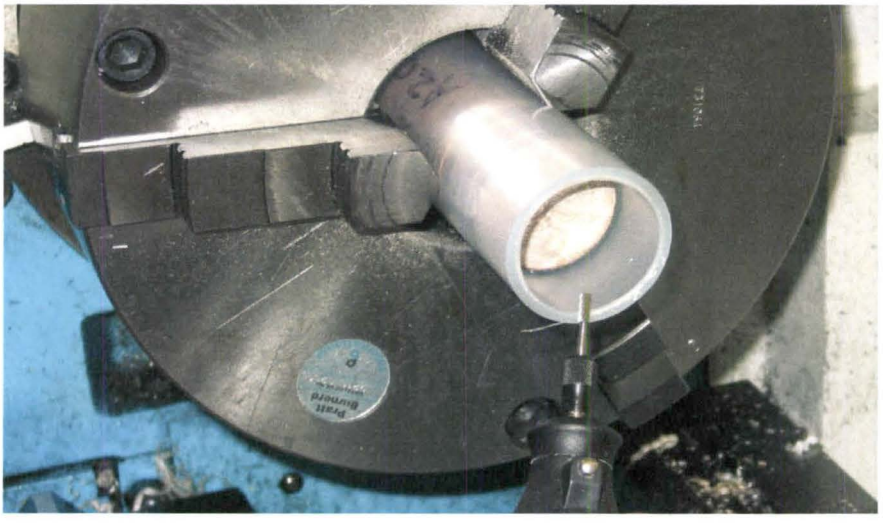

Figure 4.2 Chamfered inner edge of tube.

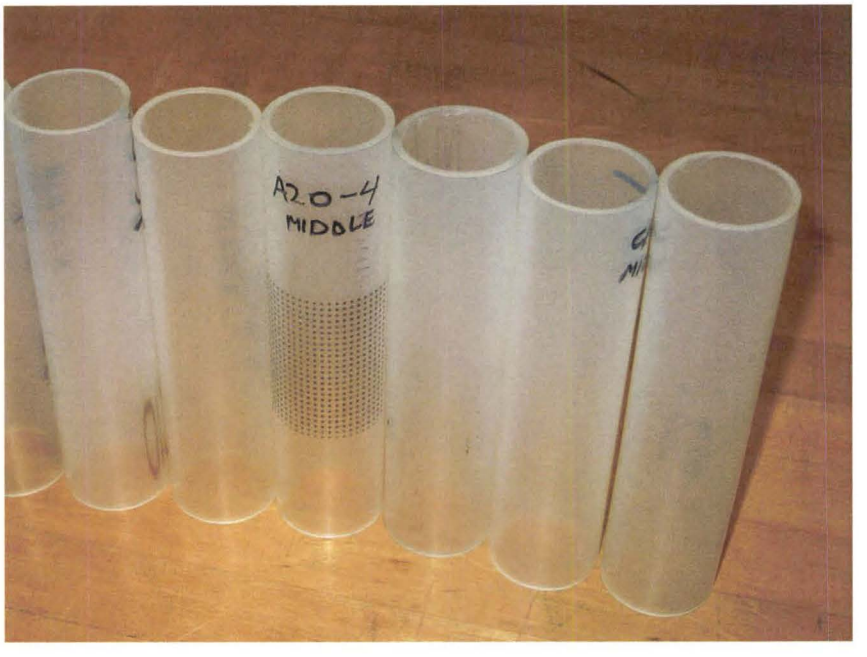

Figure 4.3 Final tube samples for forming.

4.2 ARAMIS Optical Strain Measurements System

An on-line non-contact optical strain measurement system (ARAMIS® system from GOM, Germany) was utilized to obtain rapid and accurate elastic and plastic strain fields at large strains during the bulging experiments. ARAMIS system uses a random speckle pattern that is typically applied using a widely available spray gun fitted with a fine nozzle thus greatly simplifying the specimen preparation effort. The CCD cameras continuously record deformation of the speckled surface of the sample during and after bulging of tube samples. In ARAMIS, the surface displacements are determined by correlating successive images recorded from the camera before and during the

deformation based on so-called digital image correlation (or DIC) method. ARAMIS with a single high-resolution digital CCD camera is capable of measuring the 2D or planar surface displacement field of a deforming body over large displacements. Figure 4.4 shows the ARAMIS 3D system with two CCD cameras and dedicated computer software that is capable of measuring 3D deformation and strain field under any quasi-static loading conditions.

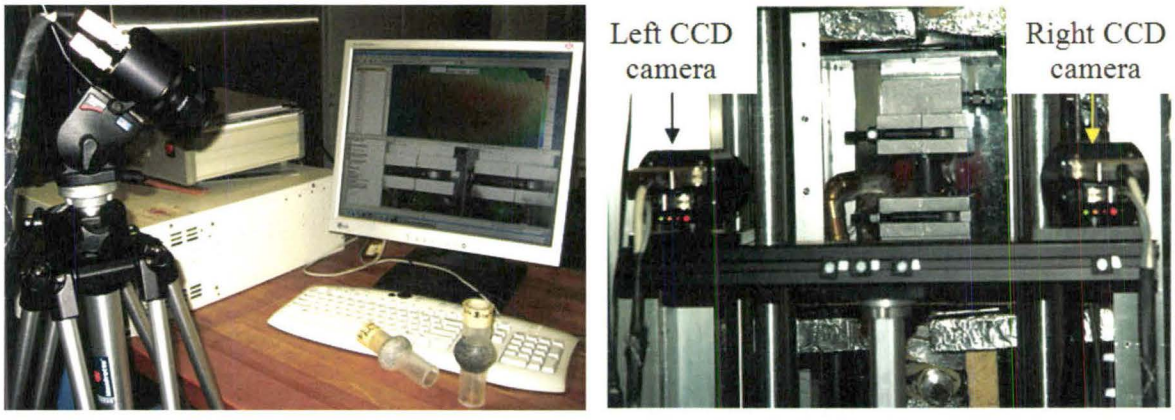

(a) (b)

Figure 4.4 ARAMIS optical strain measurement system (a) single CCD camera (b) two CCD cameras.

4.2.1 Strain Measurement Procedure Using ARAMIS System

The following strain measurement procedure was utilized:

1. A random speckle pattern (black and white) was applied to the surface of the tube sample, and then the tube was inserted between two plugs as shown in Figure 4.5.

2. The tube under a small pre-load was viewed by two CCD cameras and a software calibration in 3D mode was carried out.

3. The bulging experiment was carried while continuously recording a large number of image frames (2 frames per second) of the bulging region of the sample tube from the two cameras. The test system was designed and built in a way to allow an 'open' view of the bulging tube.

4. All recorded images were processed using dedicated strain analysis software with the ARAMIS system utilizing micro-image facets of size 15 pixels x 13 pixels (i.e. 0.3 mm x 0.26 mm). There facets were tracked in each successive image with sub-pixel accuracy (0.015 pixels x 0.013 pixels (i.e. 0.3 μm x 0.26 μm).

5. The 3D coordinates of the tube surface which are related to the facets at each stage of load were obtained and the strain maps and profiles of interest were plotted for analysis. The major (axial) and minor (circumferential) strains at any location on the viewed surface of the tube and at any stage of the deformation (i.e., spatial and temporal strain data) could be obtained.

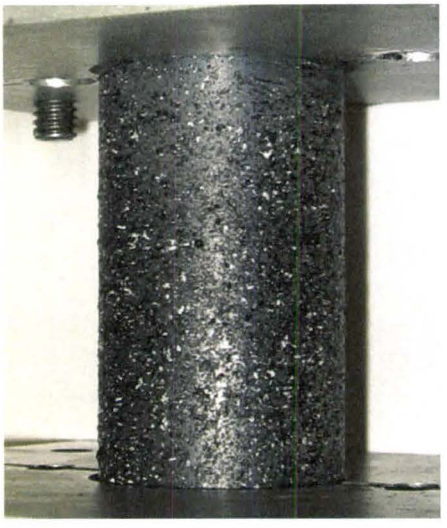

Figure 4.5 A photograph showing random black and white speckle on the surface of OPP tube.

4.3 Axial Feed Hot Oil Tube Forming System (AF-HOTF)

The open tube bulge testing system (AF-HOTF) was designed, fabricated, commissioned and then used to conduct formability tests on OPP tubes. Tube sealing system, shown in Figure 4.6, was designed as part of this research and fabricated. The test system was built around a hydraulically powered 25 kip mechanical test frame (MTS model 311.11). This frame is equipped with two hydraulically powered actuators connected to a PC-based control and data acquisition system (refer to Figure 4.7).

This system was designed to operate up to a temperature of 160°C and an oil pressure up to 3000 psi. A pressure transducer capable of measuring pressures up to

3000 psi was added to the system to record the internal pressure continuously as a function of time during the test. Also two air gun heaters were added to the system to minimize the diffrence in temprature inside and outside of the tube (refer to Figure 4.8). The design of this system allowed for better temperature control, optimization of strain rates, and repeatability of test conditions. Also, the 'open' design allowed for continuous observation of expanding tube using ARAMIS optical strain measurement system.

The tubes were heated by blowing hot air on outer surface of the tube and by circulating hot silicon oil from a tank to a hydraulic cylinder (instead of preheating the tube in an oven), through the polypropylene tube (specimen), and back to the tank. Figure 4.9 shows a schematic diagram describing the circulation of heated oil in the tube bulging system. A controlled pressurization rate for the expansion and/or bursting up to a pressure of 3000 psi was achieved at a range of temperatures between 20°C and 160°C. The upper actuator was moved downward to seal the tube as well as to provide axial feeding of the tube specimen during the bulging process. The lower actuator was used in tandem with the pressure intensifier to intensify the pressure inside the tube.

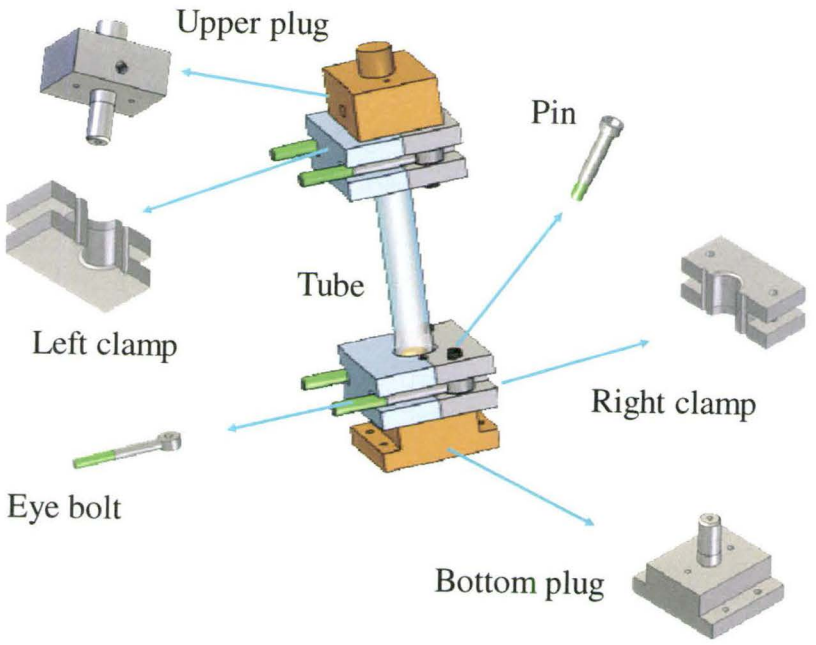

Figure 4.6 Tube sealing system (open die).

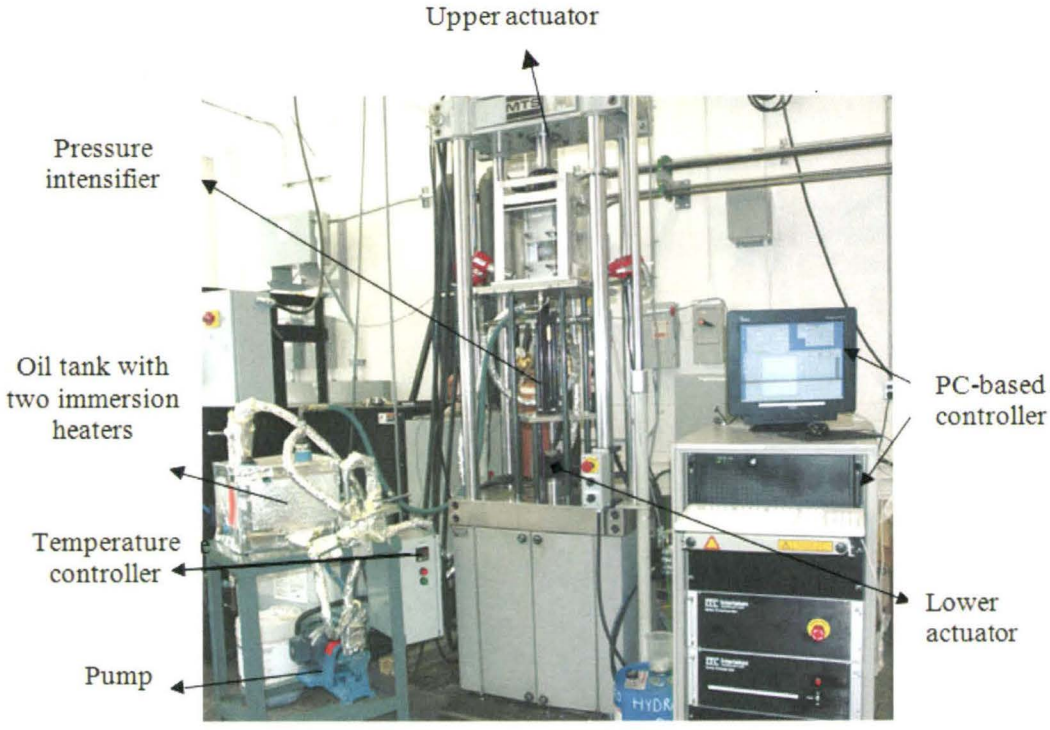

Figure 4.7 A photograph of oil based tube bulging system (AF-HOTF) built on MTS test frame.

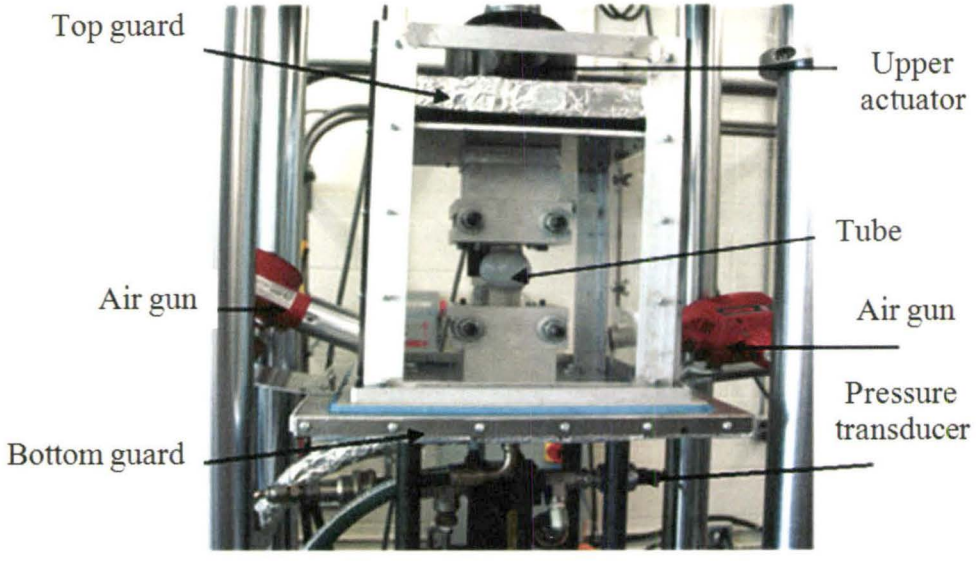

Figure 4.8 A close-up of AF-HOTF test system

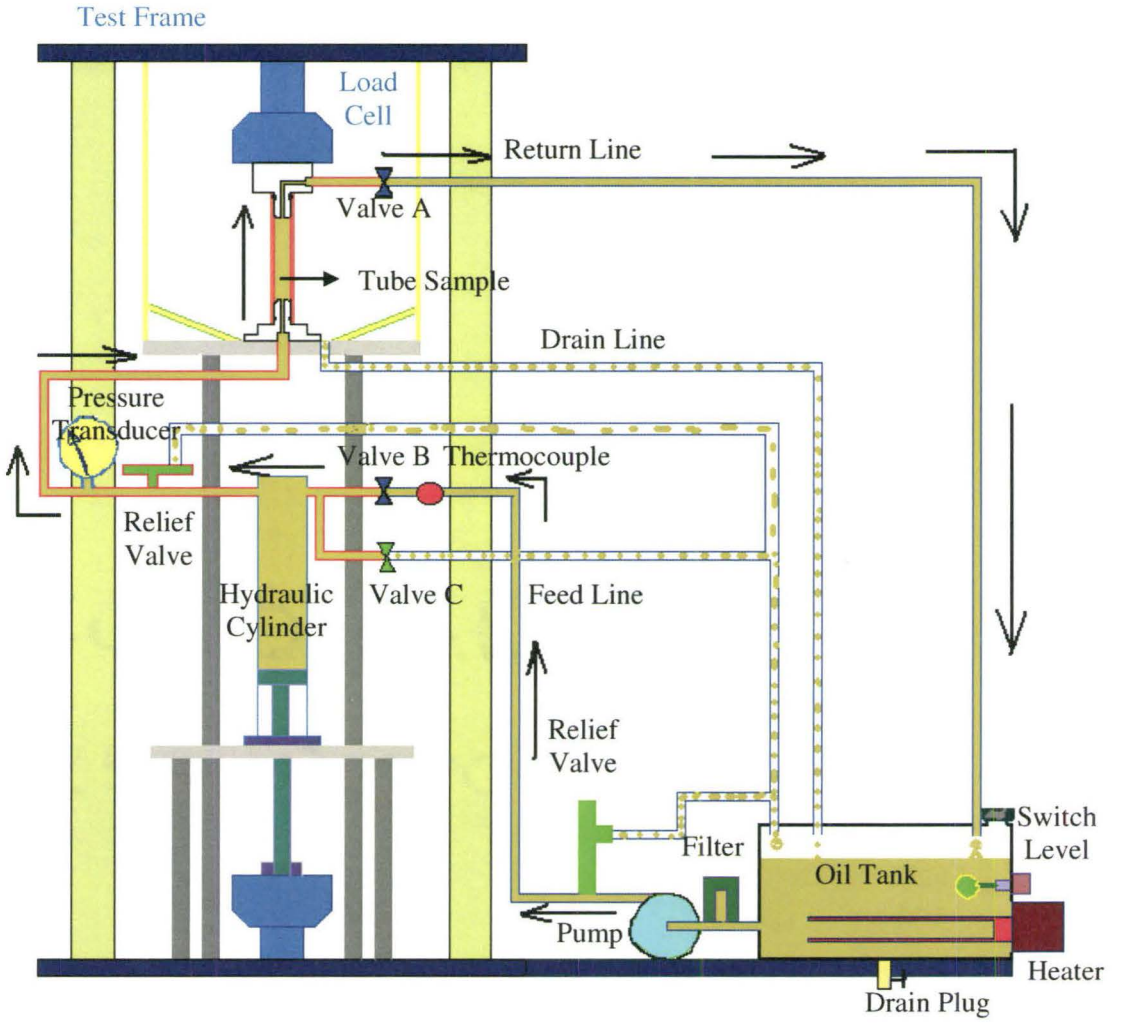

Figure 4.9 A schematic diagram of axial-feed oil based tube bulging system (AF-HOTF) showing details of the hydraulic and mechanical components.

4.3.1 Process Sequence for Bulging Tubes

Successful forming of a tube requires precise control of many forming conditions such as end sealing, tube temperature and cycle time. To note here is that a certain amount of external axial force needs to be applied to seal the tube-ends so as to prevent

leakage or loss of pressure during thermoforming. Other important parameters include internal pressure versus time sequence and axial feeding at the ends of the tube. These process parameters directly affect failure modes such as, bursting, wrinkling, and buckling in any axial feed forming process.

Bursting failure is an irrecoverable failure mode and occurs as a result of excessive high internal pressure. On the other hand, buckling is due to high axial force that acts at the beginning of the process, while wrinkling is due to excessive compressive load during the initial and intermediate stages of hot forming process, it can be often eliminated by an increase in internal pressure at the final stage of hot forming process. The loading paths for internal pressure and axial-feed were obtained by an iterative trial and error procedure. The final chosen sequence is shown in Figure 4.10. A special program was used in the controller of the test system to control each of the 6 process steps illustrated in Figure 4.10.

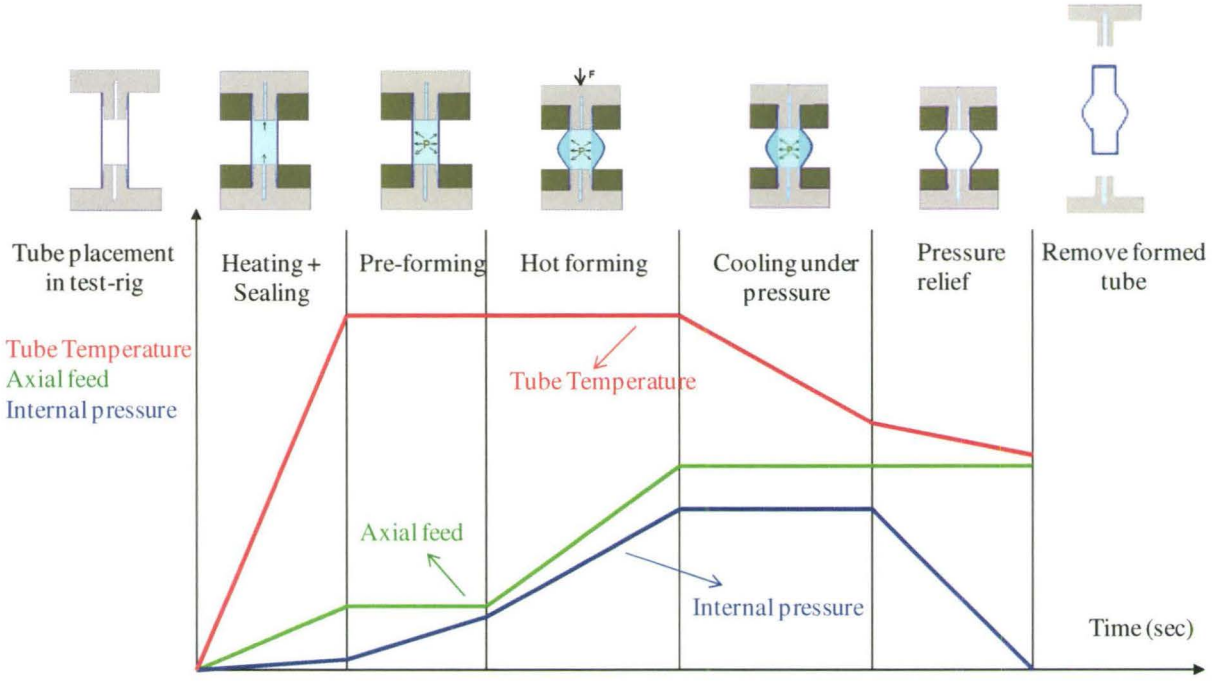

Figure 4.10 A typical process sequence for axial-feed hot oil tube forming (AF-HOTF) process (open die).

4.4 Axial Feed Hot Gas Tube Forming System (AF-HGTF)

An axial feed hot gas tube forming system (closed die) was also designed and used to conduct formability tests on OPP tubes (see Figure 4.11). This system consisted of a computer controlled hydraulic press (Interlaken 150 Ton Servo Press), front and back actuators, upper and lower dies, heating and cooling systems, and a PC-based control and a data acquisition system with the press. The test system allowed for simultaneous internal pressurization and axial end feeding of the tube. As a result of the internal gas pressure and axial feed, the tube expands and deforms to the desired shape controlled by

the geometry of the die-cavity. A die with an expanded cylindrical region in the centre was utilized for these experiments.

4.4.1 The Process Sequence for Deforming Tubes at a High Temperature Inside a Die

Forming a plastic tube in the die without defects requires precise control of a combination of many process parameters such as end feeding, internal gas pressure and tube temperature. A range of values of process parameters were applied in experiments to form the tube into a larger cylindrical shape at its centre.

The process sequence for a hot gas tube forming process is described below (refer to Figure 4.12):

a. Insert a preheated tube in the lower die. The tube was preheated in a nearby oven to a controlled temperature.
b. Close the die by moving the lower half of the die up and start preheating the die.
c. Move the front and back actuators (so called docking rods) towards the middle of the tube to sealing position at tube ends and then start pressurizing (performing).
d. Increase the internal pressure and axial feed simultaneously, as per Figure 4.12.
e. In this stage stop increasing internal pressure and axial feed (to calibrate tube material in die cavity) and cool formed tube inside the closed die under pressure.

f. At the end of the process when the temperature of the deformed tube has dropped to 80°C, release the pressure, retract the front and back actuators to the original position, open die and remove the formed tube.

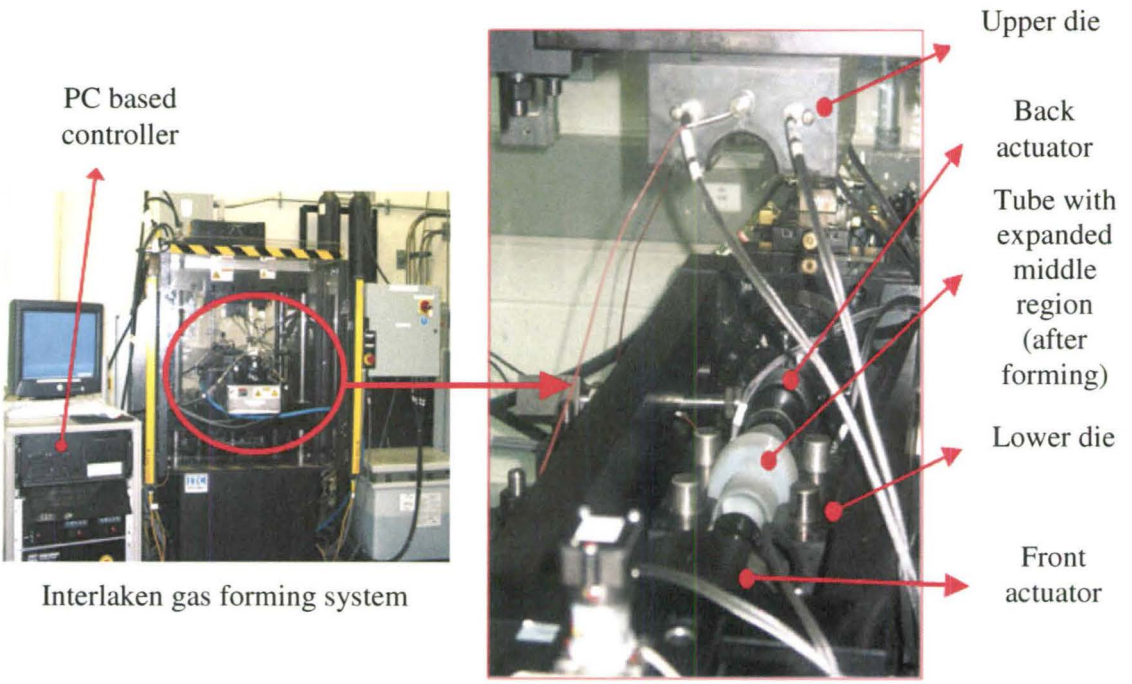

Figure 4.11 A photograph of Interlaken gas forming system, AF-HOTF. The system is show in open position

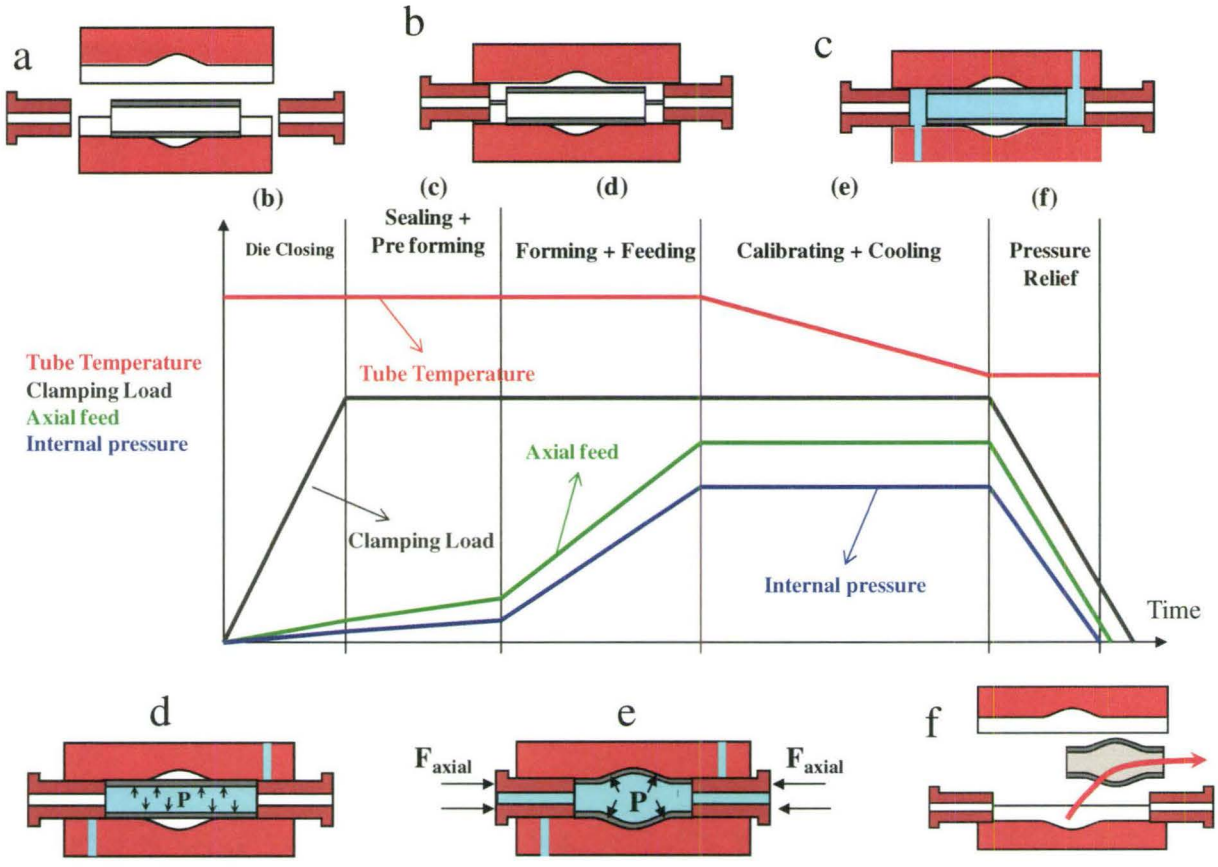

Figure 4.12 A typical process sequence for AF-HOTF process (closed die).

4.5 Axial Feed Hot Tube Forming Process Parameters

The most important process parameters in the axial-feed hot forming experiments are axial feed displacement, forming temperature, rate of forming, tube dimensions and maximum pressure applied. These process parameters depend on the size of tube and bulge system. To optimize process sequence and form a good quality part free of defects

(wrinkling, bursting and thinning), some parameters were held constant while others were systematically varied.

Table 4.1 summarizes all important process parameters and their range of values using open tube hot oil bulge testing (AF-HOTF) and closed die (AF-HGTF) systems.

Test systems	Tube dimensions	Hot forming process parameters	Range of values
Open tube hot oil bulge testing system (AF-HOTF process)	6 inch length ID =1.0 in OD = 1.4 in	Axial feed displacement Forming temperature Rate of forming Maximum pressure	0.0 to 0.9 in 20-160°C 4-15 psi/sec 400-600 psi
Closed die hot gas tube forming system (AF-HGTF process)	8 inch length ID =1.74 in OD = 2.0 in	Axial feed displacement Forming temperature Rate of forming Maximum pressure	0.0 to 1.5 in 20-160°C 3-15 psi/sec 300-500 psi

Table 4.1 Process parameters and the range of values utilized in the two experimental test systems.

4.6 Biaxial Ball Stretching Test System (BBST)

Open tube bulge test (AF-HOTF) involving simultaneous axial end feeding and internal pressurization was successful in generating strain paths to the left hand side of the forming limit diagram. Similarly, bulging tests with internal pressure and no axial end feeding were successful in subjecting the tube to close to the plane strain condition (refer to Figure 2.7).

In order to construct experimental forming limit diagram for OPP tube corresponding to the right hand side (i.e., biaxial tensile side) of the forming limit diagram (FLD), a new test rig was designed and machined. The test rig enabled stretching OPP tube with no axial end feeding to obtain strain paths closer to the equal biaxial strain path. Figure 4.13 shows a photograph of this system, referred to as biaxial ball stretching test (BBST) system. Detailed sketches of the various test rig components are illustrated in an exploded view in Figure 4.14. The upper part and lower part of the test rig were held in the grips, which were installed on MTS 250 kN servo-hydraulic test machine, fitted with an environmental chamber for conducting the elevated temperature tests. A horizontal movement of rod towards inner surface of tube, resulting from downward movement of the lower actuator, caused biaxial stretching of tube sample. Aramis camera was directed to the die opening to record the punch stretching process.

Tubes with a draw ratio of 6.3 produced via solid state ram extrusion were cut into two halves. The outer and inner diameters of the tubes were 35 mm and 25 mm respectively with 150 mm length. Tube samples were placed in test rig and heated to elevated temperatures of 150°C, 160°C and 170°C. Biaxial stretching tests were performed at an initial strain rate of 0.002/sec. The strain measurements during the biaxial stretching tests were made using ARAMIS system. The images were continuously recorded at the rate of 2 frames/sec during the test.

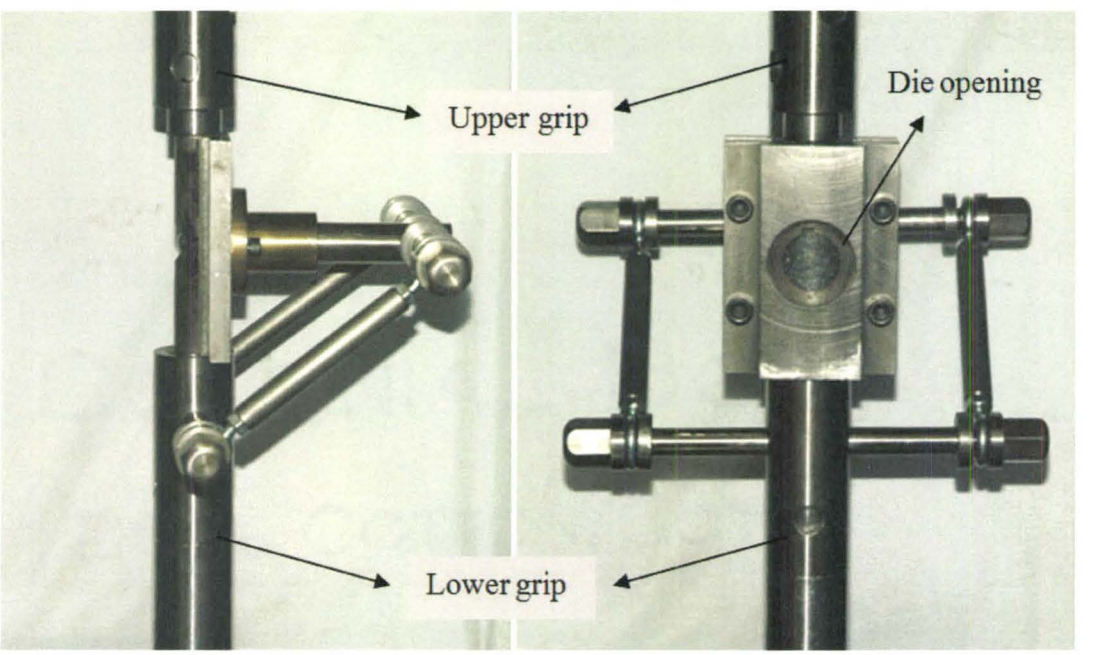

Figure 4.13 Side and front views of biaxial stretching ball test (BBST) system.

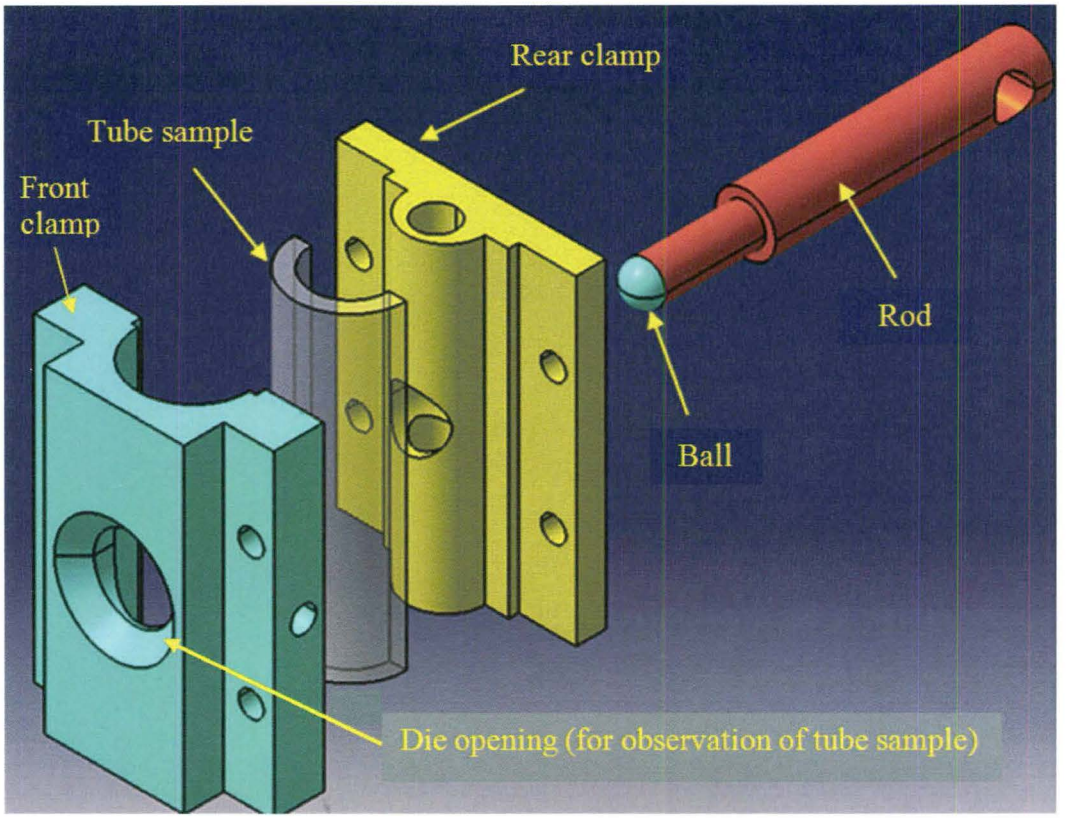

Figure 4.14 Tube sample insert between clamps in biaxial stretching ball test system.

4.7 Post-forming Tensile Tests

Tubes with a draw ratio of 6.3 produced via solid state ram extrusion were used for carrying out uniaxial tensile tests. The outer and inner diameters of the tubes were 35 mm and 25 mm respectively. All tensile samples for testing were machined from the wall regions, prior to and after hot forming as shown in Figure 4.15.

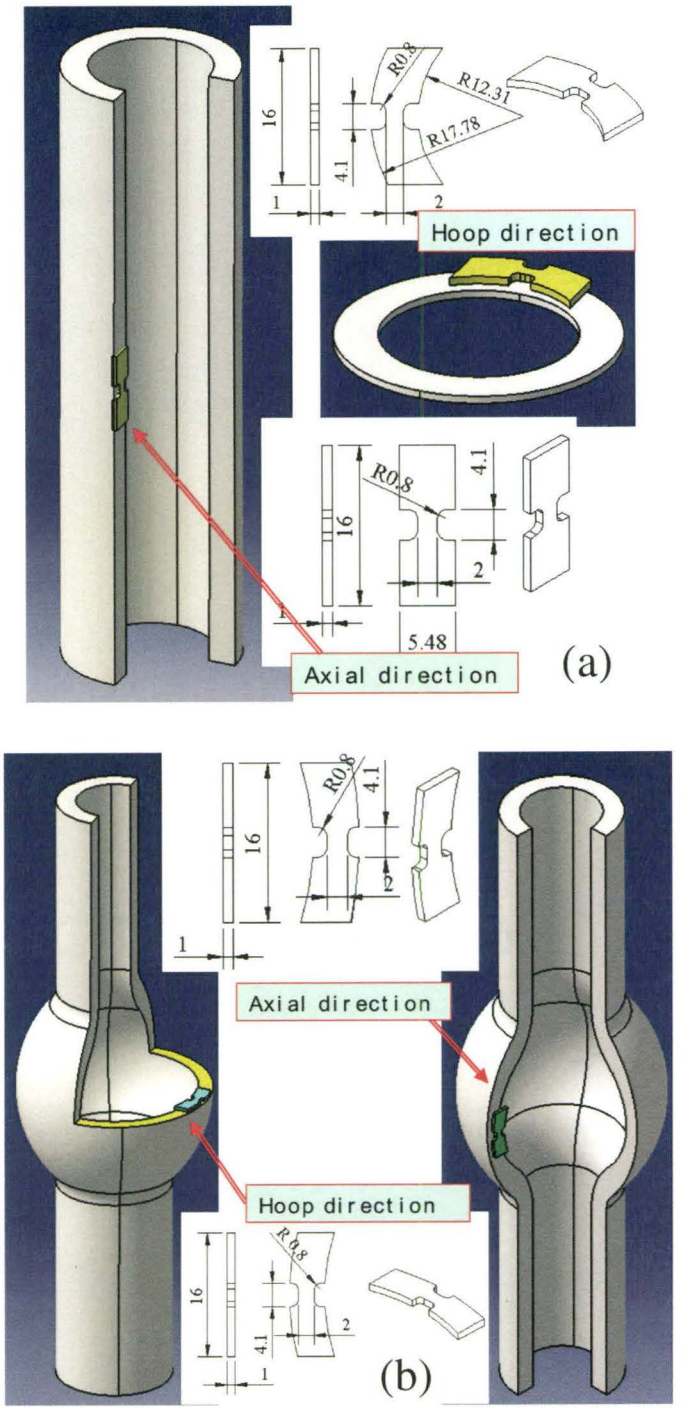

Figure 4.15 Machining position on the tensile samples (a) before, and (b) after bulging.

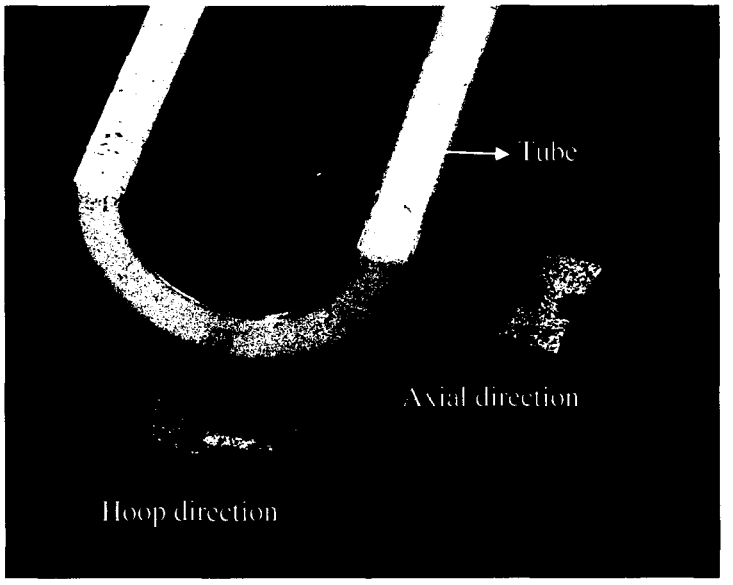

Figure 4.16 A photograph of the machining tensile samples before bulging.

The width of the gauge section of the tensile samples could not be larger than the tube wall thickness (see Figure 4.16). Therefore, specimens gauge length and width of 4.1 mm and 2 mm respectively were chosen. Uniaxial tensile tests were carried out at a nominal initial strain rate of 0.044/sec on a MTS 100 kN servo-hydraulic test machine with a load cell of 22.24 kN (5 kipf) capacity. The load versus displacement curves were continuously recorded during the tests. The strain measurements during the tension tests were also made using the ARAMIS system.

Chapter 5

Experimental Results

This chapter is divided into two sections. First, the results from physical and microstructural characterization of extruded tubes produced by solid state extrusion process are presented using the various techniques described in Chapter 3. Also included in this section are the mechanical properties of the billet extruded tubes via tensile testing. Second, the results from various hot forming experiments using AF-HOTF, AF-HGTF and BBST processes are presented. Also, an analytical model for the AF-HOTF process to predict the onset of instability (and hence the forming limits) is presented. Results for the model are then compared with the experiments. Further, microstructure results after tube forming are presented in terms of morphological changes, orientation factor and ODF data. Finally, post-forming mechanical properties from tensile test coupons are presented.

5.1 Physical, Microstructural and Mechanical Characteristics of Starting Billet and Extruded OPP Tubes

5.1.1 Physical Properties

As explained earlier in Chapter 2, the physical properties such as crystallization, melting temperature and an estimation of percent crystallinity were obtained for the starting tube stock (billet), extruded tube and bulged oriented polypropylene samples by DSC. Figure 5.1 shows a typical DSC result from instrument (DSC Q1000 V9.0 Build 275) for the billet during heating and cooling cycles. The results for the initial billet, extruded tube with a draw ratio of 4.0 and a bulged OPP tube sample are summarized in Table 5.1. The melting points (T_m) of the samples were between 164°C and 169°C, the crystallization temperatures (T_c) were in the range of 120°C to 123°C and the percent crystallinity was between 42% and 50%.

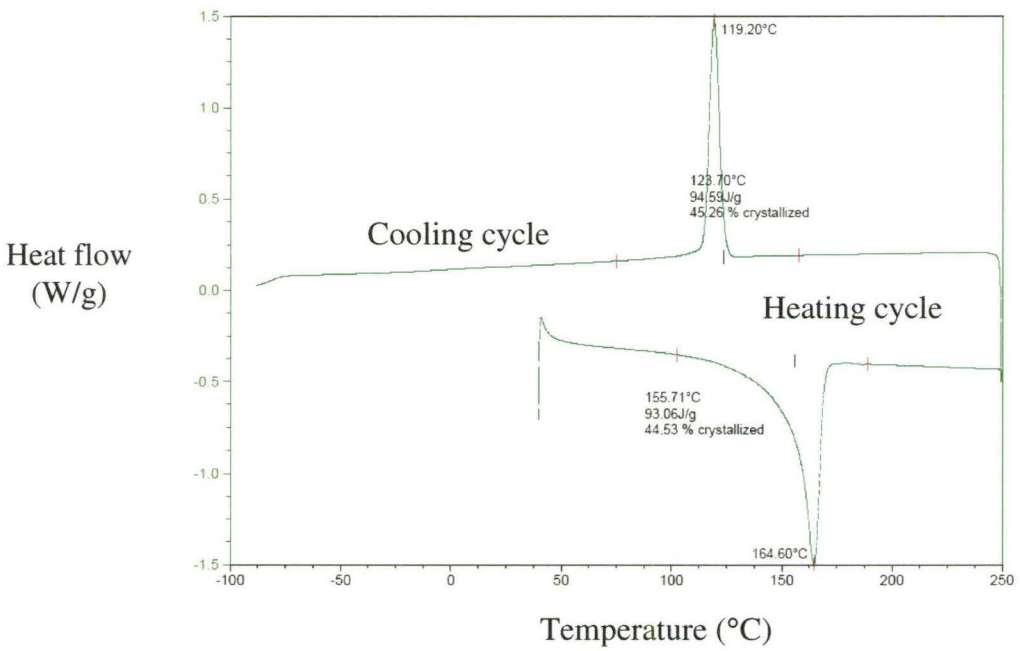

Figure 5.1 DSC test result (heating and cooling cycles) for the billet, atmosphere (N_2), heating rate 10°C/min.

Specific gravity tests were also performed as per the ASTM D792 A1 standard for a billet and an extruded tube. This resulted in a value of 0.9 g/cm^3 for specific gravity of the two PP samples.

Material Type (PP)	Draw Ratio (DR)	T_m (°C)	T_c (°C)	% Crystallized
Billet	-	164	121	45.1
Extruded sample cooled with air compressor	4.0	169	123	41.8
Extruded sample cooled in room temperature	4.0	165	120	49.8
Bulge extruded sample	4.0	169	123	45.8

Table 5.1 A summary of DSC test results for different PP samples.

5.1.2 Microstructural Characterization

5.1.2.1 Cryotomy and Optical Microscopy

Different samples from un-oriented PP billet and OPP tubes were sectioned (refer to section 3.7 in Chapter 3) after cooling below glass transition temperature for examination in a polarizing microscope. A spherulite structure, consisting of a combination of both crystalline and amorphous regions was observed for un-oriented PP billet (Figure 5.2a). The spherulitic morphologies parallel and perpendicular to the extrusion direction are shown in Figures 5.2b and 5.2c respectively (magnification 1000X). Each spherulite consists of numerous chain-folded lamellae that originated at the centre of the spherulite and grew in the radial direction. These chain-folded lamellae are separated and interconnected to one another by interlamellar areas of amorphous regions (tie chains) as observed by others [Dasari et al., 2003].

The spherulite diameter was measured from micrographs corresponding to parallel and perpendicular extrusion directions. Results show that spherulites in billet (unoriented) were homogeneous and had an average spherulite size of 35 μm. The average size of these spherulites was within the range of spherulite sizes observed in polypropylene [Brusselle-Dupend et al., 2001, Phillips and Wolkowicz, 1996].

During the extrusion process, spherulites broke apart as blocks of lamellae slipped past each other and aligned themselves in the extrusion direction to create a fibrillar

structure as shown in Figure 5.3. This fibril structure has been defined as an aggregate of microfibrils, and microfibril as one that contains a bundle of lamellae crystallites [Coulon et al., 1998]. The structure of the extruded samples at draw ratios of 5 and higher was completely changed from a spherulite structure to an oriented structure (fibrils). This observation of the transformation from spherulitic to fibrous structure is in agreement with other researchers [Stojanovic et al., 2005]. Fibrils had a size (width) of 200nm – 500nm. This size range of fibrils did not change significantly during the orientation process, because fibers suddenly became thinner at necking (and did not do so gradually). As a result of that the sizes of fibrils after orientation process at different draw ratios (4.5-6.3) were approximately the same.

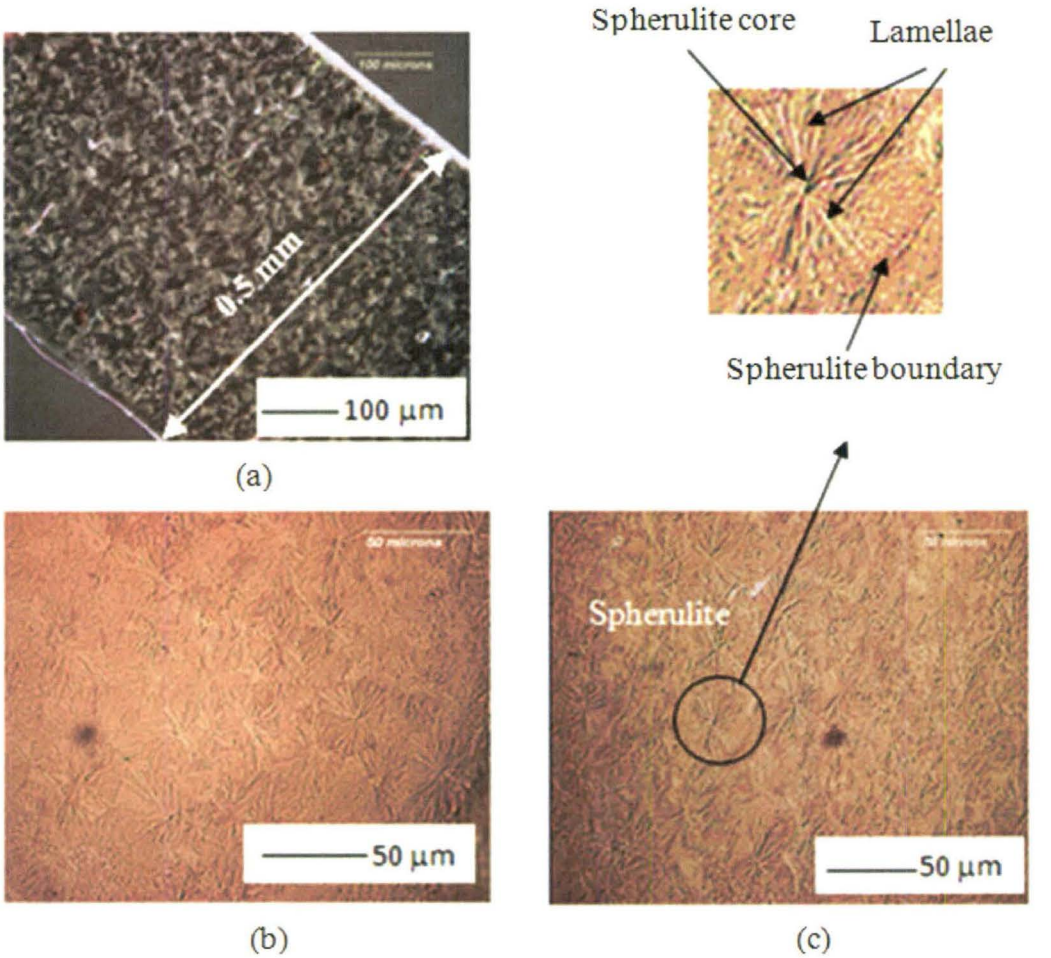

Figure 5.2 Polarizing microscopy images of the spherulitic morphology of un-oriented PP billet (a) at a low magnification, (b) at a high magnification parallel to the extrusion direction, and (c) at a high magnification perpendicular to the extrusion direction.

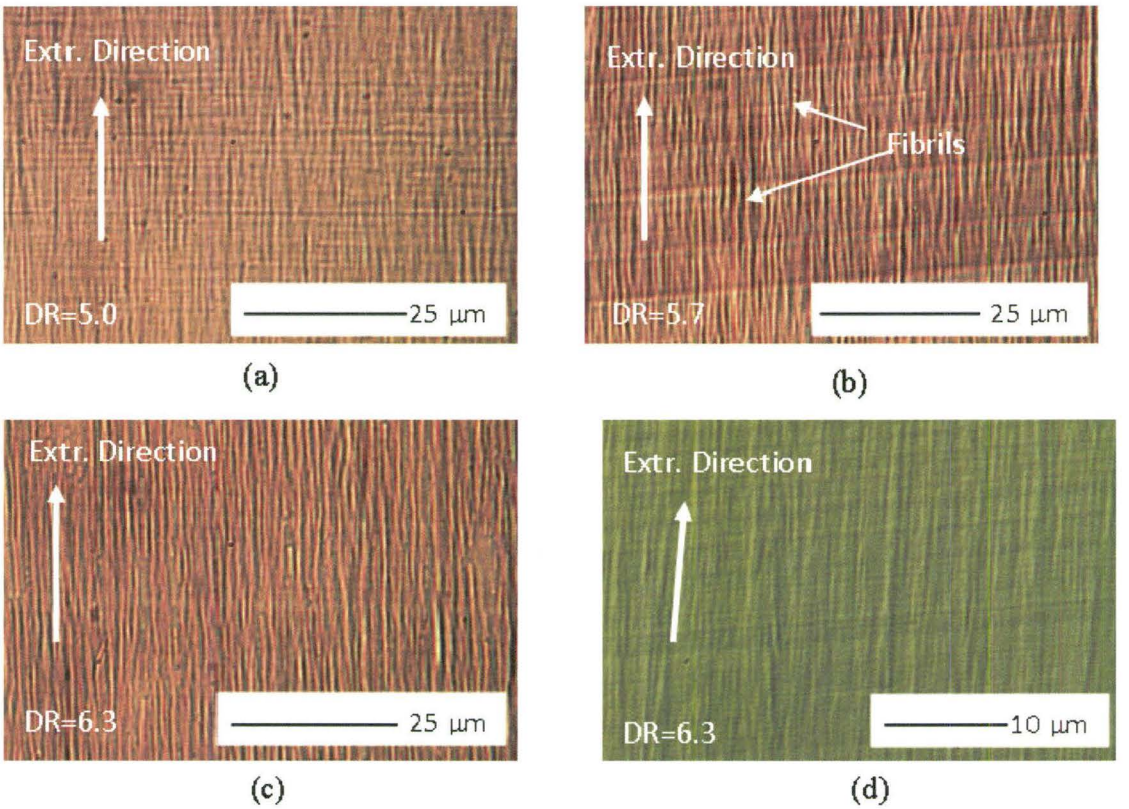

Figure 5.3 Polarizing microscopy images of extruded PP tube after cryotomy at draw ratios of 5.0, 5.7 and 6.3 (a, b and c), and image (d) of extruded PP tube at a draw ratio of 6.3 after polishing and etching with permanganic solution.

5.1.2.2 FE-SEM Observations

Samples of thickness approximately 0.5 mm from un-oriented PP billet and extruded tube parallel and perpendicular to the extrusion direction were fractured in liquid nitrogen and then observed under a low voltage field emission scanning electron microscope (for procedural details, refer to section 3.8 in Chapter 3). Figure 5.4 shows

that the void morphology of the extruded PP was aligned with the extrusion direction. The fibrils are clearly visible on fracture surfaces and aligned to the extrusion direction.

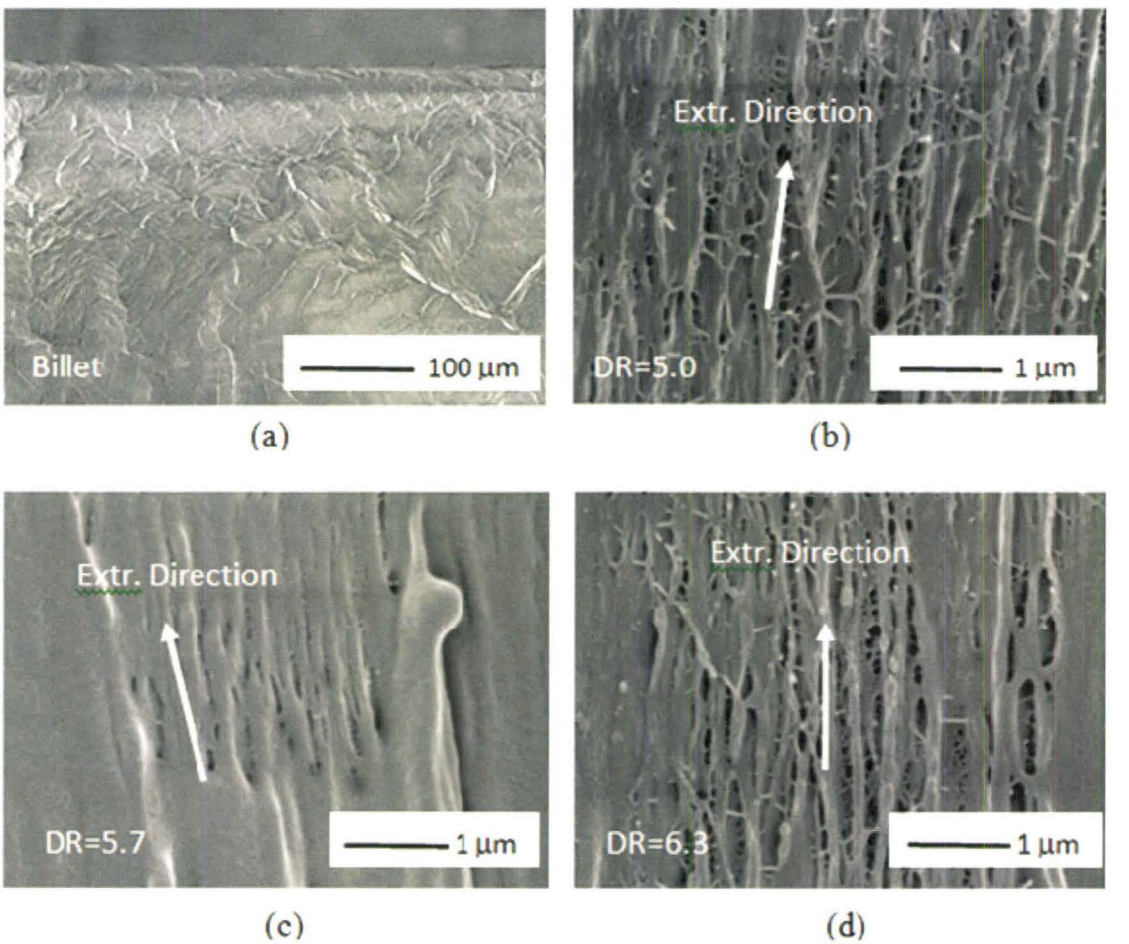

Figure 5.4 FE-SEM micrographs of extruded PP fracture surface in liquid nitrogen at different draw ratios: (a) billet, DR=1, (b) extruded tube, DR=5, (c) extruded tube, DR=5.7, (d) extruded tube, DR=6.3.

5.1.2.3 WAXD Observations

The specimens were cut from un-oriented PP billet and extruded tubes at different positions in the extrusion direction from the inner to the outer surface (refer to section 3.9 in Chapter 3). The size of these fibers was about (0.5mm x 0.5mm) as shown in Figure 5.5. The preferred orientation was recorded using Debye patterns. Reflections associated with all 8 Debye rings were identified from the inner ring to the outer ring as (110)α, (040)α, (130)α, and (111)α + (041)α in the billet. The reflections were converted to arcing in extruded samples but the γ-phase, i.e., (117)γ reflections, were diffuse and weak in the billet sample. Also, (060)α, and (220)α reflections were weak in all samples (refer to Figure 5.6). The Debye rings in all samples were similar except that the (117) γ-phase was present in the billet (although with a poorly defined peak) but was non-existent in the oriented samples. The results indicate that the crystalline fraction in the billet contained α and γ forms. Figure 5.7 shows intensity peaks (110), (040), (130), (111), (041), (060), and (220) for α-phase reflections and (117) peak for γ- phase reflection from the billet. However, the oriented specimens contained only α-phase.

The pole figures for the billet and extruded polypropylene tubes were plotted in stereographic projection as shown in Figure 5.8. The (110)α pole figures, of all extruded through-thickness samples (Figure 5.8a) and at different draw ratios (Figure 5.8b), show orientation patterns as uniaxial and rotationally symmetric around the extrusion direction (ED). In the billet sample, the pole figure shows a random orientation around ED.

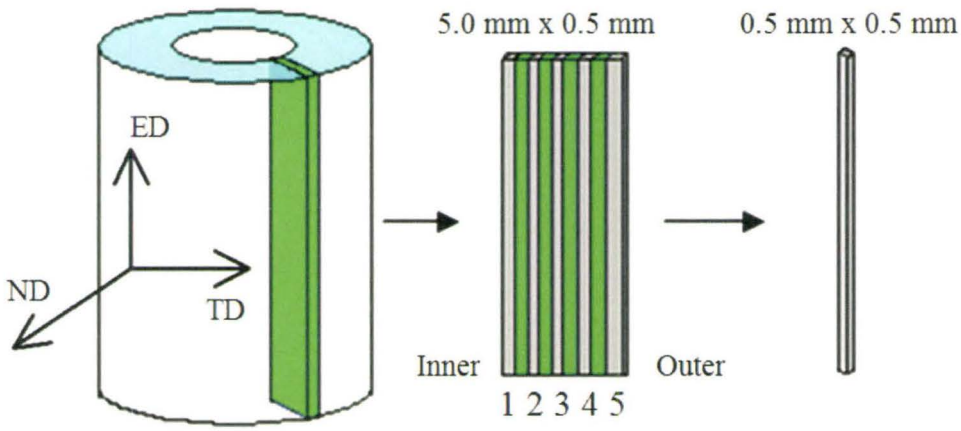

Figure 5.5 Fibers cut out of extruded tubes at different positions in the extrusion direction from inner to outer surface.

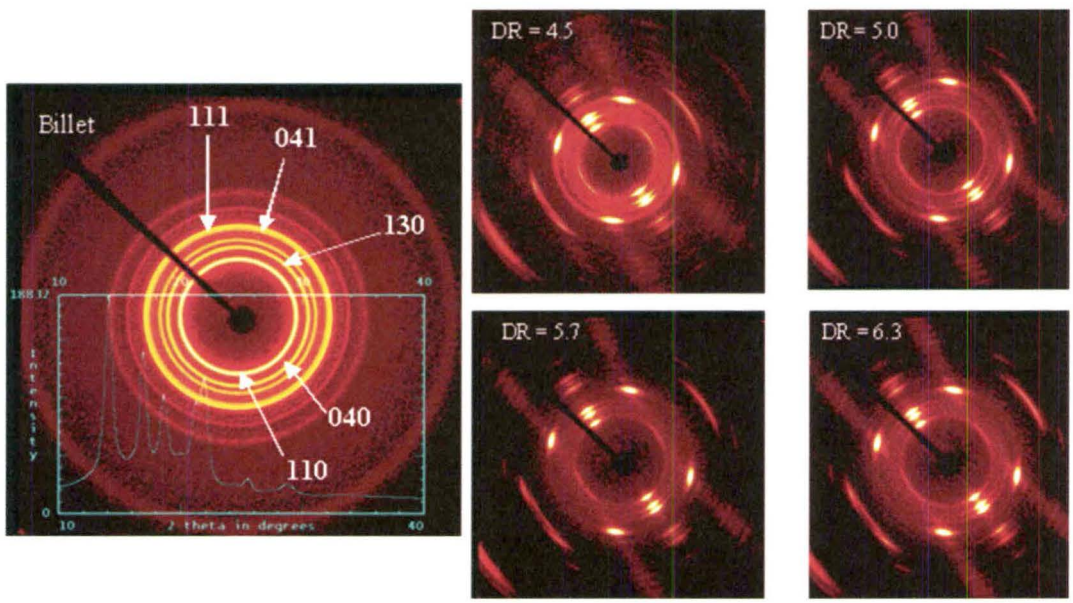

Figure 5.6 X-ray diffraction pattern of PP billet (un-oriented) and PP extruded tube at different draw ratios.

Orientation factors of crystallographic axes were determined from the diffraction intensities of (110)α reflections for PP billet and extruded tubes. The orientation factor was represented in terms of the Herman's orientation factor (refer to earlier section 2.7). The orientation changes from the inner to the outer thickness layer were relatively small as shown in Figure 5.9. The outer layer crystallinity was about 3% less than for the inner layer (refer to Figure 5.10). As the extruded tubes were cooled from outside surface, a lower crystallinity was to be expected in the outer thickness layer.

Crystallinity, as shown in Figure 5.11, was observed to increase with increasing draw ratios because the alignment of the polymer chains in OPP tube makes formation of a crystalline structure easier, resulting in increased crystallinity [Maier and Calafut, 1998]. The crystallographic c-axis (chain axis) of all extruded samples was aligned parallel to the extrusion direction (fibre axis) and the orientation factor $f_{c,ED}$ was approximately (-0.5). In the billet sample, the crystallographic c-axis (chain axis) was distributed randomly and the orientation factor $f_{c,ED}$ was approximately zero as shown in Figure 5.12.

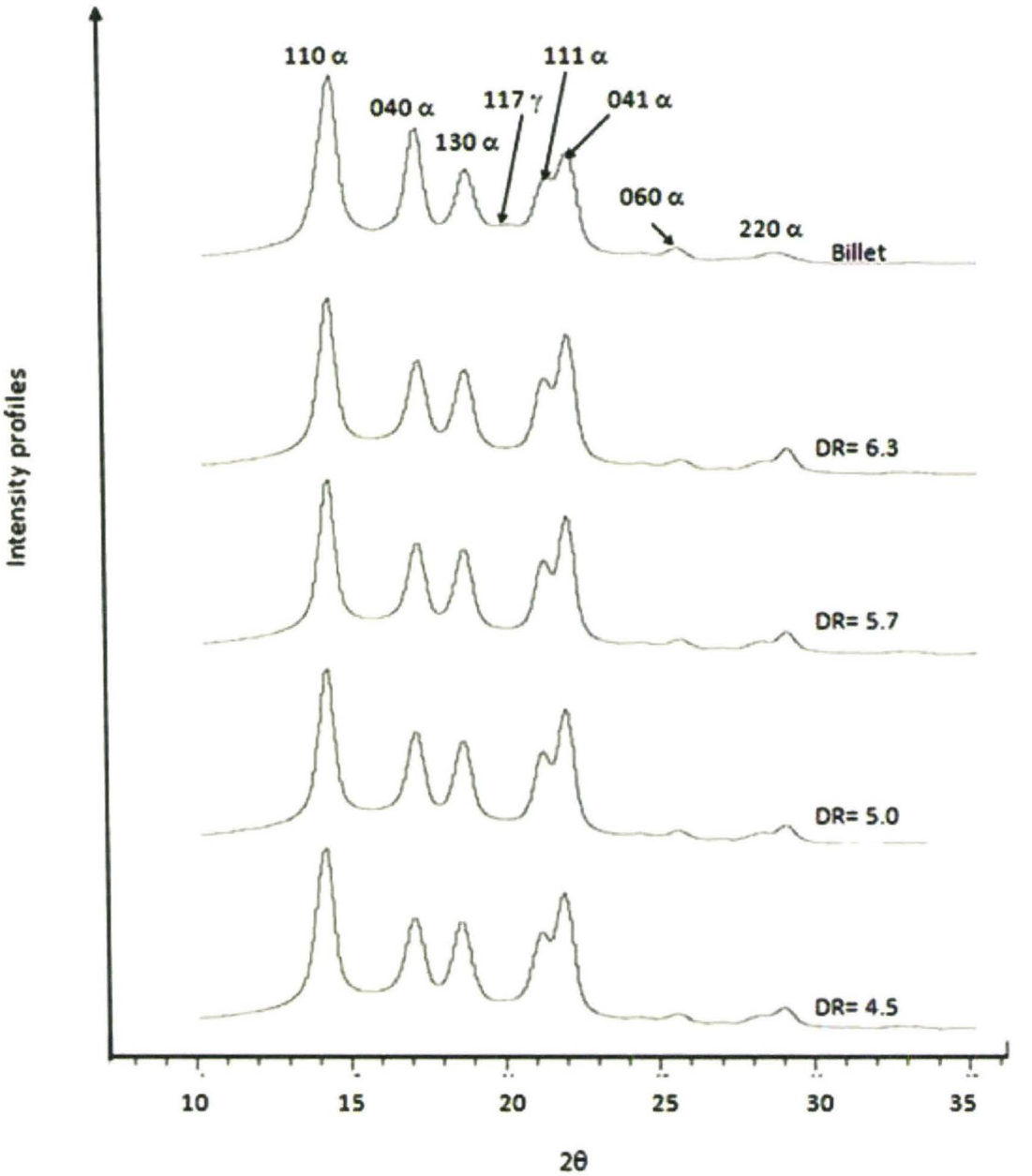

Figure 5.7 X-ray diffraction intensity profiles from PP billet and extruded samples at different draw ratios.

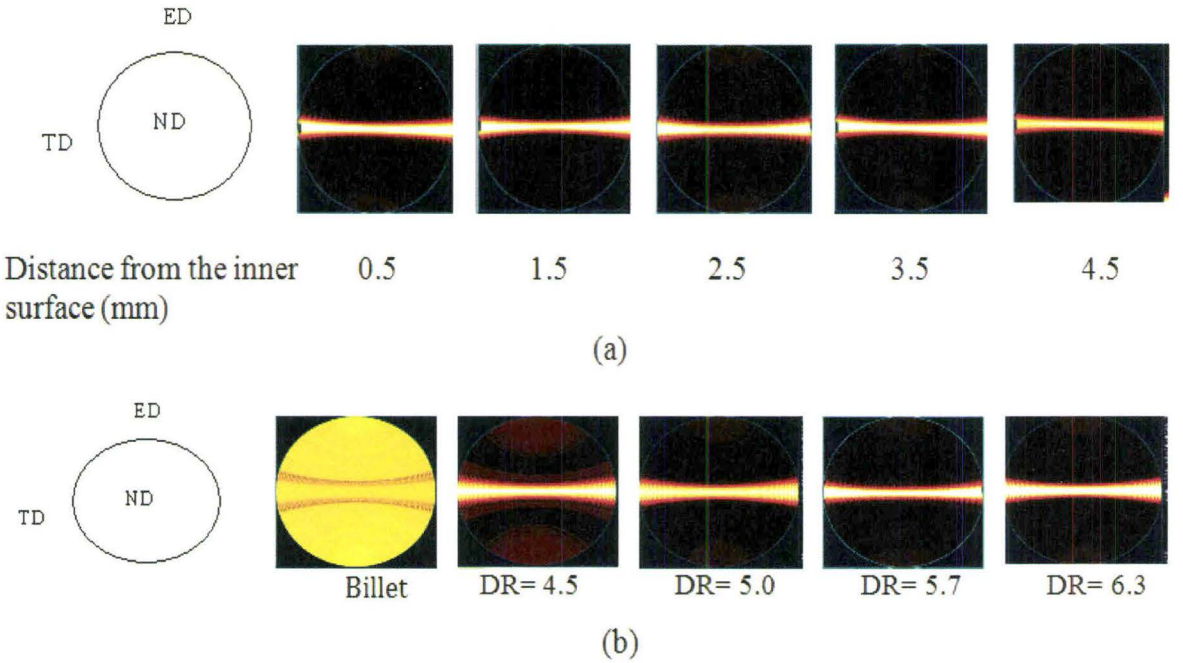

Figure 5.8 The pole figures of (110) plane of monoclinic α form plotted in stereographic projection (a) inner to outer thickness layer of extruded polypropylene tube at DR=6.3, and (b) billet and extruded polypropylene tubes at different draw ratios.

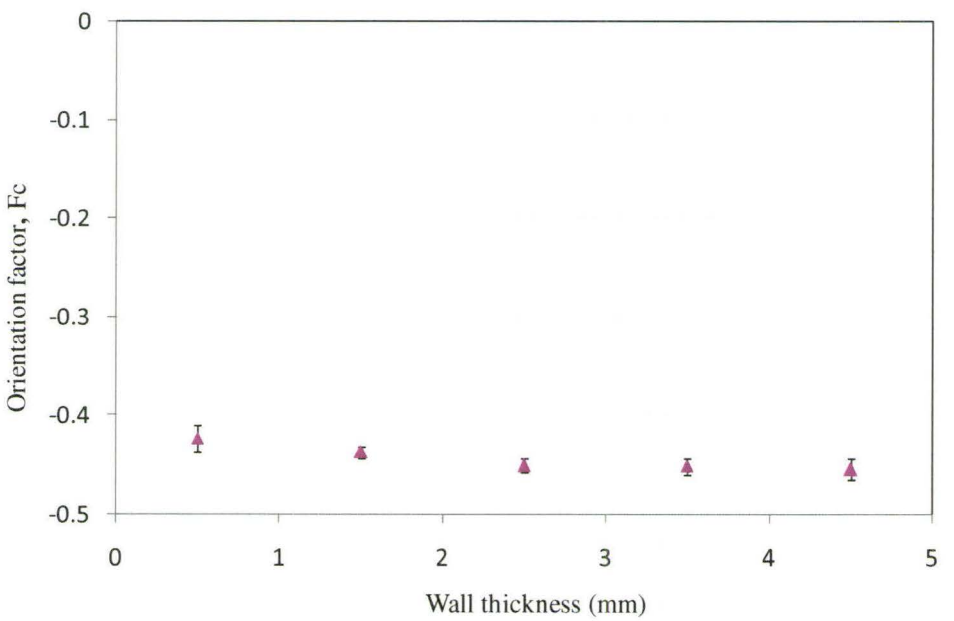

Figure 5.9 Orientation factor changes through wall thickness of extruded tube at DR= 6.3.

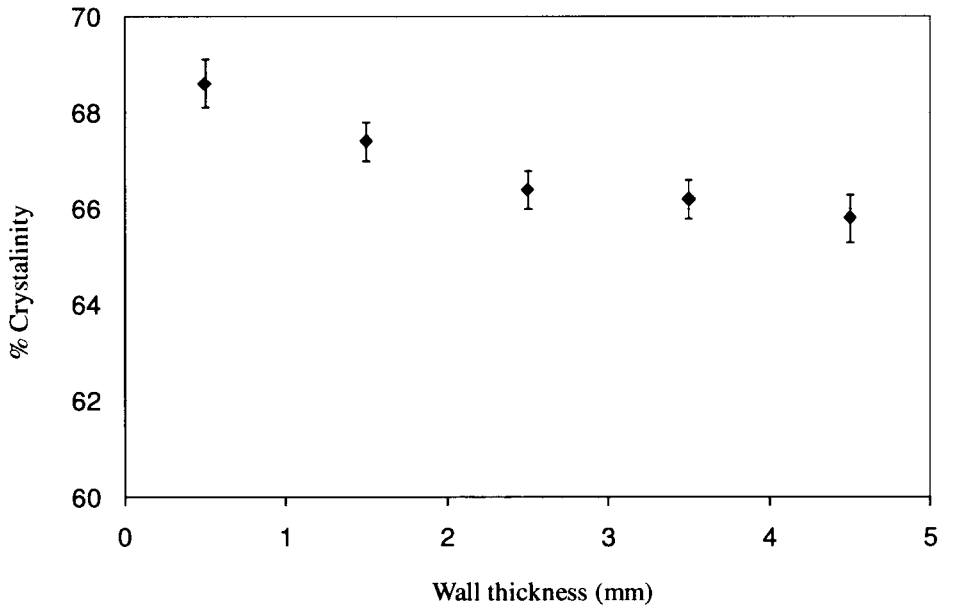

Figure 5.10 Crystallinity through wall thickness of extruded tube at DR = 6.3.

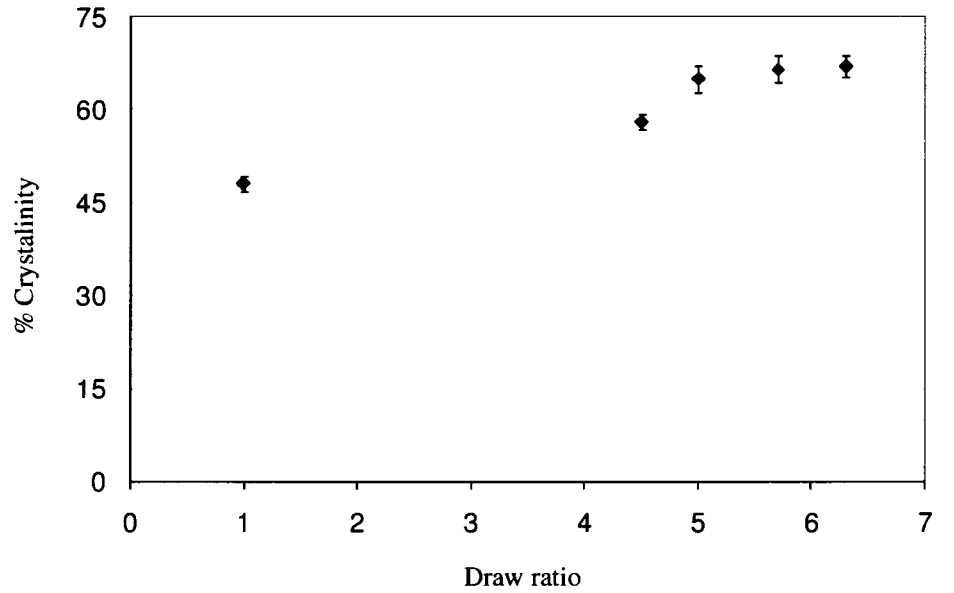

Figure 5.11 Draw ratio versus % crystallinity of billet and extruded polypropylene tubes.

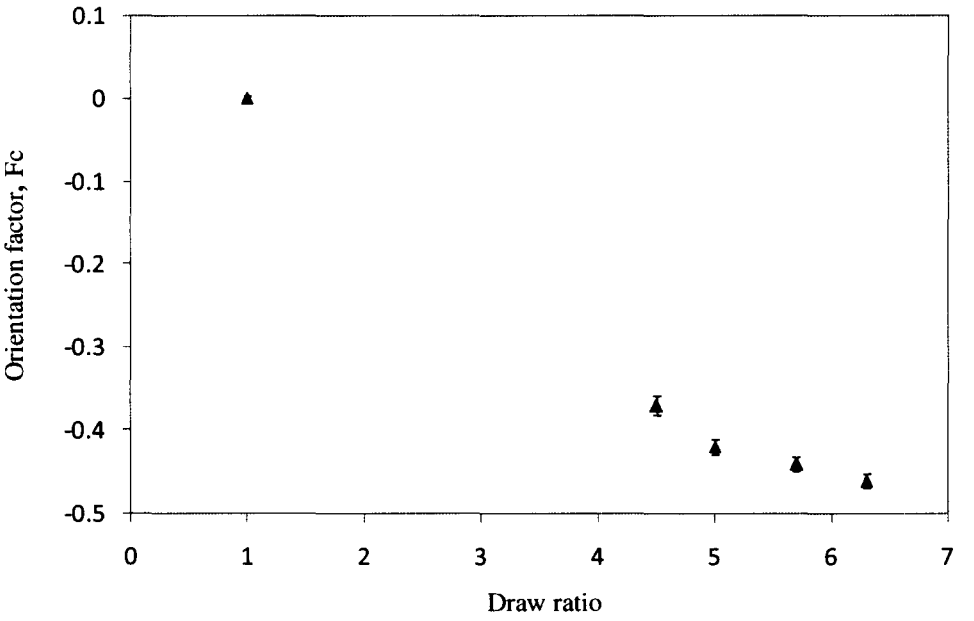

Figure 5.12 Draw ratio versus orientation factor of billet and extruded polypropylene tubes.

5.1.3 Room Temperature Mechanical Properties of Billet and Extruded Tubes

The results of tensile tests for tubes at two different draw ratios of 4.0 and 5.0 and at two speeds are shown the form of true stress versus true strain curves in Figures 5.13 and 5.14 respectively. The standard error is defined as a ratio of standard deviation over the square root of number of measurements that make up the mean. The maximum standard error for the cross-sectional area (width times thickness) of tensile sample measurements was 9.7 ±0.28 mm^2 or 2.8%. All measurements were performed 3 times on each specimen using a micrometer. The materials exhibited ductile behaviour and fractured at a strain of about 0.6 after extensive deformation. The results for un-oriented polypropylene (billet)

samples differ significantly from those for extruded polypropylene (oriented) samples. In billet samples, extensive local necking and a much larger strain of about 2.5 was observed at fracture, the neck propagation occurred along the gauge length with the same constant cross-section as at the start of necking, while no local necking was observed in extruded samples. Splitting along the longitudinal (extrusion direction) was observed at fracture for the two draw ratios and i as well as for the billet samples. Figures 5.15 and 5.16 show that the yield strength and elastic modulus were increased with draw ratio and initial test speed respectively. It is to be noted that these tests were conducted at a constant cross-head velocity and not at a constant strain rate. Therefore, only the initial strain rate data has been reported. This data is calculated from cross-head velocity and initial gauge length of the test specimen.

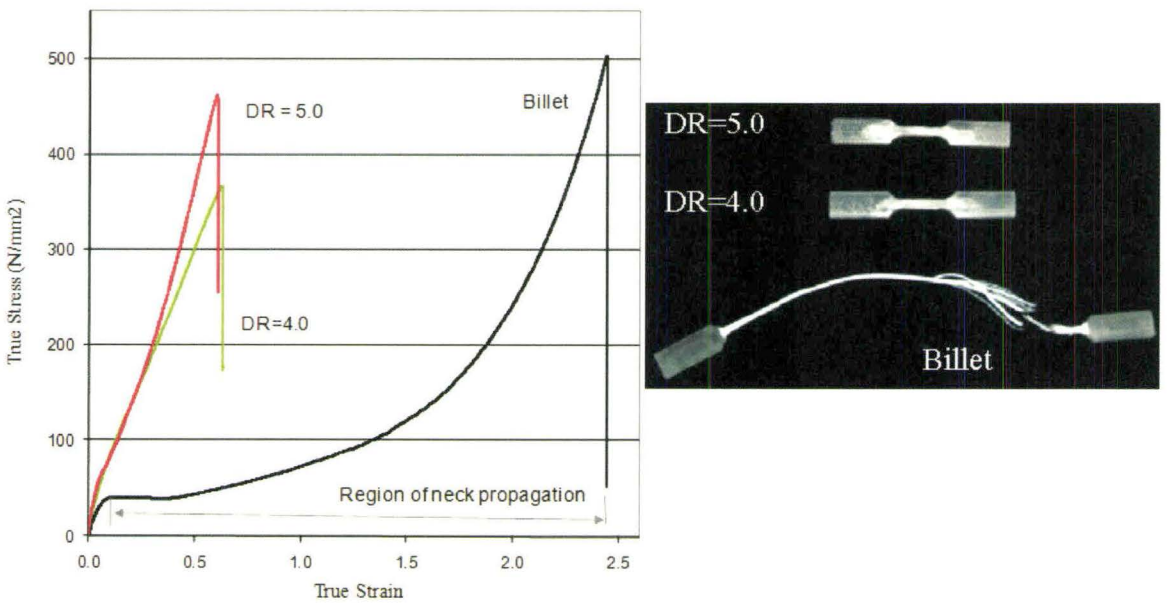

Figure 5.13 True stress-strain curves from extruded PP tubes for draw ratios of 4.0, 5.0 and for un-oriented billet at an initial strain rate 0.002/sec.

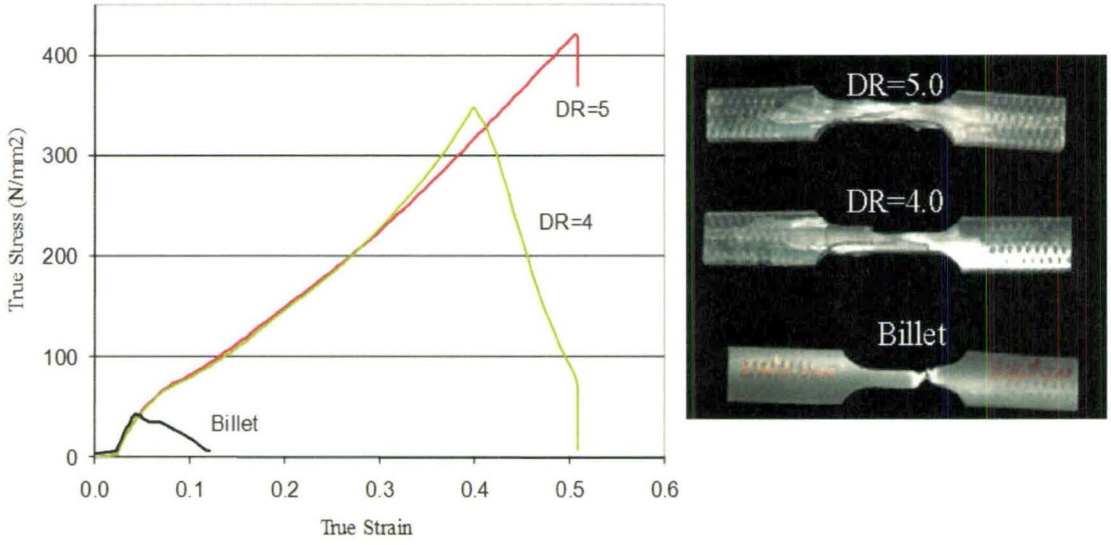

Figure 5.14 True stress-strain curves from extruded PP tubes for draw ratios of 4.0, 5.0 and for un-oriented billet at an initial strain rate 0.044/sec.

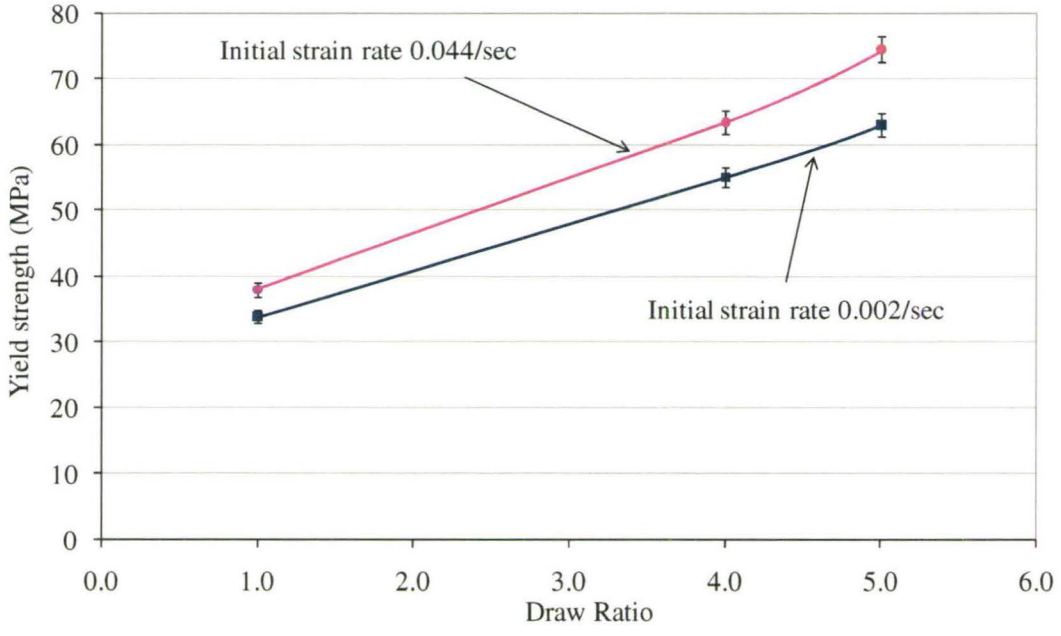

Figure 5.15 Draw ratio versus tensile yield strength at two initial strains rate of 0.002 and 0.044/sec.

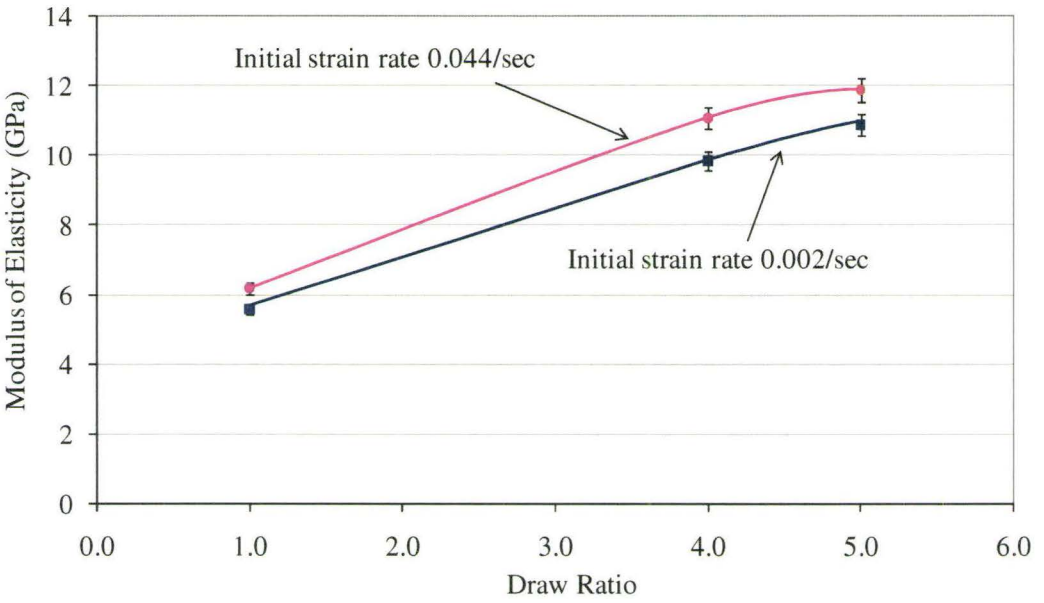

Figure 5.16 Draw ratio versus tensile modulus of elasticity at initial strains rate of 0.002 and 0.044/sec.

5.2 Assessment of Forming Behaviour of Extruded OPP Tubes

5.2.1 Axial Feed Hot Oil Tube Forming (AF-HOTF) Experiments

Temperature, rate of forming (pressure rate) and axial feed were varied in the axial feed hot oil tube forming (AF-HOTF) experiments. Table 5.2 summarizes the parameters held constant and those that were varied and the key results from tube free bulging experiments. Photographs of bulged samples are presented in Figures 5.17 and 5.18. These results give a good starting point to understand the effects of forming process parameters on forming performance of polypropylene.

Test	Objective (To determine)	Parameters held constant	Parameters varied	Conclusions
(1) (Fig. 5.17a)	The effect of temperature on the bulge profile	P= 65 KPa/sec) and no feed	T= 120°C O.D =35.5, 33.5 and 31 mm	Tubes burst with poor expansion
(2) (Fig. 5.17b)	The effect of axial feed on the bulge profile	T=150°C-160°C P = 65 KPa/sec O.D = 35.5 mm	Feeds (0, 13 and 30 mm)	Higher expansion and delay bursting and thinning
(3) (Fig. 5.18a)	The effect of process property variation along the tube	P= 65 KPa/sec O.D = 35.3 mm	Temperature variation along the tube, T=10 - 15°C, <10°C and uniform	Bulge is uniform with uniform temperature along tube
(4) (Fig. 5.18b)	The combined effect of forming rate and axial feed on the bulge profile	T= 150°C O.D = 35.3 mm	P= 140 KPa/sec and no feed, P= 35KPa and 13 mm feed	Tubes burst with poor expansion, higher expansion and uniform bulge

Table 5.2 A summary of results from tube free bulging experiments with AF-HOTF system.

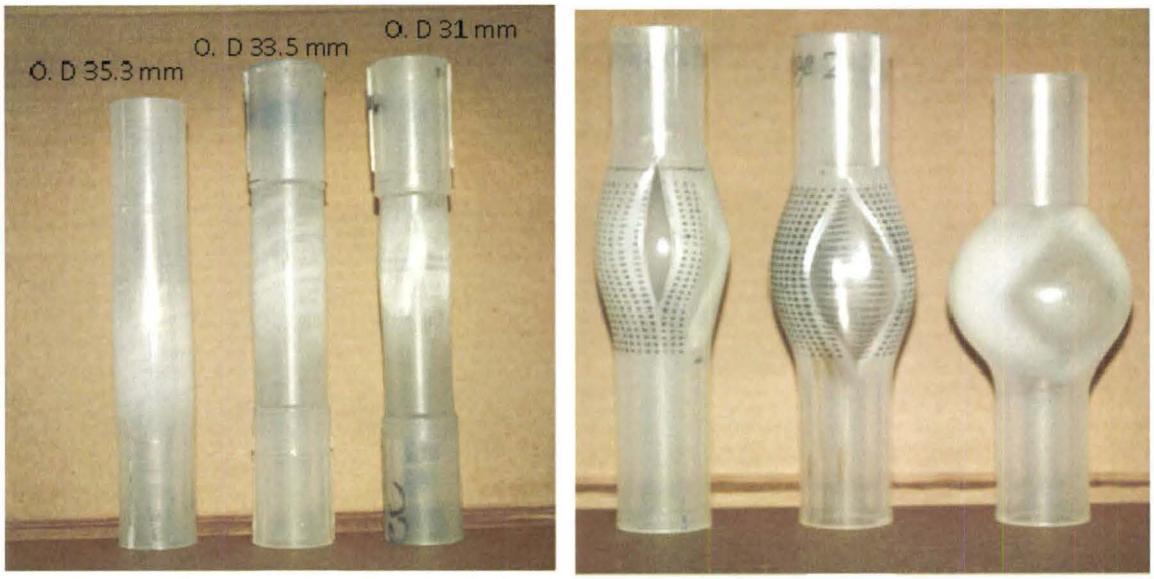

Figure 5.17 (a) Bulge tests with different diameter tubes at 120°C. (b) Bulge tests at temperature between 150-160°C with axial feeding (0, 13 and 30 mm from left to right).

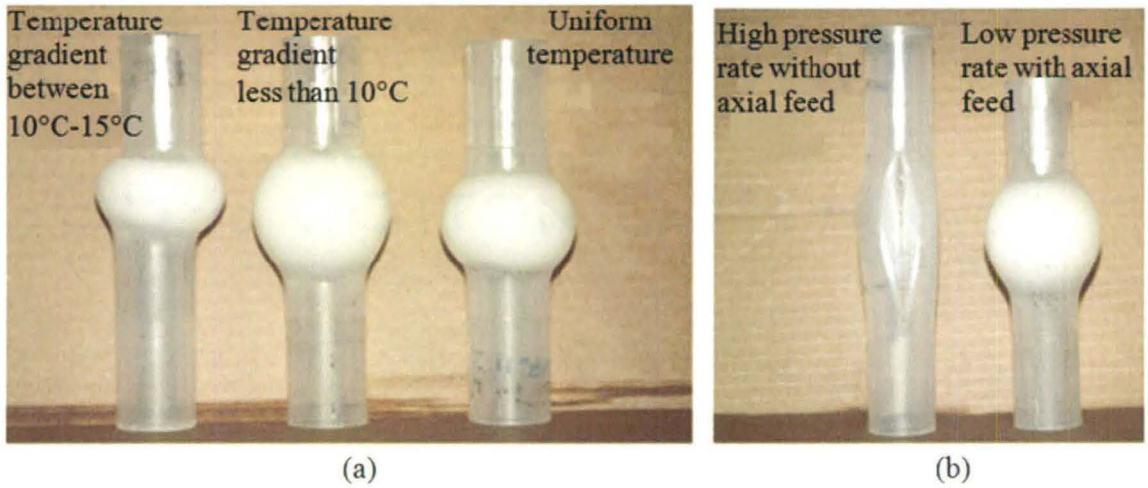

Figure 5.18 (a) Bulge tests in the presence of a temperature gradients measuring difference between top and bottom ends (b) Bulge tests at 150°C.

Several tubes were tested at different temperatures by applying a linear pressurizing path (no axial feed) until the tubes burst. Failure occurred when the deformation was concentrated in a local area under the influence of large tensile force and can be characterized by localized thinning parallel to the extrusion direction that proceeded rapidly towards fracture. The burst pressures versus tube forming temperatures are plotted in Figure 5.19 and, as shown, the burst pressure decreases with increasing forming temperature. The cracks clearly appear (as captured by CCD camera during the experiment) on the outer surface of the tube prior to bursting at forming temperatures less than 150 °C (refer to Figure 5.20), while localized thinning occurred at the inner surface of the tube followed by "eyeball formation" and/or bursting at higher forming temperatures. Figure 5.21 shows the three typical failure stages in the forming temperatures range of 140°C -150°C.

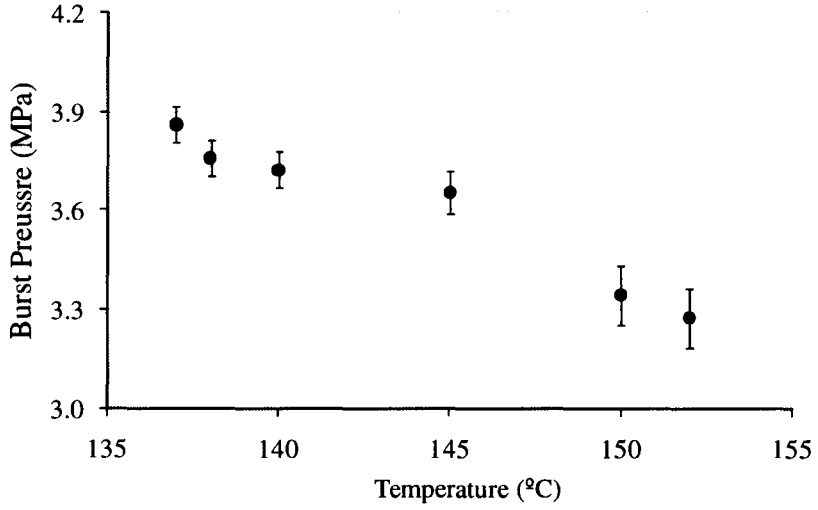

Figure 5.19 Burst pressure at different forming temperature without axial feed.

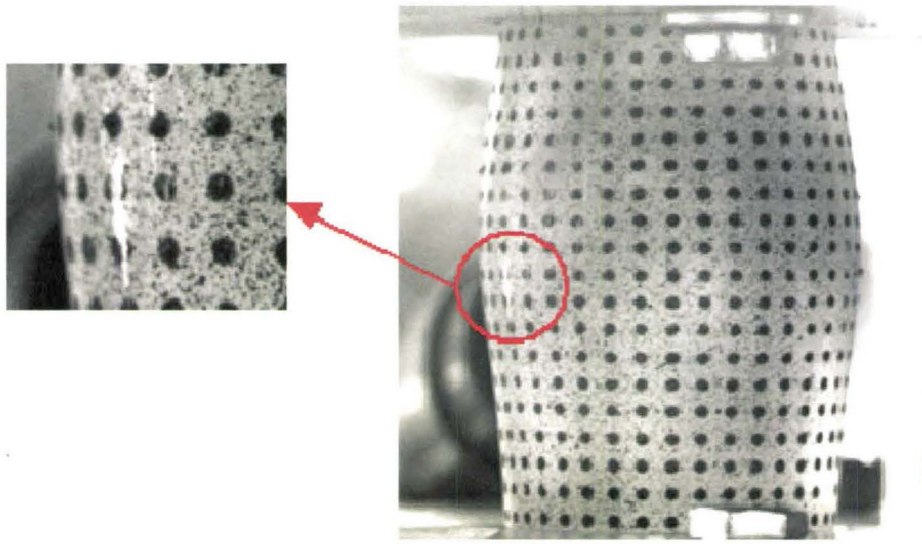

Figure 5.20 Crack on the surface of a bulged tube specimen imprinted with a periodic grid pattern prior to bursting (no axial-feed).

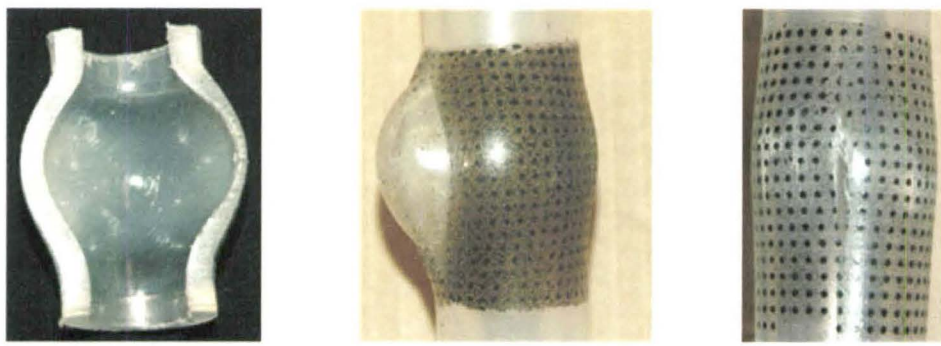

Figure 5.21 Different failure modes in the forming temperature range of 140°C - 150°C.

During the AF-HOTF experiments, the bulge height of the tube was monitored using the ARAMIS system (described earlier in Chapter 3) by selecting a point at the center of the expanding region. Different amounts of axial feed were applied with internal pressure to investigate its effect on bulge height and surface strains. When no axial feed was applied, the bulge height increased slowly during the early stages of the experiment until a certain level of pressure was reached and then increased dramatically over a smaller range of pressure before the burst occurred (refer to Figure 5.22). The failure occurred at low bulge height (low formability). On the other hand, when axial feed was applied after a certain level of pressure (to prevent buckling or wrinkling) the bulge height increased rapidly during the feeding stage, depending on the amount of feeding and feeding rate. As the amount of axial feeding increased, the bulge height (formability) also increased and thinning and/or bursting failure was delayed. This is because more material was fed into the expansion zone to reduce the severity of the deformation. A balance of axial feed and internal pressure was required to obtain a good product free of failure. Excessive feeding of material in the bulge zone led to wrinkling or folding failure (refer to Figure 5.23).

True principal strains in the hoop and longitudinal directions (refer to Figure 5.24) as measured by ARAMIS are plotted in Figure 5.25. Clearly, an increase in axial feed resulted in a higher forming limit (the lowest forming limit was obtained in the test with no axial feed). The strain in the hoop direction was positive while the strain in the axial direction was negative. In most of the tests, the magnitude of the hoop strain was larger

than the axial strain and this is in agreement with the direction of failure as shown earlier in Figure 5.21.

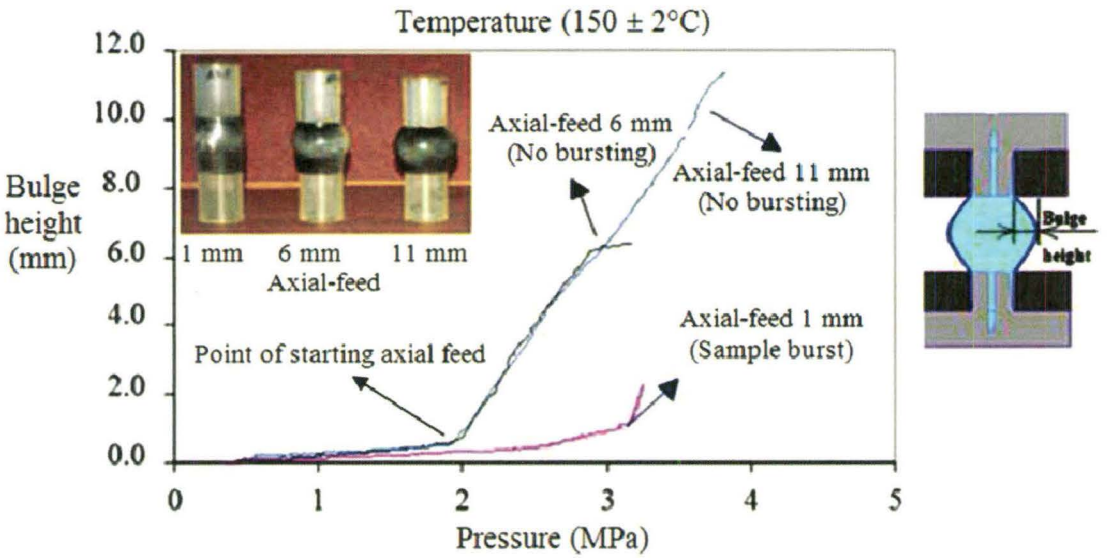

Figure 5-22 Bulge height versus pressure for different amounts of axial-feed.

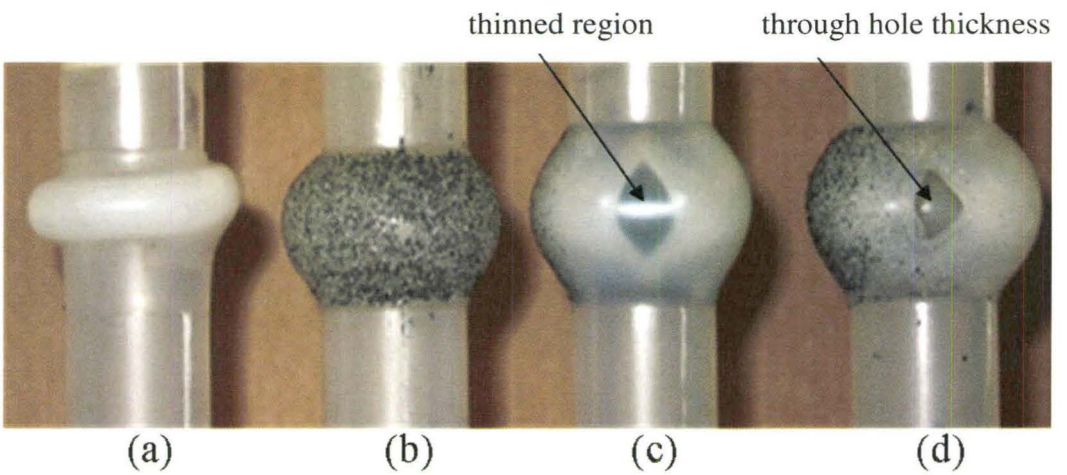

Figure 5-23 The failure modes and uniform bulge of free tube with axial feed, a- folding, b- uniform bulge, c- thinning, d- bursting.

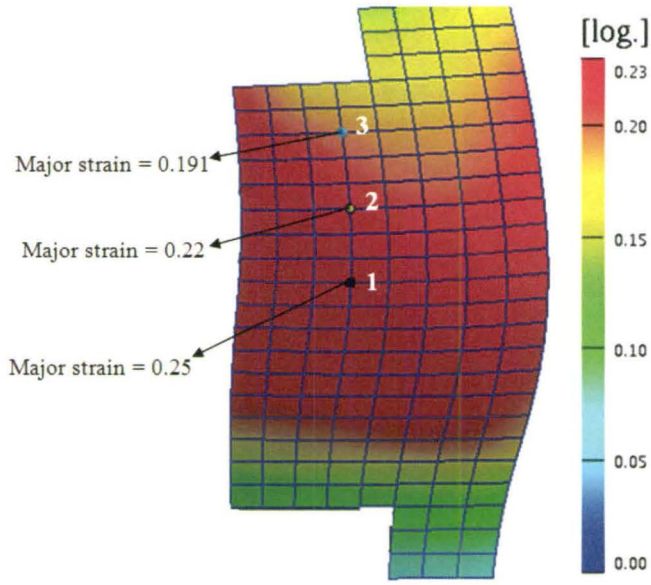

Figure 5-24 ARAMIS 3D map of the measured major strain at the middle of bulge for a test with an axial-feed of 7.5 mm for bulge height of 8 mm.

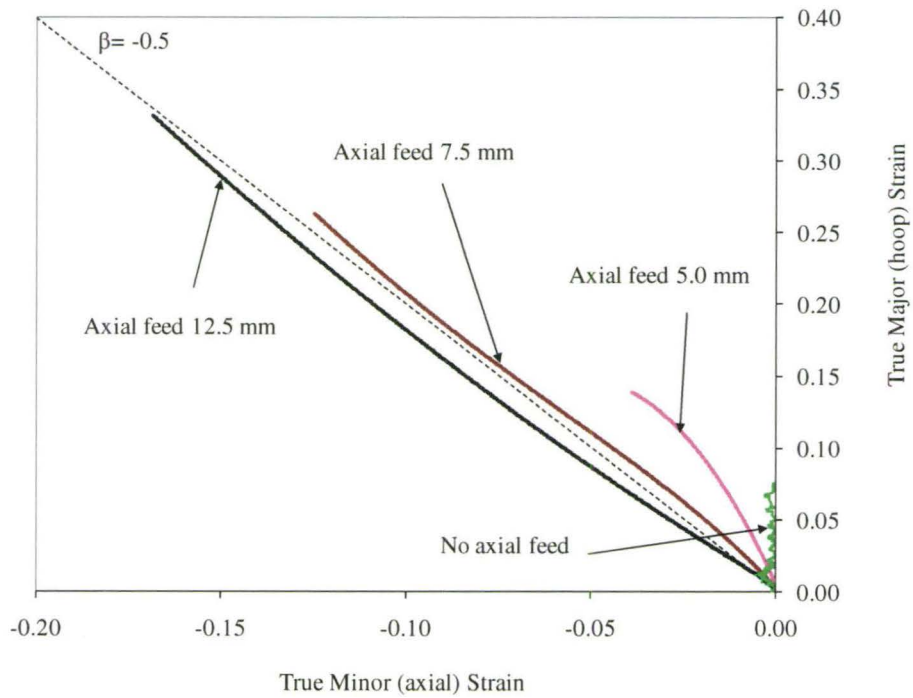

Figure 5-25 A plot of measured major – minor strains at the middle of bulge with different axial-feeds (ARAMIS system).

5.2.1.1 AF-HOTF System for Forming with Different Load Paths

The input loading paths for the internal pressure and axial feed displacements were controlled by PC-based test controller attached to the AF-HOTF system. To prevent leakage, for each of these cases, the internal pressure was applied simultaneously with axial feed during the bulging test up to the maximum pressure. Four input load paths (A, B, C and D) with the same axial feed are shown in Figure 5.26. The corresponding output data is shown in Figure 5.27 in terms of internal pressure versus axial feed (displacement) plot of a series of bulging tests for a tube with a DR of 6.3. The tests were conducted at a forming temperature of 150 °C and pressure rates of 20-65 kPa/sec. With the same amount of the axial feed of 18 mm and at different maximum pressure, case (A) resulted in bursting while cases (B) and (C) resulted in uniform bulge, and case (D) resulted in wrinkling.

Figure 5.28 shows a series of bulging tests up to bursting at a forming temperature of 150 °C and a pressure rate of 65 KPa/sec with different loading paths E, F, G and H. All of the tests resulted in uniform bulging followed by bursting without any wrinkling. The true principal strains in the hoop and longitudinal directions were measured from the middle of the bulged area of the tube by the ARAMIS system during the test (Figure 5.29). The experimental data of the strain path in case H was lost during the test because of severe expansion at the middle of bulge area before tube burst. Clearly, an increase in axial feed shifted the strain path to the left and resulted in higher forming limits. In most

of the tests, the magnitude of the hoop strain was larger than the axial strain and this is in agreement with the direction of failure (burst) as shown in Figure 5.23.

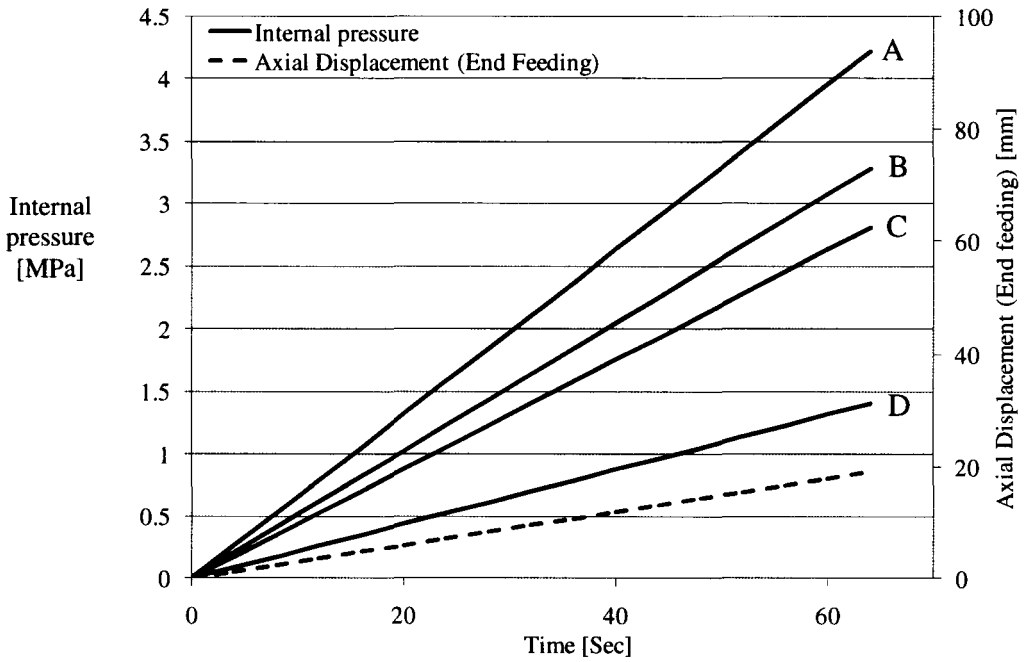

Figure 5.26 Input loading paths with four different maximum pressures, (A- 4.0MPa, B- 3.1MPa, C- 2.2MPa, D- 1.3MPa), DR= 6.3.

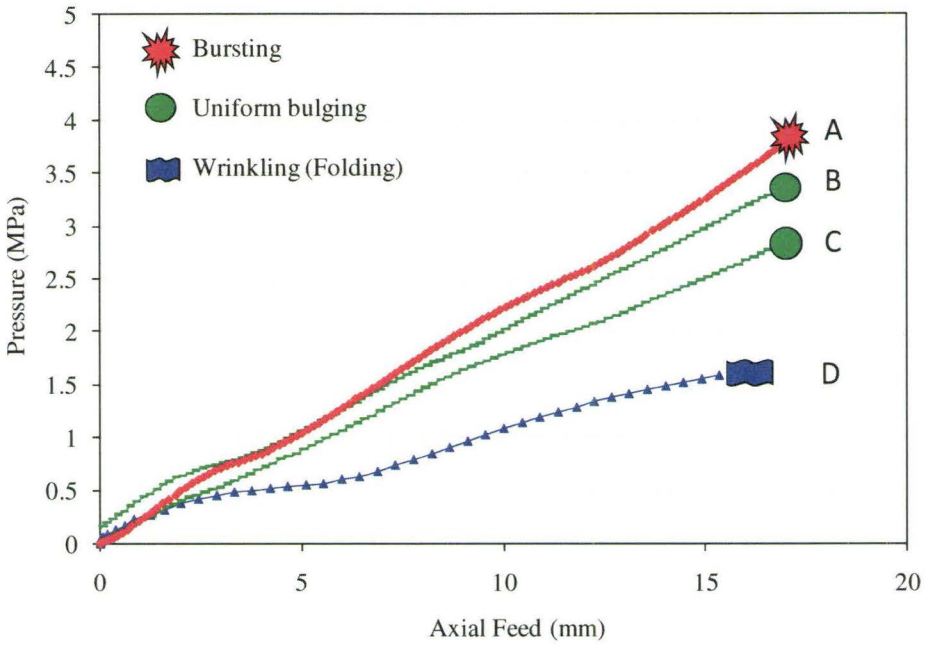

Figure 5.27 Experimental results of bursting, wrinkling failures and uniform bulging obtained from hot forming tests on tubes produced with a DR = 6.3 under different loading paths (A, B, C and D).

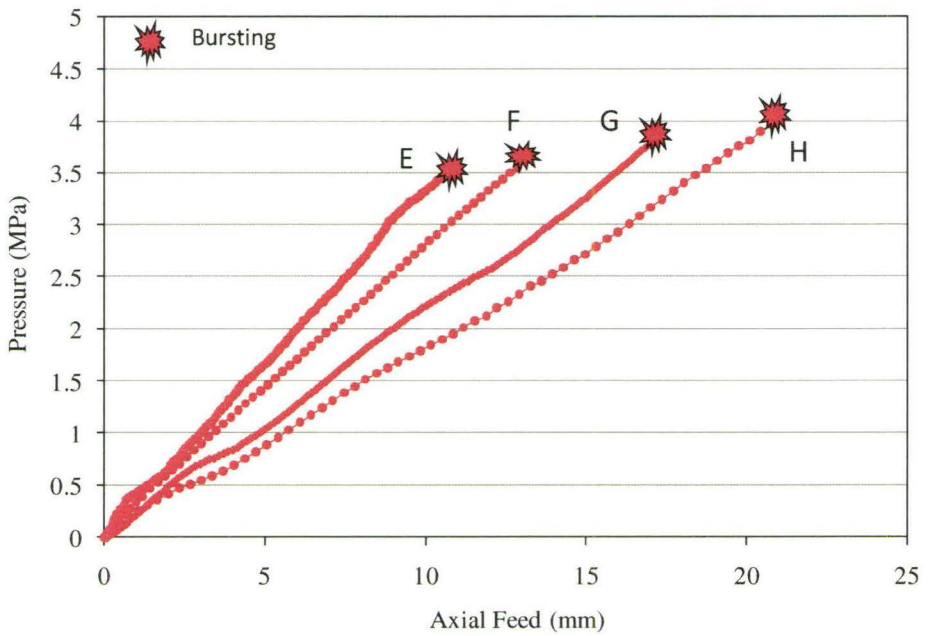

Figure 5.28 Experimental results of bursting obtained from hot forming tests under the same pressure rate (65 KPa/sec) and at different axial feeds (E- 13 mm, F- 15 mm, G- 18 mm and H- 23 mm), test temperature of 150°C.

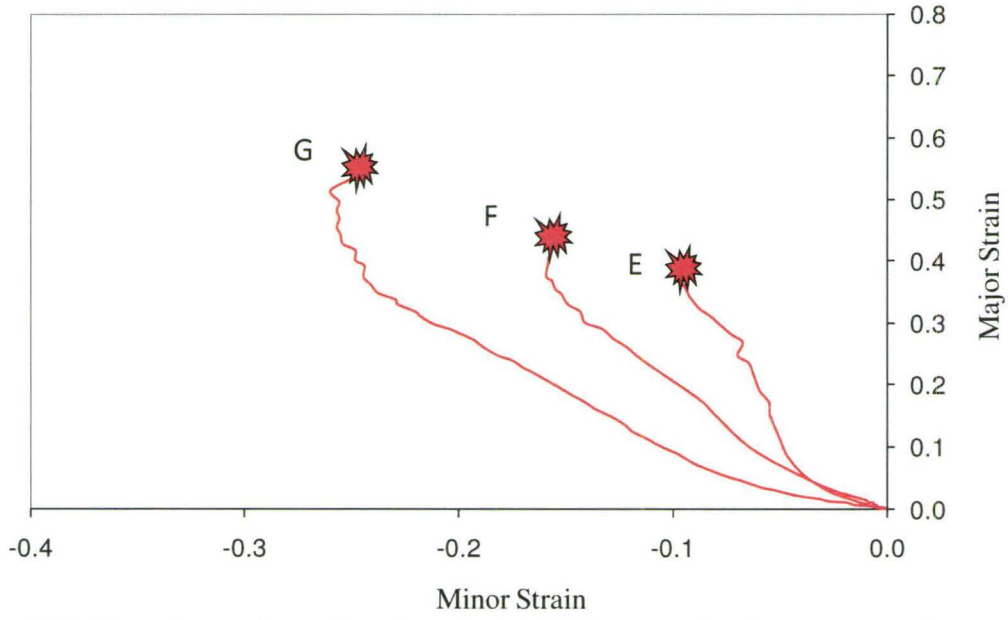

Figure 5.29 Experimental results of major and minor strains instantaneously measured from the middle of bulging tubes produced with a draw ratio of DR = 6.3 and a forming temperature of 150°C for the cases E, F and G.

5.2.2 Analytical Model of AF-HOTF Process

An existing analytical model for axial feed tube hydroforming was utilized to model the present AF-HOTF process [Asnafi, 1999, Kim et al., 2006]. It is a strain rate and temperature independent model. The prediction of bursting pressure and forming limit was based on a diffuse necking criterion. In keeping with the experiments, the criterion assumes that necking occurs when the axial force and the internal pressure reach their maximum values simultaneously. In the experimental work the internal pressure and the axial displacements were recorded during the test, which enabled a comparison of the experimental and analytical results.

The following assumptions are made in the analysis:

1. The tube is thin-walled.
2. The ends of the tube are closed.
3. The material of the tube is incompressible.
4. The material behaves like a power law material $\left(\sigma = K\varepsilon^{n}\right)$, where K and n are strength coefficient and strain hardening exponent respectively.
5. The profile of the tube at the free bulge region is considered elliptical in the axial direction as shown in Figure B.1 (Appendix B).

The axial feed for free bulge tube is given by [Asnafi, 1999].

$$s = \frac{2h}{3}\left(\frac{l_f - 2r_d}{d_0 - t_0} + \frac{2h}{l_f - 2r_d}\right) \tag{5.1}$$

where

s : Axial feeding displacement
h : Bulge height
t_o : Initial tube thickness
d_o : Initial outer tube diameter
l_o : Initial tube length
l_f : length of the free tube
r_d : Clamp profile radius

From Hill's quadratic yield criterion for anisotropic materials, the plastic instability criterion based on the diffuse necking for tube hydroforming [Kim et al., 2006] is represented as critical sub-tangent Z,

$$\frac{1}{Z}=\frac{1}{\bar{\sigma}}\frac{d\bar{\sigma}}{d\bar{\varepsilon}}=\frac{n}{\bar{\varepsilon}}=\left[\frac{\alpha(2\alpha-\rho)^2+2(2-\alpha\rho)(2-\alpha\rho+2\alpha-\rho)}{4(1-\alpha\rho+\alpha^2)^{3/2}}\right] \tag{5.2}$$

where

$$\rho=\frac{2R}{1+R}$$

R : Hill's normal anisotropy parameter, α : Stress ratio $\left(\frac{\sigma_2}{\sigma_1}\right)$

$\bar{\varepsilon}$: Effective strain, $\bar{\sigma}$: Effective stress

The critical principal strains ε_1^c, ε_2^c along the hoop and the axial direction respectively, based on plastic instability, are found to be

$$\bar{\varepsilon}=\theta\varepsilon_1^c=\frac{n}{\left(\frac{1}{Z}\right)} \tag{5.3a}$$

$$\varepsilon_1^c=\frac{n}{\theta\left(\frac{1}{Z}\right)} \tag{5.3b}$$

where

$$\theta=\frac{1+R}{\sqrt{1+2R}}\sqrt{1+\beta\rho+\beta^2} \tag{5.4a}$$

$$\beta = \varepsilon_2^c / \varepsilon_1^c \tag{5.4b}$$

$$\varepsilon_2^c = \beta \varepsilon_1^c \tag{5.4c}$$

where β = strain ratio.

The burst pressure, p^c, based on diffuse necking is

$$p^c = \frac{(1+R)^2}{1+2R} \frac{\bar{\sigma}}{\bar{\varepsilon}} \frac{t_c}{r_c} \left[\varepsilon_1^c + \frac{R}{1+R} \varepsilon_2^c \right] \tag{5.5}$$

where

$$t_c = t_o e^{-(\varepsilon_1^c + \varepsilon_2^c)} \tag{5.6a}$$

$$r_c = r_o e^{\varepsilon_2^c} \tag{5.6b}$$

r_o and t_o are initial values of tube thickness.

Further details of the analytical model and the determination of all material properties and anisotropic parameters from uniaxial tests in hoop and axial directions are reported in Appendix A.

5.2.2.1 The Effect of Material Properties on Bulge Characteristics

A 'formability window' for tube forming can be obtained with the bursting failure mode. Bursting failure occurs at a high-pressure or with a combination of high pressure

and axial feed. Figure 5.30 provides in the form of flow chart a sequence of calculations required for prediction of burst pressure and forming limits for OPP tube at a given temperature. The burst pressure during bulging tube is predicted for tube dimensions and material properties shown in Table B.1 in appendix B. The influence of material properties on bursting pressure from the analytical model are shown in the form of 'forming limit' curves in Figures 5.31 to 5.33, based on flow chart in Figure 5.30. For example, the three burst pressure versus axial feed curves in Figure 5.31 are generated for anisotropy parameters R= 1, 1.5 and 2 while the other parameters are kept the same as in Table B.1. Similarly, in Figure 5.32 and Figure 5.33, the three curves in each figure are generated at strain hardening n= 0.14, 0.17 and 0.2 and at strength coefficient K= 5, 6 and 7 MPa respectively.

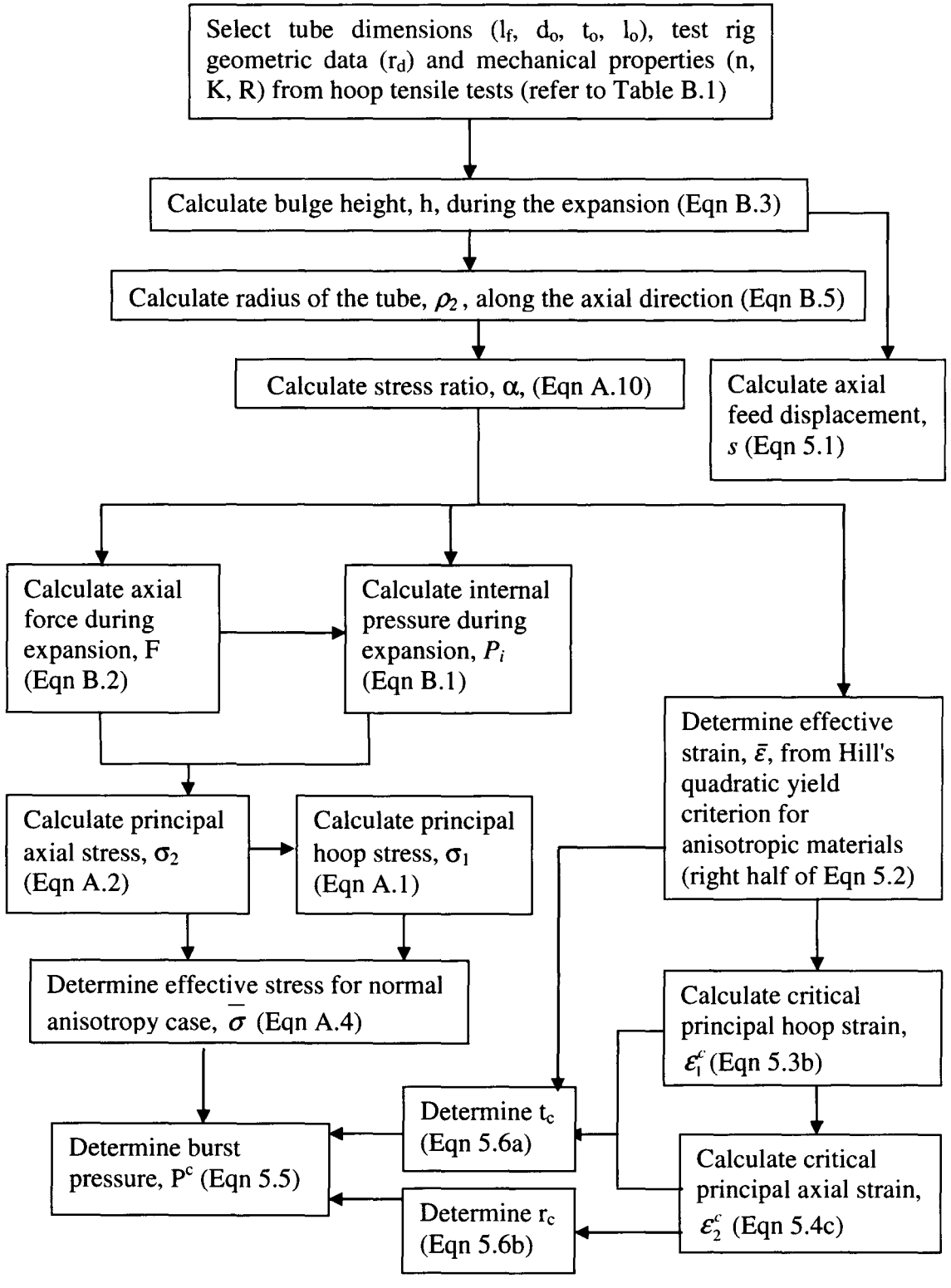

Figure 5.30 Flowchart outlining the sequence of calculations for prediction of burst pressure and forming limits for OPP tube at a given temperature.

Any loading combination of internal pressure and axial feed that falls under the curve indicates a 'safe' region for forming. It is to be noted that all bursting pressure versus axial feed curves reach saturation at large axial feeds. Figure 5.31 and Figure 5.32 show that the bursting pressure increases with increasing anisotropy parameter R, and decreases with increasing strain hardening exponent n respectively. Figure 5.33 shows that the safe region under the burst pressure versus axial feed curve is increased with an increasing strength coefficient K.

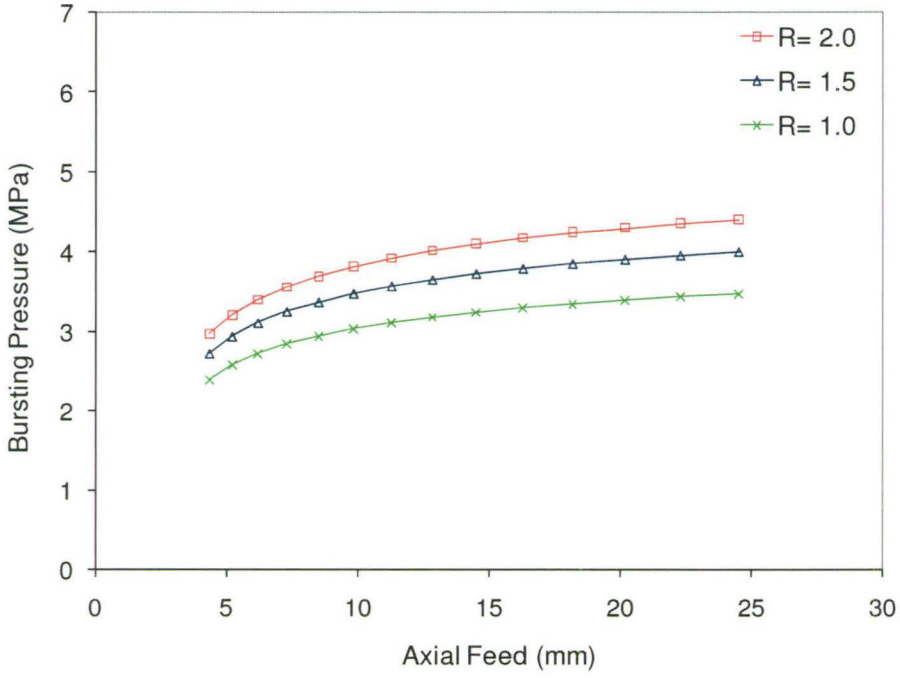

Figure 5.31 Effects of anisotropy parameter R on burst pressure during bulging tube (K= 6 MPa, n = 0.17).

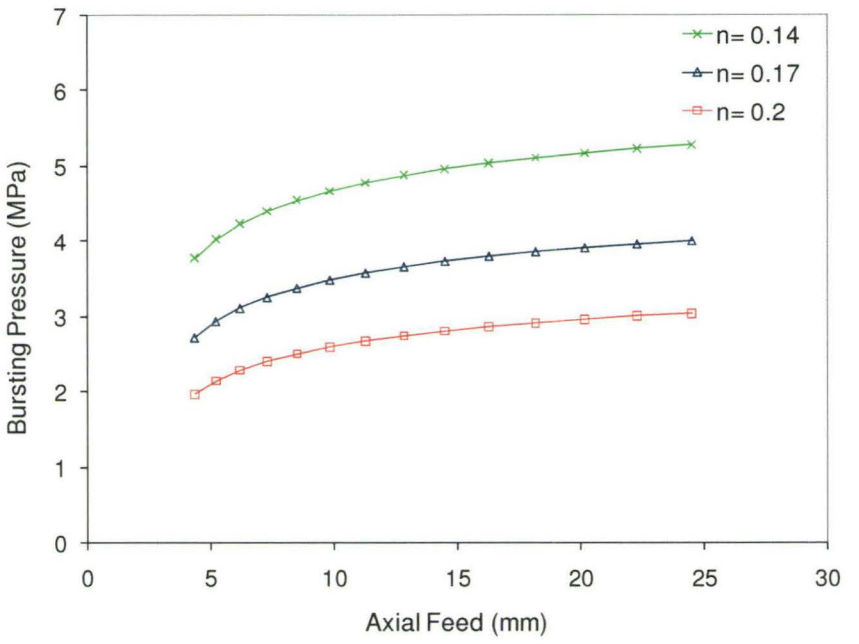

Figure 5.32 Effects of strain hardening n on burst pressure during bulging tube (K= 6 MPa, R = 1.5).

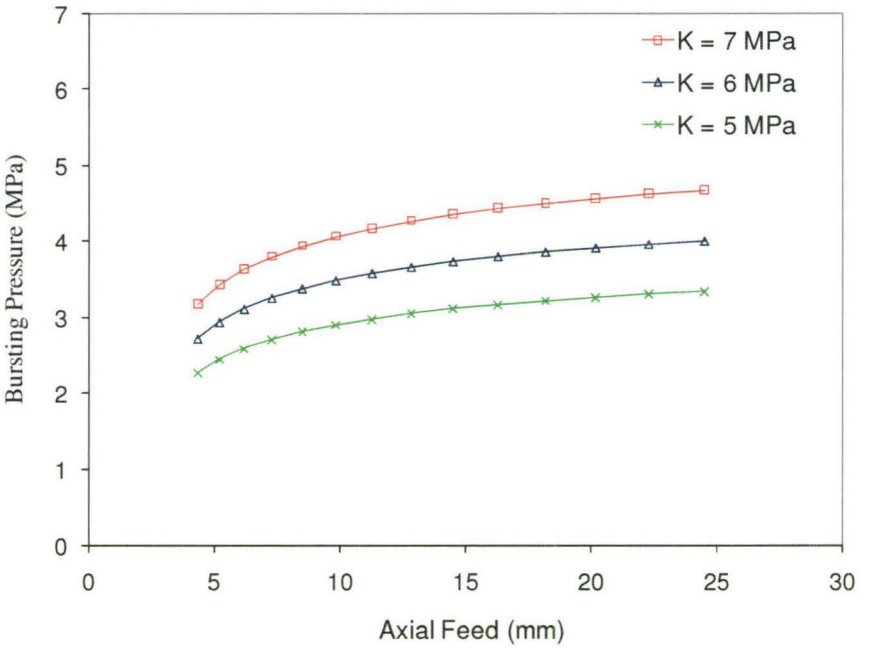

Figure 5.33 Effects of strength coefficient K on burst pressure during bulging tube (n = 0.17, R = 1.5).

5.2.2.2 A Comparison of Predicted Burst Pressure and Forming Limit with Experimental Results

The analytical prediction of burst pressure versus axial feed displacement, using the sequence of calculations outlined in Figure 5.30, is compared with the experimental results for tests conducted at 150ºC as shown in Figure 5.34. The result shows a good agreement with the experimental bursting pressure results. Similarly, Figure 5.35 shows that the predicted forming limits based on diffuse necking criterion for tube. These predictions are in good general agreement with the experimental strain measurements from bulge tests up to the onset of bursting. The maximum standard errors were obtained as 1.9 % and 2.3 % for major and minor strains respectively.

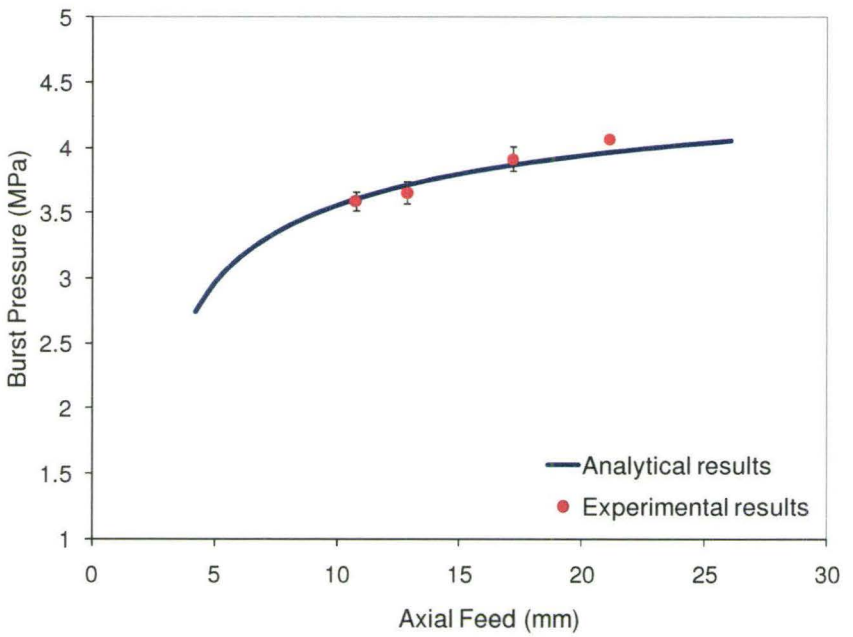

Figure 5.34 Comparison between experimental results and analytical predictions of burst pressure with axial feed for the cases (E, F, G and H). The test H was performed only once while other test cases were repeated three times.

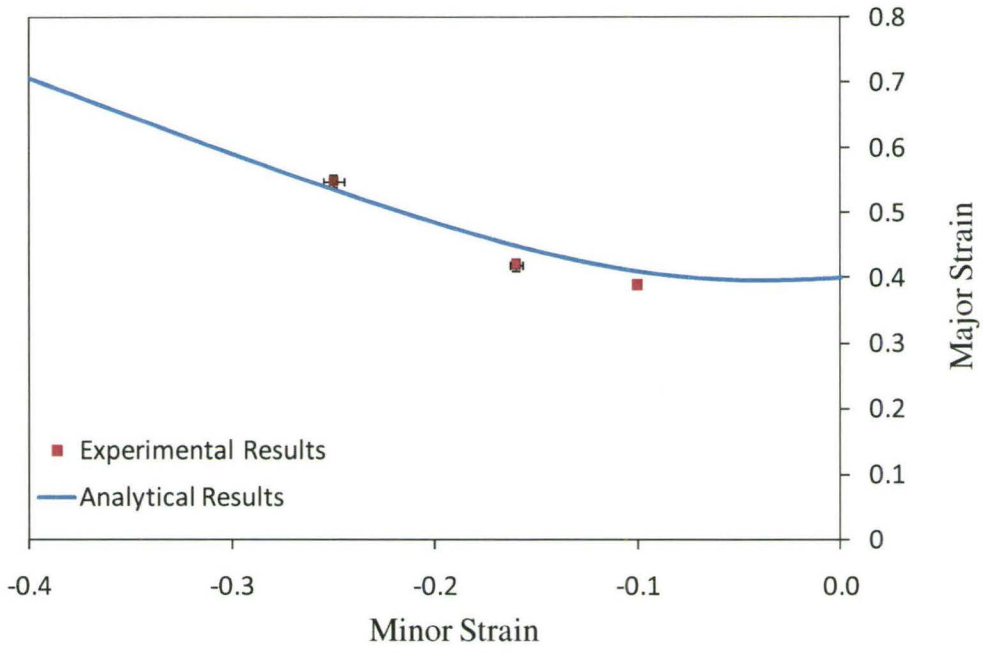

Figure 5.35 Comparison between predicted and experimental forming limits results for cases E, F and G. It is to be noted that the error bars for major and minor strains are barely noticeable.

5.2.3 Microstructural Characteristics of OPP Tubes after Forming

5.2.3.1 Morphological Changes in the Tube Material from AF- HOTF Process

The specimens were cut from hot formed tubes in the middle of the bulge area in the extrusion direction and through the thickness. The size of these fibers was about (15 mm x 0.5 mm × 0.5 mm) as shown in Figure 5.36. The diffraction pattern revealed full rings in the billet that changed to strong peaks in extruded samples (refer to earlier Figure

5.6). The bulge samples exhibited broadly distributed intensity with increase in axial feed. Also, (060)α, (022)α, and (220)α diffraction lines were weak in all samples, the extruded and bulge specimens contained only α-phase form.

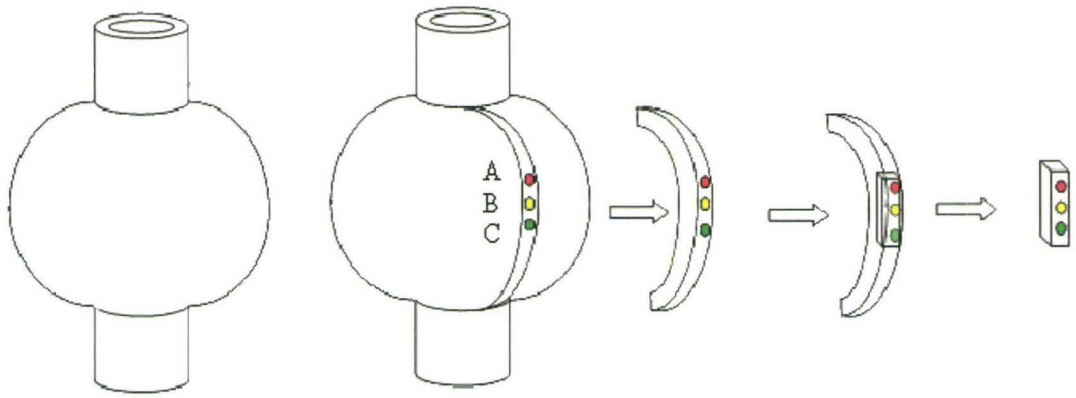

Figure 5.36 Fibers cut out of bulged tubes at middle of bulge area in the extrusion direction.

Figure 5.37 presents the (110)α and (040)α pole figures from the bulged samples for a range of axial feeds. With no axial feed, the b-axis shows a concentration in the transverse direction with only a slight difference as compared to the extruded samples. However, with the axial feed of 8.0 mm, the (110)α and (040)α poles are distributed around the transverse direction in a band making an angle of about 30°. For an axial feed of 18.0 mm, the (110)α and (040)α poles are distributed in an even broader band making an angle of about (35-60°) to the extrusion direction. The pole figures have a high concentration in the transverse direction making an angle of about 72° to the normal direction in the ND-TD plane.

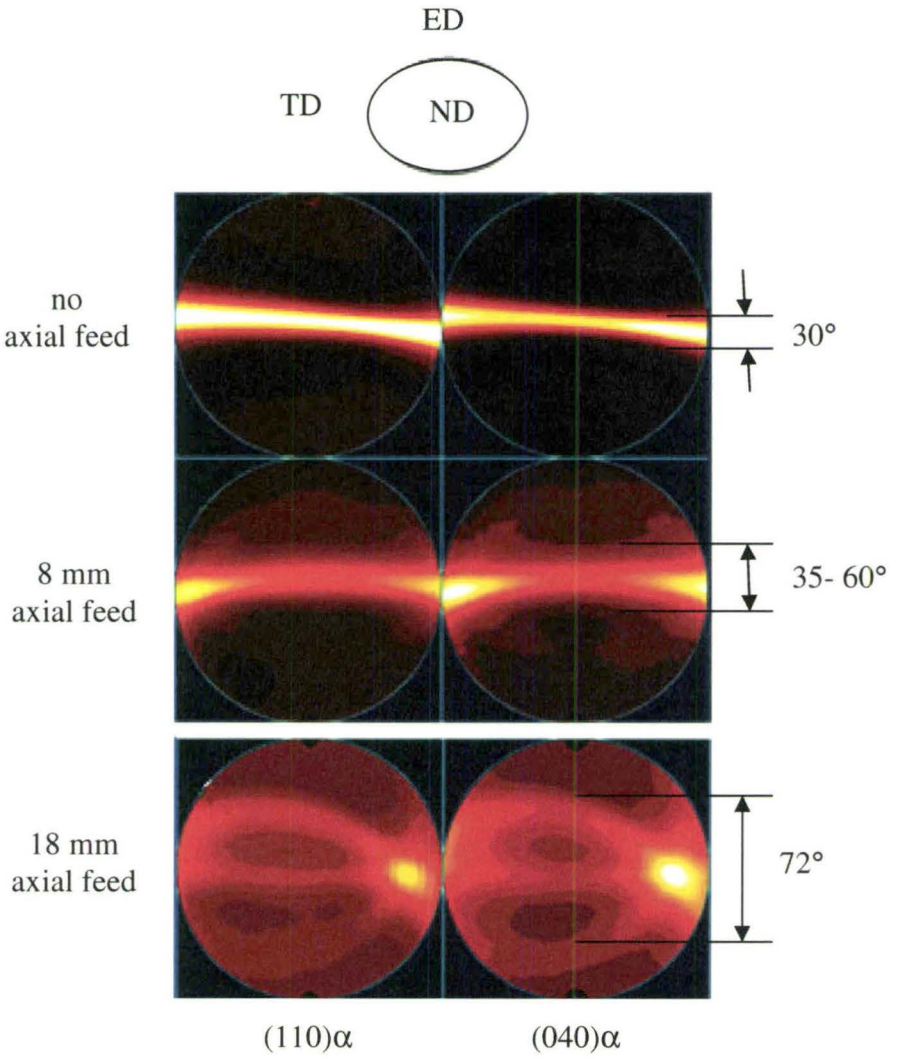

Figure 5.37 Pole figures for the $(110)\alpha$ (left column) and $(040)\alpha$ (right column) reflections from the middle of the bulge area with no axial feed, 8.0 mm and 18.0 mm axial feeds.

5.2.3.2 Orientation Factors

Crystallographic axes orientation factors were determined from the diffraction intensities of $(110)\alpha$ and $(040)\alpha$ reflections for PP billet, extruded and bulged tubes. The

orientation factor was represented in terms of the Herman's orientation factor to quantitatively represent the degree of axial orientation in crystalline fibers. Results from Wide Angle X-Ray Diffraction (WAXD) patterns of extruded and bulged polypropylene samples indicated that they had a monoclinic structure with dimensions a = 6.63 Å, b = 20.78 Å, c = 6.5 Å, β = 99.5° for the unit cell (Figure 5.38(a, b)). As shown, the (040)α planes are perpendicular to the b-axis. Thus, the b-axis orientation factors can be directly computed from the 040 intensity distribution. Also, as the angle between a and a′ axis is small (9.5°) and the a′-axis is perpendicular on the plane of axes b and c, the orientation of the a′-axis can be computed [Mendoza et al., 2003]. Since there is no set of reflecting planes perpendicular to the c-axis, the a′-axis orientation factors can be computed by using the variation of the intensity distribution in the 110 and 040 reflections as per Eq. 2.4 (refer to earlier section 2.7).

The Herman's orientation factors of billet and extruded samples are plotted on Stein triangle as shown in Figure 5.39 after calculating the c-axis orientation factors from Eq. 2.4. The results show that the billet sample, located at the origin, is randomly oriented. The orientation of the extruded samples moves toward the c apex as the draw ratios increased. This indicates that the chain orientation moves from being randomly oriented to being parallel to the extrusion direction and there is greater chain alignment in the extrusion direction with increasing draw ratio.

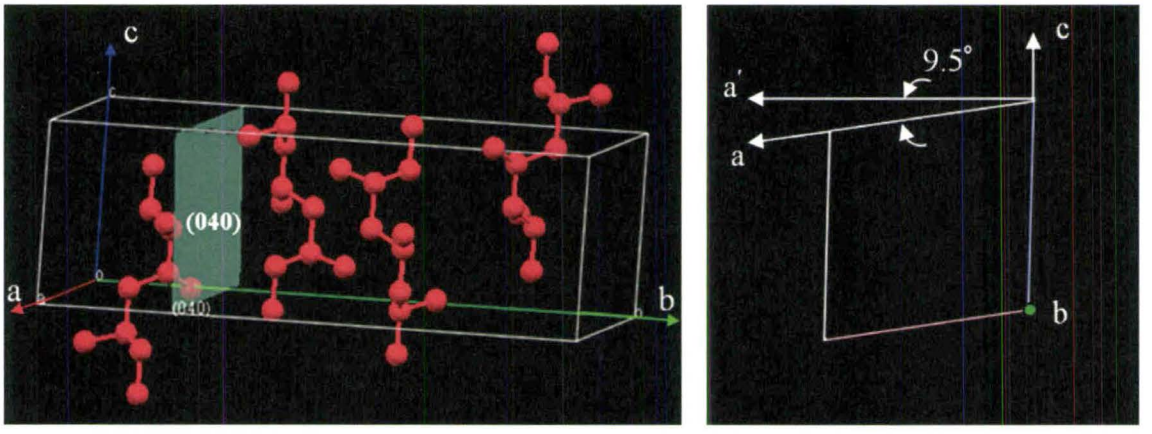

(a) (b)

Figure 5.38 A monoclinic crystal system in isotactic polypropylene (a) the crystal system with carbon chains parallel to c-axis, and (b) side view show the angle between a and a′ axis.

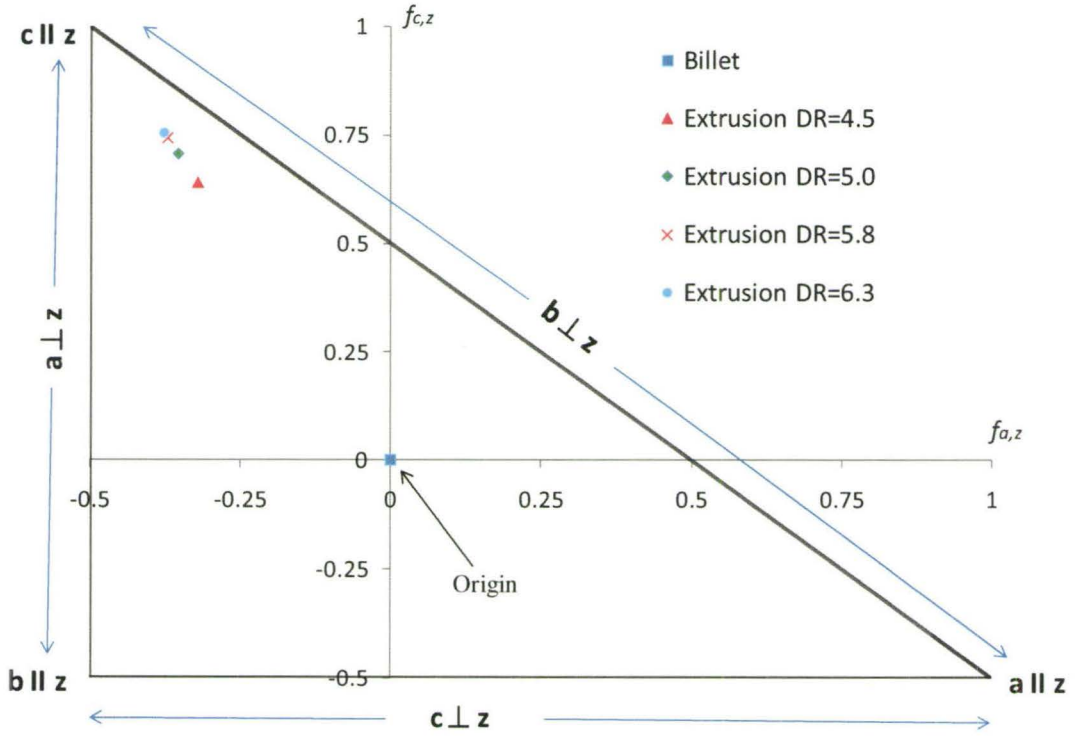

Figure 5.39 Representation of the axial orientation by a point of billet and extruded polypropylene samples at different draw ratios in the form of stein triangle.

White and Spruiell triangles are plotted in Figure 5.40 using the biaxial orientation factors f_{ED}^{B} and f_{TD}^{B} for billet, extruded and bulged polypropylene samples as described earlier in Chapter 2. The plot clearly shows indicates that the chains limited to ND-ED plane and the c-axis chain orientation move from being parallel to the extrusion direction at apex (1,0) to being perpendicular to it at apex (-1, -1) with an increase in the draw ratio.

In Figure 5.40, the White–Spruiell biaxial orientation factor for the starting billet sample is located at the origin. The orientation factors of the extruded samples move along the extrusion direction toward (0, 1) apex with the increase in the draw ratio which represents the case of uniaxial orientation. On the other hand, the orientation factors of the bulge samples starts at the highest orientation factor on the extrusion direction axis and moves along the side of the triangle with the increases in the axial feed and towards the apex (-1,-1) with thinning.

In bulged tubes, the results show that the development of biaxial orientation factors lie between the planar strain state and equal biaxial strain. The development of orientation is affected by two processes, the uniaxial orientation (i.e., solid state extrusion) and axial feed hot forming resulting in different biaxial orientation factors from a polypropylene blown film.

Biaxial orientation factors for the extruded and bulged tube samples are summarized in Table 5.3 The extrusion direction orientation factors f_{ED}^{B} of extruded samples versus draw ratio are plotted in Figure 5.41 where it is shown that the $f_{ED,c}^{B}$ values are positive and increase with the draw ratio, while the $f_{ED,b}^{B}$ and $f_{ED,a}^{B}$ values are negative and decrease with the draw ratio. All of the f_{TD}^{B} values ($f_{TD,a}^{B}$,$f_{TD,b}^{B}$ and $f_{TD,c}^{B}$) are zero, which represents the case of uniaxial orientation. For the bulge samples, the extrusion and transverse orientation factors (f_{ED}^{B}, f_{TD}^{B}) versus axial feed are plotted in Figure 5.42(a, b). As shown, the $f_{ED,c}^{B}$ values are positive and $f_{TD,c}^{B}$ values are negative and both decrease with the axial feed. On the other hand, the $f_{ED,b}^{B}$ and $f_{ED,a}^{B}$ values are negative and the $f_{TD,b}^{B}$ and $f_{TD,a}^{B}$ values are positive, and both sets increase with the axial feed.

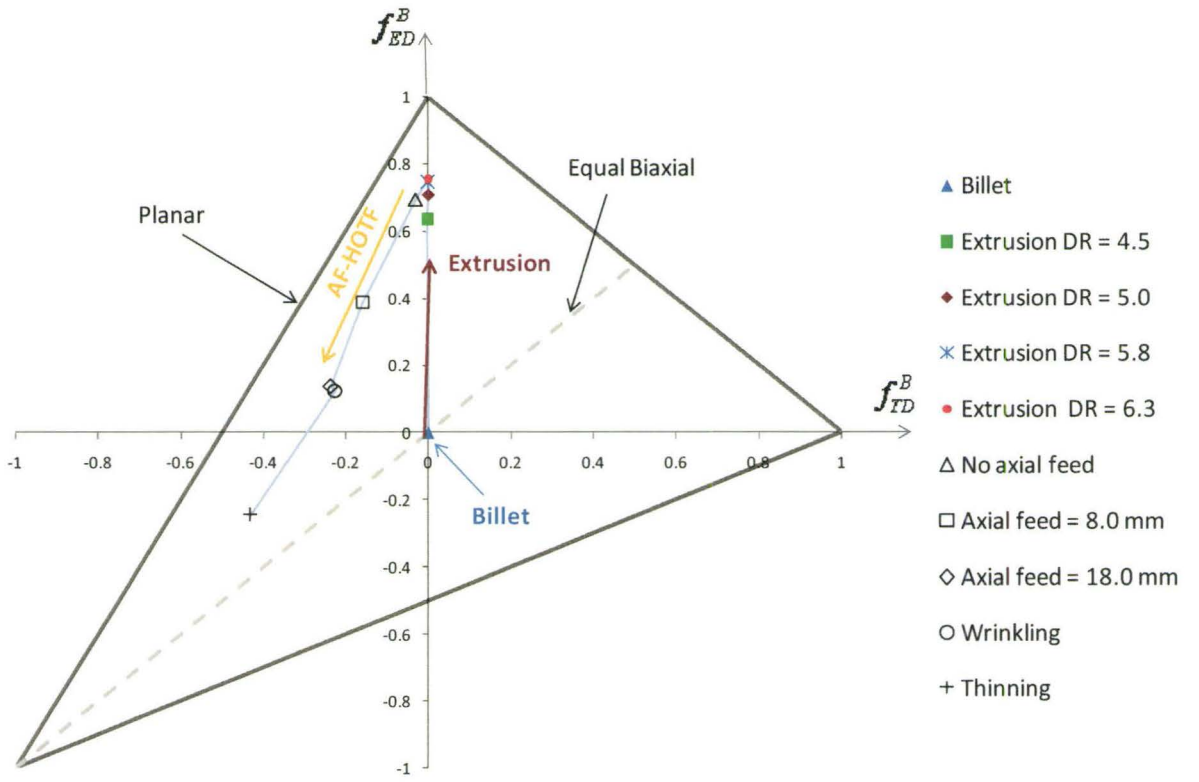

Figure 5.40 White and Spruiell representation of biaxial orientation of billet, extruded polypropylene, and subsequently formed tube samples at different draw ratios and bulge samples.

Sample type	$f^B_{ED,c}$	$f^B_{TD,c}$	$f^B_{ED,b}$	$f^B_{TD,b}$	$f^B_{ED,a}$	$f^B_{TD,a}$
Billet	0.000	0.000	0.000	0.000	0.000	0.000
Extrusion DR = 4.5	0.639	-0.003	-0.350	0.000	-0.297	0.000
Extrusion DR = 5.0	0.708	0.002	-0.370	0.000	-0.340	0.000
Extrusion DR = 5.7	0.744	0.001	-0.380	0.000	-0.367	0.000
Extrusion DR = 6.3	0.756	0.000	-0.386	0.000	-0.372	0.000
Axial feed = 0.0 mm	0.693	-0.029	-0.330	0.040	-0.357	0.000
Axial feed = 8.0 mm	0.388	-0.158	-0.176	0.120	-0.201	0.059
Axial feed = 18.0 mm	0.139	-0.236	-0.070	0.160	-0.065	0.094

Table 5.3 Crystalline orientation characteristics of extruded and bulged polypropylene tubes.

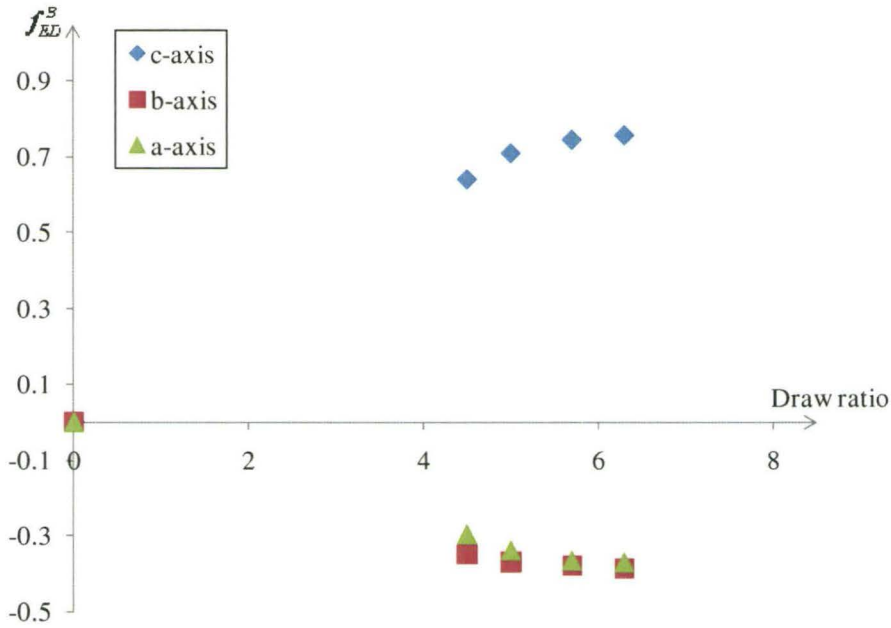

Figure 5.41 Variation in orientation factor f_{ED}^{B} with draw ratio for extruded samples.

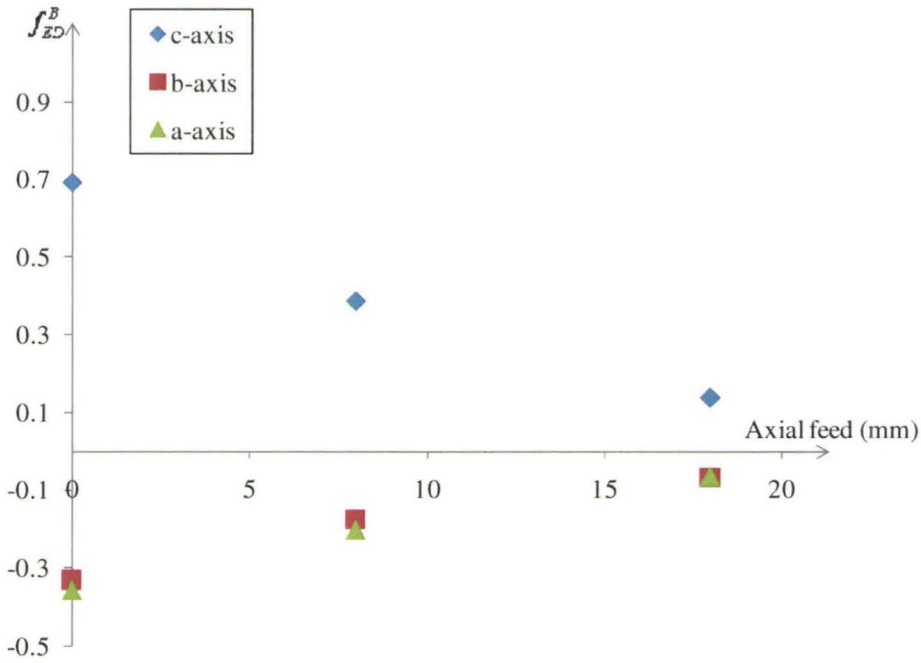

(a)

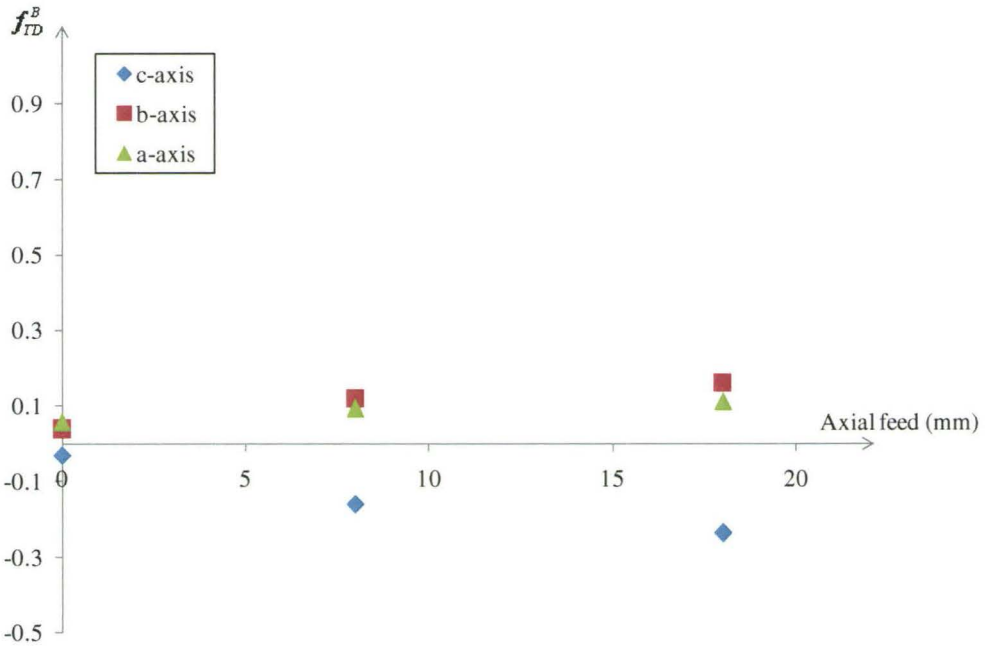

(b)

Figure 5.42 Variation in the orientation factors, (a) f_{ED}^{B} and (b) f_{TD}^{B} with axial feed of bulged samples (DR = 6.3).

5.2.3.3 ODF Results from Multex Area 2

Using the Multex Area 2 software from Bruker AXS, Inc. (Version 2) (2006), the orientation distribution function (ODF) was calculated for the extruded PP tube (DR=6.3) and for the bulged tubes with different axial feed displacements. The experimental pole figures with Bragg reflections of (110) and (040) were used in the simulation. The component fit window, as illustrated in Figure 5.43, contains the experimental pole figures, recalculated pole figures and the difference column, which shows the difference

between the experimental and the recalculated pole figures. As shown in Figure 5.43, the simulation results are in good agreement with the experiments.

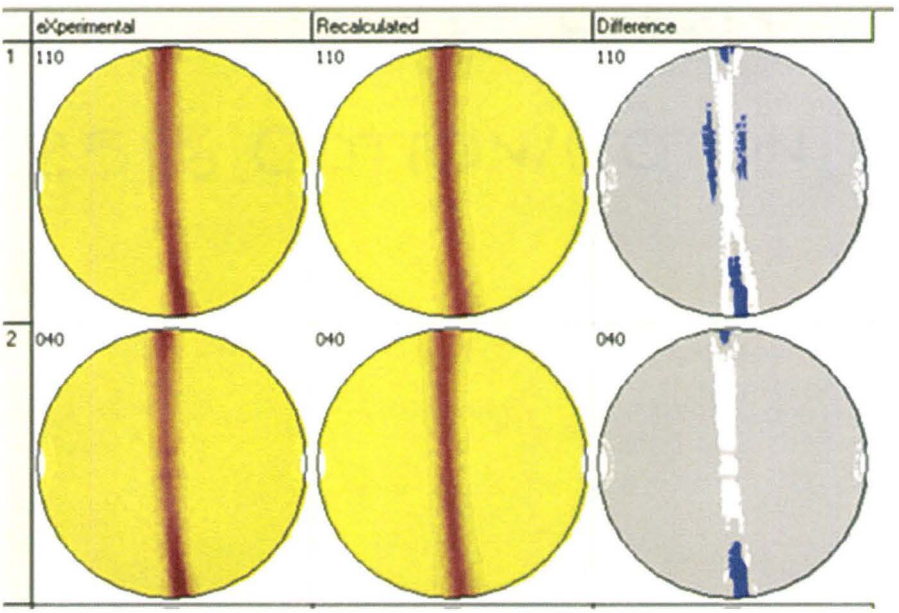

Figure 5.43 Component fit window for the extruded sample with draw a ratio of 6.3.

The volume fraction of crystallites and their intensity, I_c, the full-width-half-maximum of the distribution, b^c , and the ODF for all samples are summarized in Table D.1 in Appendix D. Figure 5.44 illustrates a 3D component presentation window of the extruded sample with pole figure (040) in three directions and Figure 5.45 shows the preferred orientation in 3D for the extruded and bulged samples at different axial feeds. The full width half maximum, b^c, for all samples are represented by different colors on the surface of the sphere, the orientation of the c-axis relative to the fiber axis is increased

with increases in the axial feed. In the extruded sample the volume fraction of crystallites (having c-axis parallel to the fiber axis) is 50% while in the bulged samples it is decreased from 30% to 15% with increases in the axial feed. This figure also shows that the preferred orientation has changed from the uniaxial, in the case of the extruded samples, to the biaxial orientation, in the case of bulged samples. This confirms the results discussed in the previous section.

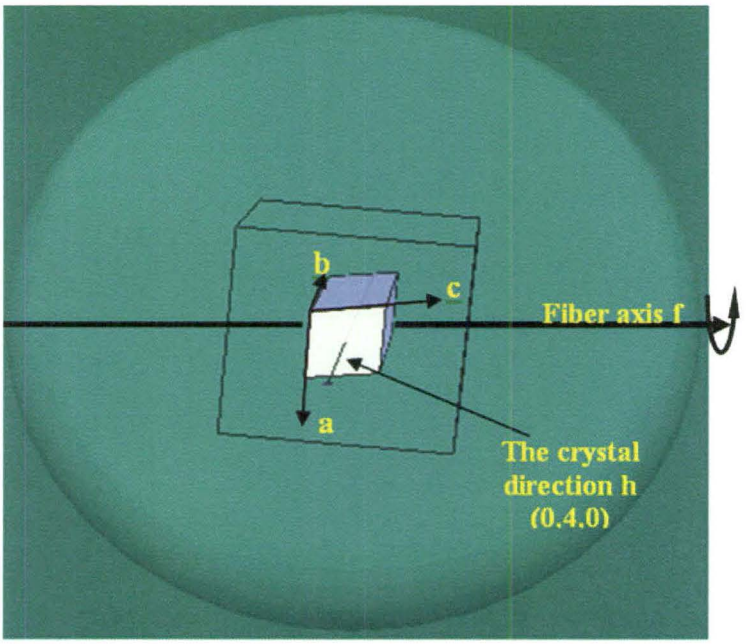

Figure 5.44 A 3D component presentation window of the extruded sample with pole figure (040) in three directions.

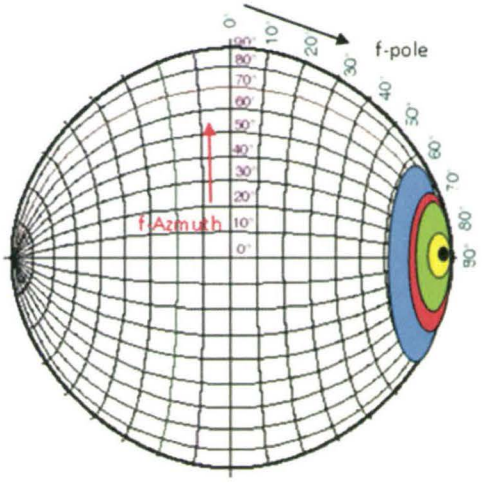

Colour code	Samples	Full-width-half-maximum (b^c)
	Fiber axis	0.0°
	Extruded	9.8°
	No axial feed	15.4°
	8 mm axial feed	17.2°
	18 mm axial feed	29.4°

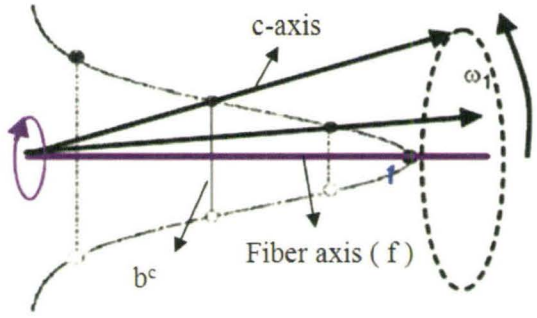

Figure 5.45 The preferred orientation in 3D for the extruded and bulged samples at different axial feeds.

5.2.4 Post-forming Mechanical Properties from Bulged Tube Samples

Samples from bulged tube specimens were tested in uniaxial tension at room temperature (refer to section 3.6). A visual inspection of the failed specimens showed a fibrous failure for all of the tensile samples. From the geometry of the dog-bone specimens machined from tubes along its longitudinal direction, two types of failures were observed as shown in Figure 5.46. First type of failure initiated where the fiber from the straight gauge line intersects the fiber from sample arc (type I). The fiber along the gauge line is longer than at the arc portion of the tensile sample. With increasing applied tensile load, the region of localized plastic deformation leads to craze formation. Second type of failure originated along the straight gauge line where the fiber was reduced by machining (type II). In this case, the fiber "diameter" was reduced by cutting and this resulted in premature failure of the specimen.

Figure 5.47 shows images from the gage regions of tensile samples machined from tube blank (Figure 5.47a) and from the bulged tube without feeding (Figure 5.47b). It is to be noted that a speckle pattern was applied to the test specimen for ARAMIS based on-line strain measurements. Both types of samples fail in a brittle manner where the fibers break at a local true strain of 0.14. In general, ductile fracture was associated with test coupons which were machined from tubes bulged with axial feeding (Figure 5.47c, d).

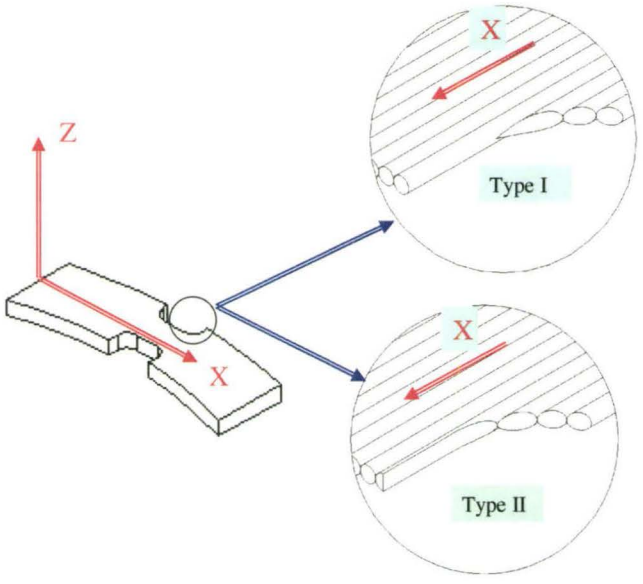

Figure 5.46 Possible damage mechanisms initiated from a single fiber break.

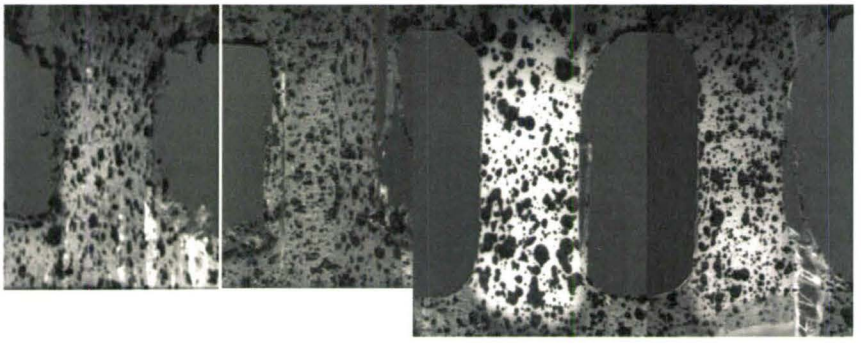

(a) (b) (c) (d)

Figure 5.47 Fracture modes in test coupons cut from the tube along extrusion direction, (a) extruded, (b) bulged without axial feeding, (c) axial feed of 8 mm, and (d) axial feed of 18 mm.

Stress whitening shown in Figure 5.47(c, d) corresponds to formation of fibrillar bridges in the craze region, similar to the results reported earlier for thermoplastic polymers (PE, PP, Nylon and PMMA) [Callister, 2007, Shercliff and Ashby, 2007]. Figure 5.48(a, b) shows the distribution of strain along the specimen axis (direction Y) at four points in the gage region of a deformed tensile test coupon. The specimen was machined along the longitudinal direction from a tube bulged with an axial feed of 8 mm. As shown, the local tensile strains were not uniform across the test coupon. The fibers were broken at point 3 at a local true strain 0.205. The fracture process typically involved three steps. First, the fibers were broken and separated along the longitudinal direction. At local true strain 0.269 fibrillar bridges were formed and subsequently crazing occurred at a local true strain of 0.376. As the deformation proceeded the crack began to propagate and the test coupon lost stability and twisted at a true strain of 0.515. For tensile samples with an axial feed of 18 mm, the damage mode was principally crazing (type I). For this test the fiber was broken at point 2 at a local true strain of 0.3. From these tests, we can conclude that the damage occurs at an equivalent true strain of 0.2 and 0.324 respectively for samples which were machined from tubes bulged with axial feeding of 8 and 18 mm respectively. However, the damage occurs at an equivalent true strain of 0.06 and 0.07 respectively for samples machined from the as-received and bulged tubes without end feeding. Figure 5.49 shows results similar to Figure 5.48 for test coupons cut along the hoop directions from 8 mm axial fed tubes. Failure of the specimen occurred at an equivalent true strains of 0.06, 0.08, 0.11 and 0.13 respectively for samples which were machined from tube blank, from the tubes bulged without end feed and for samples with

axial feeds of 8 mm and 18 mm respectively. The results demonstrate significant improvement in the formability of the tubes with axial feed during bulging.

Figures 5.50 and 5.51 show the room temperature true stress-strain behaviour of the tensile samples machined from the middle of the extruded and bulged tubes with a draw ratio of DR= 6.3 in the extrusion and hoop directions respectively. Extruded and bulged samples without axial feed exhibited brittle failure in the extrusion direction and almost the same tensile strength at fracture strain. With increasing axial feed the stress-strain curves exhibited elastic deformation followed by an elastic-plastic transition and a significant region of plastic deformation. The material strength and fracture strains for 18 mm axial feed were considerably higher than that for the 8 mm axial feed sample. The stress-strain curves in the hoop direction exhibited trends similar to the axial direction but with reduced strength and ductility (see Figure 5.51). As earlier, the material strength and fracture strains for 18 mm axial feed were higher compared to that for 8 mm. In general, increasing axial feed led to more ductile behaviour and failure occurred after strain hardening and extensive deformation.

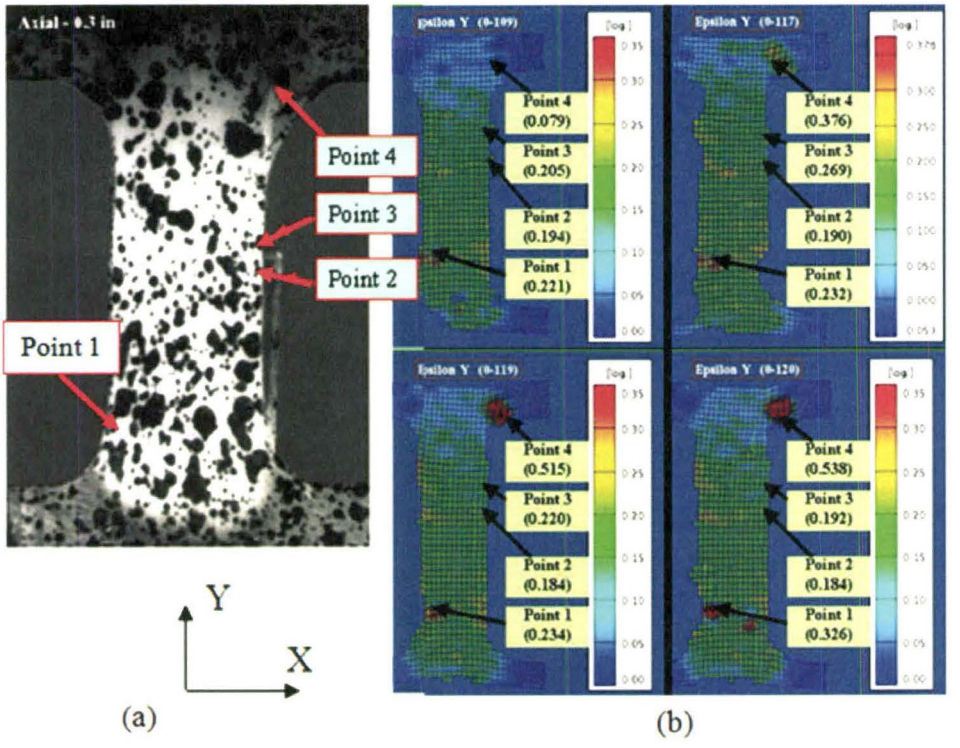

Figure 5.48 Axial strain distributions in tensile sample from the tube bulged with axial feed of 8 mm.

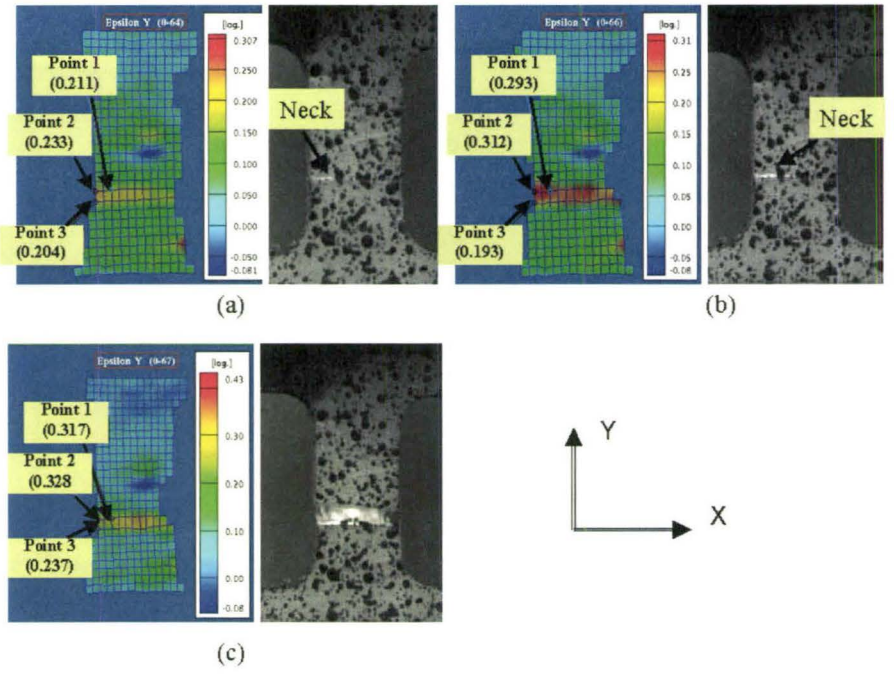

Figure 5.49 Hoop strain distributions in a tensile sample from a bulged tube with axial feed of 8 mm.

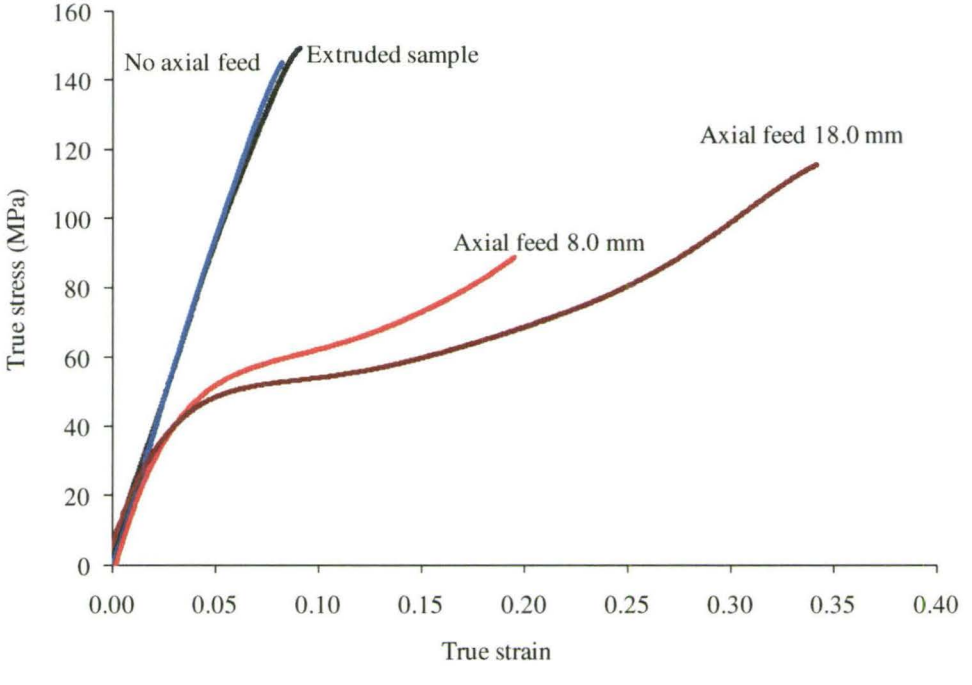

Figure 5.50 Stress-strain curves for samples machined from the middle of the extruded and bulged tubes with a draw ratio of DR= 6.3 in the extrusion direction.

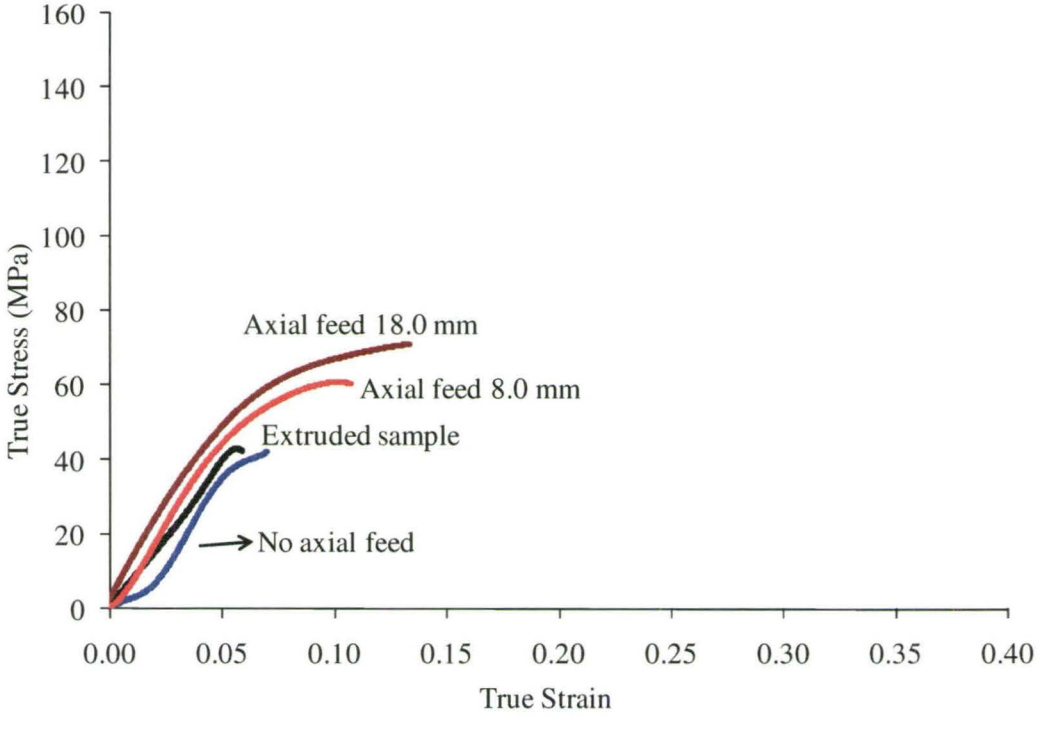

Figure 5.51 Stress-strain curves for samples machined from the middle of the extruded and bulged tubes with a draw ratio of DR= 6.3 in the hoop direction.

5.2.5 Biaxial Ball Stretching Test (BBST) Results

BBST tests allow the specimen to undergo biaxial stretching. The BBST tool set-up was described earlier in section 4.6. Deformed specimen geometry from these tests are shown in Figure 5.52. In the case of biaxial stretching, another mode of deformation was observed. At the beginning of the test, plastic deformation begins with bending at point A when the tube material enters the die cavity. The bending and stretching occurs at point C as the tube conforms to the punch profile and at point B the material unbends.

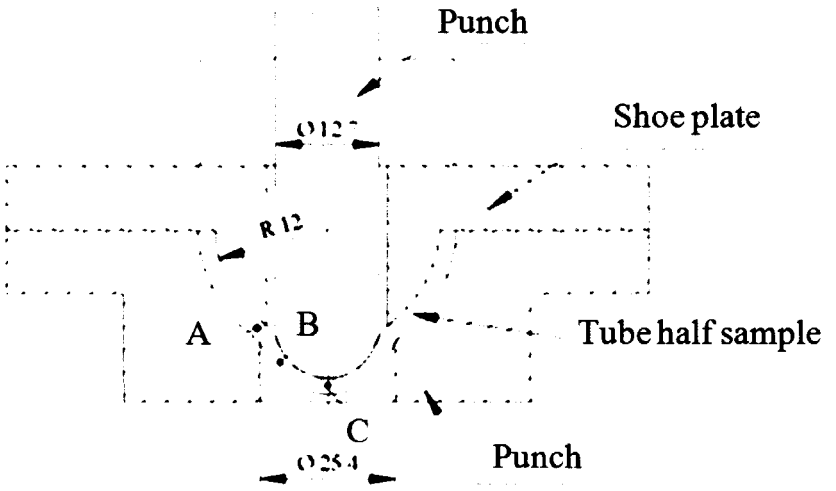

Figure 5.52 Geometry of a clamped tube sample loaded by a hemispherical punch.

Figures 5.53-5.55 show the deformed dome regions of OPP tube samples (DR=6.3) after biaxial ball stretching tests at 150°C, 160°C and 170°C respectively. The ARAMIS CCD camera was set to record video with a speed of 2 frames per second (fps) and a punch speed of 2 mm/min. Strain mapping results show that localized necking and fracture developed at low strains for OPP tubes. Hoop (major) and axial (minor) strains in the vicinity of crack were measured. At 150°C, the limiting major and minor strains were 0.04 and 0.02 respectively. At 160°C, crack occurred at major and minor strains of 0.124 and 0.07 respectively. The tube started to sink at 170°C but the tests were still carried out to yield the major and minor limit strains of 0.22 and 0.04 respectively.

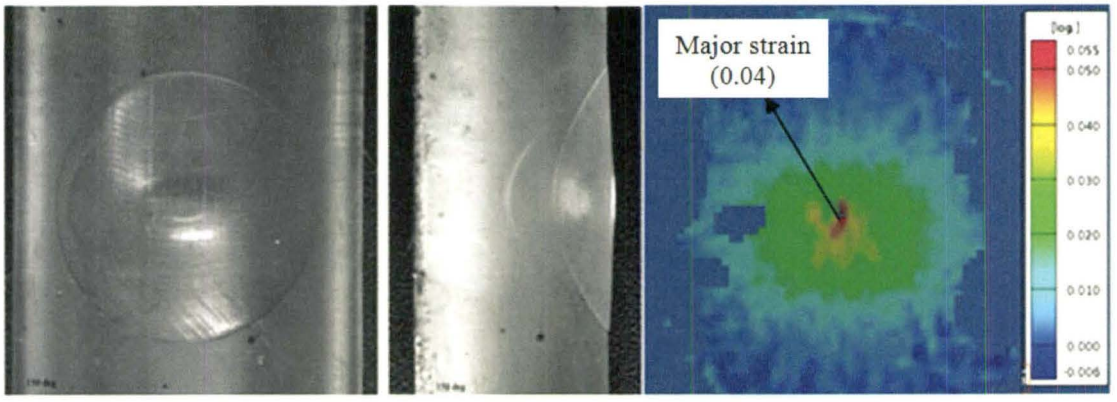

(a) (b) (c)

Figure 5.53 BBST results from OPP tubes, (a) cracks at the pole of the dome (front view), (b) a side view of the dome, and (c) a strain map from dome region at 150°C from ARAMIS showing localization.

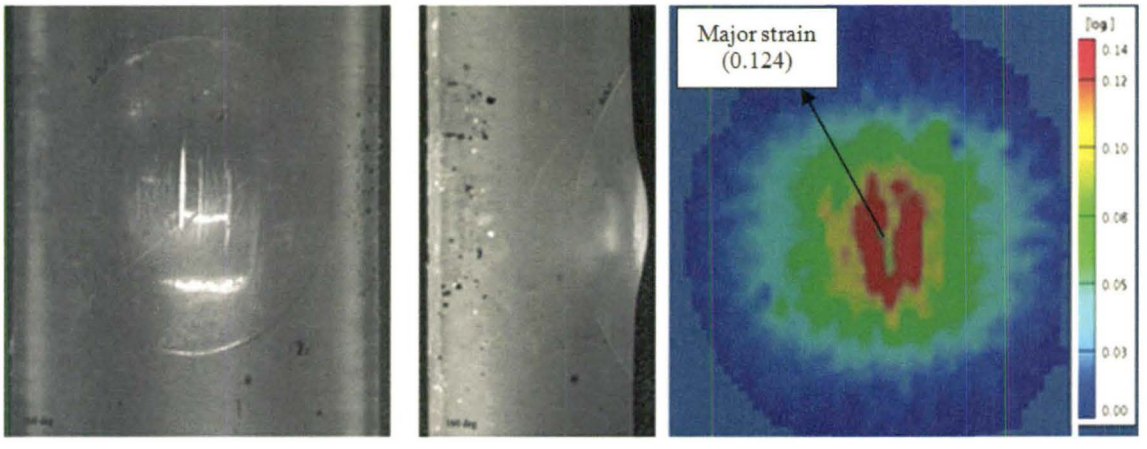

(a) (b) (c)

Figure 5.54 BBST results from OPP tubes, (a) cracks at the pole of the dome (front view), (b) a side view of the dome, and (c) a strain map from dome region at 160°C from ARAMIS showing localization at earlier stage.

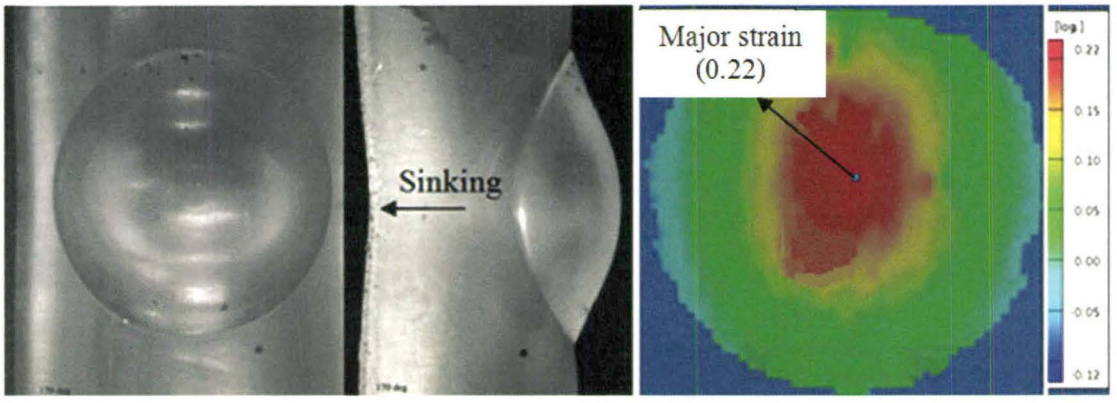

(a) (b) (c)

Figure 5.55 BBST results from OPP tubes, (a) no cracks at the pole of the dome (front view), (b) a side view of the dome (sample sink), and (c) a strain map from dome region at 170°C from ARAMIS showing localization.

The deformation behaviour of OPP tube under biaxial tension is different from that of EPP tube (i.e., tubes obtained by machining from solid cylindrical, melt-extruded, polypropylene billets). The calculated strain paths up to fracture point using ARAMIS system are shown in Figures 5.56 and 5.57 at the three temperatures. The local axial and hoop strains were obtained at the pole of the dome, where the largest amount of wall thinning took place. In the temperature range between 150°C and 160°C, the strain paths of EPP tubes are close to balanced-biaxial tension as shown in Figure 5.56. As temperature increases to 170°C, the material becomes more temperature sensitive and the tube samples starts to sink and the strain path deviates from the balanced biaxial state to a plane strain state. The BBST tests for EPP tube samples were not carried out up to fracture, because this material could not be deformed without cracks.

The BBST tests on OPP tubes showed very little strain prior to crack formation. In this case all tests were carried out up to fracture. At 150°C and 160°C the axial cracks occurred at about 4 to 13% hoop strain as shown in Figure 5.57. As the temperature is increased to 170°C, the strain ratio at a certain point remains constant and then the material transitions to a plane strain state. A hoop strain close to 22% is reached. However, the axial strain has a maximum value of only 4%. As shown previously in tube bulging experiments (refer to Figure 5.25), the axial feeding applied to the end of the tube significant increases the formability of OPP tubes. BBST tests do not allow for any feeding of the material in the die.

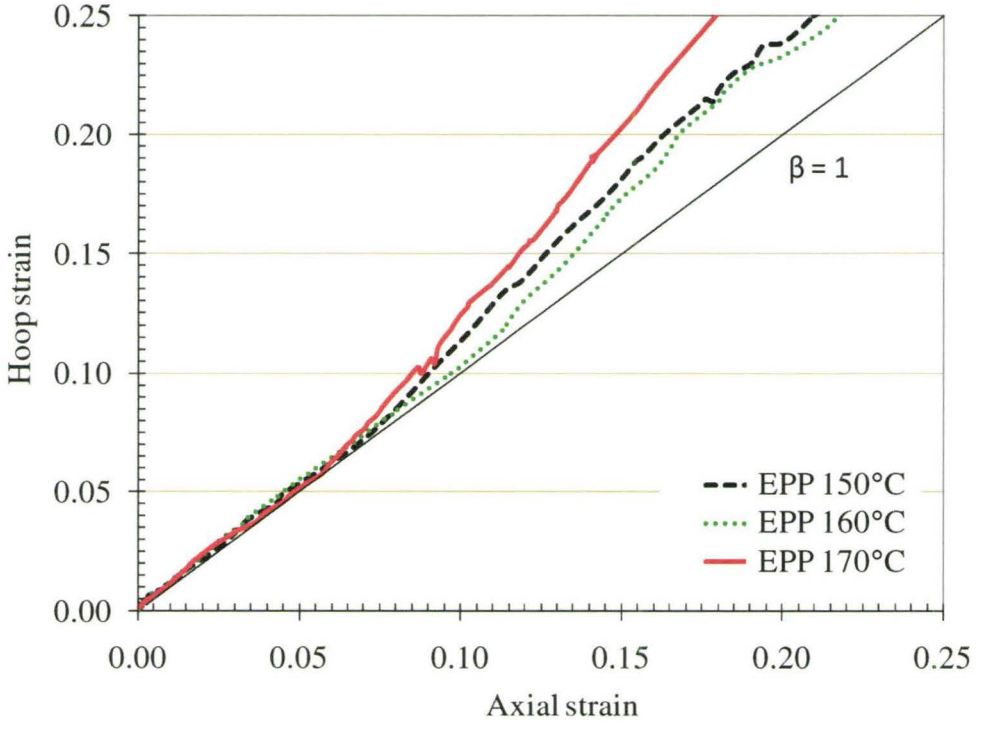

Figure 5.56 Strain paths as a function of temperature for the melt-extruded (EPP) tubes.

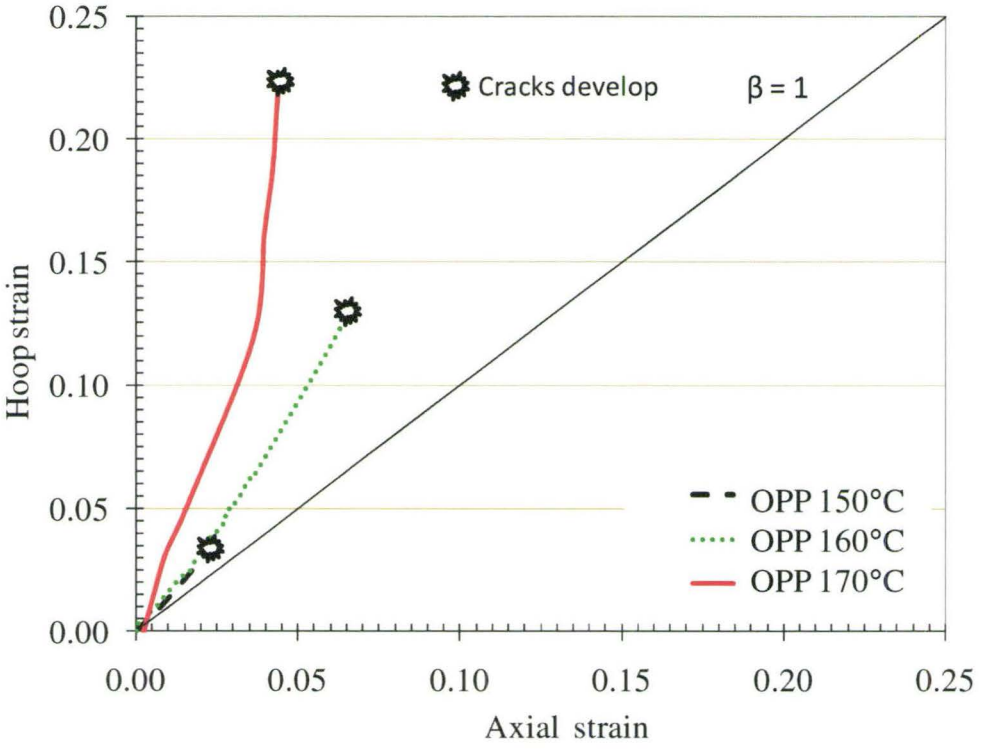

Figure 5.57 Strain paths as a function of temperature for the OPP tubes.

5.2.6 Microstructural Characteristics after Ball Stretching

The X-ray diffraction patterns from billet tube and earlier OPP tube samples after BBST were recorded using the method described earlier in section 5.1.2.3. Figures 5.58 presents X-ray diffraction patterns of billet tubes formed at 150°C, 160°C and 170°C corresponding to effective strains of 0.78, 0.78 and 0.8 respectively for different orientation positions (ϕ = 0°, 45° and 90°). The Debye rings in all billet tube samples were similar to the starting billet sample.

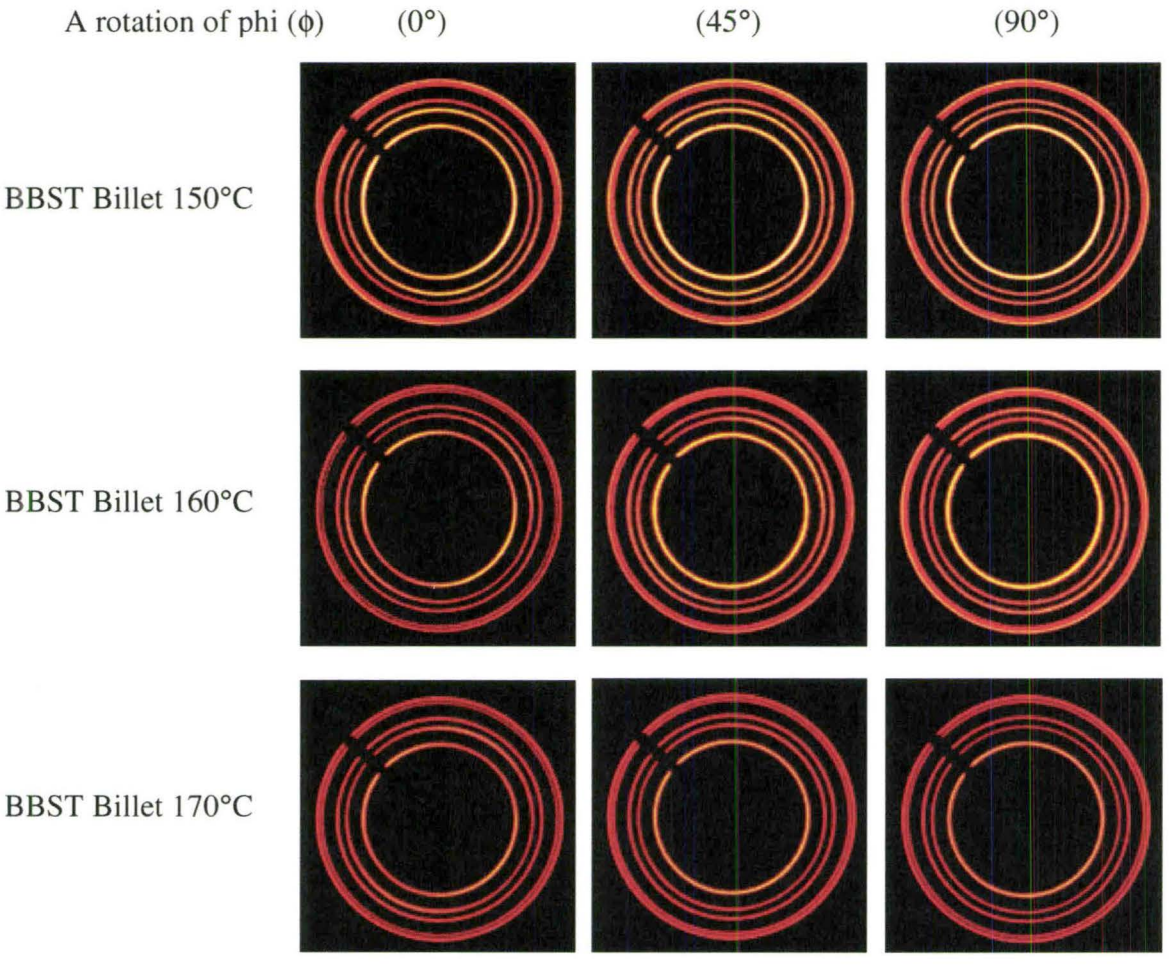

Figure 5.58 X-ray diffraction patterns of billet tube samples after BBST rotated at different ϕ angles (0°, 45° and 90°) and at different forming temperatures (150°C, 160°C and 170°C) effective strains (0.78, 0.78 and 0.8).

Figure 5.59 shows the X-ray diffraction patterns of OPP tube samples after BBST tests at 150°C and 160°C for the three ϕ angles (effective strains of 0.31 and 0.52). The patterns are quite similar and show the same arcing as in OPP tube sample at DR=6.3 (refer to earlier Figure 5.6). For the OPP tube samples at 170°C (effective strain of 0.48),

however, the arcing appears to be getting broader with increasing ϕ angle, i.e., by fiber rotation from 0° at TD-ED plane to 90° at ND-ED plane.

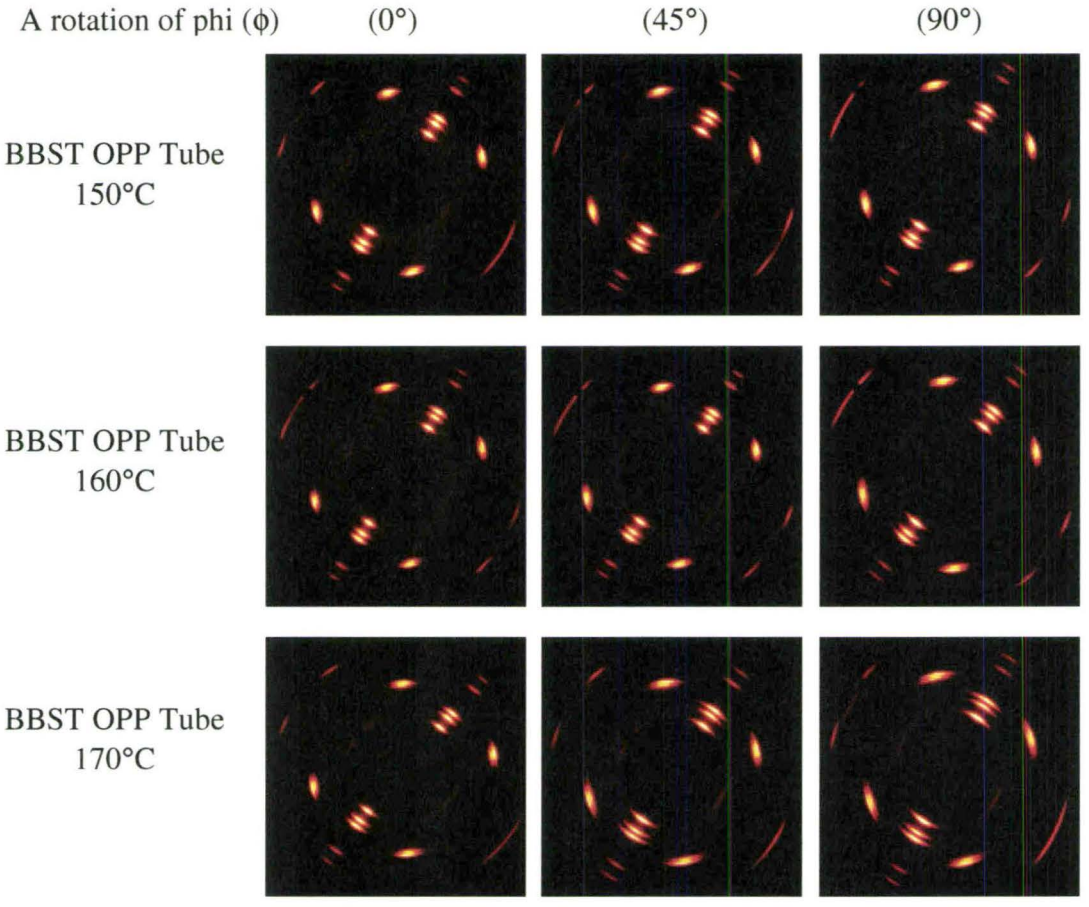

Figure 5.59 X-ray diffraction patterns of BBST OPP tube samples rotated at different ϕ angles (0°, 45° and 90°) and at different forming temperatures (150°C, 160°C and 170°C) (effective strains 0.31, 0.52 and 0.48).

Figure 5.60 presents the (040)α pole figures of the starting billet sample and various billet tube samples formed via BBST at various temperatures. In the starting billet sample (refer to Figure 5.60a), the pole figure shows random intensity distribution and no concentration of the b-axis. The pole figure of billet tube sample formed at 150°C shows a concentration of the b-axis between the transverse and extrusion directions in a broad band making an angle of about (20°- 60°) (refer to Figure 5.60b). For billet tube after BBST at 160°C, the b-axis is concentrated at an angle of about (35°- 80°) between the transverse and extrusion directions (refer to Figure 5.60c). However, for billet tube formed at 170°C, the (040)α pole are distributed around the transverse direction in a band making an angle of about 45°(refer to Figure 5.60d).

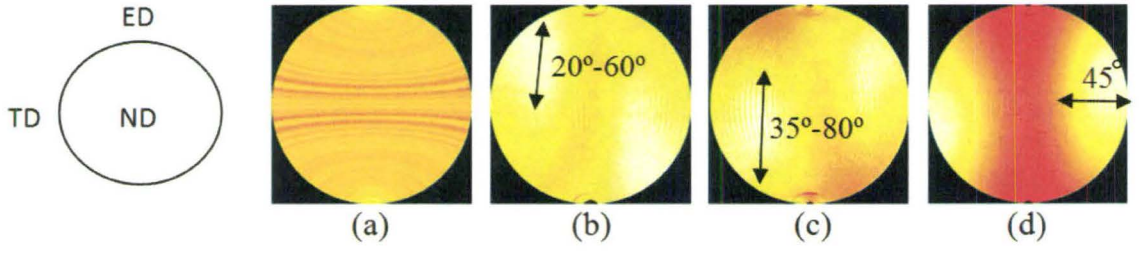

Figure 5.60 The pole figures of (040) plane of monoclinic α form plotted in stereographic projection (a) starting billet sample, (b) billet tube after BBST at 150°C, (c) billet tube after BBST at 160°C, and (d) billet tube after BBST at 170°C.

The pole figures for OPP tube at DR = 6.3 and OPP tube samples after BBST at different forming temperatures are compared in stereographic projection in Figure 5.61. The (040)α pole figure of OPP sample (Figure 5.61a), show uniaxial orientation pattern

distributed symmetrically around the extrusion direction (ED). The (040)α pole figures of OPP tube samples after BBST show orientation patterns similar to the initial OPP tube. A slight tendency towards the transverse direction can be noted Figure 5.61(b, c and d).

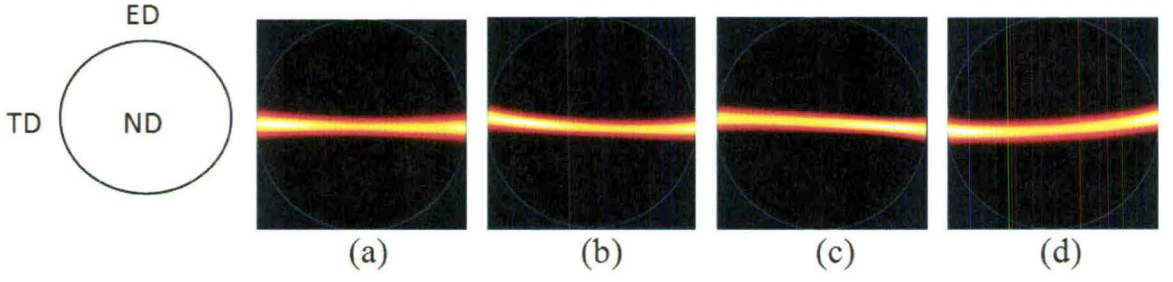

Figure 5.61 Pole figures of (040) plane of monoclinic α form plotted in stereographic projection, (a) extruded polypropylene tube at DR=6.3, (b) OPP tube after BBST at 150°C, (c) OPP tube after BBST at 160°C, and (d) billet tube after BBST at 170°C.

In Figure 5.62, the White–Spruiell biaxial orientation factor for the various deformed states of the tube materials are shown. The undeformed billet tube sample is located at the origin. The orientation factor of the BBST billet tube sample at 150°C move slightly toward positive side of the transverse direction with slightly away from the origin. The BBST billet tube sample at 160°C shows that the orientation factor moves further towards the positive side between the extrusion and transverse directions and closer to the equibiaxial strain state. At 170°C, the orientation factor of BBST billet tube samples moved slightly away from the origin along the extrusion direction in the positive direction. At this temperature, the material becomes more temperature sensitive and the tube samples started to sink in the transverse direction. On the other hand, the orientation

factor of the BBST OPP tube samples at 150°C, 160°C and 170°C, started at the highest orientation factor (OPP tube DR = 6.3) on the extrusion direction axis (uniaxial direction) and moved towards the right side of the triangle (i.e., planar film surface, refer to Figure 2.12) slightly away from the apex (0, 1).

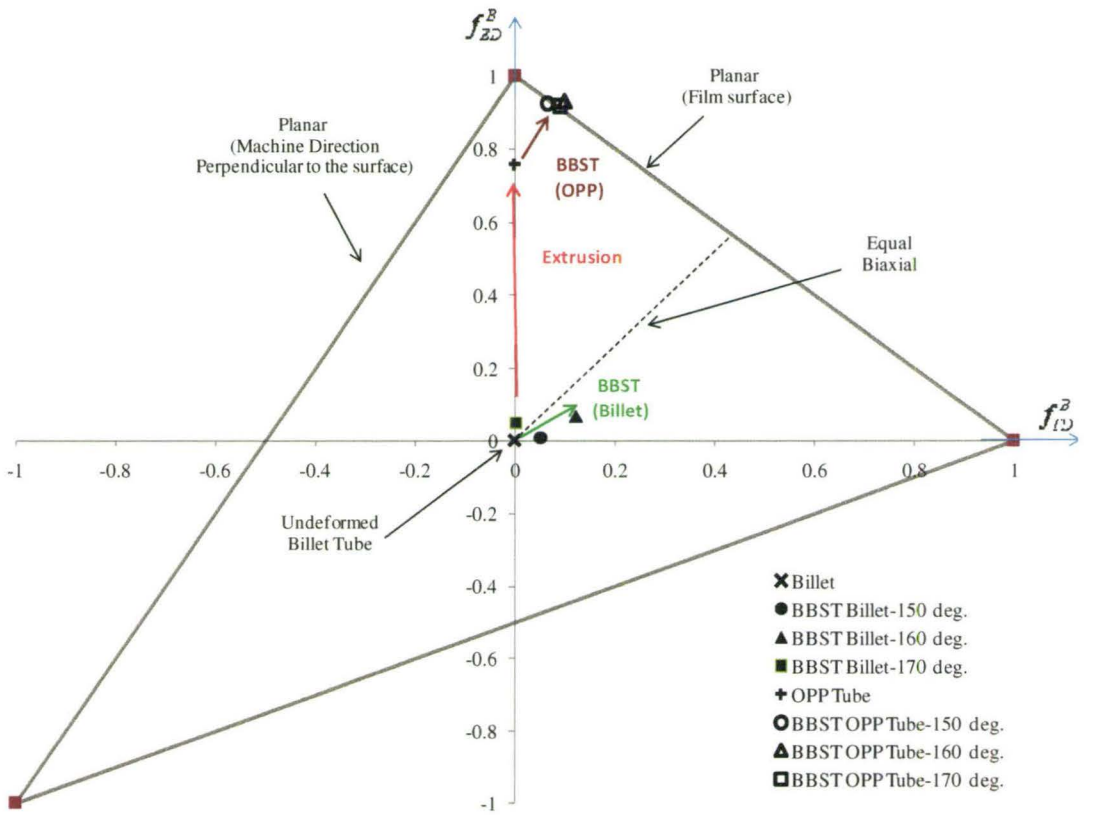

Figure 5.62 White and Spruiell representation of biaxial orientation of billet, OPP tube (DR=6.3), and subsequently formed tube samples with biaxial ball stretching test (BBST) at different forming temperatures (150°C, 160°C and 170°C).

5.2.7 Axial Feed Hot Gas Tube Forming (AF-HGTF) Experiments

The test apparatus utilized for these experiments was described earlier in chapter 4 (section 4.4). Based on the previous experimental results on free bulging tubes, a number of process parameters were fixed such as forming temperature (155°C), total axial feed (38 mm), tube length (200 mm), rate of forming (34 kPa/sec) and maximum applied pressure (3.1 MPa). These process parameters were then applied in experiments using the axial feed hot gas tube forming system to form the tube into a larger cylindrical component in a closed die. Seven formed tube samples are shown in Figure 5.63. The effect of cooling time and pressure release rate on overall tube shape after forming was studied and a procedure was developed for forming a good quality part (refer to earlier section 4.4.1). Table 5.4 summarizes the experimental results and observations from axial feed hot gas tube forming experiments. No microstructural studies of post-formed samples were carried out as the objective here was to develop optimum conditions for forming the tubes in a closed die.

Test	Objective (To determine)	Parameters held constant	Parameters varied	conclusion
(1) (Fig. 5.63a)	The effect of cooling time on forming tube	Pre-heating time T=155°C P = 34 kPa/sec Feed= 38 mm	Cooling temperature and Time holding	Release pressure at T= 80°C or less is sufficient to maintain the shape of formed part
(2) (Fig. 5.63b)	The combination effect of pressure release rate and cooling time on forming tube	Pre-heating time T=155°C P = 34 kPa/sec Feed= 38 mm Pressure released at high rate	Cooling temperature and Time holding	Pressure may be released quickly with no negative effect on the forming shape at T= 80°C or less
(3) (Fig. 5.63c)	A suitable amount of feeding and P_{max} for uniform shape and formed tube final thickness	Pre-heating time T=155°C P = 34 kPa/sec Feed= 38 mm P_{max} =3.1MPa	None	Produce parts of uniform thickness that fill the entire die cavity

Table 5.4 Experiments carried out on axial feed hot gas tube forming system.

(a) (b) (c)

Figure 5.63 Various AF-HGTF test samples, (a) released pressure at 155°C for no time holding, at 120°C for 20 minutes time holding and at 80°C for 45 minutes time holding (from left to right), (b) released pressure at 120°C for 20 minutes time holding and at 80°C for 45 minutes time holding (from left to right), (The pressure was released at high rate while tube was under pressure (345 kPa)), (c) samples formed by a combination of feeding (38.0 mm total), pressurization (3.1MPa) and cooling down to 80°C under pressure.

Chapter 6

Discussion

6.1 Solid State Extrusion

6.1.1 Process Parameter Adjustments

In ram extrusion, deformation induced heating in the tubular billet cannot be properly conducted away through the chamber and die, resulting in a rise in the tubular billet temperature. This increase in temperature during extrusion was taken into account by adjusting the chamber temperature to 145ºC and the die temperature to 140ºC, to obtain on extrusion temperature of 150ºC.

Accurate tube diameters were required for sealing the ends of the tube during hot bulge forming experiments. However, increases or decreases in die drawing load (or haul-off tension) above or below the preset load of 550 lbs resulted in a some variation in the size of the oriented tubes. This resulted in mis-match of the tube inner diameter and end plug diameter during tube bulging experiments. This variation in the tube diameter was accounted for by a novel design of the end plugs (see Figure 4.6).

6.1.2 Morphological Changes through Wall Thickness of Extruded Tube

An extruded PP sheet and tube show a similar skin-core structure to that developed in injection molding [Karger-Kocsis, 1999]. In both cases, the molecular orientation tends to be stronger at the surfaces and decreases toward the mid-thickness. The crystallinity is low at the sheet surface and increases toward the mid-thickness because of slow cooling. Also the skin-core structure in injection molded polypropylene was observed and the structure distributed in a three-layer structure composed of a surface skin layer, a transition layer, and an inner core [Liu and Edward, 2001]. This three- layer structure of an injection-molded part is dependent on the thermal and shear history of the injection molding process. The surface skin layer is crystallized under very high cooling rate and low shear rate. The transition layer is crystallized under a higher shear rate that results in high molecular orientation in the flow direction and a highest crystallinity. The inner core layer is crystallized under very low cooling rate and low shear rate. The spherulitic morphology of the inner core layer is similar to the morphology of compression molded samples where polymers crystallize from a quiescent melt.

In general, skin-core differences are not desirable in the extruded tube cross-section. The extruded polypropylene tube by solid-state extrusion (OPP) was investigated through the thickness (from inner to outer surface) by wide angle X-ray diffraction. The results show a small difference in estimated percent crystallinity of about 3% between the

outer and inner tube surfaces (refer to Figure 5.10), As the tube cooled from the outer surface, the rate of cooling is fastest on the outside and decreases toward the inner layer. This results in lower crystallinity for the outer surface as well as small changes in orientation factor of about 6% from the inner to outer layers through the thickness of extruded tube (refer to Figure 5.9). This observation, a homogenous skin-core structure throughout the extruded tube (OPP) thickness, shows the advantage of using the solid state extrusion process over the injection molding process.

The morphology changes in the billet by solid-state extrusion were observed and investigated, the spherulite structure was destroyed during the deformation process and gradually transformed into the fibrillar structure continuously aligned in the extrusion direction at high draw ratios (refer to Figures 5.2, 5.3 and 5.4). These are clearly recorded using the Debye patterns, the reflections appear as full rings in the billet sample but transform to arcing in the extruded samples (refer to Figure 5.6). With increases in draw ratio, the crystallinity increased in the OPP tube because the alignment of the polypropylene chains made the formation of the crystalline structure easier.

The three known possible crystalline phases in polypropylene are monoclinic (α), hexagonal (β), and orthorhombic (γ), all three phases influence the physical properties of the end product. X-ray diffraction profiles for polypropylene billet showed a strong intensity peaks for α-phase and the presence of $(117)_\gamma$ with a rather poorly defined peak for the occurrence of γ-phase. X-ray diffraction profiles for the oriented specimens

presented peaks for only α-phase form, the γ-phase peak in the billet sample did not appear after billet was reheated and extruded by solid-state extrusion to tubes with different draw ratios. In injection molding, on the other hand, the γ-phase begins to coexist with the α-phase until it becomes dominant at a pressure of 200 MPa [Mezghani and Phillips, 1996].

6.1.3 Effect of Mechanical Properties

The true stress-strain curves of the billet and the oriented polypropylene samples tested in the extrusion direction at room temperature with different initial strain rate were shown in Figures 5.13 and 5.14. It was found that the yield strength and elastic modulus were increased with draw ratio and strain rate. After yielding, the initial spherulitic structure of the billet was changed to an oriented structure from cold drawing. In the true stress-strain curve for the billet sample, from tests with an initial strain rate of 0.002/sec, a small amount of strain softening was observed at first, followed by strain hardening to large strains. Neck propagation occurred uniformly along the gauge length with the same constant cross-section as at the start of necking. However, local necking was observed very early in the test at an initial strain rate of 0.044/sec. Also, a drop in stress after the yield point was observed in a small range of strain and with no cold drawing until fracture. This is because of brittle-ductile failure, a mixed mode ductile and brittle crazing fracture related to the rate of applied strain to the sample [Scheirs, 2000].

In the case of OPP samples, the molecules were pre-oriented in the extrusion direction and the curves show neither upper yield points nor necking behaviour. Thus, the OPP samples exhibited much enhanced stiffness and toughness. The yield stress increased significantly with increasing draw ratio and with initial strain rate in all oriented polypropylene tubes. Stress drop was observed after yielding until fracture. This is because the covalent bond strength is much greater than the strength of the intermolecular Van der Waals forces holding adjacent molecules together. Also, for the same reason, the characteristic failure mode for OPP samples for various draw ratios was fracture along the axial direction due to the highly fibrous structure that exists in the oriented samples parallel to the extrusion direction. These observations are similar to those reported by other investigators for PE and PP produced by die drawing and have been subjected to tensile tests [Bekhet et al., 1993].

6.2 Axial Feed Hot Oil Tube Forming (AF-HOTF)

6.2.1 Effect of Process Parameters

The advantage of the AF-HOTF system that was developed as part of this research was primarily in terms of continuous measurement of strain and bulge height during the test. The process was easily observed at different forming stages by incorporating an on-line optical strain measurement system for continuous strain measurements during the forming process.

Preparation of tube samples prior to AF-HOTF experiment plays an important role. The inner edge of the tube was carefully chamfered for good sealing between the tube ends and the outer surface of the plugs to prevent an oil pressure drop, which consequently contributed to accurate pressure readings as well as reproducible part shapes under identical test conditions.

To understand the effects of forming process parameters on the forming performance of polypropylene tubes, several tubes were tested and the results were shown in Figures 5.17 and 5.18. Forming temperature is the single most important factor in the hot forming of OPP tubes. Bulge tests with different diameter tubes at stress relaxation temperature of 120°C and with no axial-feed resulted in early onset of bursting with poor expansion. On the other hand, tubes bulged at temperature between 150°C-160°C with axial-feed resulted in higher expansion, reduced the bulge pressure and delayed bursting and thinning (refer to Table 5.2). The magnitude of axial feed and pressure needed to form the tube is dependent on forming temperature. Solid phase forming of polypropylene is carried out below the crystalline melting point, the forming force varies greatly within the narrow recommended process window which covers a temperature range of only 10°C (refer to Figure 2.10). When forming is performed at temperatures towards the lower end of solid phase range, a higher degree of orientation could be achieved with improved transparency. However, forming at the higher end of the temperature range (close to melting point) led to a more uniform distribution of wall

thickness in the present work. Others have reported similar effects of temperature for polypropylene [Maier and Calafut, 1998].

The temperature variation along the tube also affected the bulge prolife, a uniform temperature along the tube resulted in a uniform bulge (refer to Figure 5.18). In sheet thermoforming, the upper limit of sheet thickness for effective one side heating is about 1 mm [Maier and Calafut, 1998]. For forming quality and consistency, the variation in temperatures in AF-HOTF was minimized to within ± 1°C throughout the thickness of the tube by heating the tube from both sides (i.e., inner and outer surfaces of the tube).

Another important factor affecting the bulge height and forming limit is the amount of axial-feed during forming (refer to Figures 5.22 and 5.34). The bulge profile of the formed tubes was improved, higher expansion, and delayed bursting occurred as a result of increase axial-feed. This is because more material was fed into the expansion zone to reduce the severity of deformation. Without axial-feed bursting failure occurred early, while excessive of axial-feed resulted in folding failure (refer to Figure 5.23). This is consistent with our knowledge of room temperature tube hydroforming.

Figure 6.1 shows relationship between pressure and axial-feed, measured from the middle of bulging tubes produced with a draw ratio of DR = 6.3 and a forming temperature of 150°C. These different combinations of pressure and axial-feed led to three different zones (bursting, safe (uniform bulge), and folding). Bulge at high pressure

rate resulted in burst with poor expansion (burst zone). For uniform bulge, a combination of pressure rate and axial-feed was required, a continuous increase in internal pressure with axial-feed during bulge test kept the tube stable and avoided folding. On the other hand, an increase in axial-feed simultaneously with inadequate internal pressure resulted in poor expansion and non-uniform bulging (fold zone). In Figure 6.1, the data points shown correspond to discrete values of pressure and axial feed from several continuous tests while observing the surface of the bulging tube with the on-line Aramis system for burst, safe and fold characteristics of the tube. The demarkated zones and the errors associated with the individual data points thus correspond to the frequency at which the images were recorded during the test. A diagrammatic representation, such as in Figure 6.1, is useful in establishing process 'window' for axial feed forming of OPP tubes.

For a better understanding the effect of process parameters on bulge profile, a series of bulging tests were conducted at a forming temperature of 150°C. All process parameters were held constant during the bulge tests except for the pressure rate (refer to tests A-D in Figure 5.27). A uniform bulge required a balance of axial-feed and pressure rate. On the other hand, excessive pressure rate led to bursting because of severe deformation in the bulge zone. Inadequate pressure rate led to folding failure as the internal pressure was not sufficient to maintain the tube from folding with increased axial-feed. The other series of specimens (E-H) were bulged at different axial-feeds but at the same pressure rate up to bursting (refer to Figure 5.28). Bursting pressure was

delayed as a result of increase in axial-feed. As more material was fed into the expansion zone, a continuous uniform bulging of the tube and a delayed burst was observed.

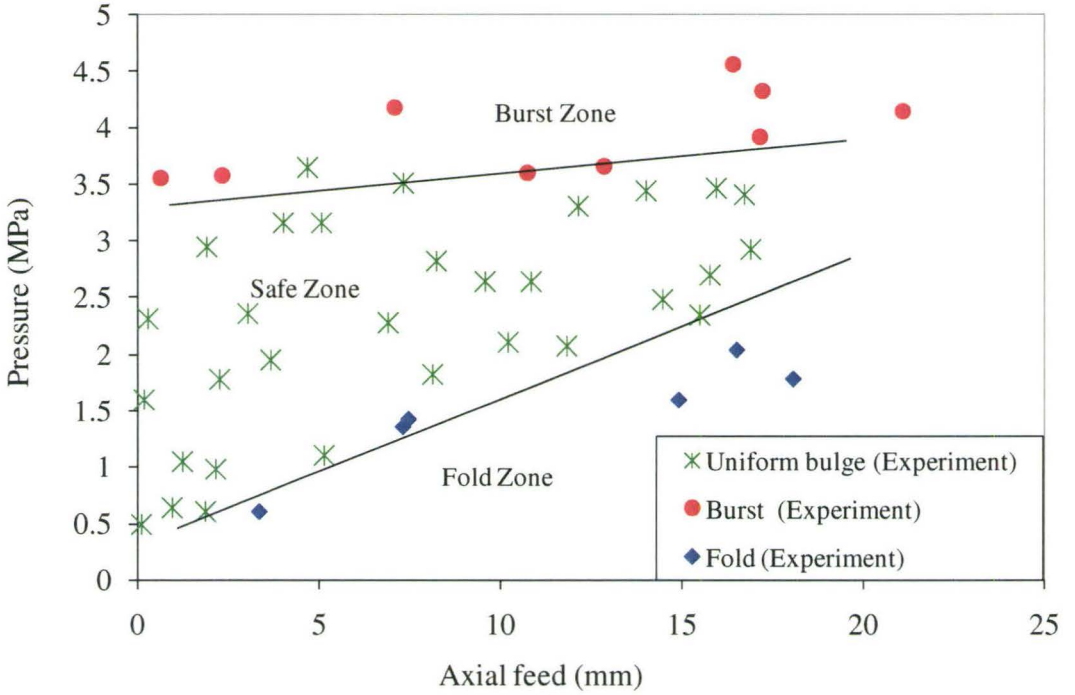

Figure 6.1 Experimental results show three different zones (bursting, safe and folding zones) after a combined of pressure rate and axial-feed were applied and instantaneously measured from the middle of bulging tubes produced with a draw ratio of DR = 6.3 and a forming temperature of 150°C.

An existing analytical model of tube forming was utilized to gain insight into the effect of material properties on bursting pressure during tube bulging. Critical internal pressure as a function of axial-feed was calculated from equations (5.1-5.6 in Chapter 5) and depicted in Figures (5.31-5.33). Forming window, which refers to the safe zone that falls under the bursting failure curve, was increased with increasing anisotropic parameter R. It can be explained by the fact that a large R-value makes the material easy to deform in the hoop direction compared with the thickness direction, these improving formability.

The effect of strain hardening exponent (n) on burst pressure (forming window) could be explained simply by considering its effect on hoop stress. The hoop stress decreases with an increase in n-value (a typical value of n in the present work was 0.17, Table B.1, Appendix B) for a hoop strain in the range below unity. Therefore, one would expect a lower value of burst pressure at higher value of n. In reality, the effect of deformation induced heating will also cause a reduction in the burst pressure [Schang et al., 1996]. This is clearly not included in the model. Similarly, based on power low, effective stress increases with increasing strength coefficient (K) by implying that the material is becoming stronger and needs a higher pressure to burst, results in an increased safe zone (refer to Figure 5.33).

The existing analytical model for axial feed tube hydroforming was used to predict bursting pressure and forming limit for oriented thermoplastic tubes based on a diffuse necking criterion. This model in the present work is a strain rate and temperature independent model. For this reason, the material properties, i.e. K, n and R used in the analytical model were obtained from mechanical tensile tests conducted at 150°C (refer to Appendix A). Also, experimental bulge tubes tests were also conducted at 150°C for a comparison with the results from analytical model. Strain rates (dependent upon the cross-head velocity in a uniaxial tension test used for determining material parameters for the model) could be kept only approximately close to the AF-HOTF tests. However, a comparison between analytical prediction and experimental results from the AF-HOTF tests (refer to Figures 5.34 and 5.35) were found to be in good general agreement.

6.2.2 Morphological Changes and Orientation Factors

As discussed earlier, the spherulite structure of the melt extruded billet was transformed into the fibrillar structure in the solid state extruded OPP tubes (see Figure 6.2), used later in hot forming tests. The monoclinic α-form was found in all bulge specimens. This was found in all solid state extrusion specimens at different draw ratios (refer to Figure 5.7). The (110) and (040) pole figures of the extruded polypropylene tube (DR=6.3) (refer to Figure 5.8) are dominated by the uniaxial c-axis orientation, the c-axis of the monoclinic unit cell is parallel to ED and a- and b-axis are randomly distributed in the TD–ND plane. The pole figures of the bulge samples with no axial-feed (refer to Figure 5.36) show that the width of the b-axis orientation distribution increased significantly, this is because the chain axis that corresponds to the c-axis orientation in the extrusion direction moved in the ED-ND plane, as a result of bulge tube being under internal pressure only. However, with an increase in axial-feed, the b-axis orientation distributed in an even broader band in ED-TD plane, and is more intensity concentrated in the transverse direction. The combination of axial feed and internal pressure rotates the b-axis of crystallites from being randomly distributed in the ND-TD plane to the transverse direction.

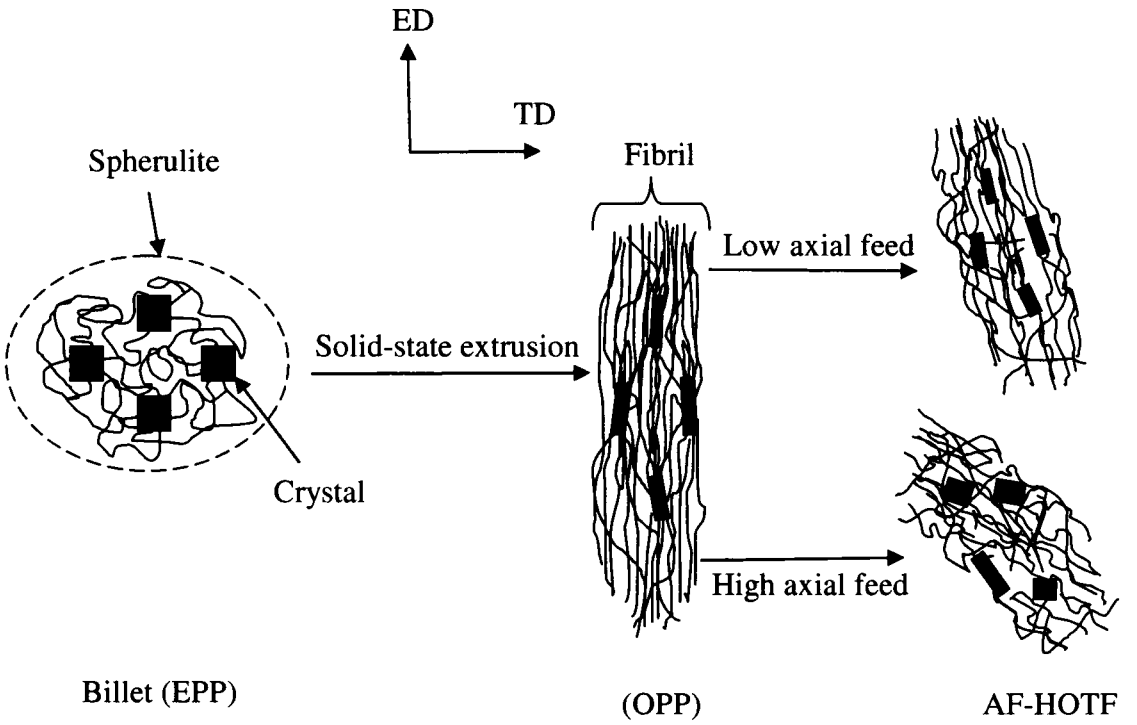

Figure 6.2 Schematic of microstructure change by Solid-state extrusion and AF-HOTF.

Significant differences in orientation factor for bulge tube compared to the extruded tube were observed (refer to Figure 5.40). Biaxial orientation factor represented by White and Spruiell triangle shows that with an increase in axial feed the chain axis reorients from the positive uniaxial direction towards the negative biaxial direction and lies between the planar strain state and the equal biaxial strain state. The negative biaxial orientation factors result from the compression axial feed that is applied continuously at the tube ends during AF-HOTF test. These changes are schematically presented in Figure

6.2 based on the results form pole figures (refer to Figure 5.37) and Biaxial orientation factor (refer to Figure 5.40).

The effect of axial feed and draw ratio on the orientation factors of the extruded and the bulged samples were earlier plotted in Figures 5.39 and 5.40. At origin, the orientation factor for c-axis is zero (for a random billet sample), with increase draw ratio the orientation factor is increased. This is because more molecular chains are oriented in the extrusion direction during solid state extrusion. Both a-axis and b-axis have the same trend and show a perpendicular orientation to the c-axis as shown in the monoclinic crystal system (refer to Figure 5.38). For bulge samples, Figure 5.40, the c-axis started at a high orientation factor, parallel to the extrusion direction (extruded tube at DR=6.3), and decreased with an increase in axial feed (also refer to Figure 5.42a). This trend shows reorientation of the c-axis away from the extrusion direction towards the transverse direction (refer to Figure 5.42b).

The orientation distribution function (ODF) for the extruded and bulged tubes in 3D using the Multex Area 2 software, show that the full width half maximum (b^c) increased with an increase in axial feed (refer to Figure 5.45), indicating that the polymer chains were reoriented transverse to the extrusion direction, i.e. towards the ND-TD plane. These are in agreement with the pole figures and the orientation factors that were calculated earlier by GADDS software (refer to Figure 5.37 and 5.42).

In post-forming, the uniaxial stress-strain curve in the extrusion direction for extruded and bulged tube with no axial-feed (refer to Figure 5.50) exhibited the same deformation behaviour and both samples failed in a brittle manner. This is because the fibers in both samples were still oriented in the extrusion direction and they had nearly the same orientation factor as shown in Figure 5.39. As the axial-feed increased, the stress-strain curve exhibited increases in strain hardening in the plastic region up to fracture. This suggests that the sample with higher axial-feed exhibited more chain reorientation in ED-TD. These chains were reoriented in the load direction (ED) during the tensile test, and this resulted in higher strength and increased elongation at break. The stress-strain curve for extruded and bulged samples in the hoop direction exhibited the same trend compared to the samples from the axial direction, with reduced strength and elongation at break. A high strength in the extrusion direction is due to the presence of covalent bond with much greater strength than the intermolecular Van der Waals forces holding adjacent molecules together. This explains improvement in strength of the bulge tube samples in hoop direction (refer to Figure 5.51) which had more chains orientated in the biaxial direction.

6.2.3 Fracture Mode

It is interesting to note that all fracture modes in tensile test, for extruded and bulged samples in axial direction, are parallel to ED-TD plane (refer to Figures 5.13, 5.14 and 5.48), in agreement with the preferred slip systems. Also, the fracture mode in the

bulge tests always occurred parallel to the tube axis because of large hoop stress, as shown in Figure 5.21. Another interesting observation is that crazing occurred followed by fracture along the thickness direction in extruded and bulged samples tested in the hoop direction, as shown in Figure 5.49. Therefore, fracture modes of all extruded and bulge samples are parallel to the chain slip direction, a consequence of crystallographic slip processes in preferred slip systems. In the monoclinic α-structure, the easiest slip systems, whose slip direction is along the c-axis, are (010) [001] and (110) [001] with respect to the extrusion direction [Aboulfaraj, et al., 1995, Lupke, et al., 2004].

6.3 Axial Feed Hot Gas Tube Forming (AF-HGTF) Results

6.3.1 Effect of Process Parameters and Cooling Rate

A combined effect of cooling time and pressure release rate on overall tube shape after forming in a closed die (AF-HGTF system) was studied. Several tests were conducted with the same process parameters, such as pre-heating time, forming temperature, injection pressure rate and axial feed. A high pressure release rate for tubes formed above 80°C resulted in poor shape of formed part (refer to Figure 5.64a and 5.64b left). This is because the material at that temperature is not strong enough and still flexible, and the quick release pressure worked as a negative pressure on the inner surface of the tube led to suction the wall inside the tube. On the other hand, good quality parts

with uniform thickness that filled the entire die cavity were produced when pressure was released more slowly to maintain the shape of formed part.

6.4 Biaxial Ball Stretching Test (BBST)

Polypropylene tubes were subjected to biaxial tension in a new BBST system, with no axial end feeding to obtain strain paths closer to the equal biaxial strain path, at various temperatures. The strains paths for the melt-extruded tube samples EPP (refer to Figure 5.56) remain close to the balanced biaxial strain state up to major and minor strains of about 0.07 and then deviate slightly towards the plane strain state. The deviation is more significant at 170°C as the material softens considerably due to its proximity to its melting point. The OPP samples, tested at 150°C and 160°C, show axial cracks only after a minor strain of about 0.02 and 0.07 respectively (see Figure 5.57). Also, a deviation from balanced biaxial strain state occurs right at the start of the test. The axial strain in OPP samples has a maximum value of only 4 % at 170°C because the fibrils in axial direction are very strong resulting in a slower expansion in this direction compared with hoop direction (see Figure 6.3). As the tube start to sink in the hoop direction at 170°C (refer to Figure 6.4), more material was fed in hoop direction to the bulge area resulting in a higher expansion in hoop direction up to 23 %. The effect of tube sinking on the strain path at the temperature of 170°C was clearly noticed in the curves for 12 % and 23 % of hoop strains (refer to Figure 5.57).

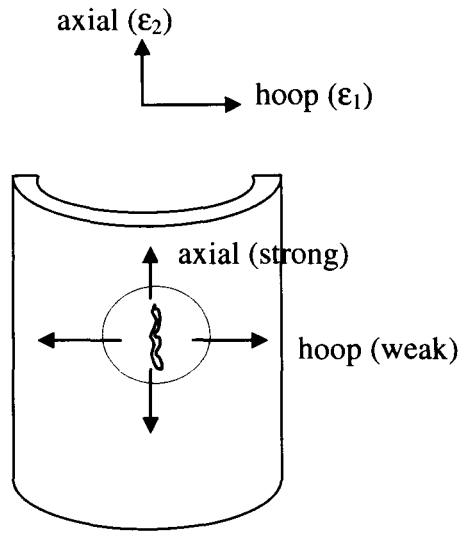

Figure 6.3 Schematic of OPP tube fractured parallel to the axial direction by BBST.

White–Spruiell biaxial orientation factor for the starting melt extruded billet sample is located at the origin. The orientation factor of BBST billet tube samples move toward equal biaxial strain state (see Figure 5.62), while the orientation factor for the BBST billet tube sample at 170°C moves in the extrusion direction only. Again, this is because the material softens considerably due to its proximity to its melting point and the material starts to sink in transverse direction resulting in uniaxial orientation (ED). This phenomenon of material softening or sagging has been observed in sheet thermoforming as well [Maier, and Calafut, 1998]. Sagging is often countered by tensioning the sheet in commercial practice. Some systems are equipped with independent edge heating zones to compensate for heat sink effect.

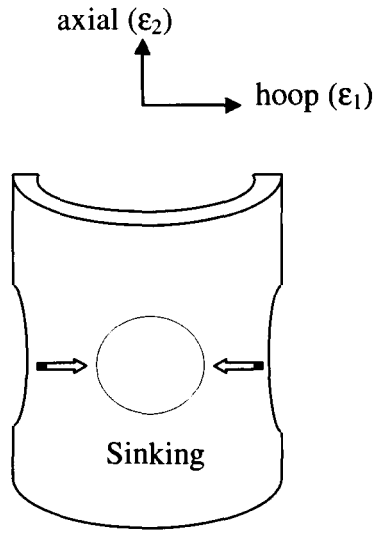

Figure 6.4 Schematic of tube sink in the hoop direction for BBST samples at 170°C.

The development of biaxial orientation factors in BBST billet tube (EPP) was different for OPP tube (see Figure 5.62). This is because the starting material structure was different as shown above in Figure 6.2. In the case of EPP, the strain history of these samples consists of melt extrusion followed by BBST process. The samples are randomly oriented after melt extrusion and therefore start at the origin in White-Spruiell diagram. The Spherulite structure slightly oriented toward equal biaxial direction as schematically presented in Figure 6.5 based on the results form the X-ray diffraction patterns (refer to Figure 5.58), pole figures (refer to Figure 5.60) and Biaxial orientation factor (refer to Figure 5.62). The orientation factor of BBST billet tube samples move toward equal biaxial with increase forming temperature, except at 170°C where material sinking reorient the material in the extrusion direction. For the OPP, the strain history of these

samples consists of solid-state extrusion followed by BBST process. The OPP samples start at a high orientation factor, parallel to the extrusion direction, and are reoriented by BBST, away from extrusion direction and towards the transverse direction (parallel to the equal biaxial direction). A Schematic of microstructure change by BBST for OPP tube (refer to Figure 6.6) show a highly fibrils still alignment together parallel to the equal biaxial direction. This is because the starting tube material was highly oriented in extrusion direction (DR=6.3), these are in agreement with the results from the X-ray diffraction patterns (refer to Figure 5.59) and pole figures (refer to Figure 5.61)

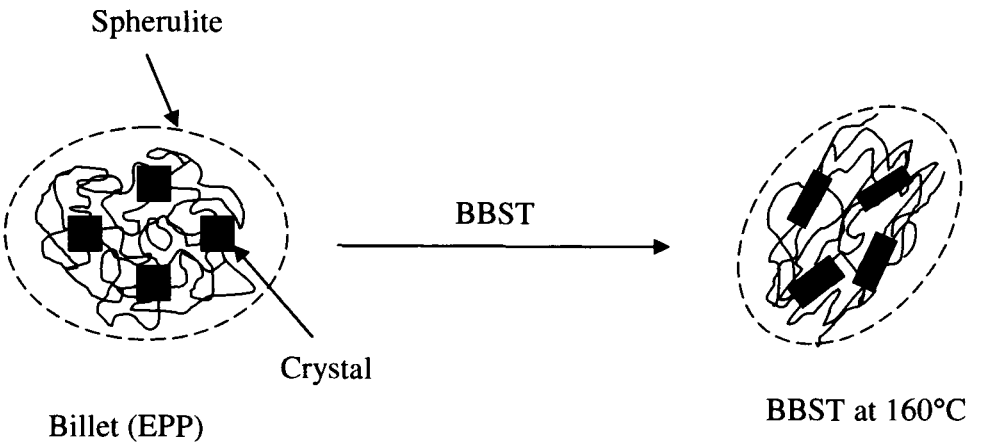

Figure 6.5 Schematic of microstructure change by BBST for billet (EPP) tube.

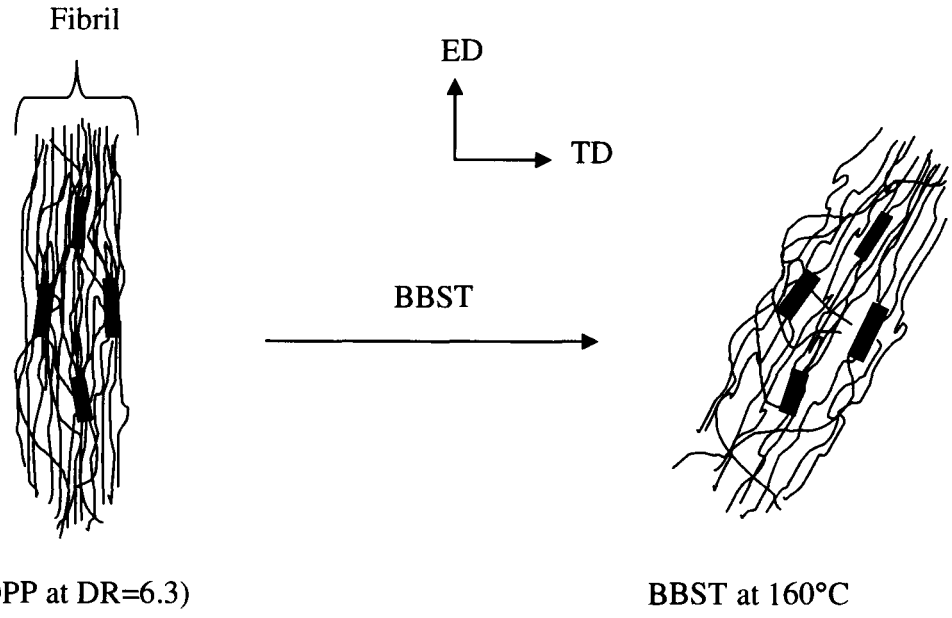

Figure 6.6 Schematic of microstructure change by BBST for OPP tube.

6.5 Error Analysis

Experimental errors can arise from several sources. As a sample cut down for X-ray experiments by using rotary steel cutter with cooling water, it is possible that a small amount of increase in temperature will occur and will influence the microstructure. For this reason the investigation of material heating due to cutting were done in Chapter 3 (refer to section 3.5). The results showed that the cut material did not exhibit a significant change in the microstructure and the maximum standard error for the percent of crystallinity was 1.2%. A further source of inaccuracy may arise from the analysis of experimental data (for example, selection of measurement point in the bulge area or

determination of boundaries of the crystalline and amorphous regions in X-ray frames). All data collected from X-ray experiments were analyzed based on two strong diffracting planes, (110) and (040), both were parallel to the c-axis. The Herman's orientation factors in uniaxial direction (extrusion samples) were directly calculated from (110) or (040) plane by using Gadds software, where each specimen was run 3 times under the same conditions. The maximum standard errors were 1.3% and 2.7% for orientation factors as observed in Figures 5.9 and 5.12 respectively. Also percent of crystallinity have a maximum standard errors of 1% (refer to Figure 5.10) and 3.4% (refer to Figure 5.11). The biaxial orientation factors were calculated from both planes (110) and (040) using Wilchinsky equation (refer to Equation 2.4). The biaxial orientation factors, plotted in White and Spruiell triangle for AF-HOTF samples (refer to Figure 5.40-5.42), have a maximum standard error of 2% and for BBST samples (refer to Figure 5.62), have a maximum standard error of 2.5%. The lower error levels associated with X-ray measurements suggest that the results obtained are accurate.

Chapter 7

Conclusions and Recommendations

7.1 Conclusions

The objectives of this study as stated in Chapter 1 were:

1. Assessment of the relationship between the most significant solid-state extrusion process parameters and the resulting microstructure of the tube. This objective will also include investigation of the effect of these parameters on microstructural changes through the tube thickness and mechanical properties in the longitudinal and transverse directions.
2. Development of the axial feed hot forming process for oriented polypropylene tube up to fracture under different forming conditions in order to establish the relationship between the hot forming process parameters, microstructure parameter (molecular orientation), and biaxial limit strains.
3. Structure-property relationships from tube formed under optimized conditions: Based on results from objectives (1) and (2), an optimum tube from the extrusion process and tube hot forming process will be subjected to various biaxial strain states up to large strains and possibly fracture. The changes in the microstructure

and onset of instability and fracture as a function of strain path (or strain state) and strain-value will be experimentally assessed to establish formability characteristic of oriented polypropylene (OPP) tubes.

With respect to objective # 1, the following conclusions can be drawn:

- PP tubes made from solid-state extrusion have a unidirectional orientation of the polymer molecules (fibrils had a size of 200nm-500nm) and provide improvements in the mechanical property along the extrusion direction. In the transverse (hoop) direction the strength of the intermolecular Van der Waals forces holding adjacent molecules together is much weaker than covalent bonding in the extrusion direction.
- Tensile test results at room temperature show that the yield strength and elastic modulus along the extrusion direction is increased by 50% at draw ratio (DR=6.3) and test speed 20 mm/min.
- The structure of the extruded samples at draw ratio 5 and higher was completely changed from spherulitic to an oriented structure (fibrils). The chain axis of all extruded samples is aligned parallel to the extrusion direction.
- The orientation and the crystallinity changes from the inner to the outer layer, through the thickness, of the extruded tubes are relatively small. However, the estimate of crystallinity increases from 47% to 68% with an increase in draw ratio.

With respect to objective # 2, the following conclusions can be drawn:

- Two tube hot forming test systems based on axial feed considerations have been designed, fabricated and tested for studying the effect of various process parameters such as axial feed, forming temperature and pressure rate on microstructural and mechanical property and formability of extruded PP tubes.
- Mechanical and microstructural characteristics from the axial feed hot forming process AF-HOTF for oriented PP tube have been examined. An increase in axial feed during the hot forming process of the OPP tube resulted in a higher formability (bulge height) and delayed failure (thinning and/or bursting).
- A series of polypropylene tubes were free bulged with different loading paths of axial feed and internal pressure at forming temperature of 150 °C up to fracture and has been compared with the analytical predictions bulge window and forming limit based on plastic instability. The bursting prediction shows good agreement with the experimental results.
- The FLD for the AF-HOTF process is in the left side and lies between uniaxial tension and pure shear. The limit strain was improved by increase axial feed up to 18mm with limit strains values of 0.55 major strain and -0.25 minor strain.
- Limitations of AF-HOTF process are:
    - The maximum forming temperature is 170°C.
    - The maximum forming pressure is 20 MPa.

- ARAMIS system could not measure strains for tubes bulged at higher axial-feed (greater than 23 mm).

With respect to objective # 3, the following conclusions can be drawn:

- Three different hot forming processes (Solid-state extrusion, AF-HOTF and BBST) were used for studying and investigating the effect of these processes on the orientation of PP tubes.
- A quantitative study of structure-property-process was presented with the change of preferred orientation for PP billet, extruded and bulged tubes with different load paths.
- The orientation factors for the bulge samples lie between the planar strain state and the equal biaxial strain state close to planar strain. These orientations are effected by two processes, the uniaxial orientation (i.e., solid state extrusion) and axial feed (AF-HOTF) resulting in different biaxial orientation factors from polypropylene blown film.
- On-line strain measurements from room temperature uniaxial tensile tests, show that failure of the fibers occurs at strains between 0.06-0.08 in the samples obtained from tubes bulged without end feed. On the other hand, with increasing axial feed the material exhibits higher failure in both axial and hoop directions as well as enhanced stiffness and toughness.

- A novel biaxial ball stretching test (BBST) to evaluate formability and to determine the biaxial strain path of tubular materials has been developed has been designed and tested. The test rig and the experimental methodology enabled an assessment of high temperature forming behaviour of two different variants of PP tubes.
- The development of biaxial orientation factors after BBST tests on OPP and billet tube samples are different from the extruded samples and AF-HOTF samples. This suggests that the microstructure of the formed PP tubes is strongly dependent on the starting material structure and the forming process.

7.2 Recommendations

Based on the discussion presented in this chapter and the previous chapters, further studies are required. The following topics are recommended for further study:

- This study is focused on structure-property-process relationships during AF-HOTF and other hot forming processes for oriented polypropylene (OPP) only. Other semi-crystalline materials like polyethylene and PVC should be studied to see if the experimental trends observed in the present work will also hold for other similar materials. This would allow for better understanding of the deformation and forming behaviour of semi-crystalline materials in general.

- In the present work, a rather narrow range of draw ratios (4.5-6.3) were utilized. It would be useful to explore a wider range of draw ratios and their effect on forming limits.
- The present experiments revealed significant shrinkage of solid state extruded tubes during preheating prior to bulging experiments. The phenomena of shrinkage should be further studied for its effect on preheating within a wide range of temperatures close to the melting point.
- A strain rate and temperature dependent analytical model for prediction of formability of OPP tube would be more useful as it can help with process design and material section for a real part. This should be developed.
- The present results revealed that the OPP tube exhibited rather poor stretchability in the hoop direction. A more isotropic solid-state extruded tube material (i.e., tubes oriented biaxially instead of uniaxial direction) should be explored with a similar experimental methodology to see if a better, i.e. stronger and more formable, tube component can be made from the AF-HOTF and AF-HGTF processes.

References

Aboulfaraj M., G'Sell C., Ulrich B. and Dahoun A., *In situ observation of the plastic deformation of polypropylene spherulites under uniaxial tension and simple shear in the scanning electron microscope*, Polymer, 36: 731-742, 1995.

Ajji A., Legros N., And Dumoulin M. M., *High Performance Materials from Oriented Plastics*, Advanced Performance Materials, 5: 117–136, 1998.

Alexander L. E., *X-Ray Diffraction Methods in Polymer Science*. Wiley Interscience: New York. Page 241, 1969.

Asnafi N., *Analytical modeling of tube hydroforming*, Thin Walled Structures, 34: 295-330, 1999.

Asnafi N., and Skogsgardh A., *Theoretical and experimental analysis of stroke-controlled tube hydroforming*, Materials Science and Engineering, A279: 95–110, 2000.

Azhikannickal E., Jain M., and Bruhis M., *Test methods for the determination of the stress–strain behaviour of oriented polypropylene (OPP) tubes in uniaxial compression*, Polymer Testing, 26: 195–201, 2007.

Azhikannickal E., Jain M., and Bruhis M., *Macroscopic yielding of oriented polypropylene (OPP) tubes at elevated temperatures*, International Journal of Mechanical Sciences, 50: 1065–1074, 2008.

Bartczak Z., Morawiec J., Galeski A., *Structure and Properties of Isotactic Polypropylene Oriented by Rolling with Side Constraints*, Journal of Applied Polymer Science, 86: 1413–1425, 2002.

Bekhet N. E., Barton D. C., and Craggs G., *The uniaxial behavior of highly-oriented polymers*. Processing of Advanced Materials, 3: 199–207, 1993.

Bhattacharyya D., Bowis M., and Jayaraman K., *Thermoforming woodfibre–polypropylene composite sheets*. Composites Science and Technology, 63: 353–365, 2003.

Bigg D. M., *Review of Techniques For Processing Ultra-High Modulus Polymers*, Polym. Eng. Sci., 16: 725, 1976.

Bigg D. M., Epstein M. M., Fiorentino R. J., and Smith E. G., *Warm Hydrostatic Extrusion of Polyethylene*, Polym. Eng. Sci., 18: 908, 1978.

Bigg D. M. and M. M. Epstein, R. J. Fiorentino, and E. G. Smith, *Continuous Extrusion of High-Modulus Semi-crystalline Polymers*, J. Appl. Polym. Sci., 26: 395-409, 1981.

Bower D. I., *An Introduction to Polymer physics*. Cambridge, United Kingdom. Page 312, 2002.

Bruker AXS, Inc., *Multex Area 2 User Manual*, Version 2, Madison, Wisconsin, USA, 2006.

Brunet M., Boumaiza S., and Nefussi G., *Unified failure analysis for tubular hydroforming*. Journal of Materials Processing Technology, 148: 269–277, 2004.

Brusselle-Dupend N., Lai D., Feaugas X., Guigon M., and Clavel M., *Mechanical Behavior of a Semicrystalline Polymer Before Necking. Part I: Characterization of Uniaxial Behavior*, Polymer Engineering and Science, 41: 66 -76, 2001.

Cakmak M. and Lee S. W., *Molecular mechanism of neck formation in uniaxially stretched poly (ethylene naphthalate) films*. Polymer, 36: 4039-4054, 1995.

Campbell D., and White J. R., *Polymer Characterization*, Physical Techniques. Champman and Hall. Page 184, 1989.

Callister Jr. William D., *Material Science and Engineering: an Introduction*, John Wiley & Sons, Inc., 2007.

Capaccio G. and Ward I. M., *Preparation of Ultra-High Modulus Linear Polyethylene; Effect of Molecular weight and Molecular weight Distribution on Drawing Behavior and Mechanical Properties*, Polymer, 15: 233, 1974.

Carleer B., van der Kevie G., de Winter L., van Veldhuizen B. *Analysis of the effect of material properties on the hydroforming process of tubes*, Journal of Materials Processing Technology, 104: 158–66, 2000.

Chen H. Y., Bishop M. T., Landes B. G., and Chum S. P., *Orientation and Property Correlations for LLDPE Blown Films*, Journal of Applied Polymer Science, 101: 898–907, 2006.

Choi D. and White J. L., *Crystal Structures and Orientation Development in Tubular Film Extrusion of Syndiotactic Polypropylene and Isotactic Polypropylene*. Pol. Eng. Sci., 41: 1743-1751, 2001.

Chow C. L., and Yang X. J., *Bursting for fixed tubular and restrained hydroforming*. Journal of Materials Processing Technology, 130-31: 107–114, 2002.

Chu E., and Xu Y., *Hydroforming of aluminum extrusion tubes for automotive applications. Part I: buckling, wrinkling and bursting analyses of aluminum tubes*, International Journal of Mechanical Sciences, 46: 263-283, 2004.

Coates P. D., Gibson A. G., and Ward I. M., *An analysis of the Mechanics of Solid Phase Extrusion of Polymers*, J. Mater. Sci., 15: 359, 1980.

Coulon G., Castelein G., and G'Sell C., *Scanning force Mechanisms microscopic investigation of plasticity and damage in polypropylene spherulites under simple shear*, Polymer, 40: 95-110, 1998.

Cullity B. D., and Stock S. R., *Elements of X-ray Diffraction*. Prentice-Hall, Inc., 2001.

Dasari A., and Misra R. D. K., *On the strain rate sensitivity of high density polyethylene and Polypropylenes*. Materials Science and Engineering, A358: 356-371, 2003.

Dasari A., Rohrmann J., Misra R. D. K., *Surface microstructural modification and fracture behavior of tensile deformed polypropylene with different percentage crystallinity*, Materials Science and Engineering, A360: 237-248, 2003.

Dasari A., Rohrmann J., and Misra R. D. K., *Microstructural evolution during tensile deformation of polypropylenes*. Materials Science and Engineering: A, 351: 200-213, 2003.

Davies R., Grant G., Herling D., Smith M., Evert B., Nykerk S., and Shoup J., *Formability investigation of aluminium extrusions under hydroforming conditions*. SAE Transactions, 109: 950-958, 2000.

Drozda T., Mitchell P. E., Wick C., and Benedict J. T., *Tool and Manufacturing Engineers Handbook: Plastic part manufacturing,* Edition: 4, Society of Manufacturing Engineers, page 2-18, 1996.

Elnagmi M., and Jain M., *Structure-property-process relationships during extrusion and thermoforming of polypropylene tubes*, 21st Canadian Congress of Applied Mechanics, Ryerson University, Toronto, Canada, June 3-7, 2007.

Elnagmi M., Bruhis M., and Jain M., *Axial-Feed Thermoforming of Oriented Polypropylene Tubes*, Polymer Engineering and Science, 49: 514–522, 2009.

Elnagmi M., Bruhis M., and Jain M., *A Method for Biaxial Dome Stretching of Thermoplastic Tubes at High Temperatures*, 22st Canadian Congress of Applied Mechanics, Dalhousie University, Halifax, Nova Scotia, Canada. May 31st - June 4, 2009.

Elnagmi M., Jain M., and Britten J. F., *Orientation Development in Solid-state Extrusion and Hot Forming of Polypropylene tubes.* Manuscript under preparation for journal submission.

Gamez-perez J., Munoz P., Velasco J. I., Martinez A. B., and Maspoch M. LL. *Determination of Essential Work of Fracture in EPBC Sheets Obtained by Different Transformation Processes,* Journal of Materials Science, 40: 1967-1974, 2005.

Gavrilidou G., and Jain M., *FEA and Multivariate Statistical Data Analysis of Polypropylene Tube Forming Process*. NUMISHEET 2005: Proceedings of the 6th International Conference and Workshop on Numerical Simulation of 3D Sheet Metal Forming Process., 778: 162-166, 2005.

Germain Y., *Burst Pressure Prediction of Polyamide Pipes*. Pol. Eng. Sci., 38: 657-661, 1998.

Gibson A. G. and Ward I. M., *Hydrostatic Extrusion of Linear Polyethylene: Effects of Molecular Weight and Product Diameter*, J. Appl. Polym. Sci. Polym. Phys. Ed., 16: 2015-2030, 1978.

Gibson A. G., Ward I. M., Cole B. N. and Parsons B., *Hydrostatic Extrusion of Linear Polyethylene*, J. Mater. Sci., 9: 1193, 1974.

Goodwin G. M., *Application of Strain Analysis to Sheet Metal Forming Problems in the Press Shop*, SAE Transactions, No. 680093, 1968.

Hill R., *The mathematical theory of plasticity*, Oxford University Press: Oxford, 1983.

Hua-Shan T., Sheng-Cheng C., and Wan-Shan S., *Investigation of the Derived Fuel Rod Formation from Auto Shredder Residue Using an Extrusion Apparatus,* Environmental Progress, 25: 335-342, 2006.

Imada K., Yamamoto T., Shigematsu K., and Takayanagi M., *Crystal Orientation and Some Properties of Solid-state Extrudate of Linear Polyethylene*, J. Mater. Sci., 6: 537-546, 1971.

Imada K. and Takayanagi M., *Plastic Deformation of High Density Polyethylene in Solid State Extrusion*, Int. J. Polym. Mater., 2: 89, 1973.

Imaninejad M., Subhash G., and Loukus A., *Influence of end-conditions during tube hydroforming of aluminum extrusions*, International Journal of Mechanical Sciences, 46: 1195–1212, 2004.

Kasai N., and Kakudo M., *X-Ray Diffraction by Macromolecules*, Kodansha Ltd. and Springer Berlin Heidelberg, Japan. Page 253, 2005.

Karger-Kocsis J., *Polypropylene: An A-Z Reference*, Kluwer Publishers, Dordrecht, ed. 1999.

Keeler S. P., and Backofen W. A., *Plastic Instability And Fracture In Sheets Stretched Over Rigid Punches*, ASM Trans., 56: 25-48, 1963.

Kim, Y. S., Guo, G., Wang, K. H., Park, C. B. and Maine, F. W., *Processing /Structure /Property Relationships of Stretched PP/Wood-fiber Composites*, CSME Forum, 2004, London, Ontario, June 1-4, 2004.

Kim J., Kang S. J., and Kang B. S., *A prediction of bursting failure in tube hydroforming processes based on ductile fracture criterion.* Int. J. Adv. Manuf. Technol., 22: 357–362, 2003.

Kim J., Kim S-W., Park H. J., and Kang B. S., *A prediction of bursting failure in tube hydroforming process based on plastic instability*, International Journal of Adv. Manuf. Technol., 27:518-524, 2006.

Kinloch A. J., and Young R. J., *Fracture Behaviour of Polymers,*Elsevier Applied Science Publishers LTD, New York, page 120, 1983.

Krishnaswamy R. K., *A Method to Characterize the Biaxial Orientation of the Crystalline Phase in Polyethylene Blown Films*, Journal of Polymer Science: Part B: Polymer Physics, 38: 182–193, 2000.

Krishnaswamy R. K., and Sukhadia A. M., *Orientation characteristics of LLDPE blown films and their implications on Elmendorf tear performance*, Polymer, 41: 9205-9217, 2000.

Kulkarni A., Biswas P., Narasimhan R., Luo A. A., Mishra R. K., Stoughton T. B., Sachdev A. K., *An experimental and numerical study of necking initiation in aluminum alloy tubes during hydroforming* , International Journal of Mechanical Sciences, 46: 1727–1746, 2004.

Legros N., Ajji A., and Dumoulin M. M., *Ram Extrusion of High-Density Polyethylene and Polypropylene in Solid State: Process Conditions and Properties*, Pol. Eng. Sci., 37: 1845-1852, 1997.

Lei L. P., Kim J., and Kang B. S., *Bursting failure prediction in tube hydroforming processes by using rigid–plastic FEM combined with ductile fracture criterion.* International Journal of Mechanical Sciences, 44: 1411–1428, 2002.

Liu G., Edward G., Morphology Distribution of Injection Molded Polypropylene and its Dependence on Processing History, ANTEC 2001, conference proceedings – Society of Plastics Engineers. Pages 613-617, 2001.

Lupke T., Dunger S., Sanze J., and Radusch H.-J., *Sequential biaxial drawing of polypropylene films*. Polymer, 45: 6861–6872, 2004.

Maier C., and Calafut T., *Polypropylene: the definitive user's guide and databook*, Norwich, NY : Plastics Design Library, 1998.

Maspoch M. Ll., Gamez-Perez J., Gimenez E., Santana O. O., and Gordillo A., *Influence of Processing on Ethylene-Propylene Block Copolymers: Structure and Mechanical Behavior*. Journal of Applied Polymer Science, 93: 2866–2878, 2004.

Mears D. R., Pae K. P., and Sauer J. A., *Effects of Hydrostatic Pressure on the Mechanical Behavior of Polyethylene and Polypropylene*, J. Appl. Phys., 40: 4229-4237, 1969.

Mendoza R., Régnier G., Seiler W., Lebrun J. L., *Spatial distribution of molecular orientation in injection molded iPP: influence of processing conditions*, Polymer, 44: 3363–3373, 2003.

Mezghani, K., Phillips, P.J., *The Morphology of the Gamma Form of Isotactic Polypropylene at 200 MPA,* ANTEC 1996, conference proceedings – Society of Plastics Engineers. Pages 1810-1814, 1996.

Mourad H. I., Bekheet N., El-Butch A., Abdel-Latif L., Nafee D., Barton D.C., *The effects of process parameters on the mechanical properties of die drawn polypropylene*, Polymer Testing, 24: 169–180, 2005.

Nakamura K., Imada K., and Takayanagi M., *Analyses of Solid state Extrusion Process of Polymeric Materials by Pressure Dependent yield Criteria*, Int. J. Polym. Mater., 3: 23, 1974.

Nakamura K. and Kanetsuna H., *Hydrostatic extrusion of Solid Polymers*, J. Mater. Sci., 10: 1105, 1975.

Nakamura K. and Kanetsuna H., *Hydrostatic Extrusion under Back Pressure of High-Density Polyethylene*, J. Appl. Polym. Sci., 23: 2543-2554, 1979.

Nakamura K., Imada K., and Takayanagi M., *Solid-state Extrusion of Isotactic Polypropylene Through a Tapered Die, I. Phenomenological Analysis*, Int. J. Polym. Mater., 2: 71, 1972.

Nefussi G., and Combescure A., *Coupled buckling and plastic instability for tube hydroforming*. International Journal of Mechanical Sciences, 44: 899–914, 2002.

Pae K. D. and Mears D. R., *The Effects of High Pressure on Mechanical Behavior and Properties of Polytetrafluoroethyene and Polyethylene*, J. Polym. Sci., B-6: 269, 1968.

Pae K. D., Mears D. R., and Sauer J. A., *Stress-Strain Behavior of Polypropylene under High Pressure*, J. Polym. Sci. Polym. Lett. Ed., 6: 773, 1968.

Parsons B. and Ward I. M., *Production Of oriented Polymers by Hydrostatic Extrusion*, Plast. Rubber Proc. Appl., 2: 215-224, 1982.

Pazur R. J. and Prud'homme R. E., *X-ray Pole Figure and Small Angle Scattering Measurements on Tubular Blown Low-Density Poly(ethylene) Films*, Macromolecules, 29: 119-128, 1996.

Phillips R. A., and Wolkowicz M. D., *Structure and Morphology, Polypropylene Handbook*, reference book (ISBN 3-446-18176-8) – Carl Hanser, Verlag, 1996.

Rauwendaal C., *Polymer Extrusion*, 4th edition, Carl Hanser Verlag, Munich, 2001.

Rhee S., and White J. L., *Investigation of Structure Development in Polyamide 11 and Polyamide 12 Tubular Film Extrusion*, Pol. Eng. Sci., 42: 134-145, 2004.

Rhee S., and White J. L., *Development of Orientation and Mechanical Properties of Extrusion Cast Polyamide 11 Films in Biaxial Stretching Process*, Pol. Eng. Sci., 42: 889- 898, 2004.

Schang O., Billon N., Muracciole J. M., and Fernagut F., *Mechanical Behavior of a Ductile Polyamide 12 During Impact*, Polymer Engineering and Science, 36: 541-550, 1996.

Scheirs J., *Compositional and Failure Analysis of Polymers*, John Wiley & Sons, Ltd. Page 343, 2000.

Schut J., *Die Drawing Makes Plastic Steel*, Plastics Technology, online Article, March 5, 2001.

Shercliff H., and Ashby D. C. M., *Materials Engineering, Science, Processing and Design*, Elsevier, 2007.

Shimomura Y., Spruiell J., and White J., *Orientation Development in the Tubular Film Extrusion of Polypropylene*. J. of Appl. Polym. Sci., 27: 2663-2674, 1982.

Snelling G. R. and Lontz J. F., *Mechanism of Lubricant-Extrusion of Teflon TFE-Tetrafluoroethylene Resins*, J. Appl. Polym.Sci., 3: 257-265, 1960.

Sperling L. H., *Introduction to Physical Polymer Science*, 3rd ed, Wiley and sons, USA, page 489, 2001.

Steger TR., Nielsen LE., J. Appl. Polym. Sci. Phys., 16:613-625, 1978.

Stojanovic Z., Kacarevic-Popovic Z., Galovic S., Milicevic D., and Suljovrujic E., *Crystallinity changes and melting behavior of the uniaxially oriented iPP exposed to high doses of gamma radiation*, Polymer Degradation and Stability, 87: 279-286, 2005.

Sungtae Kim, Youngsuk Kim, *Analytical study for tube hydroforming*, Journal of Materials Processing Technology, 128, 232-239, 2002.

Tang H., and Martin D. C., *Near-surface deformation under scratches in polypropylene blends*. Journal of Materials Science, 38: 803– 815, 2003.

Taraiya A. K. and Ward I. M., *Production and Properties of Biaxially Oriented Polyethylene Tubes*. Journal of Applied Polymer Science, 59: 627-638, 1996.

Ward I. M., Coates P. D., and Dumoulin M. M., *Solid phase processing of polymers*. Hanser Gardner. Pages 70, 266, 2000.

Ward I. M., *Mechanical Properties of Solid Polymers,* 2'nd Ed. Wiley, NY, 1983.

Ward I. M., *Review of recent developments in the processing and properties of oriented polyethylene*, Plast. Rubb. Process. Applic., 19: 7, 1993.

Ward I. M., *Recent Developments in the Science and Technology of High Modulus Flexible Polymers*. Macromol. Symp., 100: 1, 1995.

Weeks N. E. and Porter R. S., *Mechanical Properties of Ultra-Oriented Polyethylene*, J. Polym. Sci., Polym. Phys., 12: 635, 1974.

White J., and Spruiell J., *Specification of Biaxial Orientation in Amorphous and Crystalline Polymers*. Polym. Eng. Sci., 21: 859-868, 1981.

Wilchinsky Z. W., *Recent Developments in the Measurement of Orientation in Polymers by X-ray Diffraction*. Advances in X-ray Analysis, 6: 231-241, 1962.

Xia Z. C., *Failure analysis of tubular hydroforming*. Journal of Engineering Materials and Technology, 123: 423–429, 2001.

Xing H. L., and Makinouchi A., *Numerical analysis and design for tubular hydroforming*. International Journal of Mechanical Sciences, 43: 1009–1026, 2001.

Yang W., Li Z., Xie B., Feng J., Shi W., and Yang M., *Stress-Induced Crystallization of Biaxially Oriented Polypropylene*. Journal of Applied Polymer Science, 89: 686–690, 2003.

Zachariades A. E. and Porter R. S., *Deformation of Plasticized Nylon6 with Ammonia by Solid-state Extrusion*, J. Polym. Sci. Polym. Lett. Ed., 17: 277, 1979.

Appendices

Appendix A

Theoretical Equations for Tube Hydroforming

Equilibrium equations of an element at the middle of the bulged tube which is subjected to internal pressure (p_i) and compressive axial force F can be written [94] as

$$\frac{\sigma_1}{\rho_1}+\frac{\sigma_2}{\rho_2}=\frac{p_i}{t_i} \tag{A.1}$$

And

$$\sigma_2=\frac{p_i\rho_1}{2t_i}-\frac{F}{2\pi\rho_1 t_i} \tag{A.2}$$

where

σ_1, σ_2 are the principal hoop and axial stresses respectively

t_i is the current thickness of the tube

ρ_1 is the radius of the tube along the hoop direction

ρ_2 is the radius of the tube along the axial direction

F is the compressive axial force

From Hill's quadratic yield criterion for anisotropic materials [101]

$$2f(\sigma_{ij}) = F(\sigma_y - \sigma_z)^2 + G(\sigma_z - \sigma_x)^2 + H(\sigma_x - \sigma_y)^2 + 2L\tau_{yz}^2 + 2M\tau_{zz}^2 + 2N\tau_{xy}^2 = 1 \quad \text{(A.3)}$$

where F, G, H, L, M and N are the anisotropy parameters. The last 3 term on the right side of equation A-3 drop out in the absence of shear stresses.

The effective stress in terms of the principal hoop and axial stresses under plane-stress condition and for normal anisotropy case can be written as follows [94]

$$\bar{\sigma} = \sqrt{\sigma_1^2 + \sigma_2^2 - \frac{2R}{R+1}\sigma_1^2\sigma_2^2} \quad \text{(A.4)}$$

and the effective strain increment is given by

$$d\bar{\varepsilon} = \frac{1+R}{\sqrt{1+2R}}\sqrt{d\varepsilon_1^2 + d\varepsilon_2^2 + \frac{2R}{R+1}d\varepsilon_1^2 d\varepsilon_2^2} \quad \text{(A.5)}$$

Specific incremental strain components are expressed as

$$d\varepsilon_1 = \frac{d\bar{\varepsilon}}{\bar{\sigma}}\left[\sigma_1 - \frac{2R}{R+1}\sigma_2\right] \quad \text{(A.6)}$$

$d\varepsilon_1 \rightarrow \varepsilon_1$ (assuming proportional loading path)

$$d\varepsilon_2 = \frac{d\bar{\varepsilon}}{\bar{\sigma}}\left[\sigma_2 - \frac{2R}{R+1}\sigma_1\right] \quad \text{(A.7)}$$

$d\varepsilon_3 = d\varepsilon_t$

where R is the average anisotropy parameter. This parameter is related to F, G and H as follows.

$$R = \frac{H}{G} = \frac{H}{F} \tag{A.8}$$

The parameters F, G and H are assumed to have the following relationships

$$R_0 = \frac{H}{G} \quad , \quad R_{90} = \frac{H}{F} \quad , \quad F = R_0 = \frac{\varepsilon_2}{\varepsilon_3} \quad , \quad G = R_{90} = \frac{\varepsilon_1}{\varepsilon_3} \text{ and} \tag{A.9}$$

$$H = R_0 R_{90}$$

where R_{90} and R_0 are the strain ratios in hoop and axial directions respectively.

Figure A.1 show the uniaxial test setup for hoop direction. The strains ε_1, ε_2 and ε_3 were measured from testing the tube of 5.0 draw ratio in uniaxial tension along the axial and hoop directions at a temperature of 150°C and initial strain rate of .002/sec (See Figures A.2, A.3). Since the hoop direction of oriented tube is much weaker than the axial direction of the tube, also the direction of failure (burst) allows perpendicular on hoop direction. For these reasons, the true stress-strain curve from the ring hoop tension test as shown in Figure A.4 was chosen and used to measure the strain hardening exponent n and the strength coefficient K as illustrated in Figure A.5.

Assuming that the principal stresses maintain constant ratios and directions, the ratio of the strain increments will be fixed

$$\alpha = \frac{\sigma_2}{\sigma_1} \quad , \quad \beta = \frac{d\varepsilon_2}{d\varepsilon_1} \tag{A.10}$$

Equation relating α and β for Hill [1983] is

$$\beta = \frac{d\varepsilon_a}{d\varepsilon_\theta} = \frac{\alpha - (R/(1+R))}{1 - (R/(1+R\alpha))} \tag{A.11}$$

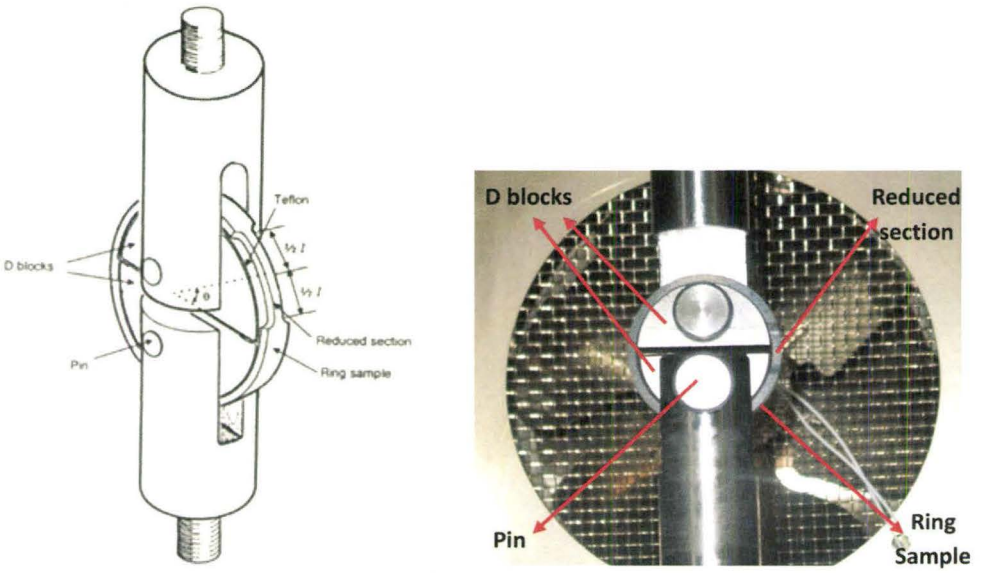

Figure A.1 Tension test in the hoop direction of tube.

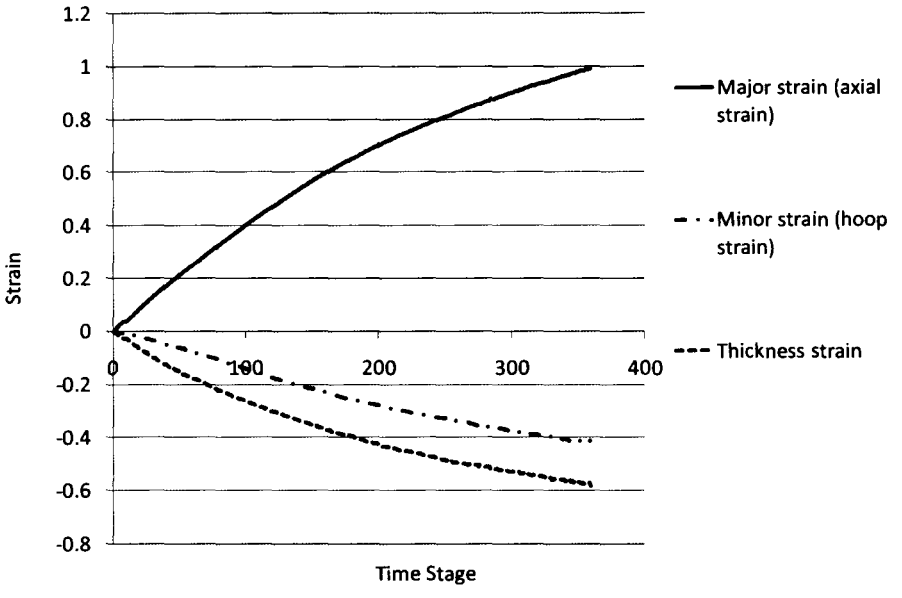

Figure A.2 True strain from tension test in axial direction of tube at 150°C, 0.002/sec and draw ratio (DR= 5.0).

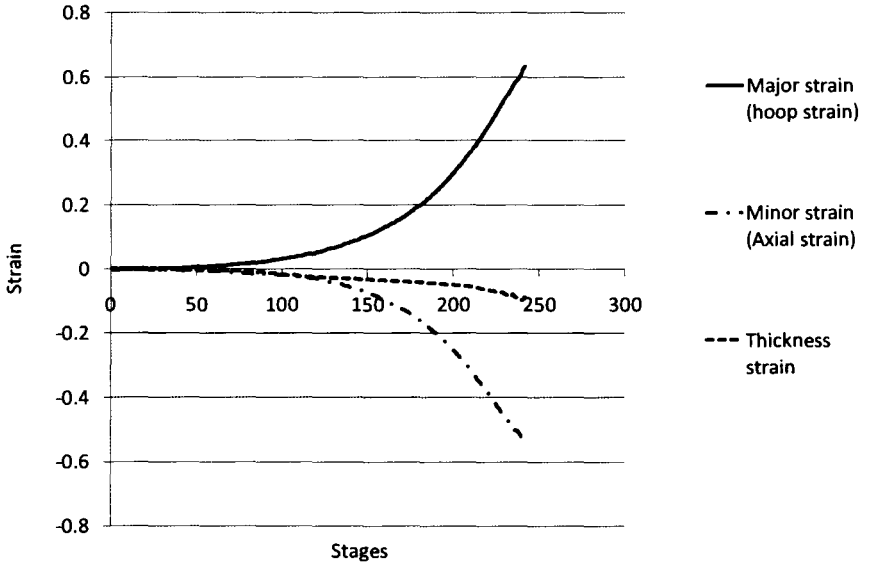

Figure A.3 True strain from tension test in hoop direction of tube at 150°C, 0.002/sec and draw ratio (DR= 5.0).

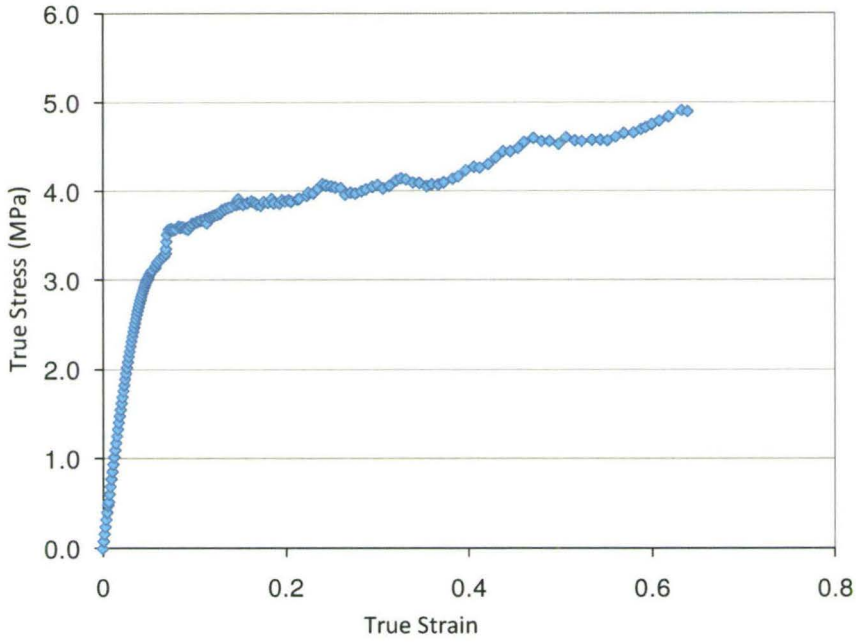

Figure A4 True stress-strain curve from tension test in the hoop direction of tube at 150°C, 1mm/min and draw ratio (DR= 5.0).

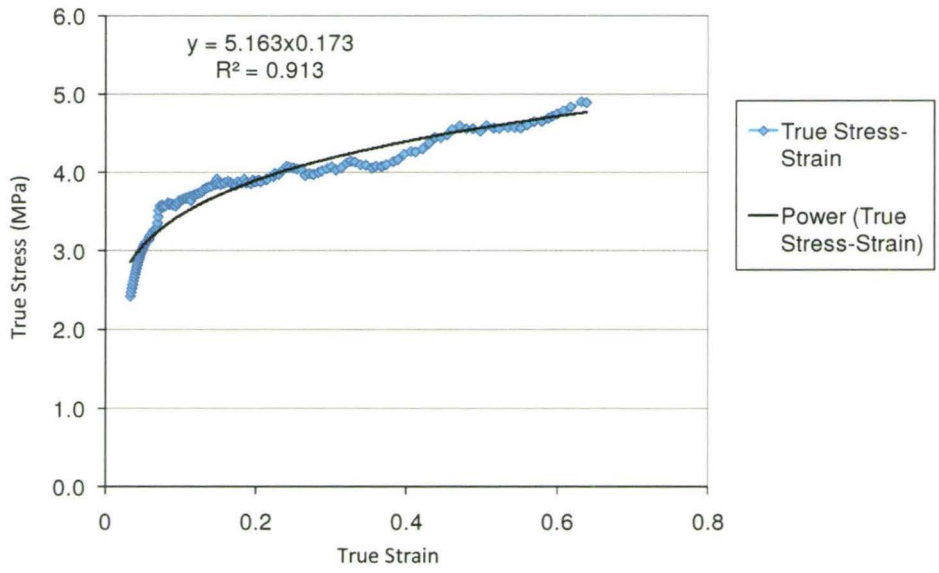

Figure A5 True stress-strain curves with a superposed fit using power law.

Appendix B

The Expansion of the Bulged Tube

The expansion of the bulge tube during free hot forming assumed occur as shown in Figure B.1

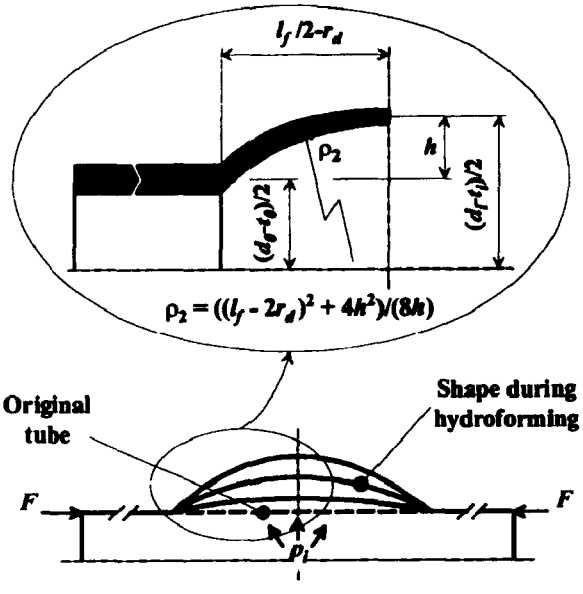

Figure B.1 The expansion of free bulge tube [Asnafi, 1999].

The internal pressure and axial force during the expansion are [Asnafi, 1999].

$$p_i = \left(\frac{2}{2-\alpha}\right)^2 \left(\sqrt{1-\alpha+\alpha^2}\right)^{n-1} .K.t_i \left(\ln\frac{d_i - t_i}{d_o - t_o}\right)^n \left(\frac{2}{d_i - t_i} + \frac{\alpha}{\rho_2}\right) \tag{B.1}$$

$$F = p_i \pi \left[\left(1 - \frac{2\alpha\rho_2}{2\rho_2 + \alpha(d_i - t_i)}\right)\frac{(d_i - t_i)^2}{2} - \frac{t_o.(2d_o - 3t_o)}{4}\right] \tag{B.2}$$

The bulge height during the expansion as shown in Figure B.1 is

$$h = \frac{(d_i - t_i) - (d_0 - t_0)}{2} \tag{B.3}$$

where

$$t_i = t_o \left(\frac{r_i}{r_o}\right)^{-(1+\beta)} \tag{B.4}$$

The radius of the tube, ρ_2, along the axial direction as shown in Figure B.1 is

$$\rho_2 = \frac{\left((l_f - 2r_d)^2 + 4h^2\right)}{(8h)} \tag{B.5}$$

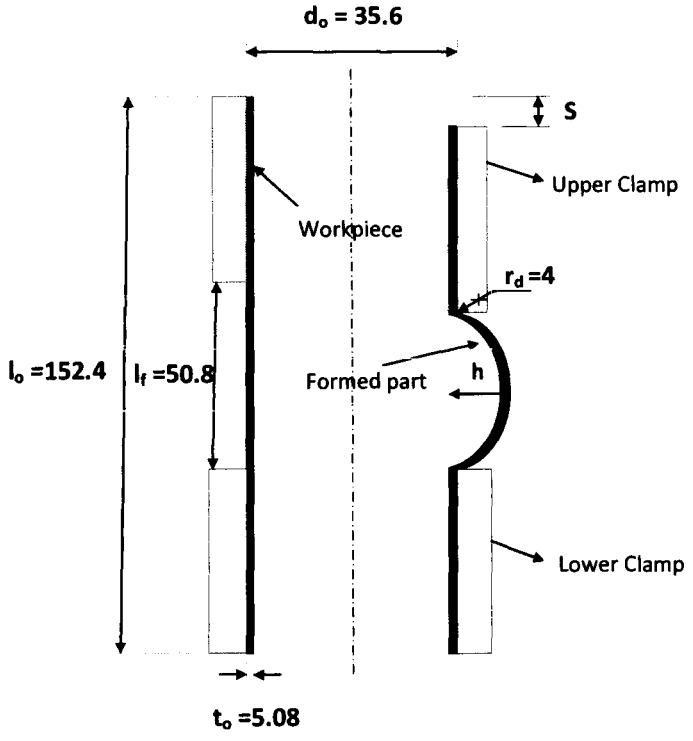

Figure B.2 A schematic of workpiece and final bulged part in mm. The nomenclature for the symbols in the sketch are as follows; s – axial feed, h - The bulge hight, t_o - Initial tube thickness, d_o - Initial outer tube diameter, l_o - Initial tube length, l_f - The length of the unsupported (or free) tube.

Parameter	Designation (see Figures B.1 and B.2)	Value
r_d	Clamp profile radius	4.0 mm
l_f	Free tube length	50.8 mm
d_o	Initial outer tube diameter	35.6 mm
t_o	Initial tube thickness	5.08 mm
l_o	Initial tube length	152.4 mm
R	Anisotropic parameter	1.50
n	Work hardening exponent	0.17
K	Strength coefficient	5.2 MPa

Table B.1 Tube dimension and material properties.

Appendix C

Orientation Distribution Function (ODF)

MULTEX AREA 2 allows the user to simultaneously view the 2-D frame data and the pole figure, the software is designed to address the entire process of texture analysis using a Bruker AXS area detector [2006]. In comparison with other methods, MULTEX AREA 2 has a small number of texture parameters that are easy to interpret geometrically.

The orientation distribution function ODF was calculated by using MULTEX AREA 2 software from the measured pole figures. The preferred orientations and directions of the texture components are first estimated interactively (by clicking the mouse in the pole figure) and then improved and calculated numerically by least squares χ^2 fit together with the other pole figure parameters. Ph(y) describes the volume fraction of crystallites having a crystallographic direction h parallel to the sample direction. For a random texture, the normalization yields Ph(y) = 1 for all sample directions **y**. The intensity of the detector signal is proportional to pole figure value Ph(y). Pole figures are proportional to the volume fraction of all crystallites whose crystal direction h is parallel to the sample vector **y**. Each component in Table C.1 is described by a Gaussian model function $f^c(g)$ and its intensity Ic, which describes the volume fraction of all crystallites

belonging to the component c. Figure C.1 represents a Gaussian model function $f^c(g)$ and a preferred orientation g^c. b^c is the full-width-half-maximum of the distribution.

A fiber component describes a preferred direction (or fiber axis) f^c relative to sample coordinate system K_S, which is parallel to the direction h relative to crystal axis K_C. The model function decreases with increasing ω, where ω is the orientation distance as shown in Figure C.2.

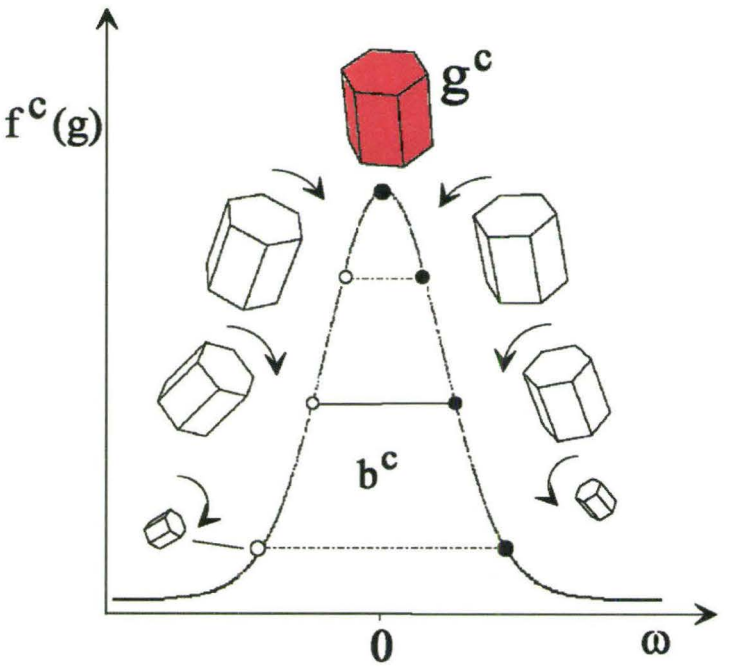

Figure C.1 A Gaussian model function with a maximum at a preferred orientation g^c. $f^c(g)$ decreases with increasing ω.

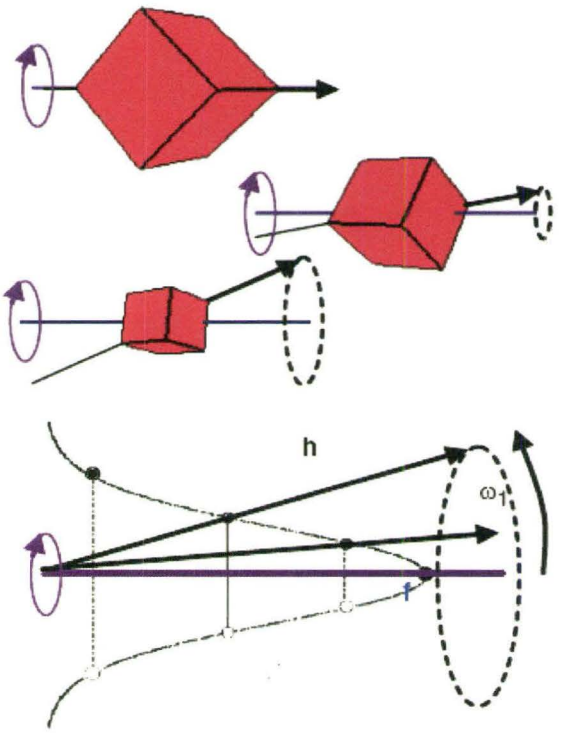

Figure C.2 A fiber component describing a preferred crystal direction h= (111) (relative to K_c) parallel to the fiber axis f (relative to K_s).

Appendix D

The Pole Figure Results and the 3D Components from MULTEX AREA 2 Software

Figures D.1, D.2 and D.3 show component fit windows for the bulged tubes with no axial feed, axial feed of 8 mm and axial feed of 18 mm respectively, also illustrated the difference between the experimental and the recalculated pole figures. The experimental pole figures with Bragg reflections of (110) and (040) were used in the simulation. Once the simulation stabilizes to a certain least square χ^2 value, a 3D component presentation window, as illustrated in Figure D.4, can be generated to display the preferred orientation of the selected component in three dimensions. This window is useful for finding correlations between intensity maxima in the pole figures and the direction of the crystal axis that belongs to the preferred orientation of the chosen component. Fiber textures in the 3D component presentation window rotate around the fiber axis f (relative to the sample coordinate system) and give an estimate of the crystal direction h that is parallel to f. The volume fraction of crystallites is a measure of how the crystal axis is oriented relative to the fibre axis. For a random texture the volume fraction is equal to 1 and, for a crystal axis oriented parallel to the fiber axis of all crystallites belonging to the component c, the volume fraction is equal to 0.

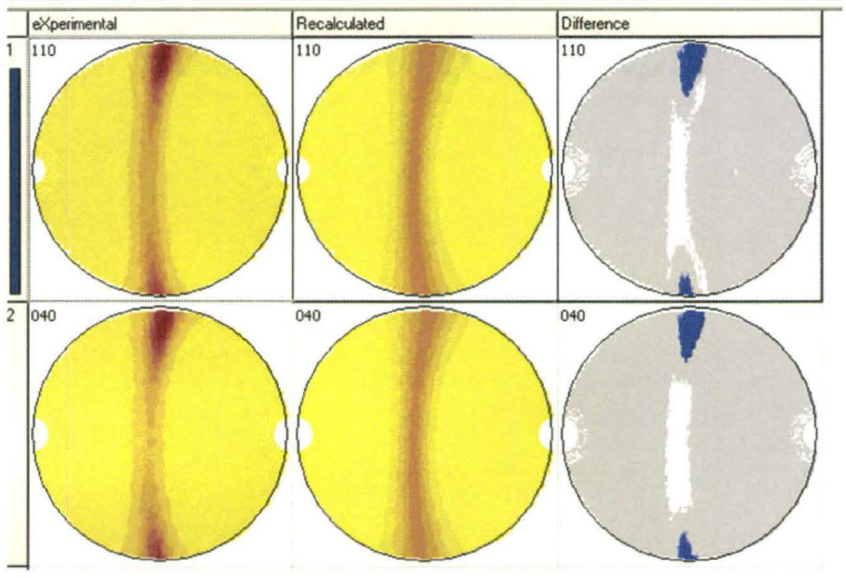

Figure D.1 Component fit window for the bulged tube with draw ratio 6.3 and no axial feed.

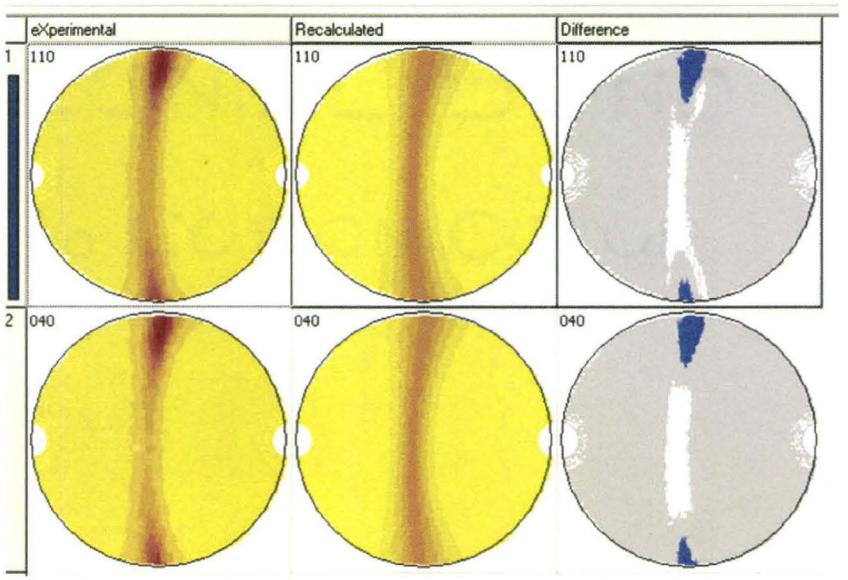

Figure D.2 Component fit window for the bulged tube with draw ratio 6.3 and axial feed of 8 mm.

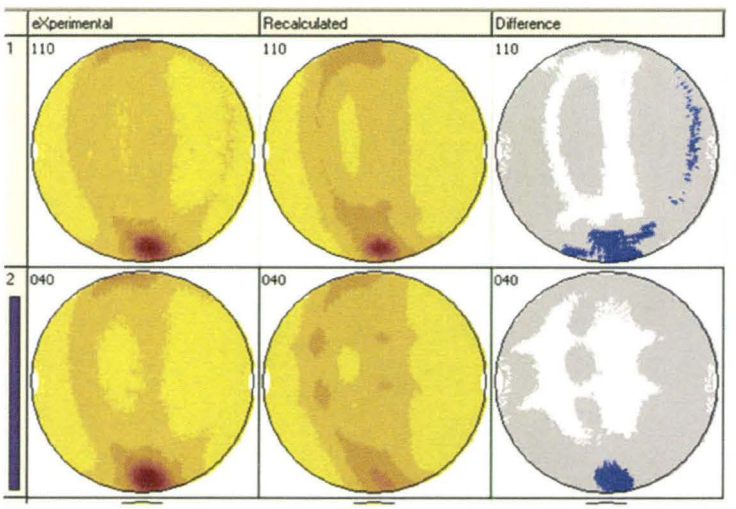

Figure D.3 Component fit window for the bulged tube with draw ratio 6.3 and axial feed of 18 mm.

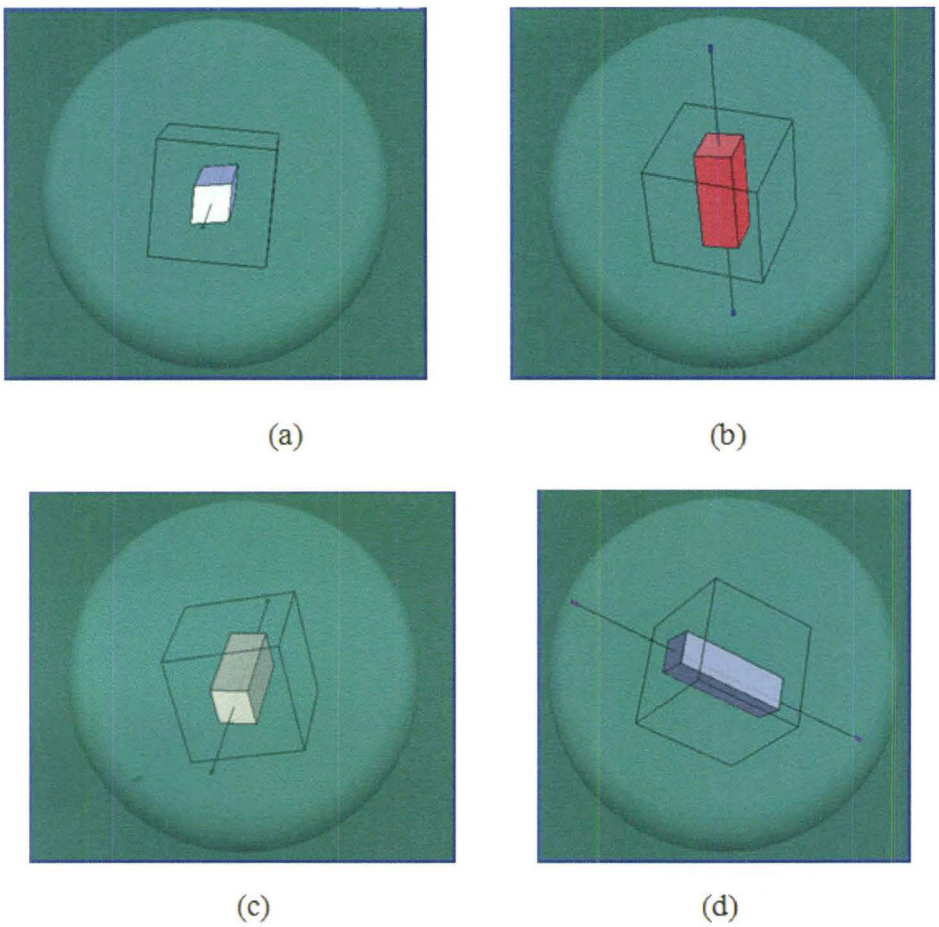

Figure D.4 A 3D component presentation window of the samples with pole figure (040), (a) The extruded tube, (b) The bulged tube with no axial feed, (c) The bulged tube with 8 mm axial feed, and (d) The bulged tube with 18 mm axial feed.

Sample Name	Bragg Reflections	Intensity (I_c)	Least Squares Fit (χ^2)	Component Number	Volume % Ph(y)	b^c	h (Pole, Azmuth)	F (Pole, Azmuth)
Ext.	(110)	777.226	817	1	50.68	9.8°	(90.7°, 99.2°)	(86.2°, 3.6°)
	(040)	681.252						
No AF	(110)	860.463	832	1	30.37	17.4°	(87.6°, 279.1°)	(78.3°, 358.2°)
	(040)	663.927		2	4.59	15.4°	(4.7°, 31.0°)	(81.2°, 89.9°)
AF=8 mm	(110)	860.748	1337	1	32.97	17.2°	(91.7°, 279.2°)	(78.3°, 358.2°)
	(040)	664.054						
AF=18mm	(110)	755.232	1044	1	3.41	12.0°	(72.1°, 9.0°)	(75.0°, 272.4°)
	(040)	686.612		2	16.64	29.4°	(89.9°, 278.4°)	(96.3°, 1.9°)

Table D.1 The results of the extruded tube with draw ratio 6.3 and the bulge tubes with axial feed 0.0, 8.0 and 18.0 mm.